## Synthesis and Design of Up-conversion Nanostructures and their Luminescence properties

## A Dissertation submitted

By

Monami Das Modak Reg. no: 14ETPM02

In partial fulfillment of the requirements for the award of degree of

Doctor of Philosophy in Materials Engineering of

School of Engineering Sciences and Technology, University of Hyderabad



## **Supervisors:**

Dr. Pradip Paik and Prof. M. Ghanashyam Krishna School of Engineering Sciences and Technology (SEST) University of Hyderabad, Central University (P.O.) Hyderabad-500 046, India.

August 2020

**Declaration** 

I hereby declare that the subject manifested in the dissertation entitled "Synthesis and Design of

Upconversion Nanostructure and their luminescence properties" is the result of the research

work carried out by me under the supervision and guidance of Dr. Pradip Paik, Associate

Professor, School of Engineering Sciences and Technology, University of Hyderabad, Hyderabad,

India for the partial fulfillment of the requirements for the award of Degree of Doctor of

Philosophy in Nanoscience and Technology. The work done and the results reported here are

original and have not been submitted in part or in full to this university or any other University or

Institution for award of any degree or diploma.

In keeping with the general practice of reporting scientific observations, due

acknowledgements have been made wherever the work described is based on the findings of their

investigations.

Date: 13<sup>th</sup> August 2020

Place: Hyderabad

Monami Das Modak,

Monamie Das Hodak

Registration No. 14ETPM02

School of Engineering Sciences and Technology

University of Hyderabad, Hyderabad, India.



#### **CERTIFICATE**

This is certified that the thesis entitled "Synthesis and Design of Upconversion Nanostructure and their luminescence properties" Submitted by Monami Das Modak bearing registration number 14ETPM02 in partial fulfilment of the requirements for award of Doctor of Philosophy in the School of Engineering Sciences and Technology is a bonafide work carried out under my supervision and guidance.

Parts of this thesis have been:

#### A. Published Papers:

- **1.** UCN–SiO2–GO: a core shell and conjugate systemfor controlling delivery of doxorubicin by 980 nm NIR pulse; Pradip Paik, K. Santhosh Kumar, **Monami Das Modak**, Koushi Kumar and Somedutta Maity; *RSC Adv.*, 2018, 8, 37492.
- 2. Graphene Oxide for Biomedical Applications; Santhosh Kumar K, Monami Das Modak and Pradip Paik; *Mini review: Journal of Nanomedicine research*, 2017, 5, 00136.
- **3.** Self-assembled pearl-necklace patterned upconverting nanocrystals with highly efficient blue and ultraviolet emission: femtosecond laser based upconversion properties; **Monami Das Modak**, Ganesh Damarla, Somedutta Maity, Anil K Chaudhary and Pradip Paik; *RSC Advances.*, 2019, 9, 38246-38256.

#### **B.** Under Communication:

- 1. Multidimensional NaYF<sub>4</sub>:Yb ,Er superlattices: Upconversion emission studied through femtosecond-laser treatment; Monami Das Modak, Anil Kumar Chaudhary and Pradip Paik.
- 2. Upconverting nanodots of NaYF<sub>4</sub>:Yb<sup>3+</sup>Er<sup>3+</sup>; Synthesis, characterization and UV-Visible luminescence study through Ti: sapphire 140-femtosecond laser—pulses; **Monami Das Modak**, Anil K Chaudhary, Ganesh Damarla, K. Santhosh Kumar, Somedutta Maity and Pradip Paik; assigned in arxiv with permanent identifier 2008.06783.

## C. Book chapter (Accepted):

1. A wide portray of Upconversion-nanoparticles: surface modification for bio-applications **Monami Das Modak**, Pradip Paik.

#### **D.** Conferences attended:

- 1. 2<sup>nd</sup> international conference on Nanoscience and Engineering applications; 2018; JNTU Hyderabad; 4<sup>th</sup> to 6<sup>th</sup> October 2018 under TEQIP-III: *Up-conversion-nanoparticles: Synthetic procedures and properties for biological applications*; **Monami Das Modak** and Pradip Paik.
- **2.** 4<sup>th</sup> International Conference on Nanotechnology for Better Living, NBL (2019) 2019; IIT-Kanpur; 6<sup>th</sup> to 7<sup>th</sup> April; *Structural and spectroscopic Properties of up converting nanoparticles: Thin-Film spectra under Femtosecond laser source*; **Monami Das Modak**, Damarala Ganesh, Anil Kumar Chaudhary and Pradip Paik.
- 3. 3<sup>rd</sup> International Conference on Advanced Materials (ICAM 2019); 2019; 9<sup>th</sup> to 11<sup>th</sup> August; *Optical properties in upconverting nanoparticles*; **Monami Das Modak** and Pradip Paik.
- **4.** International Conference on Functional Materials (ICFM-2020); 2020; IIT Kharagpur; 6<sup>th</sup> to 8<sup>th</sup> Jan; *Formations of highly fluorescent Upconverting nanoparticles (UCNPs)*; **Monami Das Modak** and Pradip Paik.
- 5. International Conference of Water energy and Environmental sustainability (WEES 2020) 13<sup>th</sup> to 15<sup>th</sup> Jan; *NIR-UV /Visible Emissions from Newly Synthesized Upconversion Nanonecklaces: Irradiations with 140- Femtosecond Pulsed-Laser*; **Monami Das Modak**, Anil K Chaudhary, Pradip Paik.

#### E. Patents Filled:

- 1. Stable upconversion nanoparticle super- lattice (UCN-SL) & in-situ process for developing thereof; Ref. No./Application No.- 201841037607
- **2.** Stable upconversion nanoparticle dendrimer (UCND) & method of making thereof; Ref. No./Application No.- 201841037609

3. upconversion nanoparticle DOT (UCN – DOT) of size 3.5 nm & its preparation process thereof; Ref. No./Application No.- 201841037608

## F. Achievements:

- 1. Best paper award in NBL-2019 conference held in IIT Kanpur on "Structural and spectroscopic Properties of up converting nanoparticles: Thin-Film spectra under Femtosecond laser source".
- **2. Best paper award** in ICAM-2019 conference held in MGIT-Kottayam on "Optical properties in upconverting nanoparticles".
- **3. Best paper award** in WEES 2020 conference held in NIT-Durgapur on "NIR-UV /Visible Emissions from Newly Synthesized Upconversion Nanonecklaces: Irradiations with 140- Femtosecond Pulsed-Laser

Further the student has passed the following courses towards fulfillment of coursework requirements for her Ph.D. Program:

Course Code	Name	Credits	Pass/Fail
MT-852	Diffusion and Kinetics & Phase Transformation	04	Pass
MT-853	Modelling and Simulation	04	Pass
MT-854	Powder Metallurgy and Ceramics	04	Pass
MT-855	Surface Engineering	04	Pass
MT-856	Metal Forming/ Design Philosophy – Selection of Materials	02	Pass
MT-857	Laboratory	04	Pass
MT-858	Seminar	02	Pass
MT-801	Research Methodology	04	Pass
MT-454	Material Characterization - II	04	Pass
MT-457	Powder Metallurgy	04	Pass



#### CERTIFICATE

This is to certify that the work contained in this Dissertation Entitled, "Synthesis and Design of Upconversion Nanostructures and their Luminescence Properties", has been carried out by Ms. Monami Das Modak (Reg. no.: 14ETPM02), under our supervision and the same has not been submitted for the award of research degree of any university. This dissertation is free from plagiarism and has not been submitted previously in part or in full to this or any other University or Institutions for the award of any degree or diploma.

Place: Hyderabad

Date: ..\3./August/2020

Posadif taik (Dr. PRADIP PAIK)

Supervisor

M-Manashyam
(Prof. M. GHANASHYAM KRISHNA -Supervisor)

Prof. M. GHANASHYAM KRISHNA Centre for Advanced Studies in Electronics Science & Technology School of Physics, University of Hyderabad HYDERABAD-500 048. Telangana, India.

Prof. Dibakar Das

DEAN

chool of Engineering Sciences and Tac

Onliversity of Hyderabad, Hyderabad 500 04

School of Engineering Sciences and Technology

3

University of Hyderabad

# DEDICATED TO MY PARENTS, MY HUSBAND, AND MY SISTER

**Acknowledgements** 

I owe sincere thankfulness to my research supervisors, Dr. Pradip Paik and Prof. M. Ghanashyam

Krishna, who guided me through the whole process of this research work and dissertation writing. I

am sure that this dissertation would not have been possible without his support, understanding, and

encouragement. I would also like to show my gratitude to my parents, my husband, my sister,

friends, and colleagues for their help and moral support.

I am truly indebted and thankful to the Dean Prof. Dibakar Das, School of Engineering Sciences

and Technology, University of Hyderabad, Hyderabad, India for his support in executing this

research work.

I would like to thank DRC member Dr. Swati Ghosh Acharyya for her constant evaluation of my

research work and her suggestions. I would like to thank all the faculty members of the School of

Engineering Sciences and Technology, University of Hyderabad, for their valuable suggestions,

encouragement, and support. I thank a lot all my lab mates who encouraged me and helped me in

executing the research work.

I would also like to thank Technical staff members, Office staff members of the School of

Engineering Sciences and Technology, technical staff of the University of Hyderabad at its various

schools and centers. I would like to thank Mr. Pankaj (TEM Operator), for their help to carry out

this research work.

I would like to give special thanks to the DST-INSPIRE fellowship scheme for providing financial

support to carry out my research work.

It is a great pleasure to thank everyone who helped me write my dissertation successfully.

Place: Hyderabad

Date: 13th August 2020

Monami Das Modak

## **Abstract**

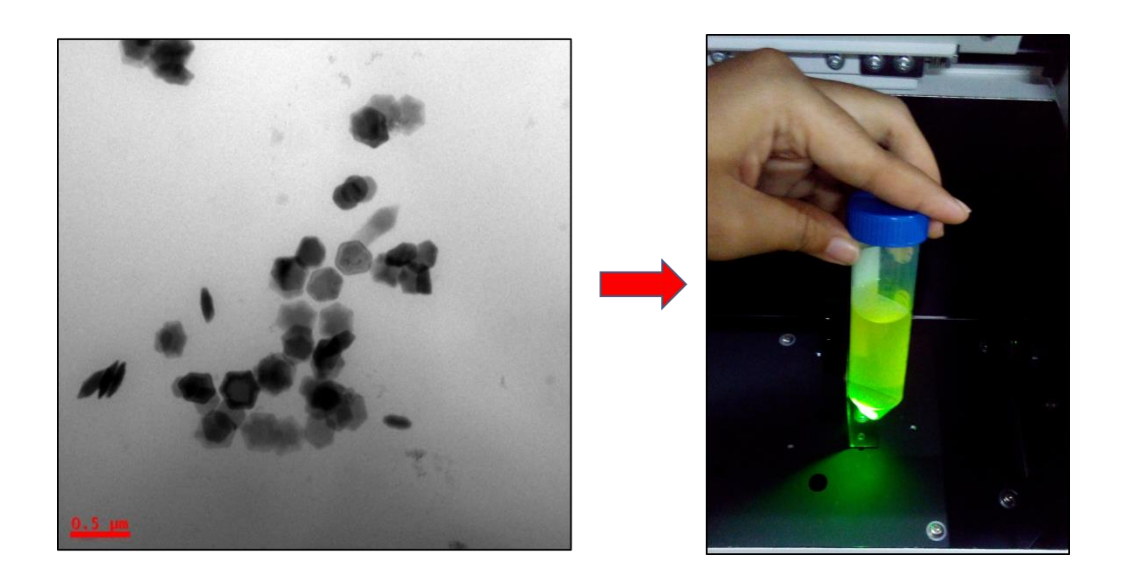
Recently there have been many innovations in research on up converting nanoparticles (UCNPs) doped with Lanthanoids (mostly Er³+, Yb³+ and Tm³+, Yb³+) through several synthetic approaches. A set of total 17 chemical elements (15 Lanthanides + Scandium +Yttrium) show up conversion phenomena by exciting with NIR radiation (lower energy, longer wavelength) which finally results in UV or visible light emission (higher energy, shorter wavelength) and makes them highly suitable for various applications. It is well known that for biological studies fluorescence/luminescence -imaging is an important phenomenon. Traditionally, high-energy photons used as excitation which results in low energy emission by down conversion process. But, this phenomenon causes some difficulties like short tissue penetration depth, lower photochemical stability, lower sensitivity, cell death, DNA damage due to excitation with higher energy. In contrast, up-conversion luminescence imaging gives better tissue penetration depth, good photochemical stability, improved sensitivity and very less probability of DNA damage and cell death, as excitation is done with low energy photons and can be used in cancer therapy for destroying cancer cells with the emerging higher energy radiation.

However, these applications are based on the emerging properties of synthesized UCNPs and obviously on their spectral properties along with fluorescence /luminescence imaging. Therefore, synthesizing UCNPs in a precisely controlled manner really remains a challenge.

The current thesis focuses on the preparation of different UCNPs synthesized with novel, one pot chemical synthesis approaches, their characterizations and spectroscopic properties along with their up-conversion fluorescence or up-conversion luminescence.

## Part-I: Synthesis of pure hexagonal -UCNPs with highly efficient upconversion fluorescence/luminescence:

In this part the novel synthetic procedure for preparation of UCNPs are explained with their characterization and efficient upconversion fluorescence in presence of continuous wavelength (CW) NIR laser source. The formation of a complete hexagonal phase, plate-like UCN nanocrystals, which can exhibit fluorescence even with laser power density of about < 50 mW/cm², is introduced.



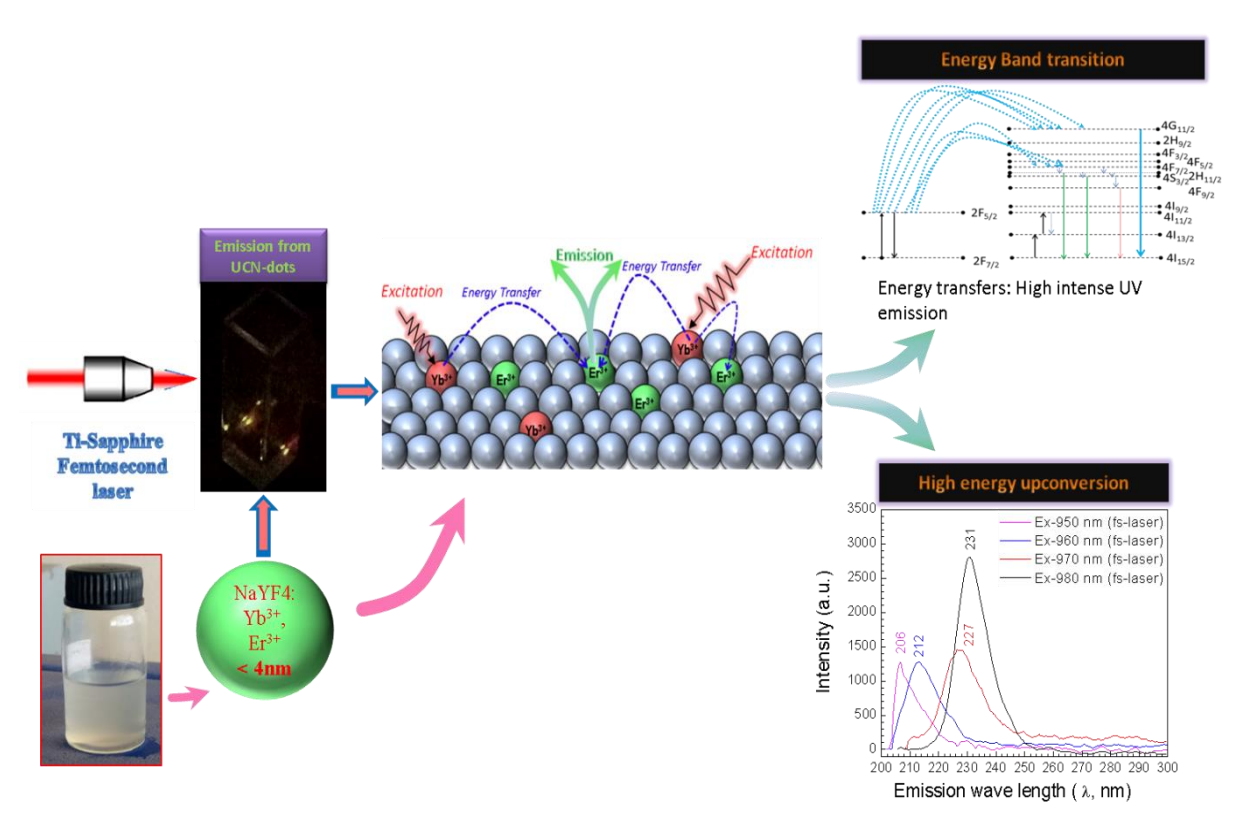
TOC 1: Figure represents the plate-like formation of UCNPs and their highly efficient fluorescence under 980nm NIR source.

Uniform hexagonal plate-like structures of NaYF<sub>4</sub>: Yb, Er UCNPs have been observed with thermal decomposition procedure. These nanocrystals show strong visible upconversion fluorescence even with low power density (<50 mW/cm<sup>2</sup>) of NIR laser. The high quality UCNPs were prepared by varying the surfactant concentrations based on previous literatures. Hence, the strategy was to consume all the fluoride reagents and then to increase the reaction temperature for improving the quality of synthesized nanocrystals. The maximum temperature

was maintained maximum upto 300 °C. The high crystallinity was confirmed with TEM and XRD analysis. These synthesized nanocrystals have great prospect in bio-imaging probes and fluorescent-labeling.

## Part II: Upconverting nanodots and generation of high energy upconversion through Ti: sapphire 140-femtosecond laser pulses

This part explains synthesis of upconverting nanodots and characterization and upconversion properties.

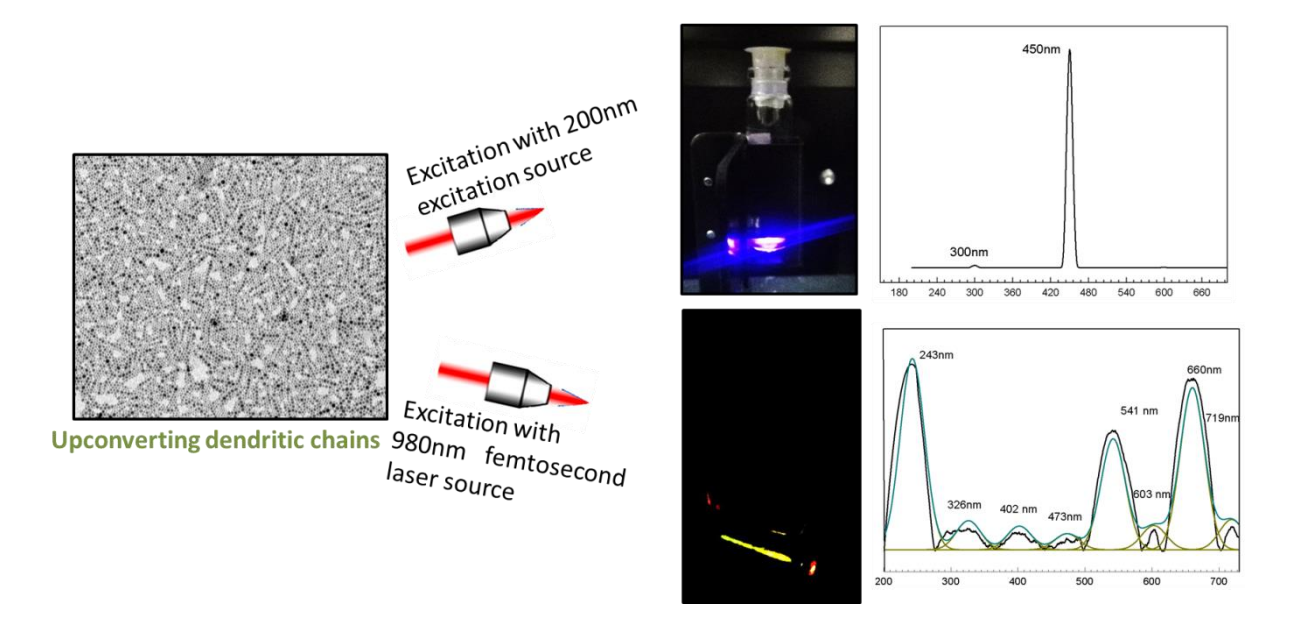


TOC 2: Figure represents the upconversion mechanism in UCN-dots (below 4nm) by different energy transferring processes

In this part of the work, dot-sized upconversion nanocrystals (UCN-dots) with diameter c.a. 3.4 ± 0.15 nm of NaYF<sub>4</sub>:Yb<sup>3+</sup>,Er<sup>3+</sup> have been synthesized. These UCN-dots exhibit blue-visible emissions under excitation with 830 nm CW-NIR laser source. Further, these UCN-dots exhibit upconversion in UV-region with Ti-sapphire femtosecond laser of 140-femtoseconds duration at 80 MHz repetition rate. This work also reports the shifting of generated UV emissions by tuning the excitations 950, 960, 970, and 980 nm irradiated from Ti: sapphire femtosecond laser under incident pump powers 1.09, 1.00, 0.955, 0.900 W, respectively and resulted an increased internal-UCQY and external-UCQY with increasing the irradiances. Further, the photo luminescence of UCN-dots in visible region has also been studied. The generation of up-conversion in UV and blue emissive regions and high UCQY could be useful further for designing optoelectronic and biomedical devices for therapeutic and for other various applications.

## Part III: Self-organized dendritic-upconverting nanocrystals with highly efficient blue and Ultraviolet emission

This work reports a new finding on the formation of self-organized upconversion nanodendrites (UCN-Ds) which exhibit strong visible emission under 980 nm NIR excitation source. Each nano-dendrite consists of several upconversion nanoparticles(UCNPs) having size c.a. 11±2 nm. UCN-Ds are arranged in a self-organized manner to form necklace type chains with an average length of 150nm. Further, UCN-Ds are comprised of almost 7 UCNPs with an average particle separation ~ 4 nm in each of the dendritic chain. Spectroscopic properties have been studied. Interestingly, these UCN-Ds exhibit high energy upconversion especially in UV region on interaction with ~140 femtosecond pulse duration at 80 MHz repetition rate and intense blue emission at 450 nm on interaction with 200nm excitation source. The preparation of self-assembled dendritic UCNPs is easy and they are very stable for a long period of time.



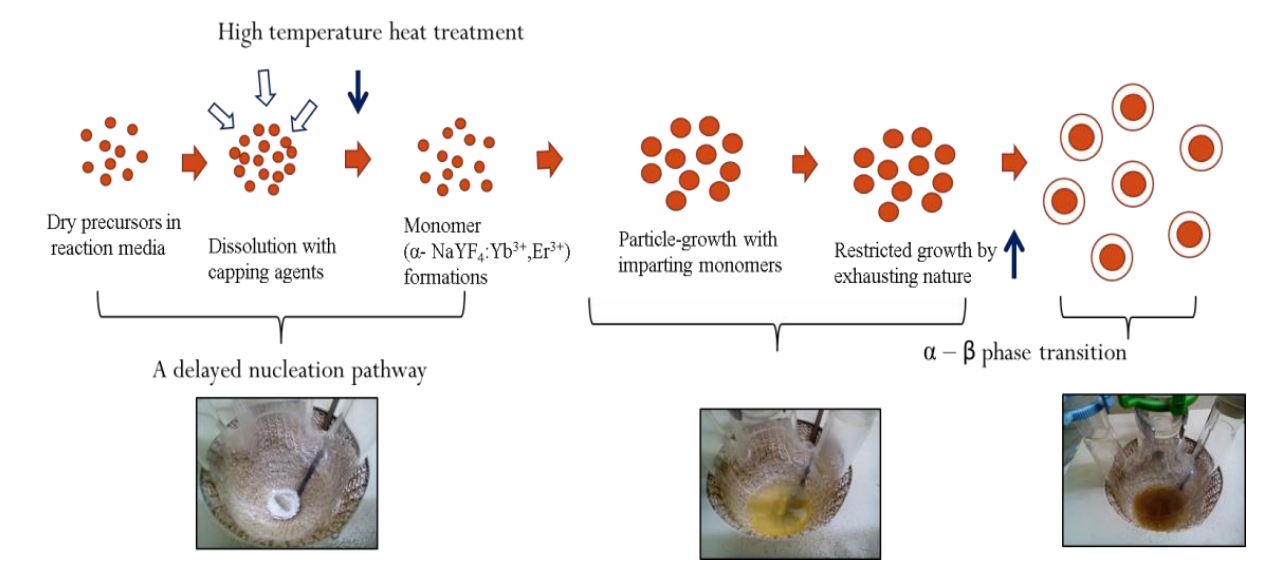
TOC 3: Figure represents the dendritic formations of UCNPs (UCN-Dendrimers) and their efficient blue emissions

Emission (fluorescence/luminescence) intensity is high which can make them a suitable unique agent in innumerable number of industrial and bio-applications.

# Part IV: Morphologically controlled upconverting self-assembled superlattices (SAM-SL UCNPs) prepared by one-pot chemical approach: Efficient luminescence observed under different pump powers

Herein this work reports on the self-assembled and in-situ formation of superlattices of upconverting nanophosphors over multiple-magnified scales prepared by one-pot chemical approach. The synthesis method is optimized. The as-synthesized nanophosphors can display sharp and bright luminescence (both in ultraviolet and visible region) and fluorescence (mostly in visible region) under Ti-Sapphire 140-femtosecond laser pulses at 80 MHz

repetition rate with 950nm-990nm excitation wavelengths and under 980nm continuous wave laser sources, respectively.



TOC 4: Figure represents schematic of the whole process succeeding the nucleation and growth mechanism along with  $\alpha - \beta$  phase transition in morphologically controlled self assembled superlattices (SAM-SL-UCNPs).

The mean particle-sizes are varied from 5-8nm. Further, the growth mechanism of differently synthesized superlattices of NaYF<sub>4</sub>:Yb,Er has also been elucidated. The internal and external quantum yield of the self-assembled superlattice structure have been expounded with different laser irradiation. The substantially improved design of nanphosphors will boost biological and energy related nanophosphor applications.

## **Table of Contents**

A	Abstract		I
T	able of Co	ntents	.VII
Τ	able of Fig	gures	XI
L	ist of Tabl	es	I
1	INTRO	DDUCTION AND LITERATURE REVIEW	1
	1.1 Ch	allenges in production	5
	1.2 Op	tical properties	6
	1.3 Dif	ferent synthetic strategies for the production of Upconversion nanoparticles	10
	1.3.1	Thermal Decomposition	10
	1.3.2	Hydrothermal or Solvothermal synthesis	12
	1.3.3	Ionic-Liquid based or ionothermal synthesis	18
	1.4 Fev	w recently developed synthetic strategies	22
	1.4.1	Microwave assisted synthesis	22
	1.4.2	Photopolymerization	23
	1.4.3	Advanced and recent Synthetic strategies in UCNPs with various advanced	
	applica	tions	24
	1.4.4	Investigation of phase transformation and morphology tuning in UCNPs	25
	1.4.5	Mechanistic Investigation of photon Upconversion	26
	1.5 Bio	ological applications of UCNPs based on their immobization to assemblies:	27
	1.6 Dif	ferent Biological applications of UCNPs	29
	1.6.1	DNA and Protein detection	33
	1.6.2	Fluorescent Resonant Energy Transfer (FRET)	35
	1.6.3	In vivo and in vitro biomedical application	36
	1.6.4	Medicinal and remedial applications	38
	1.7 Co	nclusions	48

	1.8	Mo	tivation of this dissertation:	.49
	1.9	Arr	angement of dissertation:	.50
2	EX	KPEF	RIMENTAL SECTION	.52
	2.1	Out	come:	. 52
	2.2	Ma	terials used to synthesize UCNPs:	.53
	2.3	Me	thods for synthesizing UCNPs:	.54
	2.3	3.1	Synthesis method for highly efficient hexagonal UCNPs:	.54
	2.3	3.2	Synthesis method for UCN-dots:	.54
	2.3	3.3	Synthesis method for UCN-Ds:	.55
	2.3	3.4	Synthesis method for SAM-SL-UCNPs:	.55
	2.4	Cha	racterization Techniques Used:	.56
	2.4	<b>l</b> .1	Transmission Electron Microscopy (TEM):	.56
	2.4	1.2	X-Ray Diffraction:	.59
	2.4	1.3	Atomic Force Microscopy:	.60
	2.4	1.4	Raman Spectroscopy:	. 62
	2.4	1.5	Fluorescence Spectroscopy:	. 64
	2.4	1.6	Fourier Transform Infrared Spectroscopy (FTIR):	.66
	2.4	1.7	Femtosecond laser (Fs) set-up:	.67
	2.4	1.8	Photoluminescence with Multimode Reader:	. 68
	2.4	1.9	Zetasizer nano series:	. 69
3	RE	ESUI	T AND DISCUSSION	.71
	3.1	(Pa	rt-I): Synthesis of pure hexagonal UCNPs with highly efficient upconversion	
	fluore	,	ce/luminescence:	.71
	3.1	.1	Introduction:	.72
	3.1	.2	Objectives:	.72
	3.1	3	Morphological studies of β-NaYF4 nanocrystals:	.72
	3.1	.4	EDAX analysis:	.73
	3.1	.5	X-ray diffraction analysis:	.75
	3.1	.6	AFM study:	.75

3.1.7	Raman spectroscopic analysis:	76
3.1.8	Upconversion fluorescence study:	77
3.1.9	Summary of Part-I:	78
Chapter 3 l	RESULT AND DISCUSSION	80
	art-II): Upconverting nanodots and generation of high energy upconversion  i: sapphire 140-femtosecond laser pulses	
3.2.1	Introduction	81
3.2.2	Materials Characterization:	82
3.2.3	Upconversion fluorescence with CW-980 nm laser source:	88
3.2.4	Photoluminescence	91
3.2.5	Up-conversion due to femtosecond laser (fs-laser) irradiation and High-P	'ower
band g	eneration in UV- region	93
3.2.6	Summary and Conclusions of PART II:	106
3.2.7	Calculation part of number of unit cells present in single UCN-dot:	106
Chapter 3	RESULT AND DISCUSSION	108
highly eff	art-III): Self-assembled pearl necklace patterned-upconverting nanocrystals ficient blue and ultraviolet emission: femtosecond laser based upconversitions	on
3.3.1	Introduction:	109
3.3.2	Experimental observations:	111
3.3.3	Study of Upconversion luminescence with Femtosecond (Fs)- laser source	e with
differe	nt excitation wavelengths	122
3.3.4	Discussion:	128
3.3.5	Summary and Conclusions of PART III:	130
Chapter 3	RESULT AND DISCUSSION	131
(SAM-SL	art-IV): Morphologically controlled upconverting self-assembled superlattic UCNPs) prepared by one-pot chemical approach: Efficient luminescence under different pump powers	
3 / 1	Introduction	132

Re	ferences		168
4	SUMN	MARY, CONCLUSIONS AND SCOPE of this WORK	162
	3.4.4	Summary and Conclusions of PART IV:	160
	3.4.3	Discussion:	155
	3.4.2	Results and Discussion:	135

## **Table of Figures**

Figure 1.1.1: Schematic of phase transformation in Na [Rare Earth (RE)] F <sub>4</sub> while doped with lanthanides, (a) Cubic phase, cations and vacancies sustain with equal numbers of F <sup>-</sup> cubes, (b) Hexagonal phase, two types of cation sites sustain with an ordered F <sup>-</sup> ion- array (Na <sup>+</sup> , RE <sup>3+</sup> /Na <sup>+</sup> ), (c) Shows the fashion of cubic - to - hexagonal phase transition as a function of ionic radius / polarizability of elements present in lanthanoid-series. Reproduced with permission (Wang et al., 2010). Copyright: Nature publication
Figure 1.2.1: (a) Excited State Absorption Mechanism (ESA).Reproduced with permission. Copyright: Nature Materials publication, (b) Detailed energy level diagram of the four multiplets of the Tm³+ ion. Reproduced with permission. Copyright: Optics Communications publication, (c)Two Energy Transfer Upconversion Processes (ETUs). Reproduced with permission. Copyright: Optics Communications publication
Figure 1.3.1: (A) TEM image, (B) Histogram for obtained particle- sizes with ~1400 nanocrystals. Reproduced with permission (Boyer et al., 2006). Copy right: Journal of American Chemical Society publication (C) Histogram of obtained particle sizes with ~ 500 nanocrystals. Reprinted with permission (Boyer et al., 2007). Copyright: Nano Letters publication
Figure 1.3.2: TEM images of the resulted nanocrystals after solvo-thermal treatment.  Reproduced with permission (Wang and Li, 2007). Copyright: Chemistry of Materials publication
Figure 1.3.3: TEM images of NaYF <sub>4</sub> :Yb, Er UCNPs obtained at different reaction temperatures. Reported with permission. Copyright: Chemistry of Materials publication21
Figure 1.6.1: Illustration of ligand-exchange with NOBF <sub>4</sub> .Reproduced with permission (Dong et al., 2011).Copyright: Journal of the American Chemical Society publication30
Figure 1.6.2: Illustration of secondary ligand-exchange exhibiting surface functionalization of BF <sub>4</sub> - modified Fe <sub>3</sub> O <sub>4</sub> nanocrystals with several capping molecules and their corresponding FTIR spectra. Reproduced with permission (Dong et al., 2011). Copyright: Journal of the American Chemical Society publication
Figure 1.6.3: UCNP/dye – images captured while centrifuged (before/after). UCNPs and dye molecules appeared as precipitate by centrifugation force while supernatant part appeared as clear colourless solutions in containers. Precipitation was not observed while centrifugation

UCNP- surface UCNP-dye com	ree dye molecules or PEG-PMHC <sub>18</sub> +dye mixtures. These images indicated the adsorbed three types of dye molecules rather than their encapsulation in applexes by amphiphilic PEG-PMHC <sub>18</sub> polymer. Reproduced with permission 011). Copyright: The Journal of Physical Chemistry C publication	
Figure 1.6.4: target molecule publication	Covalent conjugation of NaYF <sub>4</sub> :Yb <sup>3+</sup> , Er <sup>3+</sup> UCNPs, photosensitizer (RB), (FA). Reproduced with permission (Liu et al., 2012). Copyright: ACS Nano	
Figure 2.4.1:	Schematic of TEM system	58
Figure 2.4.2:	A schematic of XRD technique showing diffraction from two parallel plane	
Figure 2.4.3:	Schematic illustrating AFM working principle	62
Figure 2.4.4: molecule	Schematic of Raman scattering effect after interacting with substance-	63
Figure 2.4.5:	Schematic representation of Raman spectroscopy instrumentation	64
Figure 2.4.6:	A simple schematic of fluorescence spectroscopy instrumentation	65
Figure 2.4.7: repetition rate	An schematic diagram of Femtosecond laser-set up with 140 Fs, 80MHz	67
Figure 2.4.8: electric field is	A diagram to understand the phenomena for arising zeta potentials while applied on sample.	69
Figure 3.1.1: formations with (panel-e).	TEM images of of the synthesized hexagonal UCNPs, clear hexagonal scale bar 1μm (panel-a,b); 500nm (panel-c);100nm(panel-d); SAED pattern	
Figure 3.1.2 presence of eler	TEM-EDAX spectrum of synthesized β-NaYF <sub>4</sub> nanocrystals showing the mental compositions	74
Figure 3.1.3: crystalline plane	XRD pattern of the resulted β-UCNPs confirming the presence of different es	75
Figure 3.1.4:	AFM study reveals the formation of perfect hexagonal shapes in $\beta$ -NaYF <sub>4</sub> .	76
Figure 3.1.5: phases below 10	Raman study of $\beta$ -NaYF <sub>4</sub> confirming the appearances of strong hexagonal $000\text{cm}^{-1}$	76
Figure 3.1.6:	The upconversion fluorescence spectrum shows violet, green and red	77

Figure 3.1.7: The intense emissions both in UV and in visible range upon interaction with femtosecond laser 980nm excitation source. The intense shows the visible emissions78
Figure 3.2.1: (a), (b) and (c) TEM micrograph of UCN-dot: low to high magnification. (c) Represents the fringes of the particles (d) Magnified image of the fringes. (e) Represents the selected area electron diffraction pattern (SAED) obtained from TEM and (f) profile of the fringes
Figure 3.2.2: Histogram particle size and distribution calculated from TEM micrograph 83
Figure 3.2.3: Zeta potential for colloidal UCN-dot sample
Figure 3.2.4 EDAX analysis of UCN-dots colloidal sample
Figure 3.2.5: XRD of UCN-dots represents the crystalline phase (cubic, FCC) of UCN-dot. In sets are showing enlarge peaks for (111), (220) and (222) planes
Figure 3.2.6: Raman Spectra for the UCN-dots, (a) for the full region. (b) band region 100 cm-1 to 1000 cm-1 representing the major $\alpha$ -phase of NaYF4:Yb3+;Er3+dots, (c) 800 cm-1 to 2600 cm-1 and (d) 2500 cm-1 to 3300 cm-1, exhibiting the presence of major capping agents in cubic phases 86
Figure 3.2.7: Fluorescence Spectra of UCN-Dot-colloidal solution in cyclohexane with a 980 nm continuous wave (CW) NIR excitation (Power Density 1000 mW/ cm2) exhibiting four significant emission bands at room temperature (b) The relevant energy diagram of dot-sized upconverting nanocrystals and upconversion processes succeeding 980 nm laser-diode excitation. Further it predicted energy transfers (with three direct energy transfers) with their corresponding pathways (c) Three images are with colloidal solutions and showing the visible emissions under 980nm laser CW
Figure 3.2.8: (a) PL spectra of the UCN-dots of size 3.5 nm. The spectrum was obtained with excitation wavelength of 450nm. The peak positions represent the different transitions of the photons at the visible region (b) energy transitions within electronic states of PL spectra obtained with excitation wavelength of 450nm
Figure 3.2.9: (a) Schematic diagram of a complete experimental set up for femtosecond laser study (b) Visible emissions (right) with femtosecond laser source (left) during experiment
Figure 3.2.10: (a) Up-conversion Luminescence spectra in the UV-region (on excitation with fs-laser), exhibited red shifting with increasing excitation wavelengths (b) Up-conversion Luminescence spectra at the visible region for different fs-laser

excitations(c) Band gap energies received from different fluorescence spectra under different excitation fs-laser sources
Figure 3.2.11: Dependence of Up-conversion luminescence intensity on fs-Laser power for (a) deep-UV, (b) Green G1(c) Green G2 and (d) Red (R) related emission (excited fs-laser), respectively. The number of absorbed photons per photon emitted under the fs-laser excitation power "n" value determined for the deep-UV, G1, G2 and R emissions for UCN-dot and their values also mentioned in the respective plots97
Figure 3.2.12: (a) Energy band diagram (energy transitions) under femtosecond laser source and (b) visible emissions in sample-cuvette during experiment (images are taken with five observations).
Figure 3.2.13: Plots intensity [a.u.] vs excitation wavelength [nm] for UV, G1, G2, R
Figure 3.2.14: (a-d) Plots for peak ratios vs excitation wavelengths (nm) (a) G1/R, G1/G2 vs $\lambda_{ex}$ (b) R/G1, R/G2 vs $\lambda_{ex}$ (c) Gfull vs $\lambda_{ex}$ (d) UV/G1, UV/G2, UV/R vs $\lambda_{ex}$ 101
Figure 3.2.15: (a) and (b) Show the External-UCQY (%) and Internal-UCQY (%) with excitation power density for emission in UV regime, respectively; (c) and (d) show External-UCQY (%) and Internal-UCQY (%) with excitation power density for the emission in visible regime, respectively for UCN-dots of NaYF4:Yb <sup>3+</sup> :Er <sup>3+</sup>
Figure 3.2.16: Brightness (w.r.t internal Q.Y. in UV emission) vs excitation power density curve
Figure 3.3.1: TEM images of the synthesized colloidal-dendritic UCNPs (UCN-Ds at different magnifications. Panels: $(a,b)=200$ nm,inset in panel (b) shows the clear formation of dendrimers (c) = 20nm, (d),(e) = High resolution micrograph showing lattice fringes, (f)=SAED ring pattern, Histogram of (g)= particle diameter, (h) nano-necklace length, (i)total number of particles per necklace, (j) interparticle-separation
Figure 3.3.2: XRD study of synthesized UCN-Ds confirms the crystalline structure. Insets show the observed peaks with their corresponding crystalline planes according to JCPDS-028-1192
Figure 3.3.3: EDXA spectrum of UCN-Ds confirming the presence of elements
Figure 3.3.4: (a) Upconversion emission spectrum examined with UCN-Ds colloidal solution (b) corresponding energy diagram, under 980nm NIR-laser excitation source 115

Figure 3.3.5: (a) Upconversion emission spectrum obtained with λexcitation of 200 nm CW laser source. In-set of (a) is showing the blue emission from UCN-ds and (b) is the corresponding energy band diagram
Figure 3.3.6: (a) Image is captured during synthesis (stirring condition) of UCN-Ds at high reaction temperature(~330°C - 340°C) with 1 hr 53 mins reaction time (b) UCN-Ds colloidal sample and (c) Intense blue emission in sample glass bottle, after washing done completely
Figure 3.3.7: Zeta potential value found to be -55.49 mV for colloidal aqua solution of UCN-Ds
Figure 3.3.8: (a) Raman spectrum between 200-1200nm, (b) Raman spectrum between 2600-3800nm, confirm the presence of both cubic ( $\alpha$ ) and beta ( $\beta$ ) phases in sample. The measurement was recorded at room temperature (figure 3.3.9)
Figure 3.3.9: Raman spectrum of UCN-Ds with entire region
Figure 3.3.10: FTIR spectrum of UCN-Ds confirming the presence of different groups in oleic acid and formation of UCNPs
Figure 3.3.11: (a) Photoluminescence (PL) spectra of colloidal UCN-Ds sample obtained with 450 nm excitation wavelength (b) Energy diagram drawn from PL emission spectra in (a)
Figure 3.3.12: Upconversion luminescence spectra and their corresponding energy diagram with femtosecond (Fs) arrangement. (a) Spectra(i) and energy level diagram(ii) under 940nm; (b) spectra (i) and energy level diagram(ii) under 950nm; excitation wavelengths
Figure 3.3.13: Upconversion luminescence spectra and their corresponding energy diagram with femtosecond (Fs) arrangement. (a) spectra(i) and energy band diagram(ii) under 960nm; (b) spectra(i) and energy level diagram(ii) under 970nm; (c) spectra(i) and diagram(ii) under 980nm excitation wavelengths
Figure 3.3.14: Shows the ratio plots for the intensity of different emission: (a) $UV_{full}/G$ , (b) $UV_{full}/R$ full; (c) $G/R1$ , $G/R2$ , $G/R3$ ; (d) $G/R_{full}$ vs excitation wavelengths
Figure 3.3.15: (a) Schematic of Femtosecond laser (Fs)set-up arrangement (b) Images are captured while visible emissions are observed in cuvette-sample once it is excited with Fs-laser sources
Figure 3.4.1: TEM images of self-assembled formations of UCNPs with 15-20 mins high reaction temperature, panel (a) - 50nm scale bar, panel (b-d) - 20nm scale bar, panel (e)-

SAED pattern. (b) - formation of {100} and {111} facets on substrate, (c,d) - formations of UCN-nanochips, (a) show planar defect-twinning effect, panel (f) The cross section of a formed nanocluster on substrate
Figure 3.4.2: TEM images of self-assembled formations of UCNPs with 51 mins of high reaction temperature, panel a- 200nm, panel b, c - 100nm, panel d-f- 50nm panel g- 20nm, panel h- SAED pattern. (a), (c), (f), (g)- Formation of monodisperse nanoparticles, (a)- Short range particle-packing order, (b) - conversion of an FFT image derived from a hexagonal cluster orientation where the synthesized nanocrystals are oriented along [100], [111] (c)-planar defect with twinning effect, (d)Hexagon arrangement and (e)rod-like parallel assembly of synthesized UCNPs
Figure 3.4.3: panel (a) -200nm, panel (b)- 100nm, panel (c,d) – 50nm, panel(e)- 20nm, panel (f)- SAED pattern, (c,d,e) - clear 3D assembly with a complete hexagon-type formations 138
Figure 3.4.4: (a) A bundle of surfactants act as channels between the assembled nanoparticles containing different stretches and vibrations; O-H, C-O, C-C, C-H, CH3; (b) A schematic diagram of planar defects appeared in SAM-SL UCNPs
Figure 3.4.5: The XRD pattern for three different Exsets (1,2,3) confirming the appearances of major cubic, mixed crystalline and major hexagonal phases, respectively
Figure 3.4.6: The Raman analysis strongly indicate the appearances of (a) major cubic (b) cubic and hexagonal (c) major hexagonal phases in exset- 1, 2 and 3 respectively
Figure 3.4.7: Fluorescence spectra recorded at room temperature with changing excitation wavelengths from 800nm to 900nm; Fluorescence with (a) exp. Set up 1 (i) Full region (ii) UV region;(b) exp. Set up 2 (only full region is shown, no fluorescence occurred in UV region;(c)exp. Set up 3 (i) Full region (ii) UV region
Figure 3.4.8: Fs-laser based upconversion spectra for (a)Exset-1 (b) Exset-2 (c) Exset 3)(d)Energy level diagram of synthesized SAM-SL –UCNPs (e) Intense visible blue emissions under NIR excitation sources (800-900nm). : (f) associated energy level diagram of different SAM-SL-UCNPs under femtosecond laser source
Figure 3.4.9: "n" –values received from fs-laser power dependent formula and have been derived in deep UV, green and red visible regions for three Exp. Sets -1, 2 and 3 in $(a)(b)(c)$ , respectively. The highest values occurred for Exset – 3
Figure 3.4.10: Ratio plots for the intensities of different emissions of three SAM-SL-UCNPs colloidal solutions with different excitation radiations (a) ratio of UV/Green emission intensity, (b) ratio of UV/Red emission intensity (c) ratio of red/green emission intensity 151

Figure 3.4.11: Plots for External and internal Quantum yields of Exset-1(a&b), Exset-2(c&	zd),
and Exset-3(e&f), respectively	154
Figure 3.4.12: A schematic of the whole process succeeding the nucleation and growth mechanism along with $\alpha-\beta$ phase transition. The corresponding exp. investigations are also placed.	
Figure 3.4.13: The mechanism associated with the formation of monomers and particle-	
growth	159

## **List of Tables**

Table 1.3.1: Different crystallization, shape and surface pattern with different amount of NaF:Ln ratio	15
Table 1.3.2: Molar ratio of chelator: lanthanide affecting the morphologies of NaYF <sub>4</sub> : Yb <sup>3+</sup> ,Er <sup>3+</sup> nanocrystals	16
Table 1.4.1: Tunable morphology of UCNPs with controlling K <sup>+</sup> ions	26
Table 2.2.1: Materials used to synthesize UCNPs:	53
Table 3.1.1: Elemental compositions in synthesized β-UCNPs	74
Table 3.2.1: Table for elemental analysis from EDAX	85
Table 3.2.2: Band Gap Energy (Eg) of UCN-dots with different excitation photon energies (Fs) and single photon energy (FL, PL)	
Table 3.3.1: Elemental compositions observed in EDAX spectrum	.114
Table 3.4.1: Tabulated form of "n" values in three different Experimental sets (Exsets) alo with their corresponding energy level diagram	_
Table 3.4.2: Tabulated form of intensity ratio values in UV and visible region under	.152
Table 3.4.3: Shows the Quantum Yield (QY) for the different samples	.153
Table 3.4.4: Shows the External Quantum yield	.153
Table 3.4.5: Shows the Internal Quantum yield	.154

## 1 INTRODUCTION AND LITERATURE REVIEW

## **Outcome:**

**Monami Das Modak**, Pradip Paik, Review article: A wide portray of upconversion-nanoparticles with their several synthetic procedures and biological applications, Manuscript accepted.

**Monami Das Modak**, Pradip Paik, Upconversion nanoparticles: synthetic procedures and properties for biological applications, conference proceedings, THEME: Advanced Nanomaterials ICONSEA-2018, ISBN No.978-81-924726-4-5

Present-days have spotted many innovations in research on upconverting nanoparticles (UCNPs) co-doped with Lanthanoids (mostly Er<sup>3+</sup>, Yb<sup>3+</sup> / Tm<sup>3+</sup>, Yb<sup>3+</sup>) through several synthetic approaches. A set of total 17 chemical elements (15 Lanthanides + Scandium +Yttrium) show upconversion phenomena by exciting with NIR radiation (lower energy, longer wavelength) and finally results in visible light (higher energy, shorter wavelength) which makes it highly delightful for various applications. It is well known that for biological studies fluorescence-imaging is an important phenomenon. Traditionally, as excitation radiation high energy lights are used which result in low energy emission by downconversion process. But, this phenomenon causes some difficulties like short tissue penetration depth, lower photochemical stability, lower sensitivity, cell death, DNA damage due to excitation with higher energy, whereas upconversion luminescence imaging gives better tissue penetration depth, good photochemical stability, improved sensitivity and very less probability of DNA damage and cell death as herein excitation is done with low energy photons and can be used in cancer therapy for destroying cancer cells with the emerging higher energy radiation. Herein this review several current progresses with Upconversion nanoparticles (UCNPs) in recent applications along with their different synthesis procedures, optical properties and growth of erection methods of different UCNPs applications have been highlighted based on their immobilization strategy.

Upconverting nanoparticles (UCNPs) have already been established for prospective use as bio-labels and in biological analysis and bio imaging which are the most promising technologies today. These promising and advanced technologies suggest that UCNPs could reconstruct the enduring technologies due to their ability to suspend as clear colloidal solutions [1]. Until now, the highest upconversion efficiencies have been reported in NaYF<sub>4</sub> hexagonal phase co-doped with Er<sup>3+</sup>/ Yb<sup>3+</sup> or Tm<sup>3+</sup>/Yb<sup>3+</sup> ion-pairs [2][3].

Selection of host material is an important factor for achieving Upconversion phenomenon properly. To achieve highest luminescence quantum yield and less probability of occurrence of non- radiative relaxation, nowadays fluoride is used in host materials such as REF<sub>3</sub> and AREF<sub>4</sub> (A=Alkali). As a result, they help to increase refractive index and transparency. Though Chlorides and Bromides can also enhance luminescence intensity, but they are mostly sensitive to moisture, so difficult for imaging bio-molecules. Therefore, adding of fluoride in host materials is an increasing phenomenon today. Photon Upconversion process is based on non-linear optics, where the optical properties of material changes with the intensity of the incident exciting light. But are they noteworthy and adaptable enough to explain the difficulties of redirecting to a new technology, conventionally a lengthy and precious procedure? Could UCNPs become the upcoming wild materials reconstructing some of the contemporaneously used technologies and leading to the advanced research? Is it flexible as many as required to transmute many features in our life? By reviewing different proposed synthetic procedures, allowing their several applications in different fields those questions will be answered. Though there are several synthetic routes for preparing UCNP nanocrystals, among which hydrothermal synthesis has a lot of favorable advantages compared to the low reaction temp process (< 250°C); and it resulted in uniform distribution of size, shape and morphology. The procedure and the experimental set-up used in these methods are easy to handle and very simple. In such case, basically three conditions are responsible to convert alpha (α- NaYF<sub>4</sub>) phase to beta (β- NaYF<sub>4</sub>) phase, they are high hydrothermal temperature, long hydrothermal time and high fluoride to lanthanide molar ratio [4].

So initially, the observed properties in UCNPs will be discussed.

By Raman spectroscopy, it has been confirmed that the dominant phonon modes in undopped NaYF4 lie in the range 300- 400 cm<sup>-1</sup>. These low energy phonon modes describe the remarkable Upconversion efficiency [5]. By the implementation of the plasmonic effects, it is possible to enhance upconversion fluorescence which has been already done by directed nano-assembly of NaYF<sub>4</sub>:Yb<sup>3+</sup>/Er<sup>3+</sup> nanocrystals with gold nanospheres [6]. From literature it has been observed that, crystallographic size, crystallographic phase (Schietinger et al., 2010) and optical emission properties of such resultant nanocrytals can be controlled simultaneously by influencing them with dopant ions[7]–[11]. By controlling concentration of trivalent

lanthanide dopant ions, it is quite possible to tune size (down to 10 nm), shape (cubic to hexagonal) and upconversion emission colour (green - blue) of NaYF<sub>4</sub> nanocrystals [12]-[14]. There are two factors of dopant ions their size and dipole polarizability that can change the crystal size and shape of resultant nanocrystals. UCNPs can offer high photochemical stability, sharp emission bandwidths and large anti-stokes shift [15]. There are four experimental variables which are, solvent in nature, reaction time and temperature, metal precursor concentration that inflict stiff sway over crystallization of resultant particles with completely explained crystal phase and size. Hexagonal UCNPs phase structure is always preferable compared to cubic structure in various applications. There is a huge difference (almost by a factor 7.5) in fluorescence intensity between its cubic and hexagonal phase nanoparticles[16]. Despite these drawbacks, in cubic-phase, sometimes we prefer cubic phases in as-synthesized UCNPs depending on their particular sizes, shapes, crystallinity, fluorescence properties and easy dispersion in non-polar solvent. Generally, it has been noticed that the structure of NaREF4 system for both cubic and hexagonal phase differ on the basis of F cubes and ions present in them. In cubic structure, cations and vacancies sustain with uniform numbers of F cubes whereas for hexagonal structure, F ions are seated in an ordered array, to fit the structural change, electron cloud deformation of cations is crucial (figure 1.1.1). Basically, one ordered way is maintained for lanthanides. As Lanthanide series start from Lanthanum (La), finishes with Lutetium (Lu) (Lanthanide series-La, Ce, Pr, Nd, Pm, Sm, Eu, Gd, Tb, Dy, Ho, Er, Tm, Yb, Lu), now if we move towards higher atomic no. and lower atomic mass i.e. from La to Lu, weight will decrease and ionic radii will increase, dipole polarizability increases, tendency towards e- distortion cloud increases which is the appreciative condition for hexagonal phase. So, formation of hexagonal phases in Lanthanides having higher atomic number will be more than that of having lower atomic number. Size of  $Y^{3+}$  ion is (r = 1.159 A°) in NaYF<sub>4</sub> host lattice. More hexagonal phases will be produced for doped lanthanide ions having larger size (i.e. for  $Gd^{3+}$  ion  $r = 1.193 \text{ A}^{\circ}$ ) than the size in  $Y^{3+}$  in host lattice and finally the growth of unit cell volume occurs due to the presence of larger sized lanthanide dopant ions [15].

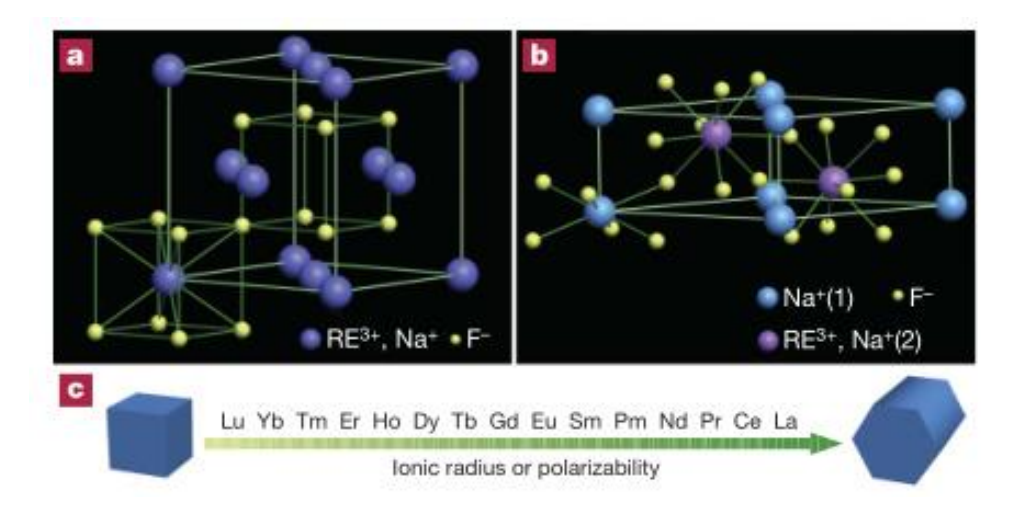


Figure 1.1.1: Schematic of phase transformation in Na [Rare Earth (RE)] F4 while doped with lanthanides, (a) Cubic phase, cations and vacancies sustain with equal numbers of F - cubes, (b) Hexagonal phase, two types of cation sites sustain with an ordered F - ion- array (Na+, RE³+/ Na+), (c) Shows the fashion of cubic - to - hexagonal phase transition as a function of ionic radius / polarizability of elements present in lanthanoid-series. Reproduced with permission (Wang et al., 2010). Copyright: Nature publication

## 1.1 Challenges in production

There are several applications of UCNPs having different shapes, sizes and structures, which can be significantly controlled by their development with a number of designed synthesis procedures and their dispersions in various media. Now depending on the notable properties and the quality of UCNP (either in dried or in colloidal form) in as-synthesized materials they can be used in different potential applications such as in silicon based solar cell as spectral converters[17]–[31], in optical imaging and MRI as a multimodal contrast agent [32], [33], in FRET Biosensors[34]–[39]; as Colour display[10], [40]–[45], versatile bio-probes in Biomimetic surface – engineering[46], nanoprobes for sensing and imaging of pH[47]–[51], cells and small animals[52]–[54], nano-transducers for killing diseased cells in deep tissues [55], the most viable luminescent bio-labels in bio-conjugation and bio-imaging [56]–[63].

Therefore, the production of those UCNPs with required sizes, shapes and structures is very crucial for different applications. During their preparation, all the reaction parameters are being controlled in a precise manner due to the high sensitivity of the products through their formation periods. Thus, the production of UCNPs is challenging.

If we go through the literature reviews, we will find that mostly several optical properties became prominent for their applications. This is the main property for which they are being broadly used in nanotransducers[55], [64]–[67], broad brands[23], [25], [68], [69], Imaging contrast agent [33], multimodal imaging [70],[71], superresolution- nanoscopy [72][73], imaging probes [74], and so on. Therefore, review has been focused briefly on optical properties with possible photonic processes for UCNPs.

## 1.2 Optical properties

Lanthanoids exist in Lanthanide series and there are total of 15 lanthanoids. Though transition metals (Scandium, Yttrium), where atoms have partially filling 'd' sub-shell and elements in actinide series can exhibit Upconversion phenomena, but specially RE elements having combination of 15 lanthanoids + Scandium + Yttrium, a set of total 17 chemical elements show Upconversion phenomena very strongly, i.e. by exciting that Lanthanide doped nanocrystals with NIR radiation. In the Upconversion process, we can get visible light with the emission of higher energy photons. Thus, Upconversion process converts low energy, long wavelength NIR radiation to high energy, short wavelength visible light. The optical properties of Upconversion nanoparticles arise due to conversion of Near Infrared radiation (NIR) into visible spectral range, which is a very efficient phenomenon in rare-earth based materials. The nanocrystals based on rare-earth ions showed strong Upconversion emission with a continuous excitation wavelength at 973 nm [6]. Therefore, they have a great potential in applications of solid-state laser materials as well as several lighting, panel and colour display technologies [75]–[77]. It is well known to us that NaYF4 nanocrystals co-doped with Yb<sup>3+</sup> and Er<sup>3+</sup>/Tm<sup>3+</sup> are the most promising Upconverting nanomaterial today as these

nanocrystals are sensitized by  $Yb^{3+}$ (sensitizer )and multicolor wavelength range can be distinguished from  $Er^{3+}$  or  $Tm^{3+}$  (activator) dopant ions.

Experimentally and theoretically it has been already proven that most of the lanthanide ions exhibit visible light under excitation with NIR radiation but sharp luminescence imaging can be observed by Upconversion process under 980nm excitation if some of them such as  $Er^{+3}$ ,  $Tm^{+3}$  are co-doped with the host lattice like NaYF<sub>4</sub>, hence the productive forms are written as NaYF<sub>4</sub>: Yb<sup>3+</sup>; Er<sup>3+</sup> / NaYF<sub>4</sub>: Yb<sup>3+</sup>; Tm<sup>3+</sup>.

Some important luminescence properties can be observed with using such UCNPs such as narrow band width with shorter wavelength compared to the excitation wavelength i.e. antistokes type emission and long-time emission[12][78]. To get Upconversion phenomenon properly, choosing of host material is an important factor. To achieve highest luminescence's quantum yield and also less probability of occurring non-radiative relaxation nowadays fluoride is used in host materials such as REF<sub>3</sub> and AREF<sub>4</sub> (A=Alkali), as a result they help to increase refractive index and transparency though chlorides/ bromides can also enhance luminescence intensity. However, they are very sensitive to moisture and possess difficulty for imaging of bio-molecules and cells. To overcome this limitation, fluoride molecules are added in the system. The main difference between fluorescent and luminescent materials is their different characteristics. Fluorescent materials absorb high-energy photons with the emission of visible light and low energy photons, which results in auto fluorescence, wide emission bands and limited sensitivity. To overcome these difficulties Upconverting luminescent nanoparticles with high quality developed promptly. Trivalent rare earth (RE) ion (Ho<sup>3+</sup>, Er<sup>3+</sup>, Tm<sup>3+</sup>) follows Upconversion process fairly [79]. By incorporating a few energytransfer related mechanisms, we will try to understand the photon-generation mechanism in UCNPs.

There are some basic mechanisms which results in highest population in excited state and after that when they come in the ground state, emit high-energy photons. Multiphoton absorption occurs by the Excited State Absorption Mechanism (ESA) [79] (figure 1.2.1) which further involves multistep excitation by the same ion and finally highest population

occurs at the excited state. This process is also known as phonon assisted electronic transitions [75][79].

Suppose, Energy of incident photons has flux  $\phi$  (Say) is resonant with the energy difference (E<sub>1</sub> – E<sub>0</sub>), then some of the photons are absorbed from the ground state by the particular ion. Similarly, while the energy of the incident photons having certain flux resonant with the energy difference (E<sub>2</sub> – E<sub>1</sub>), then only incoming photons can be absorbed in the intermediate state by the same ion. Now the population in the excited state becomes high and consequently the ion reaches to its high-excited state, but this phase is not stable from this excited state and finally, upconversion luminescence occurs by radiating photons. We have considered this process for a single ion so we can assume that it is independent on ion-concentration. According to literature, anti-stokes fluorescence is proportional to the incident photon flux such that, for above-mentioned case fluorescence is directly proportional to the square of the incident photon flux. ESA process is quite relative with the laser pumping process. As it avoids transfer losses, so it is assumed to be a suitable pumping process for Upconversion single-doped mechanism. In ESA case, finally we can conclude that by absorbing atleast two photons having sufficient energy, a single ion can reach its emitting level from which it undergoes luminescence.

In photon avalanche process (PA) four energy states are involved instead of three as in ESA. Cross relaxations (CR) and Energy transfer process are very important in upconversion phenomenon. Cross Relaxation occurs due to overlapping of the spectra. For example, in Silica between  $3H_4 > 3F_4$  Fluorescence spectra there is a strong overlapping between them. Previously it has already been examined for  $Tm^{3+}$  doped silica fiber lasers[80]. The cross-relaxation mechanism with its energy level diagram of the four multiplets  $3H_6$ ,  $3F_4$ ,  $3H_5$ ,  $3H_4$  is shown in figure 1.2.1.

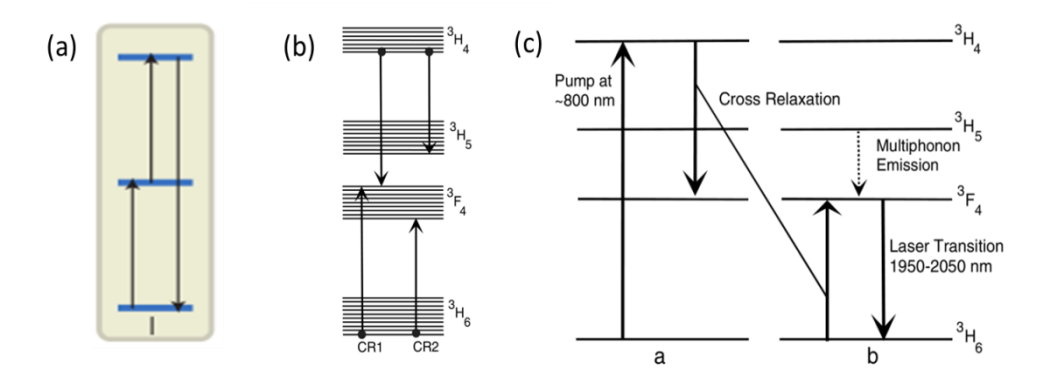


Figure 1.2.1: (a) Excited State Absorption Mechanism (ESA).Reproduced with permission. Copyright: Nature Materials publication, (b) Detailed energy level diagram of the four multiplets of the Tm³+ion. Reproduced with permission. Copyright: Optics Communications publication, (c)Two Energy Transfer Upconversion Processes (ETUs). Reproduced with permission. Copyright: Optics Communications publication

Unlike ESA, (figure 1.2.1) where Energy Transfer Upconversion process ETU is a pump power independent process and it involves two ions system – one is sensitizer ion and another one is activator ion. Sensitizer ion (S) can transfer its energy to activator ion (A) as they are placed much closer to each other. On excitation with suitable light "A" goes from its ground state to excited state and it is only possible if excited energies of two ions are equal or nearly equal to each other. After reaching the excited state, S ion can transfer its energy to the nearly placed A-ion whose excited state energy are equal. Here it is to be notified that before emitting photons by S-ion, A goes from ground state to the excited state.

Several spectral properties of RE doped UCNPs have huge scope in biomedical imaging and therapeutics [80]–[83]. Other exciting optical properties in the same material can be aroused by tuning their spectral properties in a proper way. Surface Plasmon resonance caused by the interaction of metal with the incident light assist for different interesting optical events like radiative and non-radiative properties of nanocrystals[84]–[86]. In literature, the Raman spectroscopy with dominant phonon modes (300cm<sup>-1</sup> - 400cm<sup>-1</sup>) of such RE based materials has been already demonstrated [5].

## 1.3 Different synthetic strategies for the production of Upconversion nanoparticles

Earlier we have already discussed, choosing of host materials is a very important factor to UCNPs as they determine their quality. Now to get better quality (such as better luminescence efficiency, chemical stability, low phonon energies giving low probability of non-radiative decay) synthesizing UCNPs in a proper way is very crucial key. Synthetic routes for Upconversion nanoparticles are based on mainly three strategies, thermal decomposition, Hydrothermal or solvo-thermal synthesis, ionic —liquid based or ionothermal synthesis. Hence, we will discuss a variety of synthetic routes based on those three basic strategies.

## **1.3.1** Thermal Decomposition

To control the shapes and sizes of nanocrystals, thermal decomposition is one of the most familiar and popular method. As reagents, organic precursors (e.g. trifluoroacetate precursor), surfactants (oleic acid, oleylamine) and organic solvents are used. By product, what we get is nuclei form of our desired nanocrystals, which then goes under growth mechanism. There after dissolution and aggregation take place. Thermal decomposition follows overall four stages- Nucleation, Growth, Dissolution and Aggregation

Most of the RE fluorides are synthesized by this route. Some examples of such prepared UCNPs are NaYF<sub>4</sub>:Yb,Er; NaYF<sub>4</sub>:Yb,Tm; NaGdF<sub>4</sub>:Yb,Er; NaGdF<sub>4</sub>:Yb,Tm; NaLuF<sub>4</sub>:Yb,Er; NaLuF<sub>4</sub>:Yb,Tm,CaF<sub>2</sub> etc .

*Drawbacks of thermal decomposition:* Though thermal decomposition[1][87] gives well shaped and sized monodispersed particles (Barnes et al., 2003) but still it holds some disadvantages like-

- a) Requires temperature in the range of 250°C 330°C, which is quite high. During maintenance such high temperature sometimes may cause burning, particle-aggregation, particle enlarging.
- b) Surfactants having long hydrocarbon chains and polar capping groups associated with organic precursors during synthesis can yield difficulties for biological applications especially while we are using them for stabilizing nanomaterials.
- c) Requires high-boiling organic solvents to dissolve organic precursors.
- d) To overcome the difficulty of using surfactants sometimes we need surface modification/engineered modified surface that can be cost-effective.
- e) Ideal condition of this experimental set up is always being used in an complete oxygen-free inert gas condition which is difficult to handle during synthesis, even a very small amount of oxygen during synthesis may damage and form an unsuccessful product.

In spite of having the above mentioned drawbacks in thermal decomposition procedure, this process has already been investigated with the production of Alpha-NaYF<sub>4</sub>:20% Yb,2% Er (cubic-phase) and Beta-NaYF<sub>4</sub>:20% Yb,2% Er (hexagonal-phase) nanocrystals in a large-scale area where successful synthesis of co-doped NaYF<sub>4</sub> nanocrystals has been built-up with thermal decomposition procedures. The final shapes, sizes and structures of UCNPs can be changed by modifying or varying the reaction time, reaction temperature, reagent concentration and the resulted modified nanocrystals can be characterized using Transmission electron microscopy(TEM), High-resolution transmission electron microscopy (HRTEM), Field emission scanning –electron microscopy (FESEM) and X-ray diffraction (XRD) patterns.

By introducing two synthetic procedures, collecting from different literature[1], [88], hereby I will describe the thermal decomposition with their required precursors, reaction

temperature and reaction time. At a recent time, Gudel et al. [1], [2], [4], [90] spotted micrometer sized hexagonal phases of NaYF<sub>4</sub>: Yb<sup>3+</sup>,Er<sup>3+</sup>/Tm<sup>3+</sup> crystals which are enable to show highest Upconversion efficiencies. It is familiar to us that metal trifluoroacetates thermally decompose providing their corresponding metal fluorides, fluorinated and oxyfluorinated carbon species, whereas lanthanide trifluoroacetate precursors can be formulated from their corresponding lanthanide oxides and trifluoroacetic acid.

TEM images of the colloidal UCNPs (NaYF<sub>4</sub> co-doped with Er<sup>3+</sup>/Yb<sup>3+</sup> and Tm<sup>3+</sup>/Yb<sup>3+</sup>) formed via thermal decomposition procedure are shown in the figure 1.3.1 with two histograms of particle size distribution (histogram result between Number of Particles and Particle Diameter (nm) for Upconverting Nanocrystals).

#### 1.3.2 Hydrothermal or Solvothermal synthesis

A convenient synthesis process for producing UCNPs with overcoming some of the difficulties associated with thermal decomposition process is termed as hydrothermal or solvothermal synthesis procedure. The advantages of this process over thermal decomposition are given by following

- a) Temperature required is relatively low (160°C to 220°C) compared to that in thermal decomposition.
- b) Oxygen free-inert gas condition is not required and that is why it is easy to handle.
- c) Organic compounds are not required as this process involves water solution phenomena.

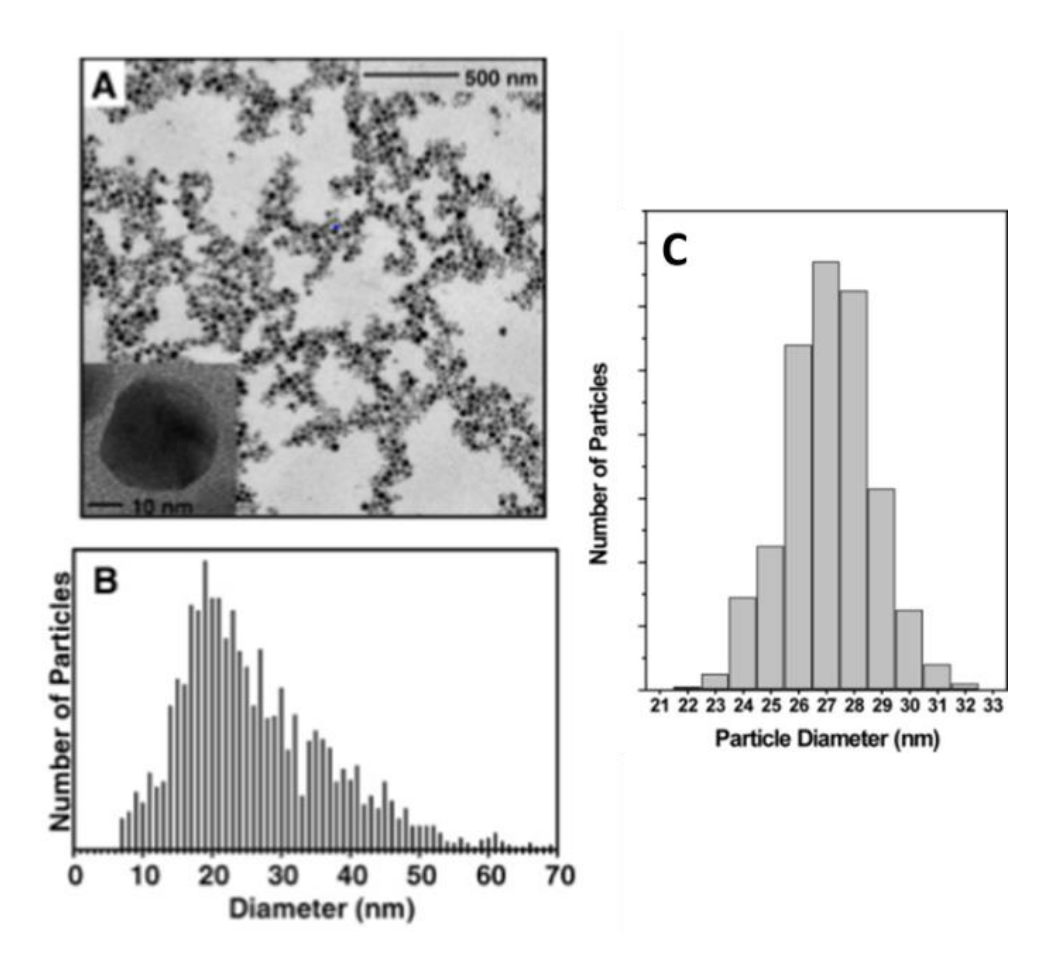


Figure 1.3.1: (A) TEM image, (B) Histogram for obtained particle- sizes with ~1400 nanocrystals. Reproduced with permission (Boyer et al., 2006). Copy right: Journal of American Chemical Society publication (C) Histogram of obtained particle sizes with ~ 500 nanocrystals. Reprinted with permission (Boyer et al., 2007). Copyright: Nano Letters publication

- d) Various nanocrystals with hexagonal and octodecahedral shapes can be formed or synthesized applying this method. By adding several fluoride sources, organic additives (e.g. trisodium citrate) we can get desired shapes and sizes with different morphologies and architectures.
- e) Synthesis through hydrothermal/solvothermal synthesis has been given in various literatures [91]–[94].

Advantages of Hydrothermal synthesis over others and morphological effect of resultant particles on hydrothermal time, temperatures and on other parameters: Compared with the other synthetic routes, hydrothermal synthetic procedure is superior following some advantages like,

- a) At relatively lower temperature, (< 250°C) synthesis can easily happen and during synthesis by changing concentration of precursors, nature of solvent reaction time and other experimental parameters size, structure and morphology of the resulting products can easily be modified.
- b) Experimentally it has been observed that the purity of the resulting particles become significant in case of hydrothermal synthesis.
- c) The synthetic process and the required equipment used in such experiment are simpler and easier to handle.
- d) Sometimes organic additives (EDTA, citrate) are used during synthesis to get small and uniform particles. The resultant size of particles differs with different organic additives due to their different chelating agent and molecular structure providing morphological product. The main reason behind that difference is the influence of chelator on the growth of particles [95]. As for example, size of the particles synthesized with citrate is much less than that synthesized with EDTA.

There are generally four factors, which substantially affect the size, structure and morphology of the resulting nanocrystals. They are described as follows,

a) Effect of fluoride-lanthanide molar ratio: The amount of NaF content is counted in NaF: Ln molar ratio to investigate its effect on size, structure and morphology of the

resulting UCNPs. Larger the fluoride-lanthanide ratio provides the better crystallization, more regular and smoother surface, more hexagonal phases (i.e. influence the crystal structure as fcc or hexagonal) of the resulting nanocrystals. Now, the effect of NaF: Ln ratio on crystallization, shape and surface pattern of the synthesized Yb<sup>3+</sup> and Er<sup>3+</sup> codoped NaYF<sub>4</sub> nanocrystals is shown in table 1.3.1.

Table 1.3.1: Different crystallization, shape and surface pattern with different amount of NaF:Ln ratio

NaF : Ln molar ratio	Crystallization	Shape	e Surface pattern	
4	Low crystallization of the sample providing more likely fcc [3], [96]	spherical	Coarse surface	
8	Improved crystallization.	More regular shape.	More smoother surface.	
12	Further improved	Pure hexagonal shaped sub-microplates	Further improved	

From table 1.3.1, it is clear that the effect of NaF content on the crystal morphology plays an important role as the crystal phase is completely transformed into hexagonal phases at the NaF: Ln molar ratio of 12 or above.

b) *Effect of citrate-lanthanide ratio*: In hydrothermal method chelating agent has appreciable effect on size and aggregation of the particles. Therefore, by choosing proper chelating agent it is quite possible to produce small-sized and dispersible nanoparticles[4], [97]. Therefore, citrate: Ln ratio plays an important role in forming different morphologies (table 1.3.2).

Table 1.3.2: Molar ratio of chelator: lanthanide affecting the morphologies of NaYF4: Yb<sup>3+</sup>,Er<sup>3+</sup>nanocrystals

Molar ratio of	Morphology of the resulting particles				
citrate– lanthanide					
0:1 (i.e. without citrate)	Formulation of resulting nanoparticles as mixtures of nanorods as well as spherical nanoparticles.				
0.5	A mixture of cubic nanoparticles and hexagonal submicroplates.				
1.0 and 1.5	Development of pure nanoparticles having size distribution in the range between 30-50 nm (With the restriction of the crystal growth).				

In conclusion the formation of cubic crystal structure is possible with citrate lanthanide and ratio is greater than unity (citrate: lanthanide > 1) and with citrate- lanthanide ratio is less than unity there exist mixed phases (cubic and hexagonal) in resulting crystal structure (citrate: lanthanide <1).

- c) Effect of Hydrothermal temperature: Generally, the hydrothermal required temperature in the range between 160 to 200° C to eventuate phase transformation. At higher hydrothermal temperature cubic to hexagonal phase transformation is possible owing to generation of energy. Lower hydrothermal temperature approves smaller sized nanoparticles having cubic phases, whereas higher hydrothermal temperature approves the formation of nanocrystals and sub-microplate mixture having hexagonal phase.
- d) Effect of Hydrothermal time: Hydrothermal time affects the crystallization and growth of the resulting nanocrystals. Long hydrothermal duration is favorable for the transformation of cubic phases into hexagonal phases. The hydrothermal time increases

the rate of several processes during synthesis such as dissolution, re-nucleation and crystallization processes. In literature it has been described that pure hexagonal phase – microplates (our required phase) of NaYF4nanocrystals have been found with hydrothermal time around 2 or 2.5 hours (keeping citrate: lanthanide ratio= 1:1; and temperature at 180°C) [4]

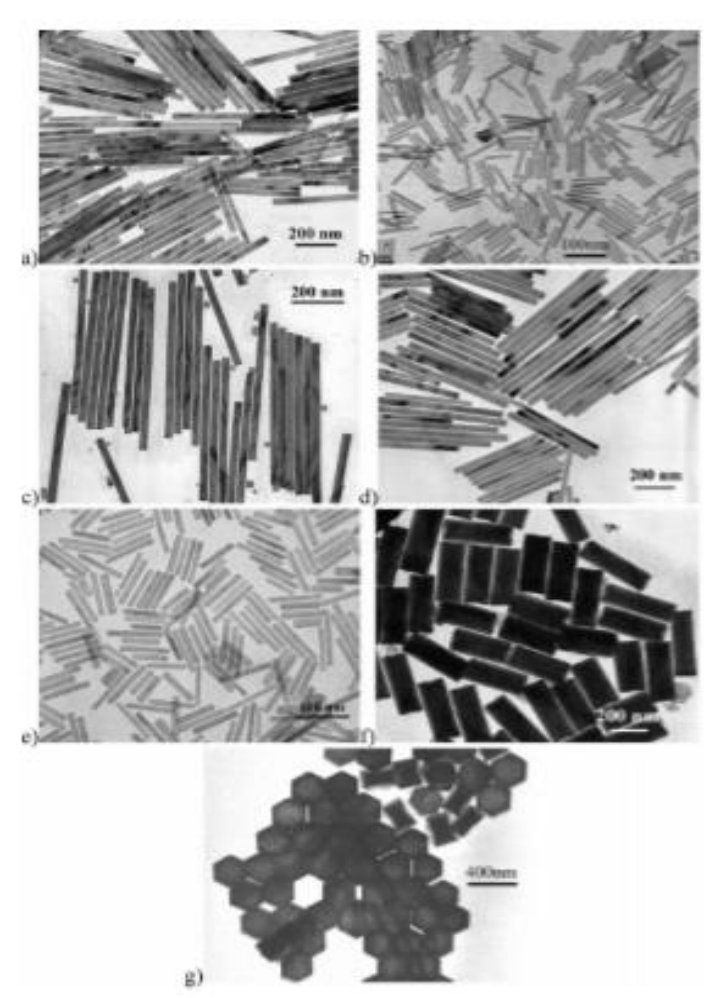


Figure 1.3.2: TEM images of the resulted nanocrystals after solvo-thermal treatment. Reproduced with permission (Wang and Li, 2007). Copyright: Chemistry of Materials publication

TEM images of the Upconversion nanoparticles (YVO<sub>4</sub>:Er<sup>3+</sup>) synthesized with hydrothermal/solvo-thermal treatment are shown in figure 1.3.2.

#### 1.3.3 Ionic-Liquid based or ionothermal synthesis

Although pure hexagonal phase (which can yield better Upconversion than the cubic one) can be obtained by this method, however, it is comparatively less popular than the previous two methods because it holds certain limitations while synthesizing nanocrystals e.g.

- a) Nanocrystals used must be non-flammable
- b) Does not require any organic solvent.
- c) Produced particles become broader in size with lower quality (less uniformity, less monodispersity, less chemical stability) than the other two processes.
- d) Various shapes and sizes cannot be found by using ionothermal synthesis, only water-soluble hexagonal phase formation is possible.

Due to these above-mentioned limitations, it can be used only for preparing a few selective nanocrystals. In spite of having such limitations, few advantages are also present such as

- a) Reaction occurs within a very short period of time.
- b) Requires low temperature range and vapor pressure that are easy to control.

Earlier, synthesis procedures for the production of  $\beta$ -phase NaYF<sub>4</sub> nanomaterials were developed [16], [91], [96], [98]–[101] with the formation of particles of size ~15 nm where most of the synthesis procedures required in high boiling solvents or in their mixtures (e.g., oleic acid, oleylamine, 1- octadecene or their solvent mixtures) owing to co- thermolysis of rare-earth trifluoroacetates and sodium trifluoroacetate [88]. But these resulting luminescent

nanomaterials seems to be difficult while using in bio-probes due to their sizes, not only that but also from literatures it is revealed that they require a very high reaction temperature and yield rather very low compared to the other methods. Therefore, production of smaller size of such nanoparticles with high yield is a demanding matter in Bio-probe imaging. Chow et al. group synthesized 10 nm sized hexagonal phase UCN nanocrystals in oleylamine at temperature above 300°C having very narrow size distribution and introduced multiple precursors e.g., – CF<sub>3</sub>COONa, (CF<sub>3</sub>COO)<sub>3</sub>Y, (CF<sub>3</sub>COO)<sub>3</sub>Yb, (CF<sub>3</sub>COO)Er /(CF<sub>3</sub>COO)<sub>3</sub>Tm etc[16], [102]. An average size of 7 nm of Yb<sup>3+</sup>, Er<sup>3+</sup>co-doped NaYF<sub>4</sub> nanocrystals were being synthesized at elevated temperature by Schafer group [102].

For synthesizing UCNPs precursor's properties also play a significant role in controlling size, shape and morphology. NaYF<sub>4</sub> nanocrystals co-doped with Er<sup>3+</sup>and Yb<sup>3+</sup> can be synthesized in the presence of precursors like- Y<sub>2</sub>(CO<sub>3</sub>)<sub>3</sub>, Yb<sub>2</sub> (CO<sub>3</sub>)<sub>3</sub>, Er<sub>2</sub> (CO<sub>3</sub>)<sub>3</sub>, Na<sub>2</sub>CO<sub>3</sub> and NH<sub>4</sub>F as they can produce nanocrystals even at room temperature or at very low temperature having hexagonal phase (β-phase) giving better luminescence and high yield. This is one of the noteworthy advantages of these precursors providing a novel method of synthesis procedures at nanoscale production. Such novel synthesis method is based on the reaction of metal carbonates with Ammonium fluoride and synthesized in organic solvents in the range of temperature 20–280°C. After decomposing of metal precursors pure, nanosized NaYF<sub>4</sub> nanocrystals co-doped with Er3+ and Yb3+ were formed having high yielded particles which are well separated, and they contribute to broad size distribution (particle size~ 4-10 nm). Thus, the transparent solution of these resulted nanoparticles exhibited visible Upconversion emission on 978 nm of wave excitation. After that novel synthesis all the diffraction peaks appeared by XRD assign to hexagonal phases and no cubic phases are assigned, that means here as all the phases belong to hexagonal phase, so luminescence efficiency which is our desirable property becomes high. Cubic phase of Er<sup>3+</sup> and Yb<sup>3+</sup> co-doped NaYF<sub>4</sub> nanocrystals can be produced at elevator temperature (250°C). All these reactions were done in pure oleylamine which can be replaced with oleic acid - oleylamine mixtures to discontinue the cubic phases formed in reaction. With the above mentioned precursors under optimized conditions 7 nm sized particles (estimated as an average particle size) were formed having 84% yields [102]. Er<sup>3+</sup>, Yb<sup>3+</sup> ions coupled in hexagonal phase NaYF<sub>4</sub> matrix provides highest up conversion efficiency [3], [98]. Proper heat treatment is an important factor to increase the luminescence efficiency.

Thus, solid-state-reaction procedure is another way to form nanoscale hexagonal NaYF<sub>4</sub> powder with releasing ammonia at room temperature grinding dry powders (such as Na<sub>2</sub>CO<sub>3</sub>, NH<sub>4</sub>F, and RE carbonates powders). However, owing to the presence of higher percentage of  $\alpha$ -phases and other phases/ impurities rather those  $\beta$ - phases in the as-synthesized sample this procedure carries less importance compared to the others mentioned above. Not only that but also it requires high reaction temperature (~300°C or above) during synthesizing Upconversion nanocrystals.

Ionothermal synthesis is the procedure where ionic liquids are used as reaction media in thermal reactions and water-soluble hexagonal phased NaYF<sub>4</sub>: Yb<sup>3+</sup>; Er<sup>3+</sup>/Tm<sup>3+</sup> nanoparticles are formed with. Mostly this procedure occurs in a molecular solvent [103], [104].

A conventional strategy for synthesis of nanocrystals is based on a simple and agreeable methodology, known as Liquid solid solution process (LSS) which provides a variation of building blocks for assembling materials in nanotechnology. To obtain high quality nanocrystals, basically noble metals have been chosen for achieving good uniformity, smooth surface and self-assembly. Three phases are developed during this process - solid phase, liquid phase and solution phase. It is possible to obtain uniform noble metal nanocrystals by the moderation (reduction) of noble metal ions from interfaces of solid, liquid and solutions at various classified temperature. Here, metal-linoleate acts as solid phase, ethanol- linoleic acid acts as liquid phase and water- ethanol solution with noble metal ions serves as solution phase. To generate liquid and solution phase ethanol is a common quantity. The greatest advantage of LSS process is to produce nanocrystals having various properties such as, magnetic, semiconducting, fluorescence, dielectric and applications in solid state lasers, luminescent probes and sensors [105].

We can divide the whole LSS process into two sections, (i) phase transfer process and (ii) phase separation process. In phase transfer process, the aqueous solution with noble metal salt conjugate with ethanol, which is also in a liquid form and produce water- ethanol solution containing noble metal ions. Again, phase transformation based on ion exchange occurs between sodium linoleate and the water- ethanol solution accommodating noble metal ions resulting in noble metal linoleate and finally sodium ions enter into the aqueous phase.

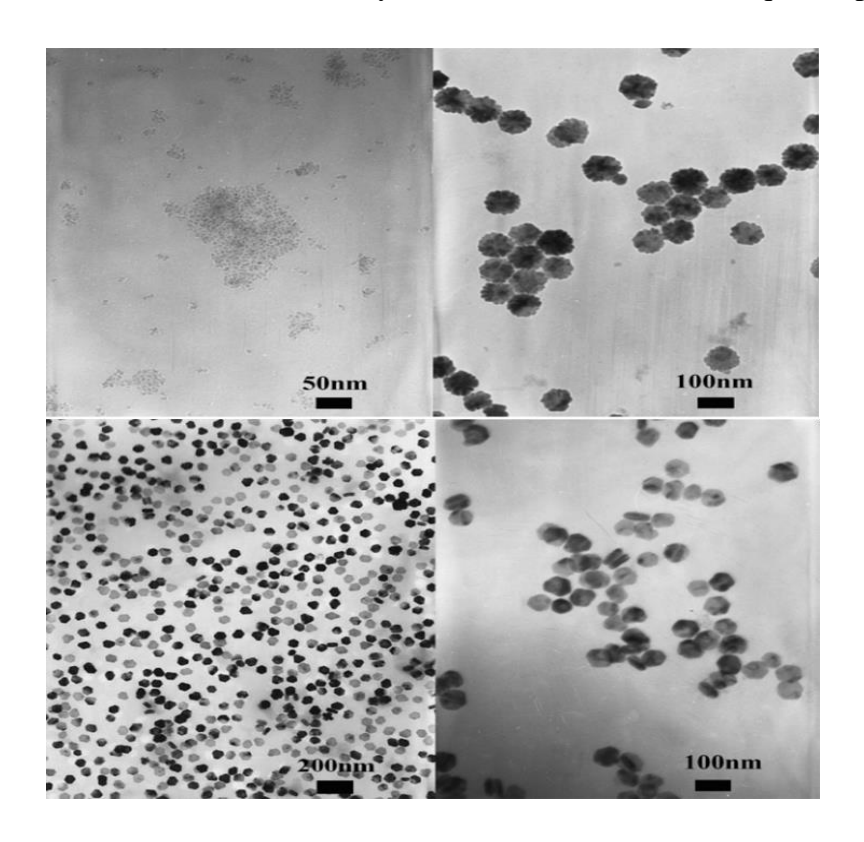


Figure 1.3.3: TEM images of NaYF4:Yb, Er UCNPs obtained at different reaction temperatures. Reported with permission. Copyright: Chemistry of Materials publication

At certain selected temperature, ethanol in both phases (liquid phase and solution phase) alleviates noble metal ions at the interfaces of solid liquid and solid – solution phases [105]. Here the only remaining quantity which not reacting with other chemicals is the linoleic acid, which is absorbed on the noble metal – nanocrystal surface further with the reduction process

(reduction of the noble metal ions). As a result, alkyl chains are developed outside the noble – metal surface enabling them to acquire hydrophobic surfaces. In LSS process phase separation occurs spontaneously owing to the weight of nanocrystals as well as incompatibility between their hydrophobic surfaces and hydrophilic surroundings.

In figure 1.3.3, TEM micrograpgs of  $\beta$ - NaYF<sub>4</sub>:Yb, Er nanoplates [96] prepared by liquid-solid dual phase - approach are shown.

# 1.4 Few recently developed synthetic strategies

Now in the subsequent section some of the recently developed synthetic strategies for UCNPs and their special investigations have been summarized.

#### 1.4.1 Microwave assisted synthesis

There are two leading mechanisms, Dipole rotation and ionic conduction, which determine the potentiality of a material for absorbing microwave radiation and transmuting it into heat. Though mostly, microwave assisted synthesis was used in organic synthesis but nowadays to prepare monodispersed Upconverting nanocrystals [106]–[109] this method is being used. Some advantages are there behind using such method, they are

- a) Convenient and reproducible method which allows preparing highly luminescent, small monodispersed nanocrystals [108].
- b) Rapid reaction takes very less time to complete the reaction and to form luminescent nanocrystals.
- c) Provides particles having different required sizes and shapes.

- d) Hence, the polar reactants (accompanied by high microwave extinction co- efficient) are excited by direct absorption of microwaves and as a result the activation energy reduces, consequently reaction rate enhances. As outcome, lower temperature is required to perform the reactions, therefore, additional temperature in inhomogeneities is being eliminated and the leading experimental parameters (time, temperature, pressure) become easier.
- e) Growth and nucleation of resulting nanocrystals in such synthesis procedure can be distinctly described with clear explanation. Hence, growth and nucleation of nanocrystals occur in three phases, in first phase, slowly the reactant concentration increases and finally exceeds solubility, in second phase, reactant concentration extends the critical limit of super saturation, therefore, rapid nucleation is obtained and eventually this nucleation burst, reactant concentration reduces to the depletion of the solute for the growth of generated nuclei and here nucleation stage ends. In the third phase, gradually nuclei grow. Such processes follow the LaMer Mechanism. In such way, the whole reaction can be managed favorably and the resulting nanocrystals exhibit excellent monodispersity and crystallinity due to polar reactants, high microwave extinction coefficient.

#### 1.4.2 Photopolymerization

Using this strategy it is possible to induce different monomers with different desired functional properties (such as- Hydrophobic or hydrophilic, charged or neutral, chemically active or inactive) within up converting nanocrystals by coating them with thin polymer shells known as photopolymerization which utilizes internal UV or emitting visible light from them on NIR excitation. This is a simple, generic and straightforward and versatile approach to functionalize, conjugate, protect and make Upconverting nanoparticles bio-compatible [110].

Utilization of NIR excitation in photo polymerization provides special advantages like, less probability of occurring photo damage to living cells owing to its high tissue penetration depth, ability (due to its higher wavelength) to avoid photo bleaching, weak chemical stability as such difficulties arise with excitation having lower wavelength [111], [112]. With photo polymerization, upconverting nanocrystals draw some disadvantage while using in biological media, as they are hydrophobic in nature and non- dispersible in nature. Therefore, after photo polymerization also their surfaces are needed to be modified and functionalized in a precisely controlled manner [113].

# 1.4.3 Advanced and recent Synthetic strategies in UCNPs with various advanced applications

Recently, unifying core and shell material became most attractive synthetic strategy yielding high quality and high sensitivity involving energy transfer process between Eu<sup>3+</sup> and Gd<sup>3+</sup> ions [114]. There exists a twisted relationship between Upconversion efficiency and lattice geometry providing a strategy for designing the quantum efficiency of any lanthanide upconverter. This strategy has been published in literature in present-day [115]. The chitosan - conjugation is the another method to increase the cell viability of Upconverting nanocrystals in human breast cancer cells, in such approach Upconverting nanocrystals exhibit bright Upconversion fluorescence with controlled size and shape on 974 nm excitation [116]. Upconversion nanoparticles can also be served as luminescent nanotherometers over a wide temperature range and such nanothermometers can be processed by affiliation of liquid-solid solution hydrothermal strategy and thermal decomposition strategy and become excellent temperature sensor [117]. Lanthanide doped Upconversion nanocomposites (such as- Ln<sup>3+</sup> doped BiPO<sub>4</sub>/BiVO<sub>4</sub>nanocomposites) can also be used for photocatalysis applications. Lanthanides, (ex. Tm3+) emit strong blue spectra, which are transferred BiVO4 resulting formation of excitations, which produces reactive oxygen species. In literature survey, it has been suggested that upon NIR and solar irradiation photocatalysis activity of such resulting

Upconverting nanocomposites are more advantageous than the reported general nanocomposite photocatalysts. In recent past years, few advanced applications of UCNPs have been established, such as, a multifunctional nanocluster having dual compositions of gold nanorod (AuNR) and UCNPs showed applications in imaging of cancer cells and treatment. In neuroscience and engineering, stimulating deep brain neurons is an important desire. Molecularly tailored UCNPs (dendritic) have been served as less invasive optogenetic actuators to stimulate deep brain neurons [118]. UCNPs based theranostic system is very useful for multi-drug resistance reversing ability for chemotherapy [119]. A UCNP based system: LiYF<sub>4</sub>:Yb<sup>3+</sup>/Tm<sup>3+</sup>@SiO<sub>2</sub> coated with chitosan (CH) hydrogel has become an excellent theranostic platform by controlling drug-delivery and deep-tissue-imaging for several important applications- tissue engineering, bio-mapping and cellular imaging [120]. Highly specific tumour-imaging can be exhibited by the conjugate forms of Upconversion-nanoprobes with cancer cell (CC) membrane, such combined form (CC-UCNPs) represents novel materials presenting attractive class of advanced materials [121].

#### 1.4.4 Investigation of phase transformation and morphology tuning in UCNPs

Phase and morphology of UCNPs can be tuned by using proper dopant ions. Zhang's group and Kal's group have been already depicted the crystal structure of such upconverting nanocrystals through K+ ions co doping [122] and there are various literature reported on the different morphologies and phases of the resulting nanocrystals [96], [123]–[125]. Phase transformation and morphology both are dependent on several experimental parameters, such as reactant's concentrations, reaction time and reaction temperature. Concentration of dopants can also play a significant role on phase transformation. For example, different concentrations of K+ ion dopants in NaYF<sub>4</sub>: Yb<sup>3+</sup>, Er<sup>3+</sup> nanocrystals display different XRD peaks. It has been reported that upto a certain limit (60 mol %) of such dopant concentration hexagonal NaYF<sub>4</sub> nanocrystals become dominant phase but beyond that limitation (when exceed 60 mol %: around 80 mol % to 100 mol %) K<sup>+</sup> ions replace Na<sup>+</sup> ions and form hexagonal KYF<sub>4</sub>

nanoparticles that mean phase transformation takes place [122]. The reason behind that phase transformation is the imbalance of the intrinsic crystal structure. K+ ions only settle in the substitution position of Na<sup>+</sup> ions and when number of occupying K+ ions becomes large compared to Na<sup>+</sup> ions (at that moment Na+ ions are too few), hexagonal KYF<sub>4</sub> appears having poor crystallinity.

Now, how the morphology of UCNPs (NaYF<sub>4</sub>:Yb $^{3+}$ ,Er $^{3+}$ ) can be tuned with tuning concentration of dopant ions (K $^{+}$  ions), is shown in the table 1.4.1 below:

Table 1.4.1: Tunable morphology of UCNPs with controlling K<sup>+</sup> ions

Concentration of k <sup>+</sup> ions (in mol %)	Morphology of nanocrys	S		Diameter of the resulting particles
0	Spherical (NaYF <sub>4</sub> )	ı		26 nm
20	Regular hexagonal cross section(plate-			-
	like; uniform in size; NaYF4)			
40	Rectangular-	like	cross	-
	section(NaYF <sub>4</sub> )			
80-100	Spherical hexagon	al(KYF <sub>4</sub> )		20 m

#### 1.4.5 Mechanistic Investigation of photon Upconversion

It is known, in most of the cases that the lanthanide doped upconverting materials (ex: NaYF<sub>4</sub>:Yb<sup>3+</sup>, Er<sup>3+</sup>) need 980 nm excitation. But this event creates problem which became a daunting challenge nowadays as absorption band of Yb<sup>3+</sup>( 980 nm), which acts as dopant in host lattice (NaYF<sub>4</sub>), dangles with absorption band of water molecules used in the biological sample. Therefore, under 980 nm excitation overexposure of biological species results in cell death and tissue damage due to overheating issues. To overcome such drawback 980 nm laser

excitation can be replaced by 800 nm laser excitation occurring low absorption coefficients and it is possible through use of Nd<sup>3+</sup> dopant ions as sensitizer due to their favorable characteristics (As their sharp absorption bands are centered around 800 nm) [126]

# 1.5 Biological applications of UCNPs based on their immobization to assemblies:

For several biological applications, surface modification of UCNPs plays an important part for upgrading their photostability and to attach with bio-molecules. Normally, UCNPs bear a good portion of surface dopant ions. Now presence of weakly bound impurities on surface and ligands can diminish the luminescence of dopant ions due to the creation of high energy oscillations. On the other side, the excitation energy of interior ions can be dissipated nonradiatively due to their transferred energy towards the crystal- surface. As a result, the crystal field - strength decreases and finally the overall UC luminescence intensity reduces abruptly. To overcome this drawback, surface modification (surface passivation and surface functionalization) is required. By surface passivation, all the dopant ions can be confined in an interior core and therefore can dominate the energy transfer towards crystal-surface. An Upconversion luminescence enhancement of about 30 times was successfully carried out by one research group with 1.5 nm thick NaYF4 shell on 8nm sized NaYF4:Yb/Tm nanocrystals [127]. By varying the thickness of the shell, UC luminescence efficiency can be well tuned and by several research groups [33], [98], [128], [129] this process has been successfully explained by immobizing the nanocrystals (UCNPs) inside a coated shell. Besides, surface passivation, surface functionalization is also an important part to use those UCNPs in biomedical and biodetection. Hence, by ligand exchange technique NaYF4:Yb/Er nanoparticles can be made water soluble by utilizing bi-functional organic molecules which replaced amine ligands and modified the crystal surfaces as water-soluble carboxyl functionalised surface[15].

Moreover, the immobilization concept of UCNPs has been confirmed by their several biological applications via bioconjugate chemistry as these techniques are, while applied to UCNPs, capable of immobilization to bio-assemblies. Based on the immobilization concept, some specific bio-applications of UCNPs are discussed below.

In cells and small animals, the innovative UCNPs have been considered to be promising molecular probes for optical imaging. In 2013, Grebenik et al. group reported UCNP-labeled cancer lesion where the synthesized nanoparticles were capped with amphiphilic polymer. Further, mini-antibodies (scFv4D5) were attached onto UCNPs for allowing their specific binding to the human cells. As a result, the UCNP based biocomplexes showed high specific immobilization on human breast adenocarcinoma cells SK-BR-3 [130]

In 2017, Shikha et al. group developed a UCNPs based multiplexed detection system to encode PEGDA microbeads and to label antibodies. Hence, the multicolour codes were produced by mixing green and red emissions from UCNPs whereas its blue emissions were used to label antibody. By immobilizing probe antibodies on red-UCNPs and anti-human C reactive protein (hCRP) on green UCNPs, specific capturing of human serum albumin (HAS) protein and multiplexed detection of HCRP and HSA proteins were done, respectively [131].

RGDS and TAT conjugated NaYF<sub>4</sub>:Yb<sup>3+</sup>/Er<sup>3+</sup>, SiO<sub>2</sub> nanoparticles were targeted in HeLa cells by in vitro study where RGDS conjugated probes were confined on cell-plasma membrane for the specific binding between the conjugated peptides and integrins. This application also clearly confirms the immobilization behaviour of UCNPs[132].

In 2016, T sang et al. group proposed a conjugated system of BaGdF<sub>5</sub>:Yb/Er UCNPs and AuNPs to increase the effective detection of limit for target Ebola virus from picomolar level to femtomolar level. The enhancement of this ultrasensitive detection exhibited a great potential for practical application due to the specificity between nanoprobes and Ebola virus oligonucleotides[133].

The bare monodisperse UCNPs were immobilized for developing bio-sensing surface. Further, for developing bio-assays and bio-sensors a high immobilization density for UCNPs

was reported by Doughan et al. group in 2014 and the reported immobilization density was calculated of about  $\sim 1.3~10^{11}~UCNP~cm^{-2}$  where PEA - UCNPs were immobilized on functionalized coverslips [134]

PEG-b-PAAc was immobilized on erbium ion doped Y<sub>2</sub>O<sub>3</sub> [Y<sub>2</sub>O<sub>3</sub>: Er] particle - surface to enhance its dispersion and prevent adsorption. Further, co- immobilization of PEG-b-PAAc and BSA occurred due to the protein installation on particle – surface[135].

According to previous report [136] the immobilized photoredox catalyst based on NaYF<sub>4</sub> nanoparticles was capable for in-vivo applications. The immobilized system successfully performed under 980nm NIR source.

#### 1.6 Different Biological applications of UCNPs

In particular, based on the immobilization strategies, Upconverting nanoparticles have given a huge response in bio-applications. In the applications of cellular and molecular biology, several bio- probes (Green fluorescent protein, (GFP), organic dyes) are used for identification of different bio-molecules, which is an indispensable step. To develop the sensitivity of some technical and analytical devices used in bio-field utilization of such available probes is a crucial step as they improve the efficiency of detection. Still some drawbacks (such as weak photo stability of probes, measuring cell response having instrumental problem with resolution) are there with such bio-probes which limit their biological applications. To overcome such drawbacks nano particles with protein-imaging, nucleic acid-detection with nanodiamonds [137], [138], metallic nanoparticles, dye-doped silica particles have been already discovered. As nanoparticles consist of a large no. of ions, so single particle and single molecule identification is favorable owing to large surface area implanting of different targeting groups at the surface and it can be done comfortably. For more advanced applications recently RE based nanoparticles have been proved to be most optimistic materials [139] due to their especial properties such as long lifetimes, narrow emission lines, high photo stability, low cytotoxicity and simplistic functionalization procedures which make them highly bio-compatible and recognizable compared with other Nano particles. In magnetic resonance imaging (MRI) due to their high magnetic moment and inoxidant detection applying reverse oxidoreduction process, the requirement of UCNPs is noticeable. In MRI RE ions can be regarded as a powerful contrast agent. To fabricate nanoparticles (e.g. silica particles) [140] as high biocompatible material various chemical properties could be induced by inducing different rare-earth compounds as dopant-agent. Mesoporous silica shell nanocomposites used for bimodal imaging is the best example of such nanoparticles doped with RE compounds.

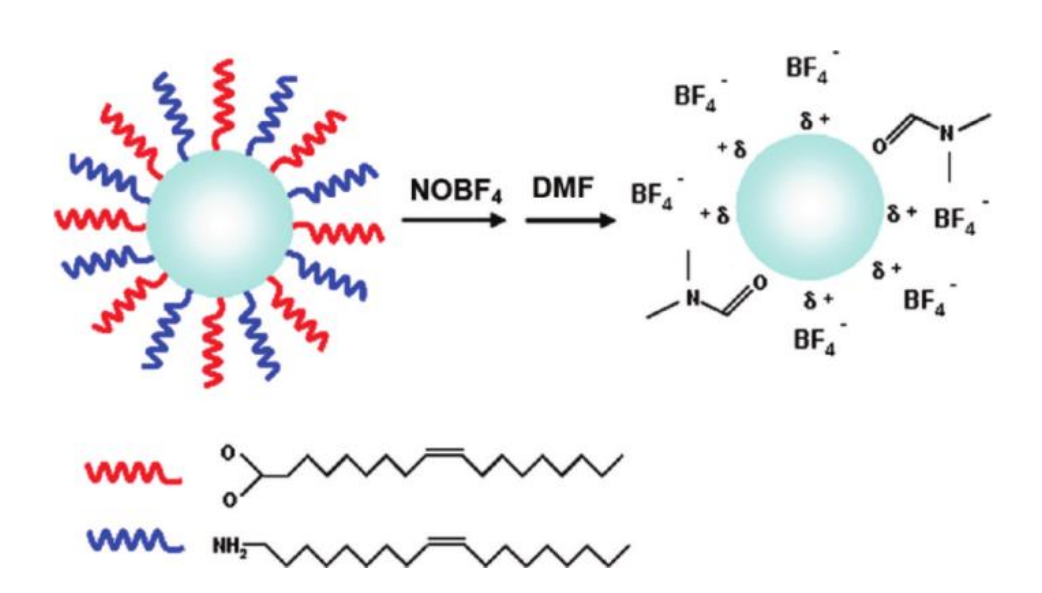


Figure 1.6.1: Illustration of ligand-exchange with NOBF4.Reproduced with permission (Dong et al., 2011).Copyright: Journal of the American Chemical Society publication

Surface modification or surface functionalization and bio-conjugation are crucial steps after synthesis known as post synthesis method before using in the biological field. Every nanoparticle has a certain surface chemistry and specific physical and chemical properties to govern nucleation or growth of resulting particles as well as to control their dispersion in the solvent used. Generally, after synthesis of Upconversion nanoparticles, due to the presence of

some organic ligands capped with them, they become non-dispersible which are not suitable for Bio-applications. For using in different bio-medical applications Upconversion nanoparticles based bio-probes are fabricated to functionalize their surfaces to ensure good dispersion in biological media and to uncover specific organic or bio organic groups from the particles and to make them appropriate for accurate targeting receptor sites (figure 1.6.1).

Ensuring the stability of hydrophobic nanoparticles in aqueous media is a necessary condition in biological applications and that can be processed by applying diverse functional strategies which are described by following: In Ligand exchange the original ligands are replaced by other molecules Citrate, PVP, PAA, TGA, PEG and finally become stable dispersible in biological media (figure 1.6.2, 1.6.3.) [141], [142].

By direct surface grafting of molecules and polymer encapsulation method, several reactive groups (e.g. amino, thiols etc.) can be attached on the resulting particle –surface [143]. Streptavidin, antibodies are some biomolecules with which nanoparticles can be directly coupled. Because of surface hydroxyl groups acting as a coupling agent with silanes present in the oxide nanoparticles, by silica and organosilane coating functionalization can be done in a quite simple way.

Layer by layer assembly is another propitious method for surface modification, obtaining by sequential adsorption of oppositely charged polyelectrolytes on particle surface. Such sequential adsorption (i.e. sequential deposition of PAA and PAH) has been already observed in literature providing superior mechanical stability and a well ordered NIR to visible Upconversion luminescence. But here some drawbacks which limits its requirement as this method is only applicable for hydrophilic nanocomposites and time-consuming, many washing steps are needed during that assembly. Surface silanization is the most frequently used surface functionalization method requiring the growth of silica shell on Upconversion nanoparticles. The importance of this process is the use of silica as silica is considered to be biocompatible and porosity is easily controllable. The encapsulation of silica layer on UCNPs is still under investigation to modify the difficulties(such as , most of the reagents used are toxic in nature, therefore before starting that encapsulating process they should be detached

carefully) introducing by silica layer and other reagents used in such encapsulating process. If we desire to use silica encapsulation in FRET- biosensors, the increasing shape and size of the resulting particles will create difficulties during experiment. To suppress those difficulties two approaches are useful, one is Stober method and other one is reverse microemulsion route.

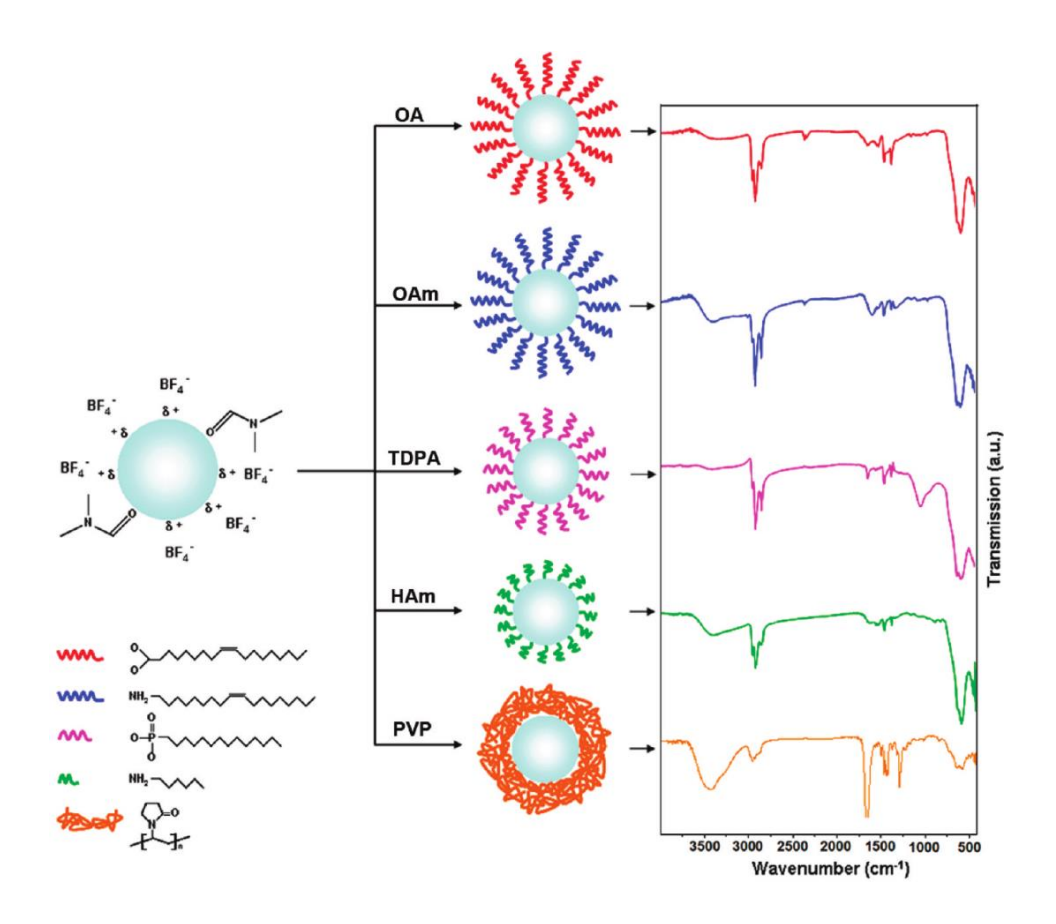


Figure 1.6.2: Illustration of secondary ligand-exchange exhibiting surface functionalization of BF4 - modified Fe $_3$ O4 nanocrystals with several capping molecules and their corresponding FTIR spectra. Reproduced with permission (Dong et al., 2011). Copyright: Journal of the American Chemical Society publication

Although controlling that Stober method is quite difficult and takes long time, thus it is straightforward and fruitful path in the presence of ethanol and ammonia, whereas reverse micro emulsion route can be controlled in the presence of homogeneous mixture of water, oil,

surfactant and TEOS to dominate the increasing thickness, size and shape of the additional silica layer. One user-friendly surface modification for providing hydrophilic nanoparticles as well as hydrophobic layer for loading hydrophobic molecules(Drug, Dyes) is the Host-Guest Self-assembly method which has a lot of advantages over the other methods due to its simplicity and efficiency. As this procedure is very fast, over 95% of nanoparticles can be transferred to water using reagents [144].

We've already discussed that by proper surface modification it is possible to affix various functional groups with UCNPs, like- carboxyl, amine, thiol groups. After such functionalization, these UCNPs with several attached groups can be decorated with various biomolecules which can contribute bio-identification of other targeted cells. There are diverse approaches of bio-conjugation. Among these the greatest advantageous method is Direct Physisorption. This method occurs via non covalent force of biomolecules. The activity of proteins and quantum yield of resulting nanoparticles remain unchanged after that bio-conjugation. Assisted Physisorption is of other crucial importance in Bio-conjugation and uses pre-bound molecules and occurs by non-covalent coupling of two molecules. This is an essential method in bio-specificity and bio- sensitivity due to the proper orientation of molecules. By direct chemical coupling of bio- molecules also bio-conjugation can be induced in UCNPs. But this method cannot be controlled easily as other complex processes such as gel electrophoresis is required for separation after completion of this process. In UCNPs' surface modification with biotin-protein bond (streptavidin- coupling) can be useful for various biomedical application, which is the strongest and most stable non-covalent interaction.

A general overview on UCNPs- applications is highlighted below.

#### 1.6.1 DNA and Protein detection

It has become a great challenge for application of RE based nanoparticles for DNA and protein detection. Implementation of such nanoparticles in DNA detection is based on two

strategies, DNA sensitive nanoparticles and DNA fragments nanoparticles. Here we are describing one by one.

In case of the first approach, DNA concentration can be computed using fluorescent Upconversion nanoparticles [145] which can be comparable to conventional measurement executed by spectrophotometer. As per optical properties we already know that fluorescence property UCNPs make them valuable for their applications. Now due to some specific dopant ions (such as:  $Ce^{3+}$ , $Tb^{3+}$  dopants in LaF<sub>3</sub>, fluorescence occur due to  $Tb^{3+}$  dopant ions) and their transitions in energy levels the fluorescence of Upconversion nanoparticles become very prominent and in the presence of DNA the amount of fluorescence can be quenched by the generating generation of hydrogen bonds between DNA and nanoparticle. As a result, the energy can be transferred from excited dopant ions (Tb<sup>3+</sup> in the given example above) to DNA. Finally, it is possible to quantify DNA concentration by determining the corresponding fluorescence intensity. In the second approach, to study mRNA pattern, DNA microarrays are used extensively for which there are two requirements, one for hybridization of probe DNA strands and other for labeling target DNA fluorescently. In such technology, also fluorescent intensity quantifies the DNA fragments in each probe. Later, other advantageous technology comparable to the depicted one, reported in literature according to which for labeling, target DNA is combined with UCNPs (for ex. Y<sub>2</sub>O<sub>2</sub>S: Yb, Er) and finally it is possible to measure the concentration of the target DNA. The later one is superior technology than the former for determining DNA concentration, as the former technology weakly express mRNA.

UCNPs can also be used for diagnosis diseases such as Fe<sub>3</sub>O<sub>4</sub>/Gd<sub>2</sub>O<sub>3</sub>: Eu nanoparticles where Fe<sub>3</sub>O<sub>4</sub> construct the magnetite core and GdO<sub>3</sub> constructs the shell of the nanoparticles and the dopant ion Eu<sup>3+</sup> make the particle fluorescent by transferring energy. Now, it is known, detection of single nucleotide polymorphisms (SNPs) is very significant phenomenon for recognition of various diseases like polycystic kidney disease (PKD) by using Reverse Transcription Polymerase Chain Reaction (RT-PCR) but due to some shortcoming vis a vis time consuming and expensive, it cannot be applied in the biomedical field. In the present

days, to solve these problems, successfully UCNPs have been introduced to detect SNPs [146]. In that approach, rare-earth based nanoparticles are used in such a systematic manner, that they can combine both magnetism and fluorescence properties to provide a strong and effective analysis.

Europium doped gadolinium oxide nanoparticles can also be used for detection of protein micro patterns for coupling with antibodies rather than organic dyes. Such rare-earth based nanoparticles with organic cores have also been successfully utilized in immunoassays. As a result sensitivity of the whole complex can be improved in the presence of rare-earth based UCPN nanoparticles.

## **1.6.2** Fluorescent Resonant Energy Transfer (FRET)

FRET has wide applications (among which protein-protein interaction is the most significant phenomenon with the usage of FRET) in Biomedical-field using other materials. For protein – protein interaction, one protein (labeled with fluorophore) acts as donor and other one acts as acceptor (labeled with fluorophore) using that fluorescence energy transfer method according to which an efficient energy is being transferred from donor to acceptor and as outcome detection of fluorescence become possible providing the basic principle of FRET process. If FRET can be done in the presence of lanthanide systems, then easily such nanoparticles can be served as donors, which gives some effective and favored conditions like prevention from direct excitation, limitations in overlapping spectra and their easy separation, long lifetimes of excited state and less probability of photo bleaching and there are certain reasons why lanthanide nanoparticles were taken in FRET experiment. Hence the lanthanide systems with the large stokes shift permits excitation having shorter wavelength than the absorption by acceptor to prevent direct excitation and UCNPs with large anti-stokes shift permits excitation at much higher wavelength than the emission by acceptor to get a clean detection from FRET. Secondly, due to narrow emission spectrum occurred by lanthanide nanoparticles, there is a very less chance of overlapping between them and acceptor emissionspectrum. Thirdly, as lanthanide systems provide excited states having long lifetime, so conducts acceptor emission with longer time and as a result separation in time-resolved experiments occurs easily. Utilizing that longer-scale phenomenon, it is possible to apply quantum dots as acceptors in FRET applications.

Advantages of Upconversion nanoparticles as donors in FRET application make them unique in biomedical applications. Most of the Upconverting nanoparticles are co-doped with Er<sup>3+</sup> and Yb<sup>3+</sup> and gives remarkable fluorescence, which make them an excellent donors having interesting potential in FRET applications. Protein detection with the help of nanoparticles is possible by coating (ex. of such coating, agent-streptavidin), mixing (ex. of such mixing, agent-biotinylated protein) and labeling (ex. of such labeling, compound-fluorescent acceptor) in a precisely controlled manner so that after IR excitation of donors, a clear detection of fluorescence becomes possible.

## 1.6.3 In vivo and in vitro biomedical application

Recently, lanthanide doped UCNPs have gathered much attention in Biomedicine .In 2012, Liang Cheng et al. showed in vivo imaging of UCNPs in his experiment [147].Auto fluorescence of the UCL imaging with long exposure time—allows in vivo detection of UCNPs. UCL emission spectra of different nanoparticles can be controlled with our requirement in biological systems by altering the concentration of the lanthanide dopant ions used during synthesis and this process is essential in multicolour vivo UCL imaging with organic dyes through hydrophobic force (figure 1.6.3) [148]. In tumour diagnosis UCL imaging plays significant role by tumour targeted molecular imaging using UCNP-based nanoprobes. Basically, for synthesis of such nanoprobes conjugating polymer coated UCNPs are used, the aim of which is to bind different cancer cells having high specificity explore a new challenge in future studies and experiments. UCNPs have also been successfully synthesized to utilize in vitro applications such as labeling and tracking rabbit bone marrow

mesenchymal stem cells (rBMSCs) [149]. In 2008, both in-vivo and in-vitro studies were performed using aqueous dispersible rare-earth-ion (Tm³+ and Yb³+) co-doped fluoride (NaYF4) nanocrystals, where Upconversion process provided deeper penetration into biological specimen resulting high contrast optical imaging [150]. In 2011, in vitro and in vivo imaging was implemented by utilizing 915 nm LASER excited NaYbF4 UCNPs co-doped with Tm³+/Er³+/Ho³+-rare-earth elements to avoid overheating irradiation caused by 980 nm laser excitation source.

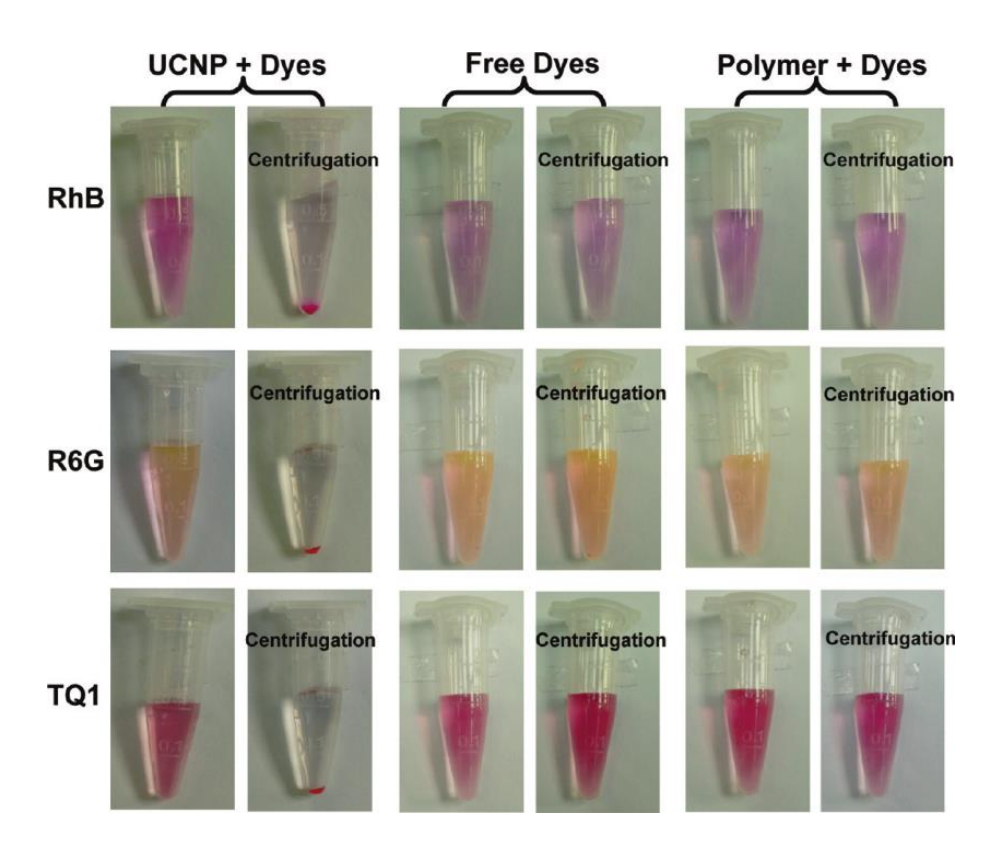


Figure 1.6.3: UCNP/dye – images captured while centrifuged (before/after). UCNPs and dye molecules appeared as precipitate by centrifugation force while supernatant part appeared as clear colourless solutions in containers. Precipitation was not observed while centrifugation occurred with free dye molecules or PEG-PMHC<sub>18</sub>+dye mixtures. These images indicated that UCNP- surface adsorbed three types of dye molecules rather than their encapsulation in UCNP-dye complexes by amphiphilic PEG-PMHC<sub>18</sub> polymer. Reproduced with permission (Cheng et al., 2011). Copyright: The Journal of Physical Chemistry C publication

Hence the experimental results were successfully investigated and showed very high contrast Upconversion bio-imaging and a successful performance for in vivo imaging where highly stable UCNPs encapsulated with DSPE-mPEG-5000 were injected into mice [151]. For delivering in vitro and in vivo operations caged UCNPs are being served as excellent platforms to improve targets along with reduction of side effects from chemotherapy by using them as NIR-triggered targets [152].

To overcome the drawbacks of single imaging approach, nowadays the multimodal imaging has gained enormous recognition in biomedical applications. There are several approaches [153]–[155] to progress UCNPs based nanoprobes for multimodal bio-imaging. UCNPs as well as their nanocomposites can be utilized to fabricate such multimodal imaging bio-probes. Also in the field of cell labeling and in vivo tracking, UCNPs are sensible enough. Recently, investigation of mesenchymal stem cells (MSCs) has been started owing to their ability of recognition various types of cells (e.g., bone) under certain circumstances in various potential applications in bio field such as in immunotherapy and gene therapy.

#### 1.6.4 Medicinal and remedial applications

In present- days, UCNPs and their composites can be considered as therapeutic agent in cancer treatment, drug gene delivery and for photodynamic therapy due to their various unique properties and functions as well as imaging capability. For imaging and therapy, chemotherapy drug molecules could be delivered with loading of UCNPs .For drug releasing system, polymer coated UCNPs can also be used. For treatment of various gene-related diseases, gene therapy with gene encoding DNA or RNA has become a challenging matter. UV light emitted from UCNPs activates definite gene expression by operating DNA and RNA, though depth of penetration. The therapeutic efficiency is very high in case of UCNPs with NIR excitation compared with UCNPs with UV light and such PDT based on UCNPs

exhibited greater potential in treatment of cancers as well as suppression of the size of large internal tumours.

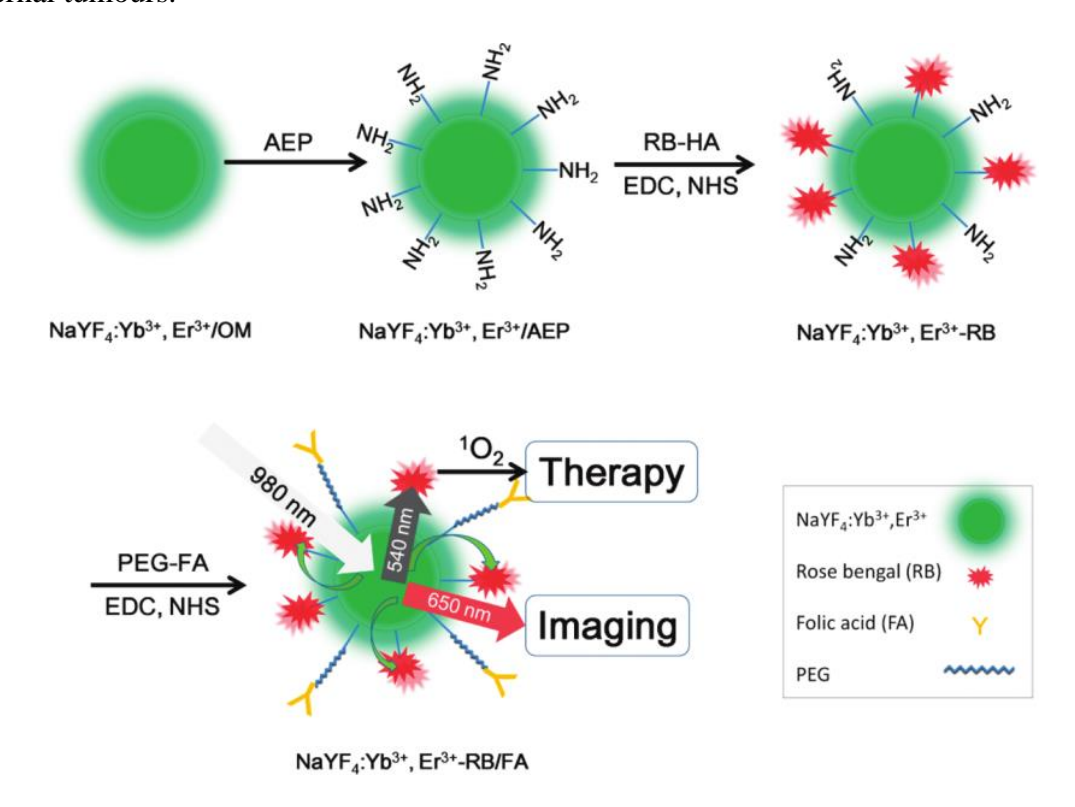


Figure 1.6.4: Covalent conjugation of NaYF4:Yb<sup>3+</sup>, Er<sup>3+</sup> UCNPs, photosensitizer (RB), target molecule (FA). Reproduced with permission (Liu et al., 2012). Copyright: ACS Nano publication

To treat cancer diseases Photodynamic Therapy (PDT) is a non-invasive and effective medical method which uses photo sensitizers (PDT drugs) and light irradiation and they interact with molecular oxygen. There are several approaches to originate PDT reagents like, silica encapsulation, polymer encapsulation, and hydrophobic interaction. At first photosensitizers are activated with light and as a result cytotoxic reactive oxygen species are formed and persuade required cell death [156]. Assembly of oxygen molecules are influenced by the energy transfer process from excited UCNPs relying on the spectral overlapping of donor and acceptor impurities in host lattice. There are two factors that quantify

photodynamic therapy, one is high energy transfer efficiency and the other is large production of singlet oxygen and these two phenomenons are related with high stability of originally loaded photo sensitizers in UCNPs. For good energy transfer process non- covalent form of UCNP-PS is not ideal as this provides low loading efficiency and finally small production of singlet oxygen. For that a covalent conjugating of UCNPs (NaYF4,Yb³+,Eb³+), photosensitizer and target molecule strategy can be adopted. For singlet oxygen and high fluorescence intensity production a multifunctional Upconversion nanoplatform has been already expanded on the basis of a particular energy- transfer from UCNPs to photosensitizer for synchronous imaging and therapy (figure 1.6.4) [157]. The therapeutic consequences of UCNP-PS compound for animal studies and cellular level have been already reported[156]. It has been reported in literature that for in vitro cancer cell destroying, mesoporous silica coated UCNP-PS combination shows an interesting and encouraging result [158]. Gu's group has revealed the uses of UCNP-PS nanocomplexes in the field of in vivo PDT [159]. For in vitro and in vivo tracking UCNPs have been used to designate stem cells by different groups [160].

Superlattices arrangement can be found in crystalline nanoparticles by synthesizing them in a controlled way with a few reaction parameters (in terms differ the interactions between nanoparticles from their bulk materials) which can result a well-defined geometries between the synthesized nanoparticles with improving their several properties such as conductivity, mechanical properties, optical properties, plasmonic properties, etc. depending on its order of packing/arrangement compared to its bulk[161]–[165]. On the other hands, self-assembly itself is an activity between nanoparticles or nano-building blocks to assemble them in a more ordered fashion without any external intercession in between synthesis procedure [166]–[168]. However, the combined strategy i.e. self-assembled superlattices would influence their properties [169], [170]. Using interfacial self-assembly approach different interesting geometrical features can be introduced with different length scales for using in different applications and nice distributions of few

ordered structures/patterns have been described in detail (e.g. Honeycomb structures, coffee rings, nanoparticles-superlattices) in a previous literature[171].

This dissertation introduces few interesting self-assembled nano-blocks which have drawn our attention due to their influenced optical properties and assembly over multiple nanoscales. Different applications of self-assembled superlattices (SAMSLs) in different nanoparticles are described as following:

As we know, self-assembly between nanoparticles have drawn our attention because of their applications in a large area, including medicinal treatments. Recently, liquid crystals along with nanoparticles have provided an ordered arrangement under controlled reactionparameters. In one recent literature, the authors have reported about their investigations on self-assembled nanoparticles on liquid-crystal droplets [172]. They have revealed that it the nanoparticles sizes and shapes which controlled the adsorption of different features on liquidcrystal nano - droplets (LC-NDs). They have further reported that sometimes, the shapes and patchiness of resulting nanoparticles could be the reason of having their strong indications of emerging properties. Suppose, if one nanoparticle is not capable of exhibiting favorable adsorption on LC-NDs, 100 nanoparticles could be agglomerated on LC-NDs allowing strong emerging properties. Now, the interactions among nanoparticles shapes, sizes and reactive constitutions have taken a dominant role in achieving self-assembly on LC-NDs. Hence, the authors have mentioned about the huge applications of self-assembled nanoparticles in new sensors and in several advanced materials. LbL - type self-assembly has been proposed to assist a better pharmacokinetics and control the releasing of RSV pursuants [173]. For achieving an improved drug delivery and to activate latent HIV, one kind of self-assembled nanoparticles were employed by researchers by loading with panobinostat (PNP-P) [174]. In 2018, by Huang et al. group, the photoluminescence study was examined with self-assembled nanoparticles (1.6-6.2 nm) conjugated with polymeric thin-film and they are believed to be used in optoelectronics applications where they can behave as host materials [175]. Further, nanostructures growth has been studied by incorporating self-assembled design on nanoparticle-surface. Depending on the surface and solutions interactions and the concentrations of the solutions used the nanostructures - growth was controlled [176]. In 2019, the Liang et. al. group has reported the formations of nanowires comprising self – assembled nanoparticles which exhibited blue-shifting emission profiles, so they declared promising applications of these self-assembled nanowires for violet/blue light emitters[177]. Even further, the self-assembled PTPPS nanoparticles found potential applications in vitro ad in vivo by reducing the cytotoxicity of TP and exhibited an improved method in chemotherapy especially in malignant tumour research [178]. It is well known, for analyzing subcellular and biological targets the fluorescence/luminescence imaging has promoted fluorescent/luminescent probes. By Long et. al. group one strong application of selfassembled nanoparticles was observed, hence the authors have reported that when the selfassembled nanoparticles were associated with bacteria surfaces, the resulted binding provided fluorescence turn-on signal which was capable to record the bacteria-imaging[179]. The antigen delivery by SAM nanoparticles has been reported to be an optimistic platform by Li et al. group[180]. For monitoring volatile organic compounds (i.e. ethanol, acetone) conductometric sensor was assisted with few SAM nanoparticles[181]. Qiu et. al. group showed the importance of SAM structural configurations by incorporating stable SAM microcapsules which was capable of encapsulating red pigments from paprika [182]. SAMnanoparticles can influence the utility of PEFC membranes [183]. The hetero-grafted macromolecular brushes provided with amphiphilic nature yielded SAM structures which allowed short backbones [184]. By developing cyclodextrin-based nanoparticles meropenem bio-accessibility and stability was enhanced by popielec et al. group [185]. Biodegradable gelatin-based nanoparticles were prepared with sustaining SAM morphologies for treating skin-diseases [186]. For destroying Bacteria, SAM formations of cationic-nanoparticles (appeared from CSM5-K5 chains) played an important role [187]. Bovine serum albumin – dextran conjugated SAM nanoparticles improved cellular antioxidant behavior in Caco-2 cells [188]. Wang et. al. group reported about the formation of microsphere with SAM nanoparticles whose sizes were adjustable[189].Guar - gum benzoate based SAM nanoparticles were synthesized for enhancing antimicrobial behavior against the water born gram (+)ve and gram (-)ve bacteria[190].Covalent phenyl-boronic acid based SAM nanoparticles were used for boosting tumour therapies by releasing drugs[191]. The importance of SAM pattern of core and shell in polymer nano-conjugate has further been revealed by Liu et al. group who showed their applications in PDT therapy[157]. Lipid ECO/SiRNA SAM nanoparticles were developed to resensitize TNBC which is a promising application in cancer therapy [192]. Using facile synthesis approach, SAM nanoparticles were derived from guar - gum propionate ester and those SAM nanoparticles showed antifungal properties [193]. Novel in-situ SAM nanoparticles (ISNPs) were discovered by Guo group for enhancing stability, palatability and bio-accessibility of RTV( ritonavir) ISNPs[194]. By Pham et. al. research group ISNPs were prepared by novel nanotechnology for reducing pill burdens on pediatric patients [195]. Formations of self-assembly by using amphiphilic derivatives were incorporated with WP<sub>5</sub> to exhibit strong NIR emissions along with their pH responses and usefulness in living cells for imaging purpose[196]. Again, previously in 2016, Fa et. al. group proposed self-assembly into nanoparticles by using a squaraine fluorescent probe and multi-interactions for detecting serum-albumin and for living-cell imaging purpose[197]. Conglycinin and chitosan based nanoparticles were prepared by self-assembly pattern with high stability and turbidity. These SAM nanoparticles exhibited drug-release operation [198] .Though Zoledronic acid (ZOL) has been proven to be most potent for inducing cell growth but ZOL encapsulated SAM PEGylated nanoparticles has been found to be most robust anticancer representative [199]. The SAM pattern was induced in nanoparticles by engineering with block-copolymer [PLGA-b-PEG NPs] which acted as nanotherapeutic agent [200]. Further, Wang et. al. group studied the interaction between Liver cancer cell and cholesterol amended SAM nanoparticles [201]. Phase - growth was rapidly controlled by using self-assembly on as-synthesized nanoparticles by Chen group [202].In 2014, by AFM study, Mukherjee et. al. group found the activity of Langmuir- Blodgett trilayers on SAM nanoparticles sustained with clear morphologies [203]. To represent biodetection system (immunosensing with free labeling) nanoparticles were assembled into a nanochannel format just like self-assembly pattern [204]. Yan et. al. group developed Tat-Suc-FA SAM nanoparticles for tumour gene treatment [205]. Cellulose SAM nanoparticles were used in bio-medicine especially in drug carrier and in study of controlled releasing behaviour [206]. To strengthen the microwave absorption potentiality, SAM nanoparticles and their morphologies with ample number of interfaces play an important role. Synthesizing these SAM patterns endures significant challenge to us. SAM nano-flower type pattern was exhibited by Li et. al. group in Cobalt monoxide (CoO) nano-configurations which was controlled during synthesis along with Oleic acid and Oleylamine. This type of nanostructure exhibited great potential in enhancing the microwave absorption. Hence the authors reported the high performances of CoO for electromagnetic shielding [207]. Self –assembled system in as-synthesized nanoparticles has already provided a vital role in drug delivery[208] and electrospinning fields owing to their flexible morphologies sustained in large- area [209]. SAM nanoparticles of  $\gamma$ -polyglutamic acid grafted with cholesterol ( $\gamma$ -PGA- graft- CH) were developed by Li et.al. Group for using them as successful carrier of drugs (i.e. hydrophilic drugs) [210]. A novel synthesis method was proposed for producing SAM nanoparticles by using (γ - PGA - Graft - CH) and hence the SAM nanoparticles acted as protein carriers[211]. According to Jhang et.al. group report, self-assembly occurred in certain nanoparticles after synthesizing them from conjugate products and here the resultant SAMNPs showed higher stability with a large zeta-potential value[212]. One review article presented about the application of SAMNPs of 3D nucleic acid as gene therapy by a significant Si-RNA delivery [213]. Antitumor doxorubicin (DOX) drugs were confined in SAMNPs by incorporating  $\pi$ -  $\pi$ interactions for drug delivery (specifically antitumor) [214]. The taurocholic acid (TCA) and heparin – docetaxel (DTX) were designed in a coupled form to conjugate with SAMNPs which located the TCA on particle-surface whereas DTX inside core. This conjugate form was capable for cancer treatment approaching with oral delivery [215]. In 2012, on Ag nanoparticles, self-assembly pattern was involved by Meikun Fan for localizing surface plasmon resonance (LSPR) owing to presence of several functional groups attached with selfassembled configurations. Hence, the author reported a 3-4 times enhanced SERS on multiple self-assembled surfaces[216]. The SAM polymeric nanoparticles have suggested being excellent materials for delivery of anti-inflammatory and antioxidative representatives in atopic dermatitis therapy [217]. The self-arranging capabilities in certain monodisperse nanoparticles provided a modulable tool for encapsulation and for controlled releasing behaviour of pharmaceutical compositions [218]. ZOL encapsulated SAMNPs were developed for human cancer therapy [219]. Chemically-assisted SAMNPs have been developed in a large scale area for several nanoscale devices (Optical/ Electrical/ Magnetic) and therefore their production has become attractive[220]. Self-assembled carbonnanotubesor polymer composites were prepared by inducing electric- field interaction[221]. By Salzano group SAM PEGylated Nps were prepared for cancer therapy followed by bisphosphonates - delivery into tumors [222]. Certain SAMNPs conjugated with PECD cationic polymers were potentially used for gene transfection where those PECD – SAMNPs served as efficient carrier agents[223]. Individually, by Cao group, the SAMNPs of PLLA-PC were produced by solvent evaporation procedure. After analysing their properties, the authors reported their great potentiality in drug-delivery system (specified for hydrophobic drug)[224]. The self-assembly was designed in block-copolymer conjugated with nanoparticles for delivering docetaxel to human-tumor cells[225]. The applications of CsB /DNA self-assembled nanoparticles (CsB/DNA NPs) found in gene delivery with influencing transfection efficiency [226]. Few authors reported about the formations of SAM nanocomplexes which were stable and bio-friendly. These nanocomplexes were formulated by incorporating self-assembly pattern of γ PGA and chitosan. Hence, the authors believed their uses in various biomedicinal applications carrying with 40-285 nm particle diameters [227] . According to one report, the supramolecular networks were assembled spontaneously and showed their efficiencies such as in energy-transfers and MRI. Few adaptive properties were also observed in this self-assembly pattern as mentioned in this report. These adaptive properties direct their biocompatible nature. Hence, the related application-oriented experiments were also depicted in this report [228]. BOXD-T8 derivatives were assembled into nanoparticles to form self-assembly pattern which showed strong fluorescence [229]. For cancer therapies (like drug delivery/gene delivery/therapy) targeting receptors became important. In an experimental study, SAMNPs were designed for presenting targeting-ligands (u-PAR) which further appeared for observing RME and drug delivery [230]. Previous report also confirmed that SAMNPs remain effective and can act as nucleation representatives for fatty acids with various lengths of its chains. The report described about the seed-mediated nucleation strategies for creating SAM pattern [231]. One group of synthesized SAM materials provided potential ability as chemosensors [232]. The shape-directed SAMNPs were used to design nano and microdevices where the SAMNPs owing to their assembled configurations were able to accommodate various functional additives and this invention was done by Desimone et al. group and was filed for an US patent (United states patent application publication, Pub. No. US 2010/0055459 A1). Stable and biodegradable SAMNPs based on γ-PGA and chitosan were prepared having particle-diameter of about 20-285nm. Here the authors believed on their uses in biomedical as also described in ref 57 [227]. Further, SAMNPs were prepared for tagging specific quantum-dots, the fluorescence intensity of those dots were influenced by tagging them with SAMNPs[233]. By developing SAMNPs, liposomal agents were delivered by linking them with Pal-PLS[234]. The importance of the engineered SAMNPs along with their present applications and advantages were discussed in detail by Dusica Maysinger [235]. The uniform and assembled nanoparticles were used to fabricate flash-memory tool as reported in an article. Hence, the SAM morphology in nanoparticles were occurred by fabricating SAM-Protein lattices (such as chaperonin) arrangement on oxide-layer and afterwards, by trapping the nanocrystals on specified-cavity spaces of SAM-Protein, the SAM pattern was developed externally by annealing -treatment and this invention was filed for US patent (United states patent application publication, Pub. No.WO2006127589 A1).From SAM-polymeric macromolecules, nanoparticles were developed particle-diameter 20-44 nm by Slomkowski et al. research group. Hence, the obtained nanoparticles showed successful drug-release behaviour in a faster-way [236]. Another study revealed about the in-vivo stability of self-aggregated nanoparticles for possessing lower concentration values [237]. Further, SAMNPs (where gold NPs bind the surface) were used for bio-detection purpose by influencing its sensitivity which depended on the binded-area [238]. By distributing hydrophobic groups of Amphipol A8-35 in an assembled pattern, SAMNPs were developed [239]. Though viral vectors used for gene therapy were efficient, still limitations are there due to deficiency of those systems in therapies. Non-viral vector system appeared to be safer. Therefore, a review has been made by focusing on synthetic and self-assembled non-viral system of nanaoparticles and it further exhibited the importance of SAMNPs in gene therapies [240]. Further, Novel SAMNPs were prepared using polycondensation method. Hence the resulted NPs were degradated in water and a narrow particle-size distribution was observed [241]. Ultrasmall SAMNPs of polyNIPAM-BA were also reported which further confirms about their stability in a large scale of temp-range. Here, the formed nanoparticles were useful to design optical nanothermometers [242]. Involving nanoprecipitation method, PTPP-SAMNPs (PTPPSN) was prepared. In both of in-vitro and in-vivo study, they have found an efficient and improved effect while compared with its original prodrug. This experiment is useful for malignant tumour therapies as described in ref 7[178]. To design biomaterials, self-assembly pattern has become an important process, has been confirmed by Paik et al. research group who have reported about 3D Zn<sub>3</sub> (PO<sub>4</sub>)<sub>2</sub> SAMNPs which has increased the surface-interactions with biosubstances. Hence, the in-vitro study confirms about their uses in bone-tissue engineering [243]. Tat-Suc-FA SAMNPs were used to further improve tumor therapy owing to their enhanced efficiency and specificity in such bio-applications [244]. Other c(RGDfk) conjugated SAMNPs were incorporated for therapies as they used in SiRNA-delivery to target specific gene VEGFR2 [245].SAMNPs have been developed for facilitating or enhancing few specific properties specially, delivery properties in cells/tissues[246]. HA-SAMNPs were useful for targeting tumors [247]. The improved silver SAMNPs were incorporated in trapping plasmonic light[248]. The DC transport has been appeared with 2D silver SAMNPs[249]. Electroluminescence was studied with CdSe SAMNPs [250] To fabricate biosensors, SAM layer formations were prepared with CNT and platinum NPs [251]. For signal amplification, electrochemical sensors, consisting with SAM monolayers, were used [252]. Electrocatalytic reduction was enhanced by employing SAM layers of copper and nickel substitutes[253].

#### 1.7 Conclusions

This review explores recent developments of UCNPs along with a detailed survey and as application part it focuses in bio-fields (imaging and therapy). Though there are tremendous amount of applications and a number of exciting aspects have been reported in literatures since past few years on this field but still many challenges are ahead especially in imaging and therapy for using UCNPs in an advanced way.

With reducing the sizes of UCNPs the quantum yield became lower which limits their use in various nano-probes. Later, several research groups modified the synthesis and production of UCNPs to increase their yield under continuous wave-excitation sources but still future efforts are required to make them useful for enormous number of in-vivo applications. The long term toxicity of RE doped UCNPs is another perturbation. Though, biocompatible coating-based UCNPs (NaYF<sub>4</sub>) appeared to be safer to cells (with precise concentrations) compared to bared UCNPs but still other factors like their interactions with immune systems, interference with the reproductive system, whether the toxicity is affecting for next generation applications, that are still not known for which more number of systematic investigations are demanded. The effects of surface functionalization and sizes of UCNPs on in- vivo behaviours are required to improve in reducing certain potential toxicity. Though imaging and therapies based on UCNPs and their different nanocomposites have been revealed in previous literatures, to achieve synergistic therapeutic effects and realize real-time scanning of treatment development an improved design of UCNPs based on novel multifunctional agents are needed further for simultaneous medical diagnosis and cancer treatment.

#### 1.8 Motivation of this dissertation:

It is evident that with reducing the sizes of UCNPs the quantum yield became lower which limits their use in various nano-probes. Later, several research groups modified the synthesis and production of UCNPs to increase their yield under continuous wave-excitation sources. However, still efforts are required to make them useful for enormous number of in-vivo applications specially with unique sizes. The long-term stability and toxicity of rare earth doped UCNPs is another challenge.

Moreover, upconversion enhancement has been an exciting topic for rare earth nanoparticles and nanolumiophores due to their potential uses in several display, electronic and laser devices including several biological applications (bio-imaging). But on all those points, we need to improve the synthesized nanoparticles by incorporating different parameters.

The effects of sizes and morphologies in UCNPs for several applications are required to improve in reducing certain potential toxicity and increasing stability in their colloidal dispersions and also to improve their upconversion efficiency under certain excitation sources. Different sized and structural configurations of UCNPs based on novel synthesis methods by varying different reaction parameters are needed further for improving their spectroscopic properties to enhance upconversion emission so that they could become potential candidates in an additional number of future applications.

Therefore, based on this the following objectives are formulated for this dissertation:

1. Synthesize UCNPs at relatively lower reaction temperatures and times as much as possible with choosing appropriate precursors and always approach a simpler and straightforward method. Control reaction time and reaction temperature to overcome some drawbacks during synthesis (Particle aggregation, enlarged particle size).

- 2. Enhance up-conversion intensity with incorporating only fluorides and avoiding bromides and chlorides as they are sensitive to moisture and therefore not worthy for bio labeling or imaging.
- 3. Synthesize high quality UCNPs with a user-friendly method (one-pot chemical approach) to avoid the existence of fluoride reagents in high reaction temperature.
- 4. Synthesizing UCNPs in different ways (by varying reaction parameters) to achieve controllable shapes, sizes and structures with an efficient UC fluorescence/luminescence.
- 5. Prepare different sized and structured UCNPs such as UCNPs-hexagonal, UCNPs-Dot, UCNPs-Dendrimers, UCNPs-Superlattices having a sufficient amount of UC emission under NIR excitation sources.
- 6. Correlate and analyze relevant findings to the spectroscopic properties along with their variations in fluorescence/luminescence by observing their emission spectra under different excitation sources (single laser laser-diode 980nm NIR, Femtosecond laser source 940-990nm NIR).

#### 1.9 Arrangement of dissertation:

The present dissertation has been organized in four chapters, which are given as,

**Chapter 1:** This chapter includes introduction, literature reviews, motivation and objectives of dissertation.

**Chapter 2:** This chapter covers experimental part along with the materials and methods that have been used for synthesis purpose and also the characterization techniques.

**Chapter 3:** The whole result and discussion part is described in chapter 3, which is divided into five parts:

Part I. In first part, hexagonal UCNPs (sizes ~200nm) have been synthesized with

highest photon upconversion efficiency with 980nm laser diode source (NIR) and

Femtosecond-laser source.

Part II. In second part, different characterizations and emission properties have been

discussed in upconverting nanodots (UCN-dots) which appeared with particle sizes below 5

nm and effectively can generate high intense UV emission while interacts with 140

femtosecond laser pulses.

Part III. In third part, a novel synthesis has been introduced for preparing upconverting-

nanodendrimers (UCN-Ds) in necklace or chain formations. Their characterizations and

emission properties have also been discussed in this part.

Part IV. In fourth one, self-assembled superlattice formations of UCNPs (SAM-

UCNPs-SL) have been shown with controlling several parameters and further their

emission properties (fluorescence, luminescence, photoluminescence) have been investigated

along with introducing characterization techniques.

**Chapter 4:** The last chapter will be presenting the summary of the research work including

conclusions and future scope.

**References**: At the end of chapter 4 references are listed accordingly.

51

## 2 EXPERIMENTAL SECTION

## 2.1 Outcome:

#### **Patents Filled:**

- 1. Stable upconversion nanoparticle super- lattice (UCN-SL) & in-situ process for developing thereof; Ref. No./Application No.- 201841037607
- **2.** Stable upconversion nanoparticle dendrimer (UCND) & method of making thereof; Ref. No./Application No.- 201841037609
- 3. upconversion nanoparticle DOT (UCN DOT) of size 3.5 nm & its preparation process thereof; Ref. No./Application No.- 201841037608

In this chapter, the materials used to synthesize different UCNPs with controlling several reaction parameters are introduced. The synthesis methods have also been depicted. Different characterization tools to characterize synthesized materials have been discussed in this section with their working principles.

## 2.2 Materials used to synthesize UCNPs:

Table 2.2.1: Materials used to synthesize UCNPs:

No.	Chemicals used	Purity in percentage	Company source
1.	Methanol	99%	FINAR
2.	Ethanol	99.5%	Merck
3.	Acetone	99.5%	Merck
4.	Ammonium Fluoride(NH <sub>4</sub> F)	97%	Kemphasol
5.	Sodium Hydroxide(NaOH)	97%	SDFCL
6.	Sulfuric Acid(H <sub>2</sub> SO <sub>4</sub> )	99%	Qualigens
7.	Potassium Permanganate (KMnO <sub>4</sub> )	99%	SDFCL
8.	Cu solution	98%	Kemphasol
9.	CaCl <sub>2</sub>	98%	SDFCL
10.	Yttrium Chloride salt (YCl <sub>3</sub> :6H <sub>2</sub> O)	99%	Sigma-Aldrich
11.	Ytterbium Chloride salt (YbCl <sub>3</sub> :6H <sub>2</sub> O)	99%	Sigma-Aldrich
12.	Erbium Chloride salt (ErCl <sub>3</sub> :6H <sub>2</sub> O)	99%	Sigma-Aldrich
13.	Oleic-Acid(C <sub>18</sub> H <sub>34</sub> O <sub>2</sub> )	63%	Qualigens
14.	Cyclohexane(C <sub>6</sub> H <sub>12</sub> )	99.9%	FINAR
15.	Inert Gas (Ar gas)	98%	Sidhi Vinayaka gas
16.	De-ionized water	-	-

## 2.3 Methods for synthesizing UCNPs:

The synthesis methods for producing different upconverting nanocrystals, such as: hexagonal UCNPs, UCN-dots, DCN-Ds, SAM-SL-UCNPs, are discussed below.

## 2.3.1 Synthesis method for highly efficient hexagonal UCNPs:

To form hexagonal UCNPs, YCl<sub>3</sub>, YbCl<sub>3</sub>, ErCl<sub>3</sub> were mixed in 6 mL of OA and 15 mL of ODE in a 250 mL of three-necked flask on heating mantle, at first the heating started towards 150°C to create a homogeneous solution and after that started for cooling at room temperature only.10 mL of methanol solution along with NH<sub>4</sub>F and NaOH was prepared and added very slowly(drop wise) into the heating flask. Now to consume all fluoride regents, the whole sample in flask was stirred for some time. From this condition onwards, slowly it was heated for evaporating methanol from sample-solutions. Thereafter, degassed condition was applied at 100°C for 10mins and finally the temperature was fixed at 300°C for 1 hour which was maintained under complete inert gas atmospheric condition. Cooling was started naturally at room temperature and continued until the sample-flask came to room temperature. Next day, from cooled flask, the nanocrystals were collected with cyclohexane and then washing method using ethanol and water (1:1 v/v) and centrifugation method.

## 2.3.2 Synthesis method for UCN-dots:

The detailed synthesis procedure of UCN-dots has been filed for Indian patent (Ref. TEMP/E-1/21071/2017CHE, dt.: 14/06/2017). In brief of the synthesis procedure: the specific amount of precursor materials (YCl<sub>3</sub>:6H<sub>2</sub>O; YbCl<sub>3</sub>:6H<sub>2</sub>O and ErCl<sub>3</sub>:6H<sub>2</sub>O) were dried from moisture and poured in 1-Octadecene and Oleic-acid followed by heating in inert gas environment. Thereafter, at room temperature a mixture (4:1) of NaOH and NH<sub>4</sub>F (dissolved in MeOH) was added. The resulted solution was heated in inert gas atmospheric condition up to 300°C for few mins and then it was cooled down to room temperature. Finally, the UCN-Dots were collected via high speed centrifugation (RPM 14000) and were preserved in cyclohexane.

## 2.3.3 Synthesis method for UCN-Ds:

UCN-Ds were synthesized by solvothermal decomposition process of lanthanide precursors and technical grade chemicals. Three different precursors were prepared in presence of de-ionized H<sub>2</sub>O. These three precursors were then decomposed at 110°C -115°C. Further, in decomposed compound organic solvents (Oleic acid and Octadecene) were added and stirred at 140° C. Then it was cooled down to room temperature. Then, a solution of CH<sub>3</sub>OH, NH<sub>4</sub>F and NaOH was added at room temperature and stirred to remove excess oxygen and water and heated further to 340° C (rate of 20° C/min). Entire synthesis was performed under argon gas atmosphere and a vacuum condition was maintained at 100° C. Next day, the synthesized sample was collected with acetone via centrifugation with 9000 rpm for 15-20 min. The precipitated product was collected by dispersing with cyclohexane (40ml). Finally, it was washed with ethanol and D.W. (1:1) for 3-4 times. The resulted solution was preserved in a container as its colloidal form. The self-assembled dendritic UCN-Ds are stable for more than a year. Surprisingly, no agglomeration or settling was found. However, after a couple of weeks the white particles seemed to be settled clearly at the bottom of container and it can be readily dispersed at room temperature and subsequent characterization revealed that dendritic net-work structures persist for more than a year. The detail of synthesis method was filed for an Indian Patent (Ref: TEMP/E-1/21065/2017CHE, dated: 14/06/2017).

## 2.3.4 Synthesis method for SAM-SL-UCNPs:

SAM-SL UCNPs were synthesized by using thermal decomposition procedure of lanthanide precursors and technical grade chemicals. The de-ionized H<sub>2</sub>O solutions of hexahydrate precursors were used. Three precursors were decomposed with reaction-temperature of about 120°C. Thereafter, organic solvents (ODE, C<sub>18</sub>H<sub>34</sub>O<sub>2</sub>) were added

and stirred with similar heating rate as in decomposing step. A mixed solution of CH<sub>3</sub>OH, NH<sub>4</sub>F and NaOH was added at room temperature and stirred vigorously to remove excess oxygen and water and heated further to 320°C for a maximum of 15-20 minutes, 51 minutes, 1 hour 50 minutes. The experiment was done under complete argon gas atmospheric condition and a vacuum condition was maintained at 100°C for 30 minutes to produce a yellow and transparent solution. Next day, the synthesized sample was collected via centrifugation with acetone and cyclohexane. Then it was washed with ethanol and D.W. The resulted solution was preserved in container as its turbid, colloidal form.

SAM-SL UCNPs are stable for a couple of weeks and surprisingly, no agglomeration or settling was found during this period, however, after few months particle settling was found.

The detailed synthetic procedure has been filled for an Indian Patent (Stable upconversion nanoparticle super lattice (UCN-SL) & in-situ process for developing thereof (Ref: TEMP/E-1/21071/2017CHE, dt.: 14/06/2017).

## 2.4 Characterization Techniques Used:

Different synthesized UCNPs were characterized through several techniques such as , Transmission Electron Microscopy (TEM) , X-ray diffraction pattern( XRD), Raman Spectroscopy, Atomic Force Microscopy (AFM) , Fourier Transform Infrared Spectroscopy (FTIR), Fluorescence Spectrophotometer, Multimode Reader (H4 synergy Reader), Zetasizer( nano- series: Malvern instruments)), Femtosecond-laser luminescence (140 femtosecond, 80 MHz repetition rate). A short description of each technique is given below.

#### **2.4.1** Transmission Electron Microscopy (TEM):

TEM probes the morphologies of an experimental sample. In the present-study, EDXA is attached with TEM instrument (ex. model FEI TecnaiG2-TWIN 200 KV) for providing information about the presence of different elemental compositions. HRTEM (high resolution transmission electron microscopy) images can also be produced with TEM. SAED pattern (selected area electron diffraction pattern) can provide us the structural configurations of a sample. An acceleration voltage of about 200kV -300kV is typically used in TEM to receive higher resolution (0.1 nm) as well as magnification (10000 KX).

The instrument is carried with three parts,

- 1. Electron gun with condenser lenses, electron gun generates the electron beam, and condenser lenses focuses accelerated beam.
- 2. Image-forming system, which basically focus the electrons to generate highly magnified image.
- 3. Image recording system, which uses objective lenses and a fluorescent screen and a camera to record the focused images.

Besides the presence of them, a vacuum system is also maintained inside the chamber to avoid the ionization of air molecules. Tungsten filament is used to accelerate the electrons. In modern TEM, two condenser lenses are used, say C1 and C2. C1 reduce the spot sizes whereas C2 intensifies the spot. These two lenses control the electron-illuminations on sample. The objective lenses can control the contrast and magnifications of the images formed.

The presence of some mechanisms forms the images on screen, one is Mass-density contrast and the other one is Diffraction contrast.

A diagram of TEM system is drawn in figure 2.3.1,

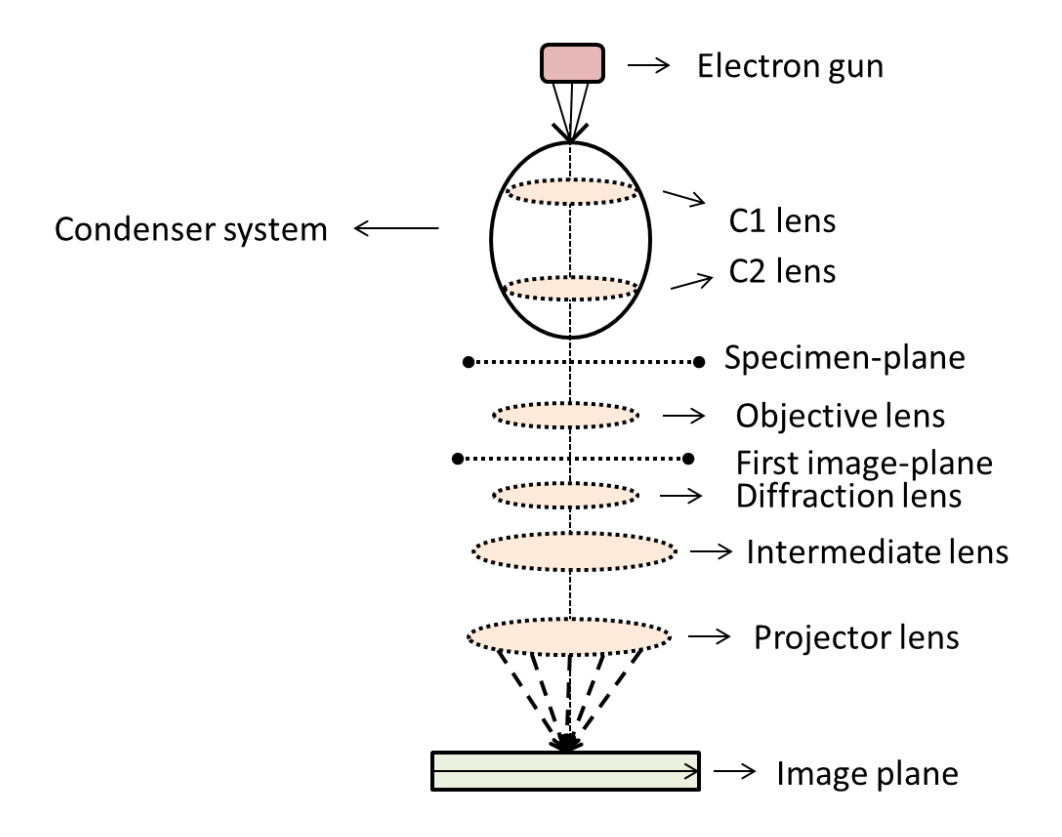


Figure 2.4.1: Schematic of TEM system

**Mass density:** Interaction between electrons and nucleus results in scattering of electrons. Hence, for a sample, the amount of scattering from a specific point of material is dependent on the mass density of that particular specimen-point.

**Diffraction-contrast:** In the formations of images for crystalline materials, diffraction-contrast takes place and undergoes with collective deflection of electrons, which are scattered by crystal planes arranged parallel. Diffraction angle appears to be very small of about  $\leq 1^{\circ}$ . Diffracted beam from collaboratively scattered electrons are focused as spot. Bright-field image is produced with allowing the transmitted beam while dark field image is produced with only passing diffracted beam.

**Phase-contrast:** Phase-contrast can be introduced as high-resolution transmission electron microscopy (HRTEM) and is different from two amplitude contrasts (Mass density and diffraction contrast). It can produce very high-resolution images of lattices and structures of crystalline specimens. While, amplitude contrasts involve change in amplitude of electronwaves, phase contrast involves two electron-waves in different phases (e.g. transmitted beam and diffracted beam appear in different phases).

However, Special care should be taken to prepare samples for receiving TEM images. Samples are always placed on carbon-coated copper-grid in a complete dried form, which must be having thin-layer, and the electrons get diffracted easily with the specimen-molecules.

For biological samples, special sample preparation techniques are used with applying low acceleration-voltage.

#### 2.4.2 X-Ray Diffraction:

X-ray diffraction is a powerful method to characterize crystalline materials. Crystallinity of sample is strongly determined with this technique. Owing to the presence of different atomic arrays in different materials, the produced diffraction pattern also becomes different. This technique is based on Bragg's law which is defined as  $2d\sin\theta = n\lambda$ , where d= interplanar spacing between two atomic layers,  $\theta =$  angle at which the beam is diffracted,  $\lambda =$  wavelength of incident light, n= integer number (reflection order). This law describes, the path difference between two incident x-rays must be equal to  $n\lambda$ . In this dissertation, Bruker AXS model D8 diffractometer has been used with using CuK $\alpha$  source to determine crystalline structure of UCN-samples. Again, from this technique, by using Debye Scherrer formula crystallite sizes are calculated which have been reported in result and discussion part. A schematic of XRD technique has been drawn in figure 2.3.2.

According to the figure 2.3.2, path difference between two x-rays = PE+EQ PE=  $dsin\theta$ = EQ

So, total path difference=  $2d\sin\theta$ Now, according to Bragg's law,  $2d\sin\theta = n\lambda$ 

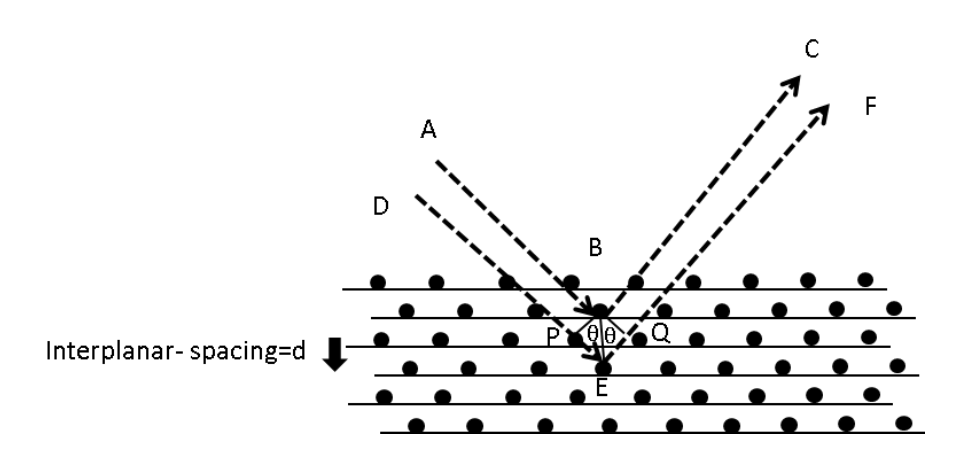


Figure 2.4.2: A schematic of XRD technique showing diffraction from two parallel planes

#### **2.4.3** Atomic Force Microscopy:

Atomic Force Microscopy can be considered as one type of high-resolution scanning probe microscopy using a cantilever with short tip (15-30 nm radius) which scans over the materials surface. As this tip approaches towards the sample-surface, it bends due to the presence of attractive force between tip surface and sample-surface. Again, the cantilever bends away from the sample-surface due to an increasing repulsive force between cantilever and sample-surface (while the cantilever comes very closer to material-surface. Additionally, two scanners are present in AFM, one for moving the cantilever up and down and the other one for moving the sample back and forth. To record the bending of cantilever, a position detector is present. Laser beam reflecting on cantilever can be tracked with the position-sensor. Direction of reflected beam can be changed with changing the bend-position of cantilever. The beam-changes are tracked and recorded with position-detector. For any material, the topography of required region appears in AFM image while the cantilever scans over the

specified region. The lowered and raised characteristics of any material-surface are measured with position detector by influencing cantilever-bending. We are able to receive a reliable topographic image of sample-surface by using AFM technique. The schematic of AFM is shown in figure 2.3.3. There are different modes of AFM, they are:

1. Contact-mode AFM: In this mode, the tip touches sample-surface and as a result the cantilever bends while passes over surface-feature. Distance between probe and sample-surface is less than 0.5nm.

Advantage: Relatively simple technology.

Disadvantage: Sample-surface can be damaged sometimes due to the close proximity of sharp-tip and sample-surface.

2. Non-Contact-mode AFM: In this mode, the tip does not touch sample-surface, rather than the cantilever oscillates just over surface-wall. Distance between probe and sample-surface is 0.1-10nm.

Advantages: This mode permits to give high quality AFM images with prolonged tipsharpness and tip-lifetime. It can also reduce the operating cost of instrument as no tipreplacement is required for scanning.

Disadvantages: Ultra high vacuum (UHV) is required receive best images. The oscillation can be disrupted with contaminant layer.

3. Intermittent –contact mode: In this mode, imaging is done specially with soft samples (e.g. biological samples). Using "tapping mode" the deformations (occurs with the exerting force by sharp-tip during scanning) of soft samples can be overcome by this technique which can afford highly sensitive signals by lowering the oscillation-

amplitude of cantilever. Distance between probe and sample-surface is 0.5- 2 nm. Oscillation- amplitude is about 20-100nm.

Advantages: High resolution images are formed and recommended for soft samples Disadvantages: More challenging in case of liquid-imaging and provides slower scanspeed.

In present study, surface topographical images have been received with non-contact mode in AFM and the model used is Model: SII Oo Seiko Instruments Inc.

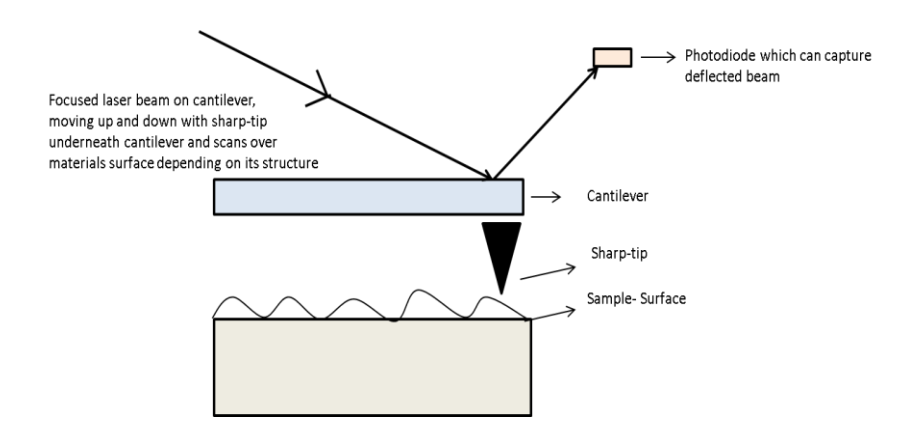


Figure 2.4.3: Schematic illustrating AFM working principle

#### 2.4.4 Raman Spectroscopy:

It is a spectroscopic technique to measure the chemical structure of any substance by detecting the vibrational modes of molecules. This technique is based on the inelastic scattering of photons which comes from monochromatic light source. The study of interaction between light and matter is observed in this technique and is termed as Raman Effect. During interaction of light with matter, the photons undergo different effects as they can be scattered or transmitted or reflected or can be absorbed fully or partially. In scattering effect, elastic (Rayleigh scattering) or in-elastic (stokes and antistokes scattering effect) scattering can take place. In Raman spectroscopy, we deal with in-elastic scattering of photons with stokes or

antistokes shifts. These shifts can provide us the information of different modes in interacted molecules (vibrational mode, rotational mode or other transition modes). This spectroscopy is used for solid, liquid and gaseous substances. Distinguishing different modes in Raman spectra, one can confirm the presence of molecules and the associated functional-groups in any specified substance.

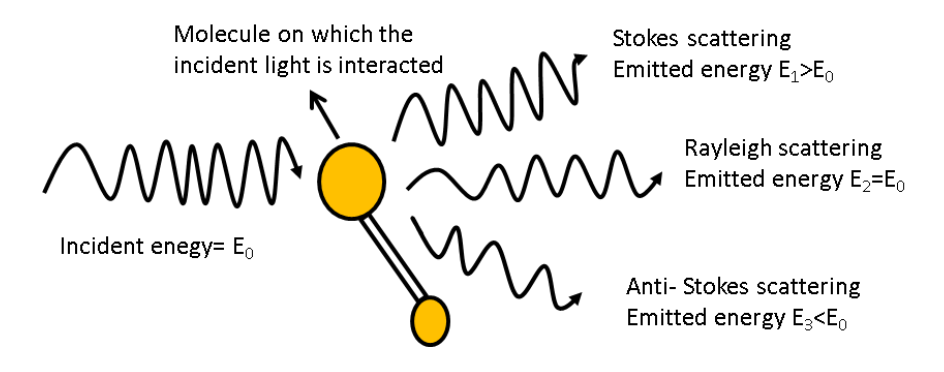


Figure 2.4.4: Schematic of Raman scattering effect after interacting with substance-molecule

The Raman spectra that we receive from Raman spectroscopy provide us various information on substance-molecules. We can interpret them in terms of either wavelength or energy. The spectra received in higher wavelength region compared to Rayleigh scattering line, originate due to antistokes scattering phenomena and the spectra received in lower wavelength region, occur due to stokes scattering effect (figure 2.3.4). So, the stokes lines always appear with higher intensity.

In Raman instrumentation, laser light is projected on sample by using single-wavelength laser source. The instrument integrates with optical microscope. Using micro Raman spectroscopy technique, we can analyze micro areas in large substance. The modern micro Raman instruments use several single-wavelength sources to avoid resonance effect. In order to produce, good Raman signals, excitation sources can be varied with varying excitation wavelengths. A schematic of Raman-instrumentation is shown in figure 2.3.5.

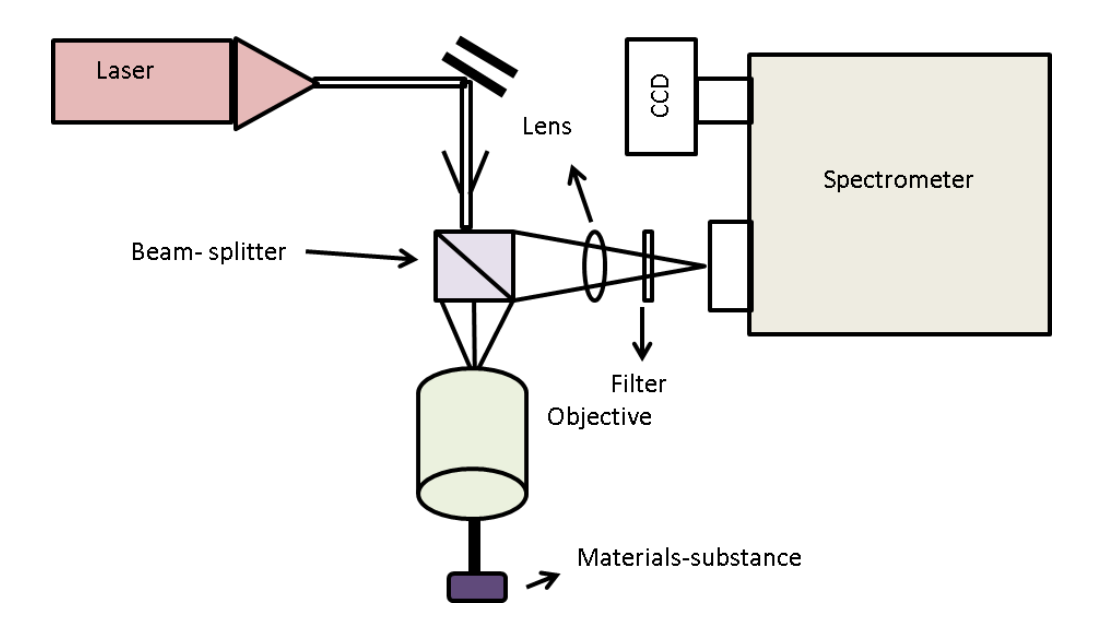


Figure 2.4.5: Schematic representation of Raman spectroscopy instrumentation

In this dissertation, samples have been characterized using "Witech Alpha 200 Raman spectrophotometer" model containing Nd YAG laser (532nm excitation Wavelength) with  $2^{nd}$  harmonics and spot size of about 2  $\mu$ m.

#### 2.4.5 Fluorescence Spectroscopy:

Fluorescence from any sample-molecules is being studied with fluorescence spectroscopy technique. It has become a powerful technique to study the chemical or physical properties of molecules due to high sensitivity. In this technique, near infrared or infrared light source is generally used to impinge on sample-molecules and the resulted fluorescence spectrum is recorded. This measurement can provide emission spectra as well as excitation spectra (due to presence of dual modes). In case of receiving emission spectra, we need to fix excitation-wavelength with varying the detector scanning- wavelength and in case of receiving excitation-

wavelength. The mechanism behind this technique is based on the presence of different energy levels with their vibrational states in molecules. While the light source impinges on the sample-molecules, the molecules become excited and jump to excited state from their ground state vibration levels. Due to efficient populations in higher excited-states or due to collision with other molecules, the excited molecule immediately comes to lowest vibrational level from which they can reach to ground state. Here, the extra energy comes out in terms of emission and is recorded in fluorescence spectroscopy with fluorescence spectra. Fluorescence intensity can be varied with different efficient populations present in different excited energy-states depending on different molecular configurations of chemical compounds.

In this dissertation work, Hitachi F-4600 spectrophotometer model is used and as excitation source Xenon lamp is present in instrument. Furthermore, an external source of 980nm excitation wavelength NIR-laser is attached with this spectroscopy. A basis diagram of Fluorescence spectroscopy is shown in figure 2.3.6.

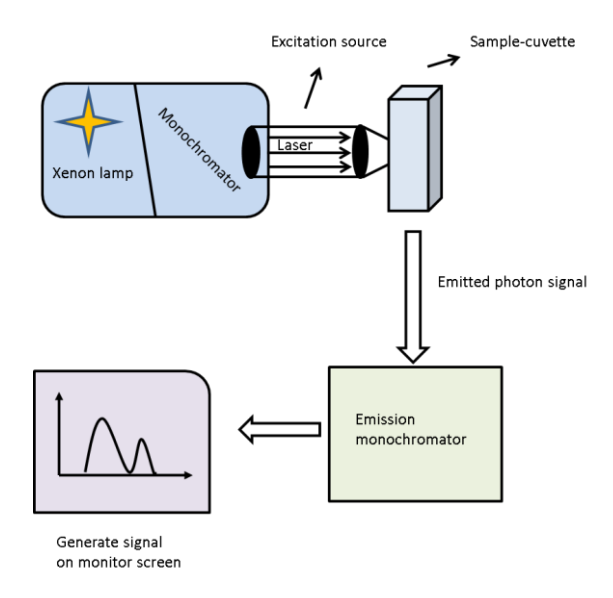


Figure 2.4.6: A simple schematic of fluorescence spectroscopy instrumentation

## **2.4.6** Fourier Transform Infrared Spectroscopy (FTIR):

FTIR is a spectroscopic technique to receive infrared spectrum of emission, absorption or Raman scattering of any substance (solid/liquid/gas). This spectrometer accumulates high-resolution spectral data over wide range. By this technique, the actual data are being transformed with Fourier transform (known as a mathematical algorithm and Lord Rayleigh introduced the existence of relation between spectrum and interferogram via Fourier transform). The sample -molecules absorb certain frequencies which provide the particular characteristics of chemical – structures. Hence, the resonant frequencies occur as the absorbed radiation matches with the bond/group- frequency under vibration.

Instead of single wavelength source (ex. Monochromatic light), FTIR uses beam carrying many frequencies. Such beam with many frequencies is being modified to provide second data point and this process repeat several times and finally computer records all datas for absorptions at each wavelength. Michelson interferometer (MI) is the core part of FTIR as MI recombines two beams to conduct them into detector.

Sample preparation can be done with few steps:

- Step 1. For using solid sample in FTIR, 200mg KBr is required with 2 mg of sample. For liquid samples, NaCl pellets are generally taken, for volatile liquid sample, sample-solution is prepared with CS<sub>2</sub>/CCl<sub>4</sub>.
- Step 2. In this step we get spectrum by collecting interferogram thereafter these raw data is being converted to frequency data via inverse Fourier transform process.
- Step 3. In this step we collect the absorption bands (and also the background spectrum) of sample from recorded spectrum.

Step 4. The ratio of the sample-spectrum and background spectrum of single beam can provide the required spectrum for analysis.

Step 5. Now, we can analyze data by observing absorption frequency bands in spectrum and by assigning them to proper vibrational modes of molecules.

In this work, an FTIR spectroscopy- Nicolet model impact-410 has been used.

## 2.4.7 Femtosecond laser (Fs) set-up:

At present days, upconversion luminescence based on 2/>2 photons (absorbing simultaneously) has drawn our attention due to an advanced technology in NIR Fs laser which can develop highly sensitive organic materials. Compared to the other lasers, NIR Fs - Laser give several merits as they can penetrate deeper in tissues/bulk materials.

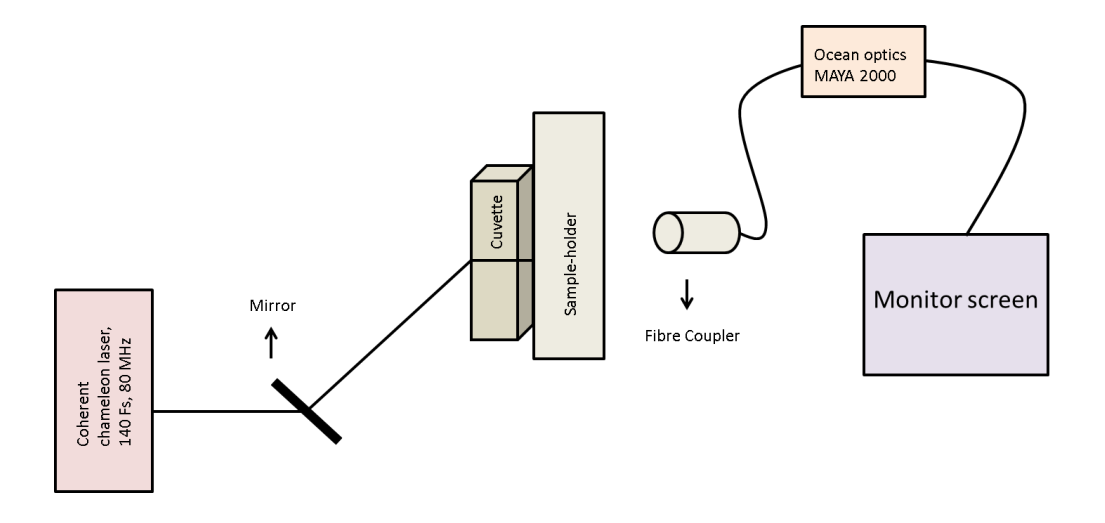


Figure 2.4.7: An schematic diagram of Femtosecond laser-set up with 140 Fs, 80MHz repetition rate

In present work, A Ti-Sapphire tunable oscillator laser with pulse duration of 140 femtosecond at a repetition rate of 80MHz (coherent chamemeon ultra-II) has been used as pumping source for sample excitation. Signal is recorded with non-gated spectrometer (Ocean optics, MAYA 2000). A schematic representation of this set-up is shown in figure 2.3.7.

#### 2.4.8 Photoluminescence with Multimode Reader:

Multimode reader device can detect reactions in samples with emitted light and can quantify them. In this technique, we can operate different detection-modes to perform and measure different experiments simultaneously such as: luminescence, fluorescence and absorbance (the most widely used modes). Besides them some advanced-modes are also available in present devices. Multiwell plates are used in this instrument for holding samples. Different samples can be performed at once by placing 1-2 drops of sample in well-plates. Generally, photomultiplier tubes (PMT tubes) are used for detecting light signal. The sensitive detector can convert the incoming photons into electricity which can be further quantified by this reader. Exciting the samples by light at certain detection modes and wavelengths we can receive output which appears with numbers quantifying the intensity of emitted light interacted by sample in plates. Hence, xenon lamp is used as excitation light source and to produce a certain excitation wavelength a specific excitation filter is used with lamp source. Though, generally such filters are employed between sample and detector but sometimes, to enhance the sensitivity and specificity, filters are placed in detection-side. For determining the experimental values, a standard curve is utilized for experiments on plate reader. For generating best fit line of standard curve sample of known concentration is used, thereafter, using linear regression experimental values can be extrapolated.

In this dissertation, Synergy H4 Hybrid Reader has been used in photoluminescence mode with fixing excitation wavelength at 450nm.

#### 2.4.9 Zetasizer nano series:

This instrument can measure three different parameters of particles suspending in liquid medium and they are: particle sizes, molecular weight and zeta potential over wide range of sample-concentrations. However, present dissertation studies only zeta potential measurements with this instrument.

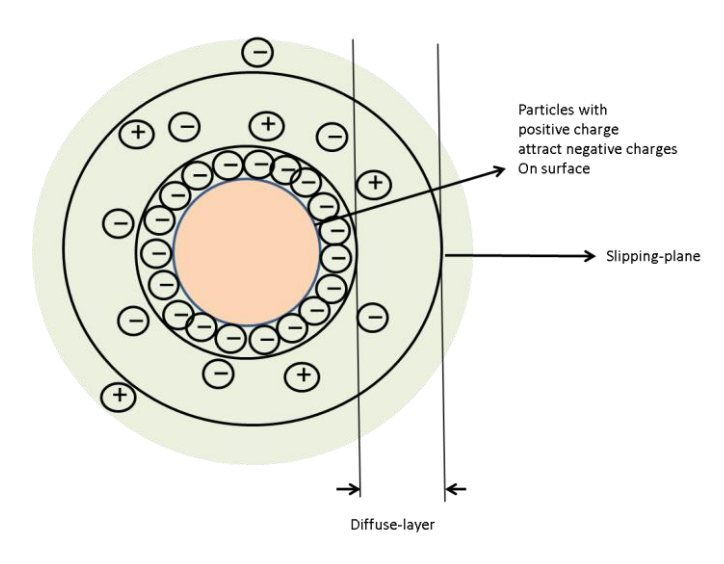


Figure 2.4.8: A diagram to understand the phenomena for arising zeta potentials while electric field is applied on sample.

Ions containing in liquids exist with positive or negative charged atoms- so called anions and cations, respectively. On the surfaces of suspending charged particles the charged atoms( oppositely charge atoms) get attracted i.e. negative charged ions get attracted on positive charged particle- surface and positive charged ions get attracted on negative charged particle- surface by electrophoresis method( A method by which electric field is applied through electrolytes). In this way, the ions bound strongly on suspending particle-surface. So, the diffuse layer with weakly bound ions appears further away of particle. Inside the boundary of diffuse layer ions can move with the suspending particles in liquid- this boundary of diffuse layer is termed as slipping-plane. The potential existing at slipping plane - is known as zeta

potential. The zeta potential value (magnitude of potential value) is a measurement of potential stability of experimental- sample. The large value of zeta potential ( $\xi$ ) is indicative of stable particles owing to existence of repelling factor between similar charged particles and because of that flocculation tendency (a tendency that particles come together) becomes very less or zero. Generally,  $\xi$ - value appearing with more positive or more negative than +30mV or -30 mV, respectively, is considered as stable colloidal system.

In this research work, Malvern Instrument; Zetasizer nano series has been used to record zeta potential values and in sample holder gold-plated brass (copper/zinc/beryllium) has been used as electrolytes. A diagram, explaining the theory that how the zeta potential appears in charged sample, is shown in figure 2.3.8.

## 3 RESULT AND DISCUSSION

## **PART I**

3.1 (Part-I): Synthesis of pure hexagonal UCNPs with highly efficient upconversion fluorescence/luminescence:

#### **Outcome:**

**Monami Das Modak,** Damarala Ganesh, Anil Kumar Chaudhary, Pradip Paik, Structural and spectroscopic Properties of up converting nanoparticles: Thin-Film spectra under Femtosecond laser source, Conference proceedings, Fourth International Conference on Nanotechnology for better living (NBL).

#### 3.1.1 Introduction:

UCNPs have potential applications in display technologies, biolabels, and bio-imaging agents. Recently, UCNPs have attracted our attention as they are able to convert light of longer wavelengths into shorter one through photon-upconversion process. Their superior spectroscopic properties make them unique while dealing in biomedical applications, especially in bio-medicine therapeutic agents. Synthesis of UCNPs is a challenging tusk. Till date, hexagonal phases of UCNPs (e.g., NaYF4:Yb³+; Er³+) have proven to be the most efficient upconverters due to highly intense visible emission under UV/NIR excitation source. In this context, I have synthesized highly intense UCNPs in in-situ conditions and their upconversion behavior for the first-time using Femtosecond-laser under 980nm excitation source.

#### 3.1.2 Objectives:

- 1. Preparing high quality, uniform monodisperse nanocrystals with strong upcoversion fluorescence.
- 2. Avoiding mixed crystalline phases and formation of non-uniformity.
- 3. To form NaYF<sub>4</sub> nanocrystals at lower reaction temperature and thereafter increasing high temperature (> 300°C) to improve the quality and uniformity.

#### **3.1.3** Morphological studies of β-NaYF4 nanocrystals:

The morphological studies reveal the formations of hexagonal UCNPs which contain uniformity throughout the sample. Figures 3.1.1(a,b,d) shows the hexagonal formations whereas figure 3.1.1c represents their plate-like formations. The SAED pattern shown in 3.1.1e confirms high crystallinity of synthesized materials.

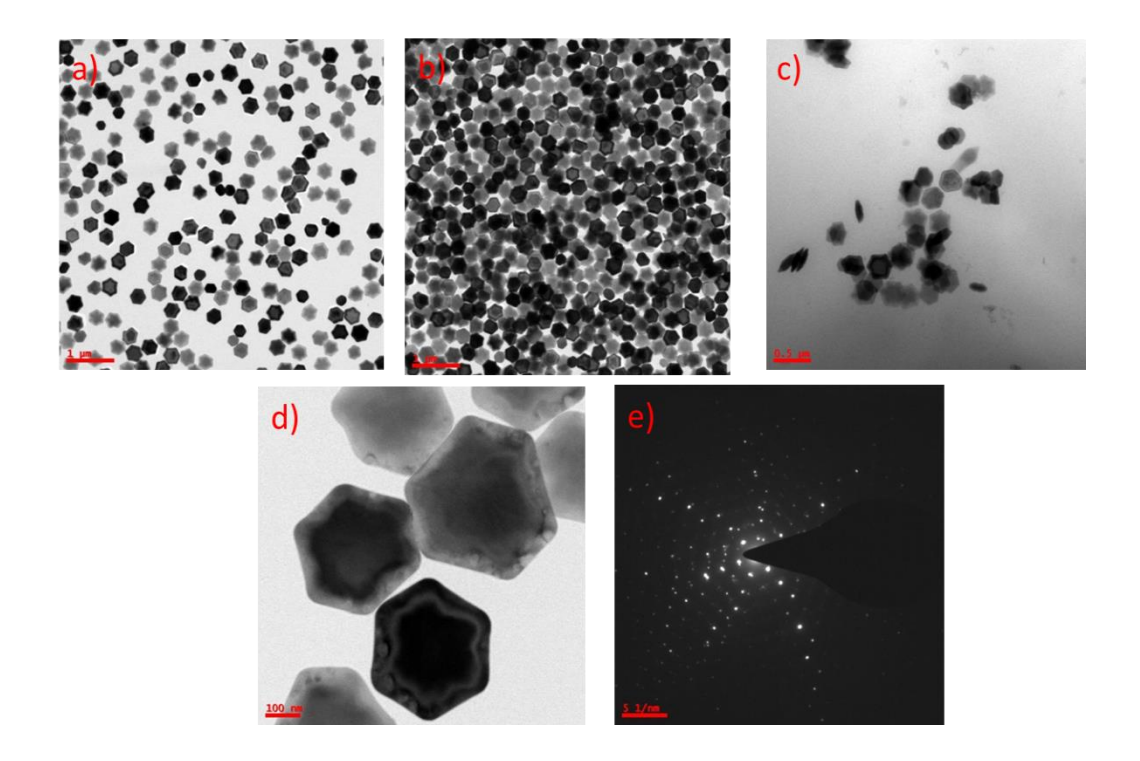


Figure 3.1.1: TEM images of of the synthesized hexagonal UCNPs, clear hexagonal formations with scale bar  $1\mu$ m (panel-a,b); 500nm (panel-c);100nm(panel-d); SAED pattern (panel-e).

## 3.1.4 EDAX analysis:

The corresponding EDAX spectrum is shown in figure 3.1.2 confirming the presence of elemental compositions. A table is drawn showing the elements present in synthesized compound in table 3.1.1.

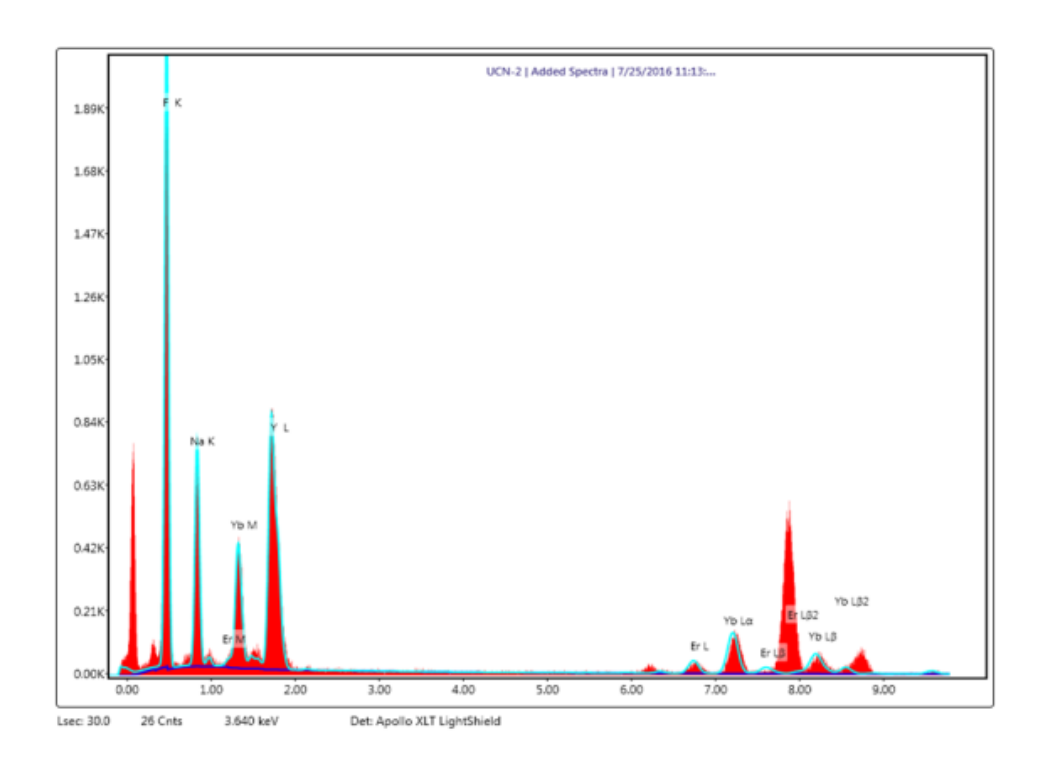


Figure 3.1.2 TEM-EDAX spectrum of synthesized  $\beta$ -NaYF4 nanocrystals showing the presence of elemental compositions.

Table 3.1.1: Elemental compositions in synthesized β-UCNPs

Element	Weight (%)	Atomic (%)
0	4.05	5.19
F	51.45	55.59
Na	43.79	39.11
Er	0.13	0.02
Yb	0.35	0.04
Y	0.23	0.05

## 3.1.5 X-ray diffraction analysis:

The presence of crystalline planes has been confirmed by x-ray diffraction study shown in figure 3.1.3, the crystalline planes appeared indicate the appearances of crystalline hexagonal phases in solid-state structures. There are no diffraction peaks assigning any cubic phases or impurities indicating a successful synthesis of pure hexagonal UCNPs. According to the JCPDS: 28-1192 pattern the crystalline planes have been found to be (100), (110), (111), (201), (210), (211), (102), (311) appearing with well-defined XRD peaks.

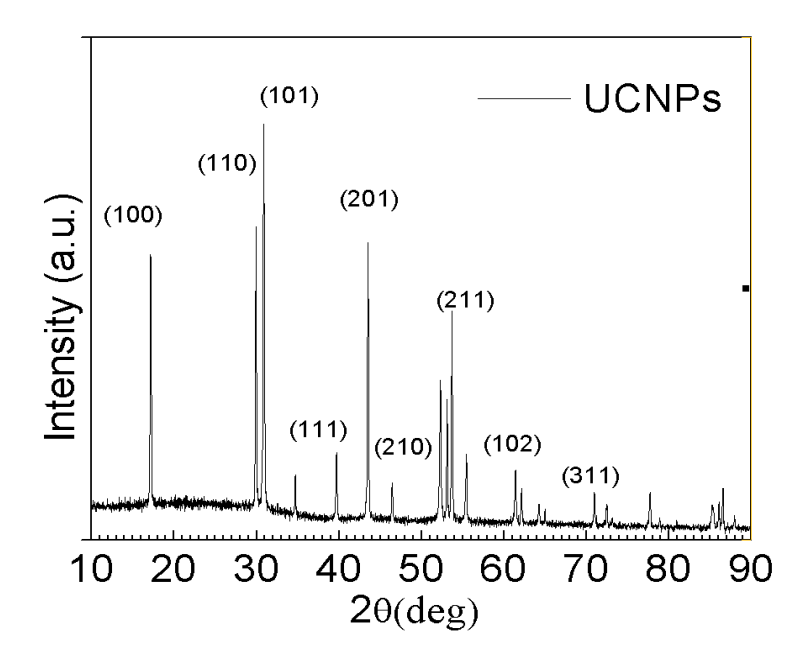


Figure 3.1.3: XRD pattern of the resulted  $\beta$ -UCNPs confirming the presence of different crystalline planes

## **3.1.6 AFM study:**

The AFM study is shown in figure 3.1.4 confirming the appearance of perfect hexagonal nano crystals. This result is matching well with TEM, XRD and Raman analysis.

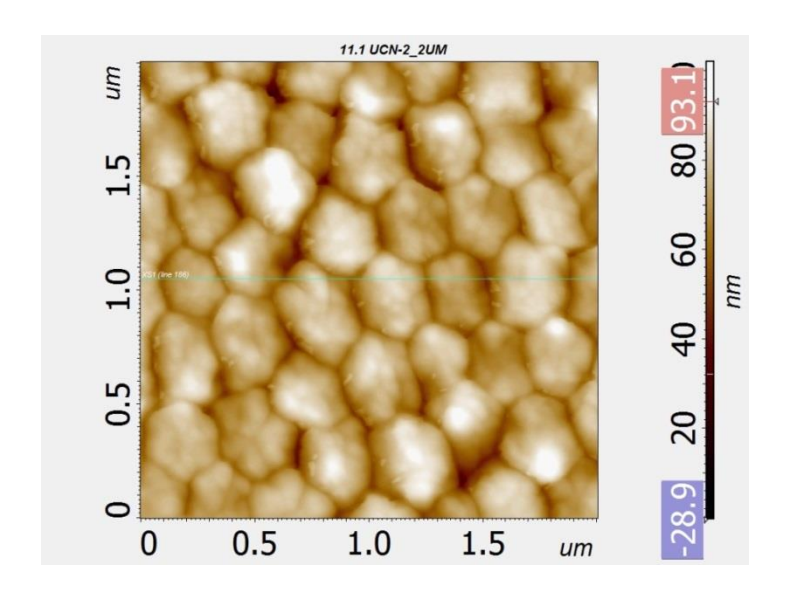


Figure 3.1.4: AFM study reveals the formation of perfect hexagonal shapes in β-NaYF<sub>4</sub>

## 3.1.7 Raman spectroscopic analysis:

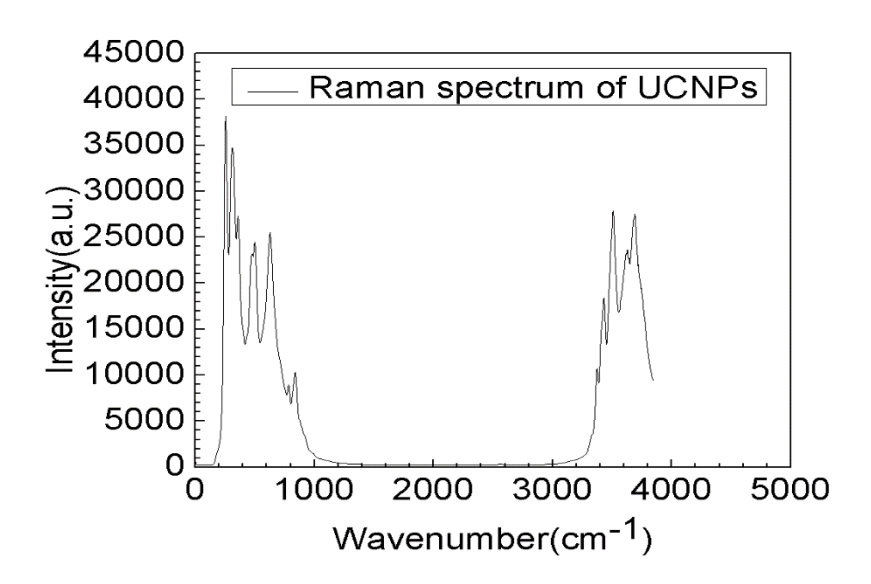


Figure 3.1.5: Raman study of  $\beta$ -NaYF4 confirming the appearances of strong hexagonal phases below  $1000 cm^{-1}$ 

The Raman spectrum shown in figure 3.1.5 shows clearly the appearances of hexagonal phases as most of the strong vibrational modes are appeared below 1000cm<sup>-1</sup>. Higher frequency modes above 3000 cm<sup>-1</sup> confirm the presence of organic solvents (Oleic acid as major capping agent) in synthesized nanoparticles and formation of pure β-NaYF<sub>4</sub>

#### 3.1.8 Upconversion fluorescence study:

The upconversion fluorescence study for  $\beta$ -NaYF<sub>4</sub> is shown in figure 3.1.6, where violet emissions corresponding to  $2H_{9/2}$  - $4I_{15/2}$  transition appears at 382nm and 411nm.Green emission corresponding to  $2H_{11/2}$  / $4S_{3/2}$  - $4I_{15/2}$  transition appears at 538nm, red emission corresponding to  $4F_{9/2}$  - $4I_{15/2}$  transition appears at 660nm and NIR emission corresponding to  $4S_{3/2}$ - $4I_{13/2}$  appears at 848nm.The photograph of visible green emissions for 1 wt% colloidal solution in figure 3.1.6 indicates the strong emissions under 980nm NIR.

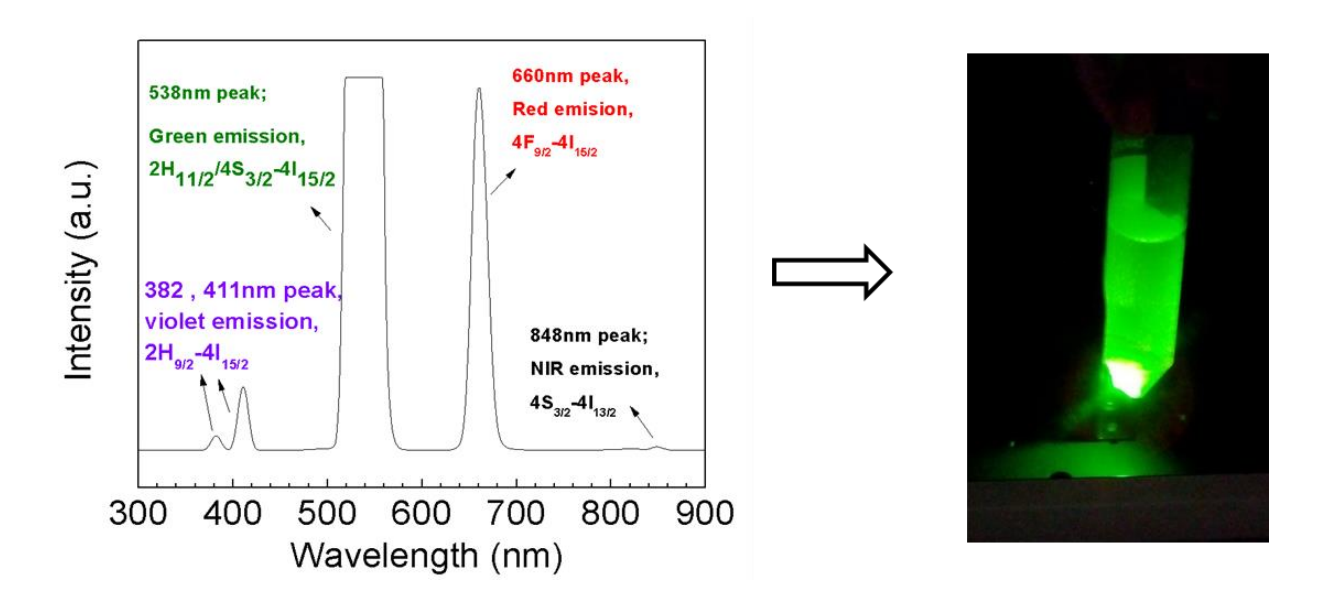


Figure 3.1.6: The upconversion fluorescence spectrum shows violet, green and red emissions under the excitation of 980nm laser-diode

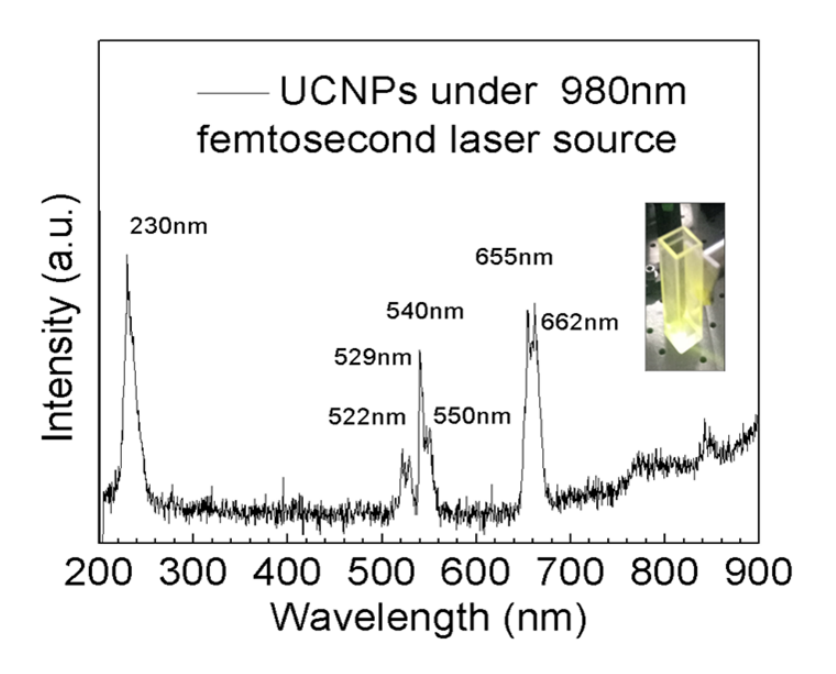


Figure 3.1.7: The intense emissions both in UV and in visible range upon interaction with femtosecond laser 980nm excitation source. The intense shows the visible emissions

Figure 3.1.7 represents the spectra after interaction of synthesized hexagonal UCNPs with femtosecond laser source maintaining 980nm excitation wavelength. Thus, emissions appeared at 230nm, 522nm, 529nm, 540nm, 550nm, 655nm, 662nm under 980nm excitations confirming their appearances in UV (230nm) and visible (520nm-670nm) region. The inset inside figure 3.1.7 shows visible green emissions under 980nm excitations.

## 3.1.9 Summary of Part-I:

To the best of this author's knowledge, the as-synthesized NaYF<sub>4</sub> nanocrystals with Yb<sup>3+</sup> and Er<sup>3+</sup> are the best UCNP reported so far as they yield fluorescence even after decreasing the laser power density below 50 mW/cm<sup>2</sup>. During synthesis, all the fluoride reactants were

consumed into solid-state NaYF<sub>4</sub> nuclei at lower reaction temperature ( $\sim 60^{\circ}$ C) as in higher reaction temperature consuming all fluorides become very unfriendly and unsafe to users.

The smaller surfaces of larger sized nanoparticles possess fewer amounts of surface defects, which could be the reason of strong fluorescence.

However, synthesis of such plate-like hexagonal UCNPs has substantial perspective in imaging, solar cells and different display devices and technologies.

## **Chapter 3 RESULT AND DISCUSSION**

# PART II

3.2 (Part-II): Upconverting nanodots and generation of high energy upconversion through Ti: sapphire 140-femtosecond laser pulses

**Outcome:** Monami Das Modak, Ganesh Damarla, Anil K Chaudhury,K Santhosh Kumar, Somedutta Maity, and Pradip Paik; Upconverting nanodots and generation of high energy upconversion through Ti: sapphire 140-femtosecond laser pulses; Manuscript is assigned in arxiv with as permanent identifier 2008.06783.

#### 3.2.1 Introduction

Upconversion phenomenon is a two photon-(one from sensitizer ion and other one from activator ion) process followed by energy transfer (ET) which contributes higher photon energy in ultraviolet (UV) and visible region under the excitation with Infrared (IR) or near infrared (NIR) radiation. The transmutation of IR/NIR photons to UV/visible photons in upconversion nanoparticles (UCNPs) make them unique for applications in electronics and biomedicines. Though there are a few lanthanide ions manifesting upconversion but substantially Yb<sup>3+</sup>, Er<sup>3+</sup>, Tm<sup>3+</sup> trivalent lanthanide ions have been used to synthesize upconversion nanocrystals due to their efficient upconversion emission[16], [88], [254].

Till date, NaYF<sub>4</sub>: Yb<sup>+3</sup>, Er<sup>+3</sup>(Tm<sup>+3</sup>) has been proven to be one of the most efficient UCNPs[3], [16], [89] due to its highest photon upconversion efficiency. It is well known that smallest luminescent-particles have been always demanding and they attract nano medicines for therapeutic applications [6,7] including bio-labelling [257], in-vivo imaging [258], bio-conjugation,[259] long term cell tracing [260] and bio-detection [261]. Owing to strong biological relevance UCNPs are useful for both in vitro and in vivo applications along with molecular bio-imaging and for targeted cancer therapy [33], [111], [262], [263]. Therefore, it would be a superior idea to combine both of the approaches. It is also reported that UCNPs can be used for solar cells, photovoltaic and plasmonic devices and also for increasing efficiency of several display devices[6], [264]–[268].

Here in this work UCN-dots have been prepared through one-pot chemical-synthesis approach. These UCN-dots are having diameter below 4 nm. All the other works reported so far contained sizes above 10 nm (dia.) and mostly appeared with hexagonal crystalline phases[1–3,5,23]. However, UCN-dots reported in this work have been synthesized within a very short period of reaction time. Short reaction period at moderately high temperature avoids the production of large NaF crystal-matrix and it could also avoid the production of

other fluorinated oxygen and carbon species during synthesis. The second objective of this part of work is to study the upconversion properties of UCN-dots with femtosecond laser source (Ti-sapphire femtosecond laser of 140-femtoseconds duration at 80 MHz repetition rate).

#### **3.2.2** Materials Characterization:

UCN-dots were synthesized as discussed in the experimental section and characterized through the several suitable methods.

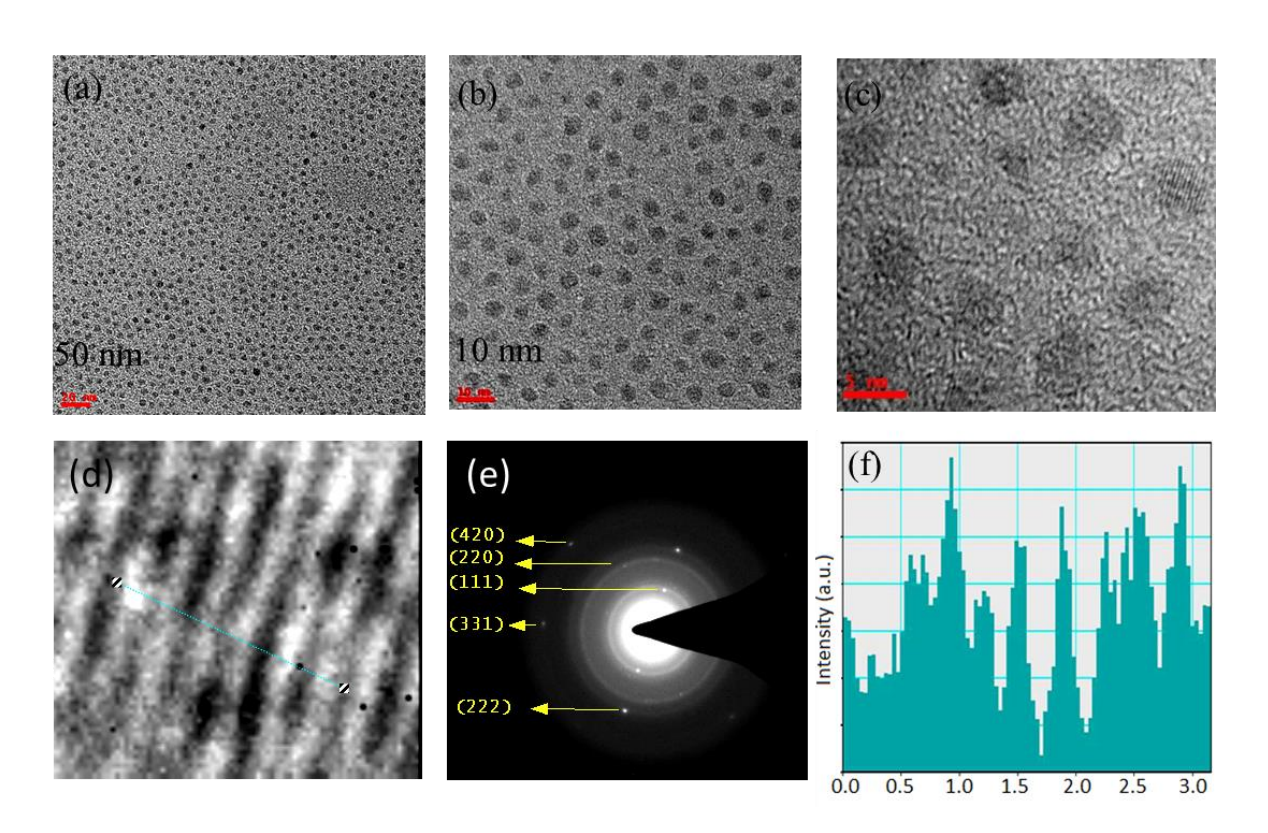


Figure 3.2.1: (a), (b) and (c) TEM micrograph of UCN-dot: low to high magnification. (c) Represents the fringes of the particles (d) Magnified image of the fringes. (e) Represents the selected area electron diffraction pattern (SAED) obtained from TEM and (f) profile of the fringes

Figures 3.2.1(a-c) show the TEM micrographs of the synthesized UCN-dots (NaYF<sub>4</sub>:Yb<sup>3+</sup>;  $Er^{3+}$ ) which possess uniform particle size distribution confining size below 4 nm in diameter and they are monodispersed in nature. These UCN-dots are appeared with average size  $\sim$ 3.4±0.15 nm in diameter (figure 3.2.2) and stable up to one year due to their high surface zeta potential of -36.39 mV (figure 3.2.3).

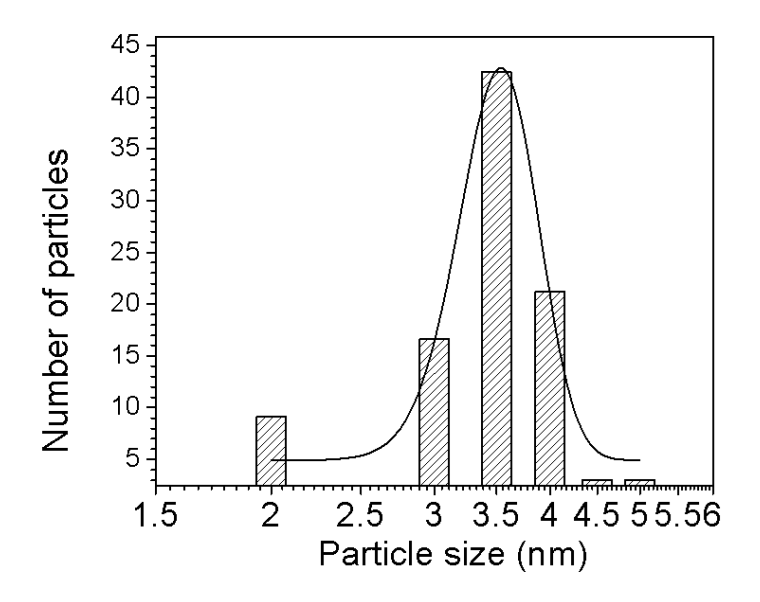


Figure 3.2.2: Histogram particle size and distribution calculated from TEM micrograph

Figures 3.2.1(c,d) shows high resolution TEM, HRTEM micrographs with clearly exhibiting the lattice fringes which confirms the crystallinity of synthesized dots. Distance between two adjacent fringes has been calculated to be 3.1 Å. Figure 3.2.1e shows SAED pattern (ring pattern) corresponding to the (111), (220), (222), (331)and (420) reflection planes for pure cubic crystal structure which further have been confirmed through the XRD and Raman spectroscopy and explained in the subsequent sections.

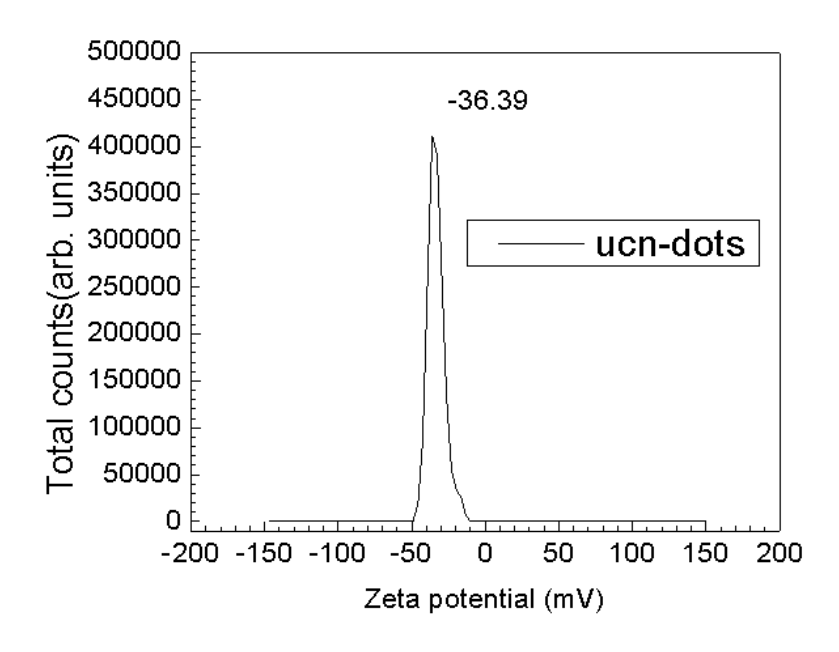


Figure 3.2.3: Zeta potential for colloidal UCN-dot sample

Crystal structure of solid powder UCN-dots has been confirmed through XRD shown in figure 3.2.5 which confirms the well-defined diffraction peaks at  $2\theta = 31.8^{\circ}$ ,  $45.5^{\circ}$  and  $66.3^{\circ}$  corresponding to the reflection planes (111), (220) and (222) respectively and represents the appearance of cubic (FCC) crystalline phases in UCN-dots. Crystallite size has been calculated using Debye-Scherer formula[2,24] and the average crystallite size has been found to be  $\sim 3.4 \pm 0.15$  nm. The Lattice parameters for cubic crystalline UCN-dots have been evaluated to be a=5.51 Å, b=5.31 Å and c=5.32 Å which is matching well for the cubic phases of UCN nanoparticles reported[127]. The elemental composition is confirmed with EDAX analysis (figure 3.2.4 and table 3.2.1). From XRD (figure 3.2.5) and from the EDAX (figure 3.2.4) results the number of unit cells present in a single UCN-dot has also been calculated and found to be: 143 [calculation part is shown at the end of this part II]. It can be noted that the number of different atoms present in a unit cell of UCN-dots are 2, 8, 1 and 1 for

Na, F, Yb and Er, respectively as a fraction of  $Y^{3+}$  ions are substituted by rare earth ions  $(Yb^{3+}$  and  $Er^{3+})[270]$ .

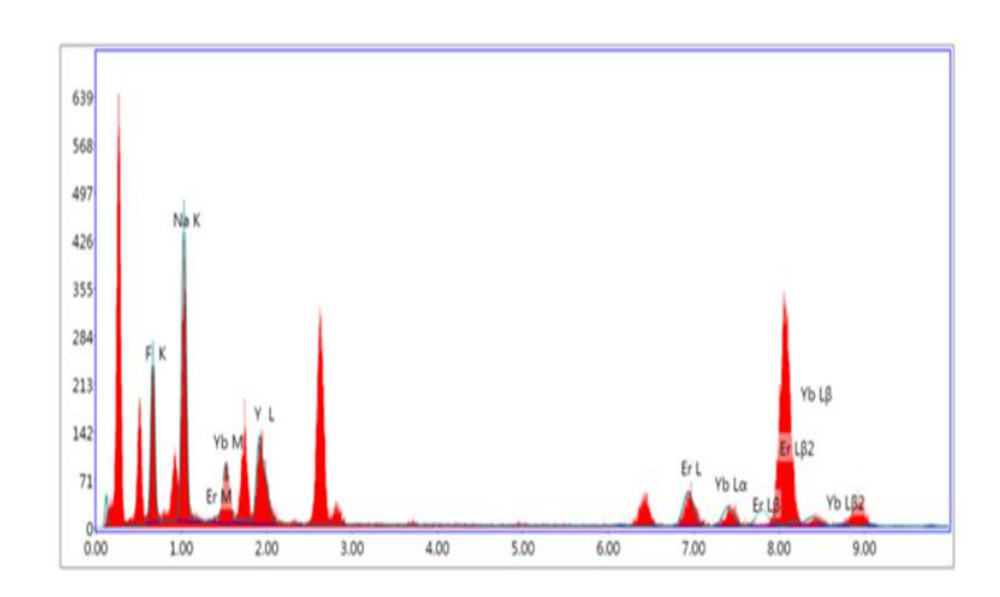


Figure 3.2.4 EDAX analysis of UCN-dots colloidal sample

Table 3.2.1: Table for elemental analysis from EDAX

Element	Weight (%)	Atomic (%)	
F	25.23	29.33	
Na	73.34	70.47	
Er	0.85	0.11	
Yb	0.43	0.05	
Y	0.16	0.04	

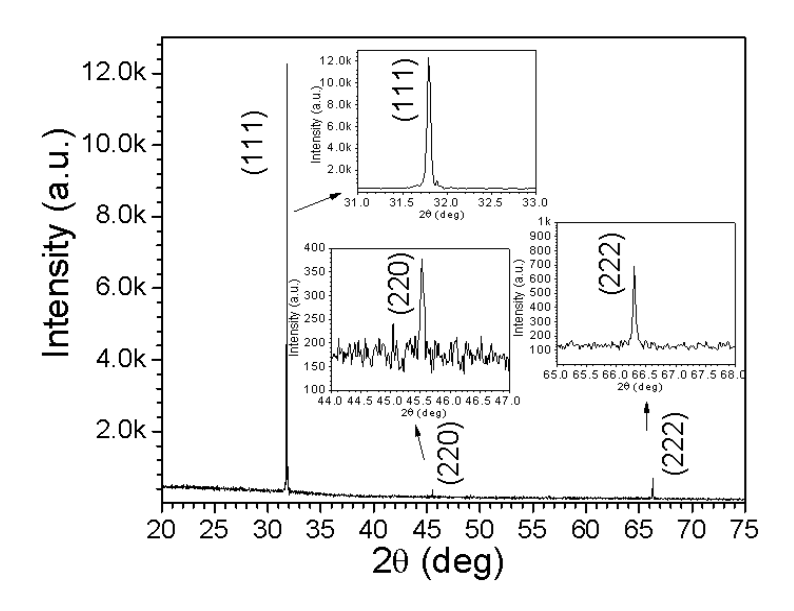


Figure 3.2.5: XRD of UCN-dots represents the crystalline phase (cubic, FCC) of UCN-dot. In sets are showing enlarge peaks for (111), (220) and (222) planes

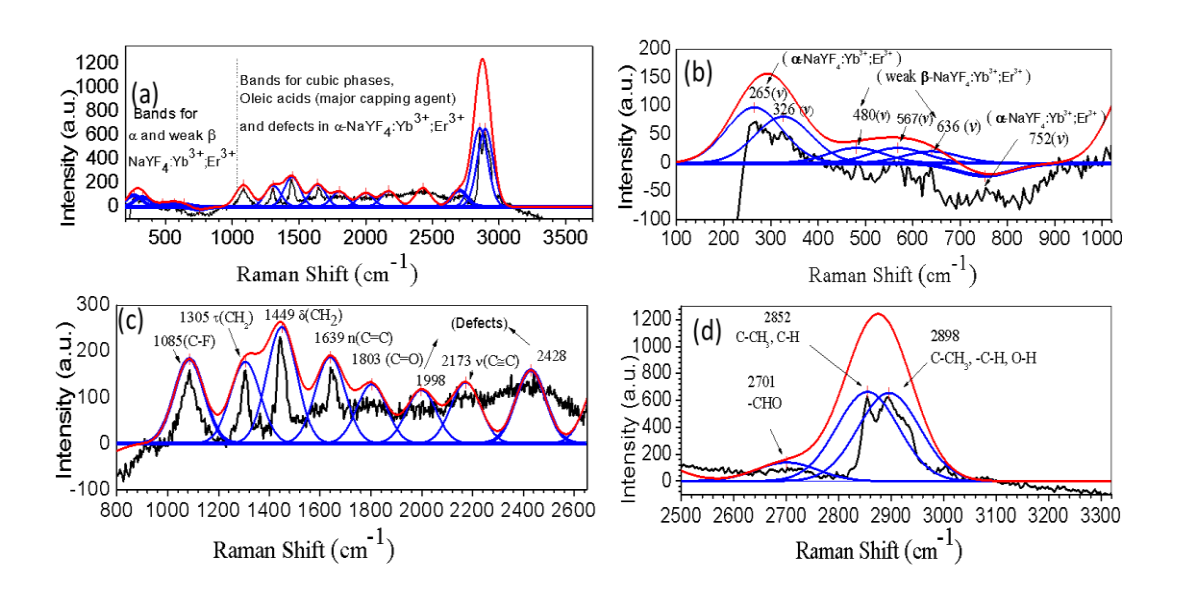


Figure 3.2.6: Raman Spectra for the UCN-dots, (a) for the full region. (b) band region 100 cm-1 to 1000 cm-1 representing the major α-phase of NaYF4:Yb3+;Er3+dots, (c) 800 cm-1 to 2600 cm-1 and (d) 2500 cm-1 to 3300 cm-1, exhibiting the presence of major capping agents in cubic phases

Figure 3.2.6 shows the Raman spectra of the UCN-dots appeared in different band regions. Figure 3.2.6a shows the entire spectra where most of the bands appeared between 100-1000 cm<sup>-1</sup> represents the appearance of cubic phases in UCN-dots ( $\alpha$ -NaYF<sub>4</sub>:Yb<sup>3+</sup>;Er<sup>3+</sup>) whereas, band region appeared between 1000 cm<sup>-1</sup> -3500 cm<sup>-1</sup> confirms the presence oleic acids (capping agent). Weak Raman bands with phonon frequency below 1000 cm<sup>-1</sup> confirm the presence of vibrational modes ( $\nu$ ) of  $\alpha$ -NaYF<sub>4</sub> or  $\beta$ -NaYF<sub>4</sub> crystals.

Hence, below 1000 cm<sup>-1</sup> phonon vibrational bands (with its maximum position) appeared at 265 cm<sup>-1</sup>, 326 cm<sup>-1</sup>, 480 cm<sup>-1</sup>, 567 cm<sup>-1</sup>, 636 cm<sup>-1</sup> and 752 cm<sup>-1</sup> (figure 3.2.6b) further satisfy the presence of major  $\alpha$ -phases along with relatively less extent of  $\beta$ -phases in UCN-dots [271]–[273].

However, presence of weak β-phases is identified with band positions at 480 cm<sup>-1</sup> and 636 cm<sup>-1</sup>. Other bands appeared at 326 cm<sup>-1</sup> and 567 cm<sup>-1</sup> can be ascribed for distinct vibrations originated from newly synthesized UCN-dots with  $\alpha$ -phases. The high frequency phonon energy modes appeared at 1085 cm<sup>-1</sup> and 1305 cm<sup>-1</sup> correspond to the presence of C-F and - CH<sub>2</sub> groups respectively.

The bands are appeared at 1449 cm<sup>-1</sup>, 1639 cm<sup>-1</sup>, 1803 cm<sup>-1</sup>, 2173 cm<sup>-1</sup> and 2701 cm<sup>-1</sup> due to the presence of CH<sub>2</sub>, -CH<sub>3</sub> groups, -C=C- bond, -C=O bond, -C=C-and–CHO, respectively of oleic acid (capping agent) (figures 3.2.6c and 3.2.6d). Two weak intense bands appeared at 1998 cm<sup>-1</sup> and 2428 cm<sup>-1</sup> due to the possible defects present in UCN-dots (figure 3.2.6c). However, bands for β- NaYF<sub>4</sub>:Yb<sup>3+</sup>; Er<sup>3+</sup> are found very weak and only bands for prominent α-NaYF<sub>4</sub>:Yb<sup>3+</sup>;Er<sup>3+</sup> are present in UCN-dots. Further, the weak bands appeared in between 687-703 cm<sup>-1</sup> and 260-279 cm<sup>-1</sup> along with the broad band in between 750-1750 cm<sup>-1</sup> are confirmed for fcc - α-NaYF<sub>4</sub>:Yb<sup>3+</sup>; Er<sup>3+</sup>. Thus, for Raman it is confirmed that UCN-dots prepared in this work is with cubic crystalline phases which can be complied with the results obtained from figures 3.2.1e and 3.2.2. The possible reasons for appearance of the higher

frequency bands in raman spectra are: (i) the dimensions of particles are very small due to which a higher number of capping agents are being absorbed on the surface, as a result high energy C-H or C-C vibrations can be caused of getting higher frequency raman bands, (ii) presence of functional groups (O=C-O<sup>-</sup> and OH<sup>-</sup>) in oleic acid attached on the surface of the particles and (iii) finally, a higher percentage of capping agents and their functional groups on UCN-dots can act as surface active agents which can initiate a compressive stress leading to closely packed surface atoms and as a result of vibrations, raman peaks are appeared with extended band positions.

# 3.2.3 Upconversion fluorescence with CW-980 nm laser source:

Up-converted materials qualify the inclusion of two or more photons resulting in the emission of higher energy photons through several energy transfers (radiative and non-radiative) either between two ions (activator ion and sensitizer ion) or within the energy states of an activator ion itself in the visible-spectrum range which has been shown in figure 3.2.7a for UCN-dots. For UCN-dots (NaYF<sub>4</sub>:Yb<sup>3+</sup>; Er<sup>3+</sup>) the Yb<sup>3+</sup> ion acts as a sensitizer and Er<sup>3+</sup>acts as an activator.

In fluorescence spectrum (FL) (figure 3.2.7a), the different emissive bands denote the intensity of the emitted higher energy photons at different wave lengths depending on the transfers of electrons from different excited states to the ground state or first excited state. Fluorescence emission spectra of colloidal solutions of UCN-Dots display well separated emissive peaks at room temperature. Only four significant emission bands are identified under the CW-laser excitation source (980 nm).

The energy transfer mechanism has been shown in figure 3.2.7b. The green emissions in between 513 nm to 533 (527 nm,  $E_g = 2.35$  eV) nm and 533 nm- 569 nm (545 nm;  $E_g = 2.28$  eV) can be assigned to the  $2H_{11/2} \rightarrow 4I_{15/2}$  and  $4S_{3/2} \rightarrow 4I_{15/2}$  transitions, respectively.

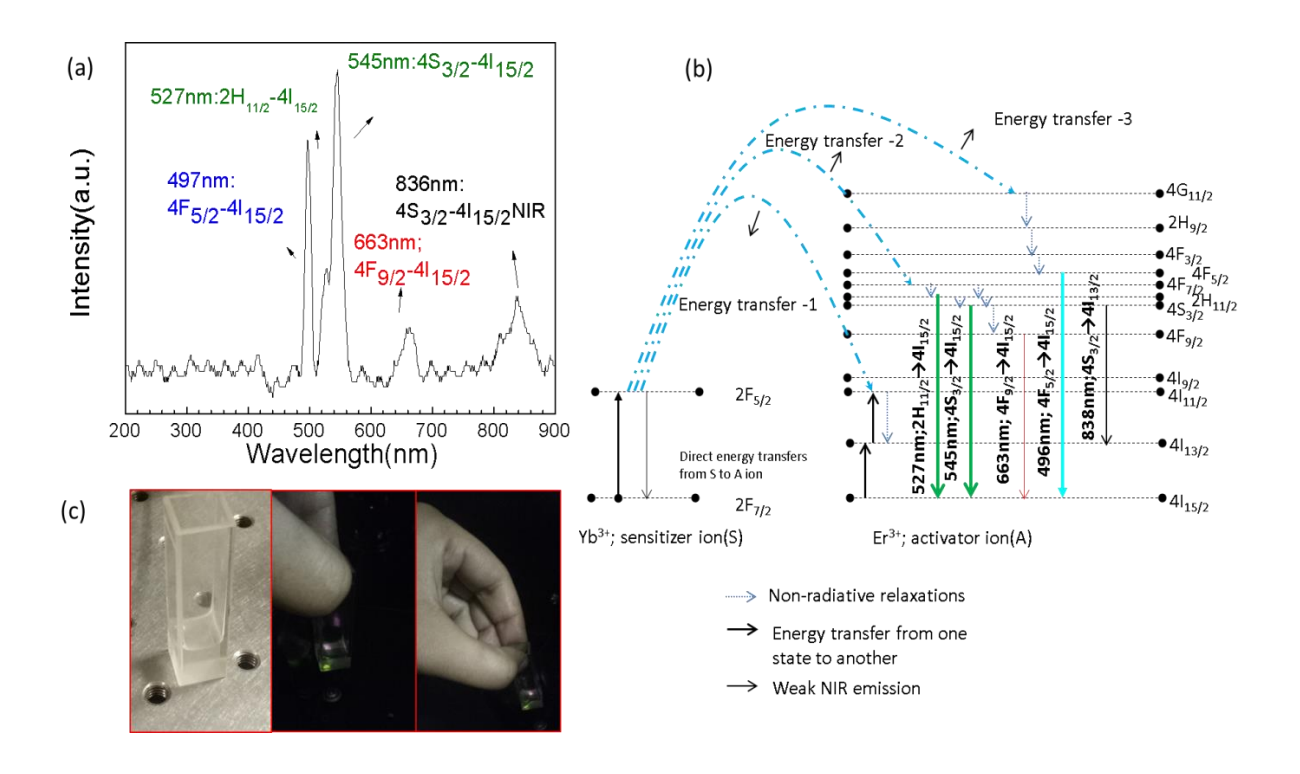


Figure 3.2.7: Fluorescence Spectra of UCN-Dot-colloidal solution in cyclohexane with a 980 nm continuous wave (CW) NIR excitation (Power Density 1000 mW/ cm2) exhibiting four significant emission bands at room temperature (b) The relevant energy diagram of dot-sized upconverting nanocrystals and upconversion processes succeeding 980 nm laser-diode excitation. Further it predicted energy transfers (with three direct energy transfers) with their corresponding pathways (c) Three images are with colloidal solutions and showing the visible emissions under 980nm laser CW

A dominant red emission is observed between 630 nm and 680 nm (663 nm;  $E_g = 1.87 \text{ eV}$ ) and can be assigned to a transition  $4F_{9/2} \rightarrow 4I_{15/2}$ . A feeble NIR emission between 795 nm and 883 nm (838 nm;  $E_g = 1.48 \text{ eV}$ ) appeared due to the  $4S_{3/2} \rightarrow 4I_{13/2}$  transition of the photons. A highly intense emission band appeared in between 485 nm to 506 nm (496 nm;  $E_g = 2.5 \text{ eV}$ ) can be assigned to the transition  $4F_{5/2} \rightarrow 4I_{15/2}$ , which occurs through a direct energy transfer from  $2F_{5/2}(Yb^{3+}) \rightarrow 4G_{11/2}(Er^{3+})$  by continuous 980 nm input excitation laser source. From the higher excited state  $Er^{3+}$  ion can be relaxed to the next lower states following the path

 $2H_{9/2} \rightarrow 4F_{3/2} \rightarrow 4F_{5/2}$  (due to close proximity of these intermediate levels) through several non-radiative multiphonon relaxations which do not emit any photons. The emission band appeared in between 485 nm and 506 nm can neither be fallen exactly under green emission band nor to blue emission due to a divergent wavelength range. Therefore, we cannot assign them directly to the transitions  $2H_{11/2}/4S_{3/2} \rightarrow 4I_{15/2}$  or  $2H_{9/2} \rightarrow 4I_{15/2}$ .

An intermediate or reservoir state (4F<sub>5/2</sub>, 4F<sub>3/2</sub>) should be responsible for such emissions which can be assigned to the transition  $4F_{5/2}\rightarrow 4I_{15/2}$  (an immediate cross relaxation occurs between  $4F_{3/2}$  and  $4F_{5/2}$  levels due to their close proximity) and follows the energy transfer path:

$$2F_{7/2}(Yb^{3+}) \rightarrow 2F_{5/2}(Yb^{3+}) \rightarrow 4G_{11/2}(Er^{3+}) \rightarrow 2H_{9/2}(Er^{3+}) \rightarrow 4F_{3/2}(Er^{3+}) \rightarrow 4F_{5/2}(Er^{3+}) \rightarrow 4I_{15/2}(Er^{3+})$$
 which includes three non-radiative relaxations such as (i)  $4G_{11/2}(Er^{3+}) \rightarrow 2H_{9/2}(Er^{3+})$ , (ii)  $2H_{9/2}(Er^{3+}) \rightarrow 4F_{3/2}(Er^{3+})$  and (iii)  $4F_{3/2}(Er^{3+}) \rightarrow 4F_{5/2}(Er^{3+})$  (figure 3.2.7b).

Nearly 50% absorbed NIR photons are upconverted from the UCN-dots resulting in visible emission spectrum. As the synthesized particles are of dot- sized particles (size~ 3.5 nm), therefore, number of non-radiative relaxations increase by the solvent molecules and an overall quantum yield (Q.Y.) decreases.

The energy level diagrams of UCN-dots and their up-conversion mechanisms following CW-980 nm laser diode excitation is shown in figure 3.2.7b, where the energy transitions occurred through several radiative and non-radiative emission pathways. As reported earlier, for NaYF<sub>4</sub>:Yb<sup>3+</sup>;Er<sup>3+</sup> nanocrystals maximum two to three emission bands were obtained from their entire fluorescence spectrum region. However, for our UCN-Dots four significant emission bands have appeared (figure 3.2.7a). The intensity ratios of green emissions from 513 nm-533 nm and 533 nm- 569 nm to red emission from 630 nm-680 nm yielded much higher values (such as 1.75 and 2.67, respectively) compared to the results reported for UCN nanoparticles with larger sizes. In previous reported a size dependent relation of GRR

(intensity ratio of green to red emission) in Yb<sup>3+</sup>; Er<sup>3+</sup>co-doped NaYF<sub>4</sub> nanocrystals and a graphical plot of GRR as a function of particle sizes has also been observed, where the green emission became more pronounced with decreasing particle size. The GRR value of the present UCN-dots appeared to be very high relative to the UCN nanoparticles with larger size. The GRR value of the present UCN-dots appeared to be high compared to the larger sized UCN particles.

This phenomenon can be explained as: the dot-sized UCN particles are responsible for an increased number of non-radiative relaxations as the dot-sized nanoparticles are having higher specific surface area to volume ratio. As a result, an increased number of doped lanthanide ions are closer to their periphery (surface) leading to a greater number of non-radiative relaxations (as shown in figure 3.2.7b with energy–diagram) between their different energy levels. As a result, the overall fluorescence intensity decreases. Please see the image (figure 3.2.7c) for the visible emissions under 980 nm laser-diode excitation sources.

### 3.2.4 Photoluminescence

Figures 3.2.8a and 3.2.8b show the photo luminescence (PL) spectra of UCN-dots in aqueous medium obtained with an excitation wavelength of  $\lambda$ = 450 nm and their corresponding energy transitions, respectively. PL bands are observed mostly in visible region (380 nm-700 nm). The obtained major bands are centred at 407 nm, 430 nm, 462 nm, 520 nm, 548 nm, 570nm, 607nm, 640nm following two direct energy transfers from Yb<sup>3+</sup> ion to Er<sup>3+</sup> ion (figures 4a, 4b). NIR-NIR PL was reported for NaYF<sub>4</sub>:Yb<sup>3+</sup>, Er<sup>3+</sup> UCNPs elsewhere[30,31]. However, excitingly in the present study visible to visible conversion is observed for UCN-dots while a 450 nm excitation source was used.

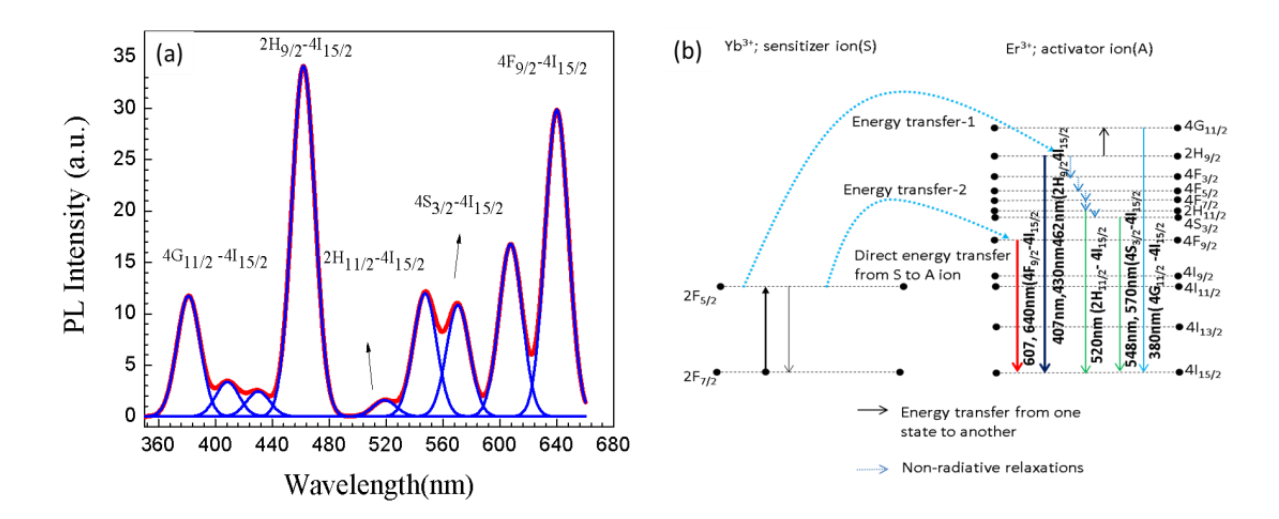


Figure 3.2.8: (a) PL spectra of the UCN-dots of size 3.5 nm. The spectrum was obtained with excitation wavelength of 450nm. The peak positions represent the different transitions of the photons at the visible region (b) energy transitions within electronic states of PL spectra obtained with excitation wavelength of 450nm

The highest PL emission bands are observed at 462 nm ( $E_g$ = 2.68 eV) and at 640 nm ( $E_g$ = 1.94 eV) a strong intense emission band is observed. Additionally, few more PL emission bands appeared relatively with weak intensity. From figures 3.2.8a and 3.2.8b the emission band appeared at 520 nm ( $E_g$ =2.38 eV) and can be attributed to the energy transition  $2H_{11/2}\rightarrow 4I_{15/2}$  and other two bands appeared at 548 nm ( $E_g$ = 2.26 eV), 570nm ( $E_g$  = 2.18eV) correspond to the  $4s_{3/2}\rightarrow 4I_{15/2}$  transition and these three are responsible for the green emission. Whereas red emission band appeared at 607 nm ( $E_g$ = 2.04 eV) and 640 nm ( $E_g$  = 1.94 eV) which is configured for the  $4F_{9/2}\rightarrow 4I_{15/2}$  transition. Emission-bands appeared at ~407 nm ( $E_g$  = 3.05eV), 430 nm ( $E_g$  =2.88 eV), 462 nm ( $E_g$ =2.68 eV) satisfied the energy transition  $2H_{9/2}\rightarrow 4I_{15/2}$ . Interestingly, one band with moderate intensity appeared (in near-UV region) at 380 nm ( $E_g$  = 3.26 eV) corresponds to the energy transfer  $4G_{11/2}\rightarrow -4I_{15/2}$  following a transitional energy transfer (indirect energy transfer) from  $2H_{9/2}\rightarrow 4G_{11/2}$ . However, the corresponding emission bands observed

from PL has been compared with fluorescence spectra (FL) obtained with the interaction of CW-980 nm laser and discussed in the subsequent sections.

# 3.2.5 Up-conversion due to femtosecond laser (fs-laser) irradiation and High-Power band generation in UV- region

A Ti sapphire tunable oscillator laser with pulse duration ~140 femtoseconds at a repetition rate of 80 MHz (coherent chameleon ultra-II made) was used as a pumping source for sample excitation. Luminescence signal was recorded using non-gated Spectrometer (Ocean Optics, MAYA 2000). The schematic of experimental setup is shown in figure 3.2.9. Luminescence results exhibits the appearance of additional bands in UV region (205 nm-231 nm) other than the appearance of a number of bands in visible region (figure 3.2.10). The generation of emission bands in UV region in interaction with femtosecond pulses is due to non-linear effects introduced by transient second order non-linearity by femtosecond pulses. Further it is noticed that appeared luminescence bands in UV region show clear shifting with respect to the incident pump wavelengths and this phenomenon is reported here for the first time.

Aktsipetrov et .al reported the magnetization induced harmonic generation and THz in Bi:YIG -a magneto photonic crystal[275]. If these samples are subjected to intense beam of laser then higher order optical harmonics are generated. The first shows the linear response due to transmission while strongest non-linear response is attributed to higher order non-linearity. However, all these processes are applicable in case of noncentro symmetrical materials. Most of the materials possess odd order non-linear susceptibility due to broken crystal tractions, defects, external field effects etc. In noncentro symmetry materials the response is from structure, however, in case of nanomaterials, structure relation response become more important and size reduction helps to generate efficient higher order harmonics which is not clear in present study.

The non-linear magneto optical effect could be the reason of getting higher order non-linear response from the UCN-dots and as a result upconversion bands are appeared in UV-region. In figures 3.2.10 (a & b), different emission bands of colloidal UCN-dots have been observed under the excitations of four different incident pump wavelengths, such as  $\lambda = 950$  nm, 960 nm, 970 nm and 980 nm in femtosecond laser (fs-laser) setup (figure 3.2.9). We have observed emissive bands in both of UV and visible regions.

In UV region (1st series of the observed emissive bands) (figure 3.2.10a), at  $\lambda = 950$  nm, 960 nm, 970 nm and 980 nm fs-excitation wavelengths, the emission bands are appeared at 206 nm, 212 nm, 227 nm and 231 nm, respectively. Thus, clear shifting of bands from 206 nm to 231 nm are observed as the excitation wavelength changes from  $\lambda = 950$  nm to 980 nm.

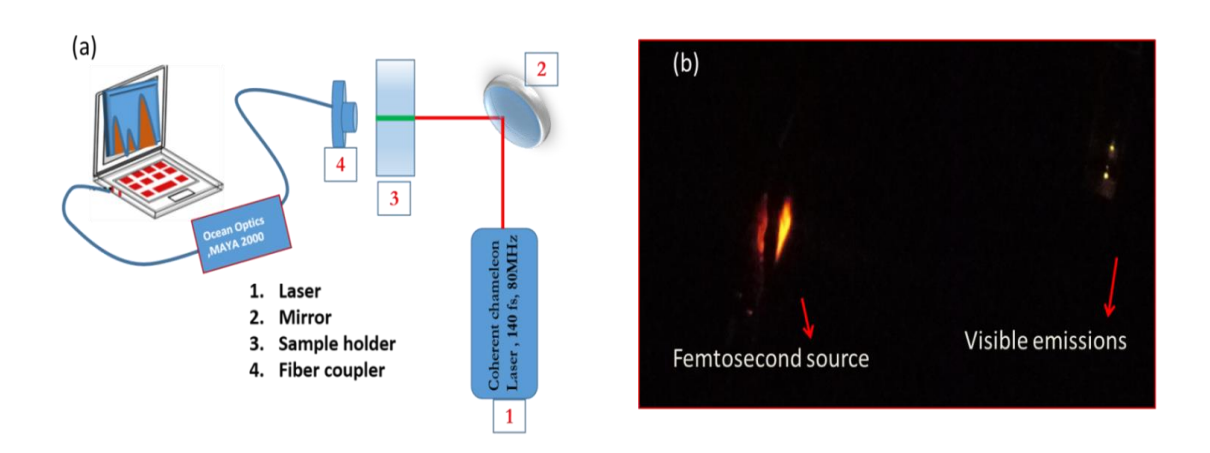


Figure 3.2.9: (a) Schematic diagram of a complete experimental set up for femtosecond laser study (b) Visible emissions (right) with femtosecond laser source (left) during experiment

Further, a number of emissive bands also appeared in visible region (figure 3.2.10b). These emissive bands in visible region are appeared with lesser intensity compared to those appeared in UV region but still their intensities are significant enough to consider. At four different excitation wavelengths 2nd series of emissive bands (G1) are appeared in the wavelength range between 506-535 nm with highest band positions at 521 nm, 522 nm, 522

nm and 524 nm along with 3rd series of bands (G2) appeared between 536 nm-562 nm containing highest positions at 540 nm, 540 nm, 541 nm and 542 nm for 950 nm, 960 nm, 970 nm and 980 nm excitations, respectively.

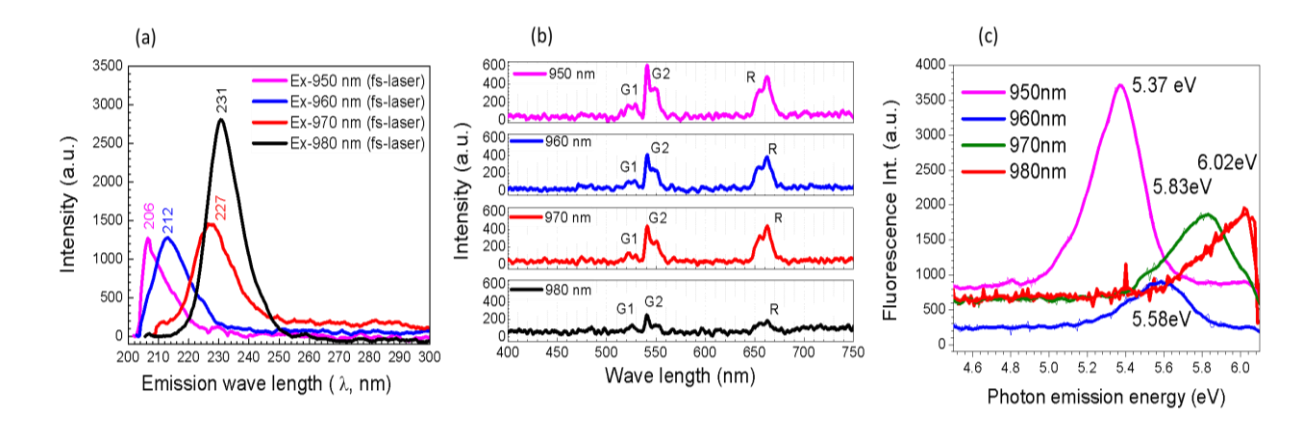


Figure 3.2.10: (a) Up-conversion Luminescence spectra in the UV-region (on excitation with fs-laser), exhibited red shifting with increasing excitation wavelengths (b) Up-conversion Luminescence spectra at the visible region for different fs-laser excitations(c) Band gap energies received from different fluorescence spectra under different excitation fs-laser sources

Thus, in visible region maximum of 2 nm band shifting has been observed. Further, 4th series of emissive bands (in visible region) are appeared in between 643 nm-677 nm having highest intense positions at 662 nm, 662 nm, 662 nm and 663 nm under fs-laser irradiation sources 950, 960, 970 and 980 nm, respectively and not comprised any significant shifting with change in irradiation wave lengths (figure 3.2.10b).

Thus, main interesting attraction is the emission in UV region once the UCN-dots are excited under fs-laser and their remarkable red shifting once they are excited from 950 nm to 980 nm fs-laser irradiation (figure 3.2.10a). It is very exciting that there is no shifting of band positions observed in the visible region for G1, G2 or R bands (figure

3.2.10b). Moreover, bands appeared in UV region exhibits noticeable red shifting as  $\lambda$  increases from 950nm to 980nm irradiation (figure 3.2.10a).

This exciting phenomenon can be explained by calculating the number of photons absorbed under fs-laser excitation, which is further strongly dependent on:

- (i) fs-laser power and number of excited photons
- (ii) the shifting of band gaps ( $E_g$ = band gap energy). To measure fs-laser power dependent luminescence and the number of absorbed photons taken part in the process, one power law concept has been used to be

$$I_{uc} \sim I_{fs}^{n} \tag{1}$$

Where  $I_{uc}$  is the luminescence intensity which is proportional to 'n<sup>th</sup>' of excitation power  $I_{fs}$ , 'n' is the number of absorbed photons per photon emitted under fs-laser excitation power  $I_{fs}$  and this has been calculated from the slopes of  $log(I_{uc})$  versus  $log(I_{fs})$  (figure 3.2.11).

Similar power law concept has been used to calculate NIR laser power dependent luminescence using NIR elsewhere [276]–[280]. It can be noticed that, for G1 and G2 luminescence bands we need to transfer a minimum pair of photons (n = 2) from one sensitizer ion i.e. from Yb<sup>3+</sup> (donor ions) to one activator ion i.e. to Er<sup>3+</sup>(acceptor ions) (1: 1 molar ratio) under fs-laser (NIR) excitations [277]–[279].

The values obtained to be n (G1) = 3.6 and n (G2) = 1.6, respectively (figures 3.2.11b), 3.2.11c; (log ( $I_{uc}$ ) versus log ( $I_{fs}$ ) plots). Further, the number of absorbed photons for UV and red- emissions have also been calculated and found to be n (UV) = 5.46 and n(R) = 0.40, respectively (figures 3.2.11a, 3.2.11d). Highest value of "n" for UV (5.46) satisfies the highest number of transferred photons compared to the other emissions. The relative energy transfers for UCN-Dots in UV-Vis region are occurred due to the

high-power fs laser and their significant relevance along with corresponding excitation path ways can be explained as:

By fs-laser excitation sources (980, 970, 960 and 950 nm), initially the Yb<sup>3+</sup> sensitizes and excites to  $2F_{5/2}$  level and transfers energy to  $Er^{3+}$  in order to excite them in different energy levels e.g.  $4I_{13/2}$ ,  $4I_{11/2}$ ,  $4F_{9/2}$ ,  $4F_{7/2}$ ,  $4G_{11/2}$  (figure 3.2.12a).

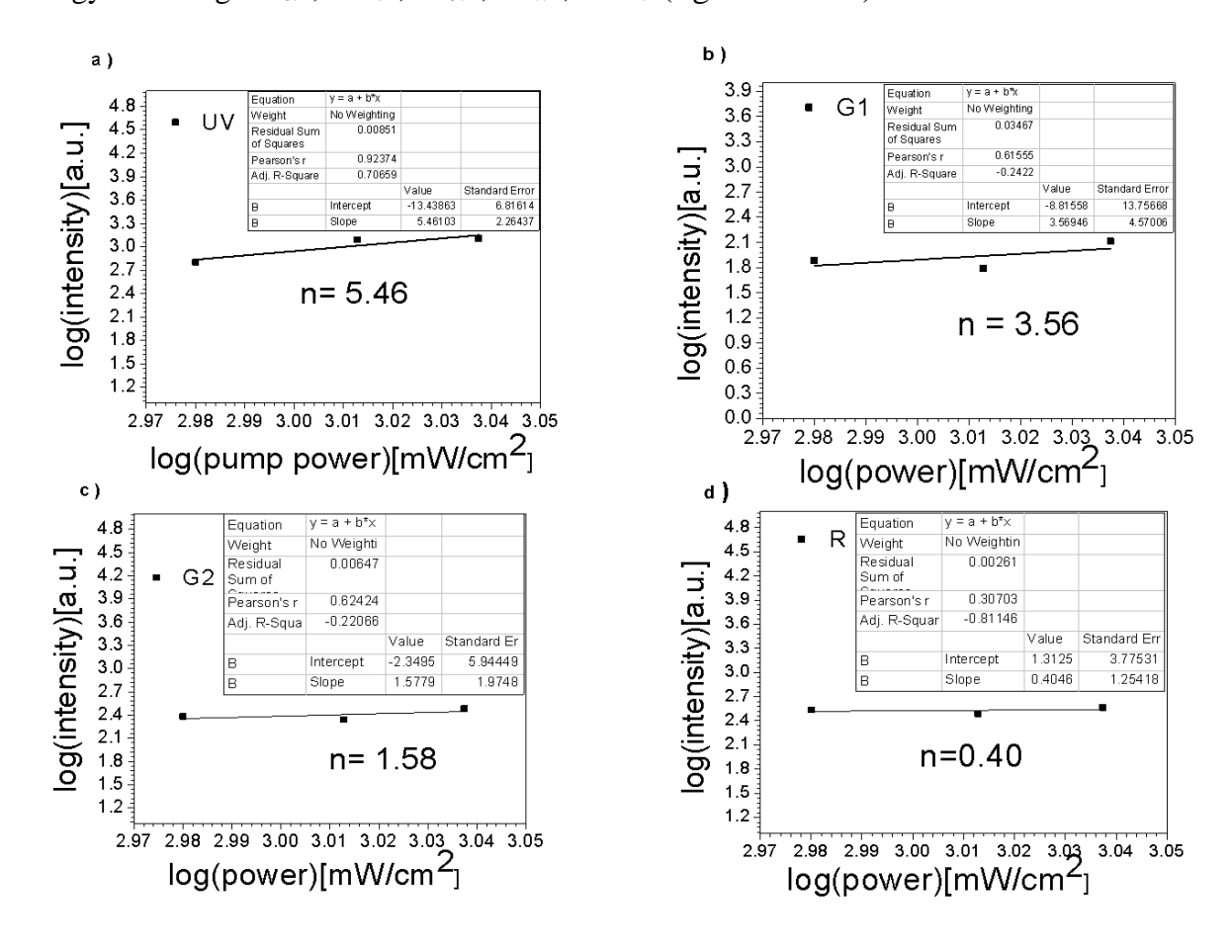


Figure 3.2.11: Dependence of Up-conversion luminescence intensity on fs-Laser power for (a) deep-UV, (b) Green G1(c) Green G2 and (d) Red (R) related emission (excited fs-laser), respectively. The number of absorbed photons per photon emitted under the fs-laser excitation power "n" value determined for the deep-UV, G1, G2 and R emissions for UCN-dot and their values also mentioned in the respective plots.

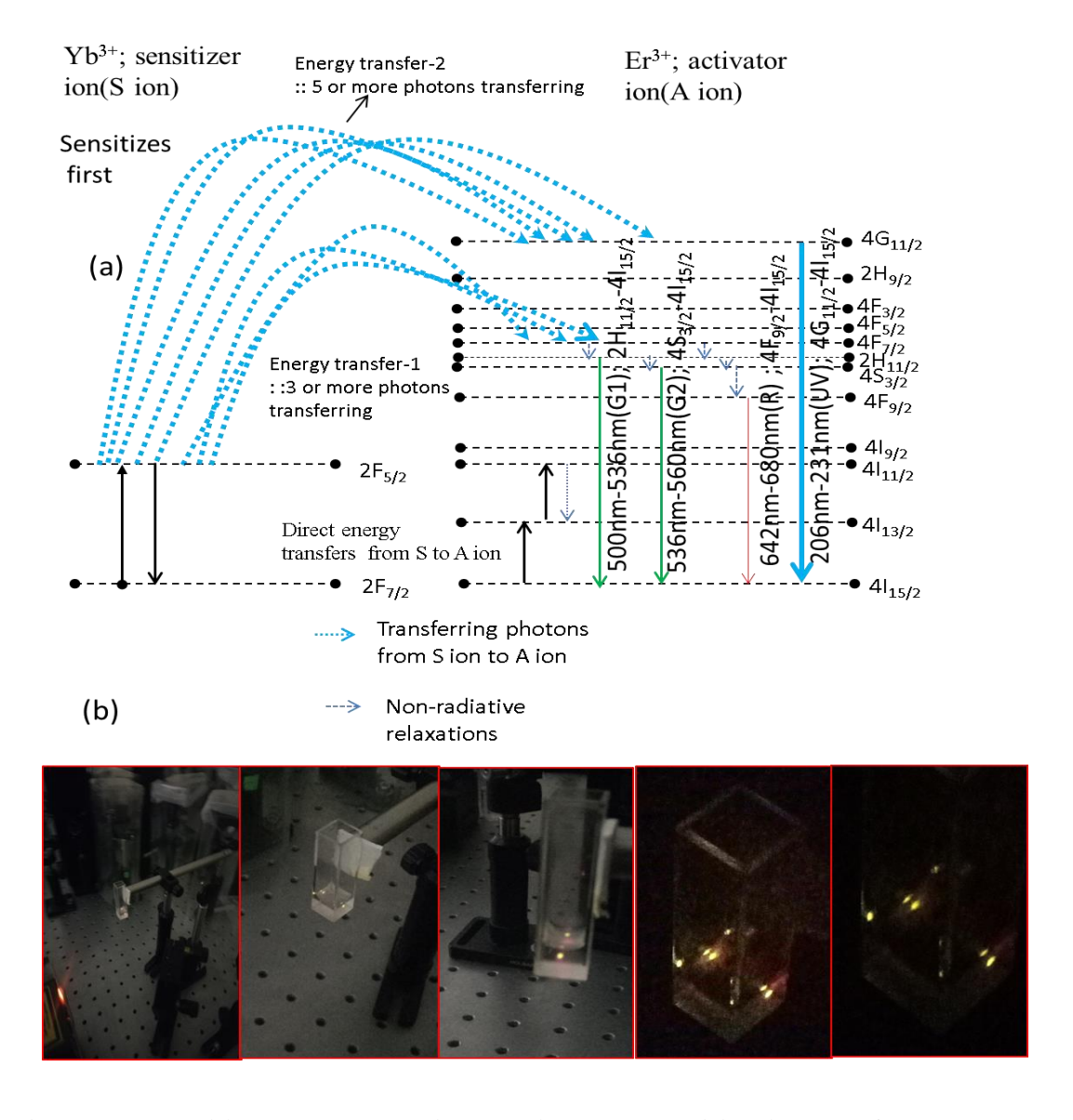


Figure 3.2.12: (a) Energy band diagram (energy transitions) under femtosecond laser source and (b) visible emissions in sample-cuvette during experiment (images are taken with five observations).

Population of  $4I_{11/2}$  energy-level occurs by transferred energy from  $2F_{5/2}$  (Yb<sup>3+</sup>) level. There are two waysto populate  $4I_{13/2}$  (Er<sup>3+</sup>) level; notably one is absorbing a 980 nm/or 970nm/or 960nm/or 950nm photon from  $4I_{15/2}$  (Er<sup>3+</sup>) energy state; another one is by

non-radiative relaxation ( $4I_{11/2} \rightarrow 4I_{13/2}$ ) between  $4I_{11/2}$  and  $4I_{13/2}$  energy levels. A direct energy transfer (designated as energy transfer 1) can be populated to  $4F_{7/2}$  level from which non-radiative relaxations occurs to  $2H_{11/2}$  level and further to  $4S_{3/2}$  level, both of which are responsible for green emissions (G1 and G2, figure 3.2.10b, 3.2.12a) following the sequence path:

 $2F_{7/2}(Yb^{3+}) \rightarrow 2F_{5/2}(Yb^{3+}) \rightarrow 4F_{7/2}(Er^{3+}) \rightarrow 2H_{11/2}/4S_{3/2}(Er^{3+}) \rightarrow 4I_{5/2}(Er^{3+})$  which includes one and/or two non-radiative relaxations such as  $4F_{7/2}(Er^{3+}) \rightarrow 2H_{11/2}$  and/or  $2H_{11/2} \rightarrow 4S_{3/2}(Er^{3+})$ .

The corresponding energy transitions for G1 and G2 emissions bands are  $2H_{11/2}$ - $4I_{15/2}$  and  $4S_{3/2}$ - $4I_{15/2}$ , respectively. The second direct energy transfer (energy transfer 2) occurs from  $2F_{5/2}(Yb^{3+}) \rightarrow 4G_{11/2}(Er^{3+})$  level by continuous high-power input excitation laser- source. From higher excited state  $(4G_{11/2})$ ,  $Er^{3+}$  ion can be relaxed directly to the ground state  $(4I_{15/2})$  with emitting high intense ultraviolet (UV) emissions corresponding to transition  $4G_{11/2} \rightarrow 4I_{15/2}$  without experiencing any kind of a non-radiative relaxations.

Energy transfer 1: 
$$2F_{7/2}(Yb^{3+}) + 4F_{7/2}(Er^{3+}) \rightarrow 2F_{5/2}(Yb^{3+}) + 4I_{11/2}(Er^{3+})$$
 (2)

Energy transfer 2: 
$$2F_{7/2}(Yb^{3+}) + 4G_{11/2}(Er^{3+}) \rightarrow 2F_{5/2}(Yb^{3+}) + 4F_{9/2}(Er^{3+})$$
 (3)

The moderate red emission (R) assigning to the  $4F_{9/2} \rightarrow 4I_{15/2}$  transition appears following the path:  $2F_{7/2}(Yb^{3+}) \rightarrow 2F_{5/2}(Yb^{3+}) \rightarrow 4F_{7/2}(Er^{3+}) \rightarrow 2H_{11/2} \rightarrow 4S_{3/2}(Er^{3+}) - 4F_{9/2}(Er^{3+}) \rightarrow 4I_{15/2}$  ( $Er^{3+}$ ) including three non-radiative relaxations such as  $4F_{7/2}(Er^{3+}) \rightarrow 2H_{11/2}$ ,  $2H_{11/2} \rightarrow 4S_{3/2}(Er^{3+})$  and  $4S_{3/2}(Er^{3+}) \rightarrow 4F_{9/2}(Er^{3+})$ ]. Thus, there are total two direct energy transfers occurred and they become responsible for UV and visible (G1, G2 and R) emissions which can be written in terms of the following two equations (equations 2 and 3 ;figure 3.2.12) considering the match of energy separation [281].

It can be noted that there is no significant change in band positions for G1, G2 or R observed with change in the fs-laser excitation wave lengths (950 to 980 nm) (figure 3.2.10), however change in intensity is observed (figure 3.2.13) with change in the excitation wave lengths.

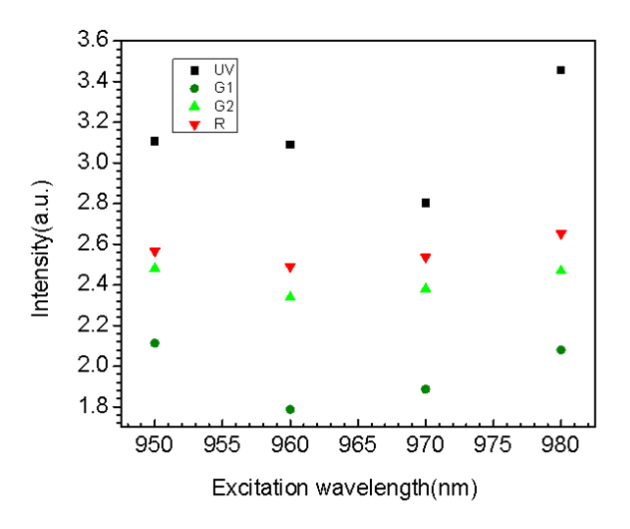


Figure 3.2.13: Plots intensity [a.u.] vs excitation wavelength [nm] for UV, G1, G2, R

A noticeable change in band intensities and their relative ratios with different excitations for (i) peak ratio (G1/G2) and (G1/R) (figure 3.2.14a), (ii) peak ratio (R/G1) and (R/G2) (figure 3.2.14b), (iii) peak ratio ( $G_{full}/R$ ) (figure 3.2.14c) and (iv) peak ratio (UV/G1), (UV/G2) and (UV/R) (figure 3.2.14d) have been observed in figure 3.2.14. These phenomena have been observed due to different efficient population causes from the effective number of excited photons, i.e., n(UV), n(G1), n(G2) and n(R) (figure 3.2.11). The fractional number of absorbed photons for red emission n(R) (actual 0.40) signifies that red emission has been occurred only due to the cross- relaxation of photons from the higher energy state ( $4F_{7/2}$ ) to the lower energy state ( $4F_{9/2}$ ) and not due to any other direct energy transfers.

However, the appearance of strong emission bands in UV region can be explained with the change of  $E_g$  values received due to the interaction with fs-laser.  $E_g$  values for different UV- bands have been calculated from fs-luminescence spectra using the method reported elsewhere [39,40] and found to be 5.37, 5.58, 5.83 and 6.02 eV (figure 3.2.10c).

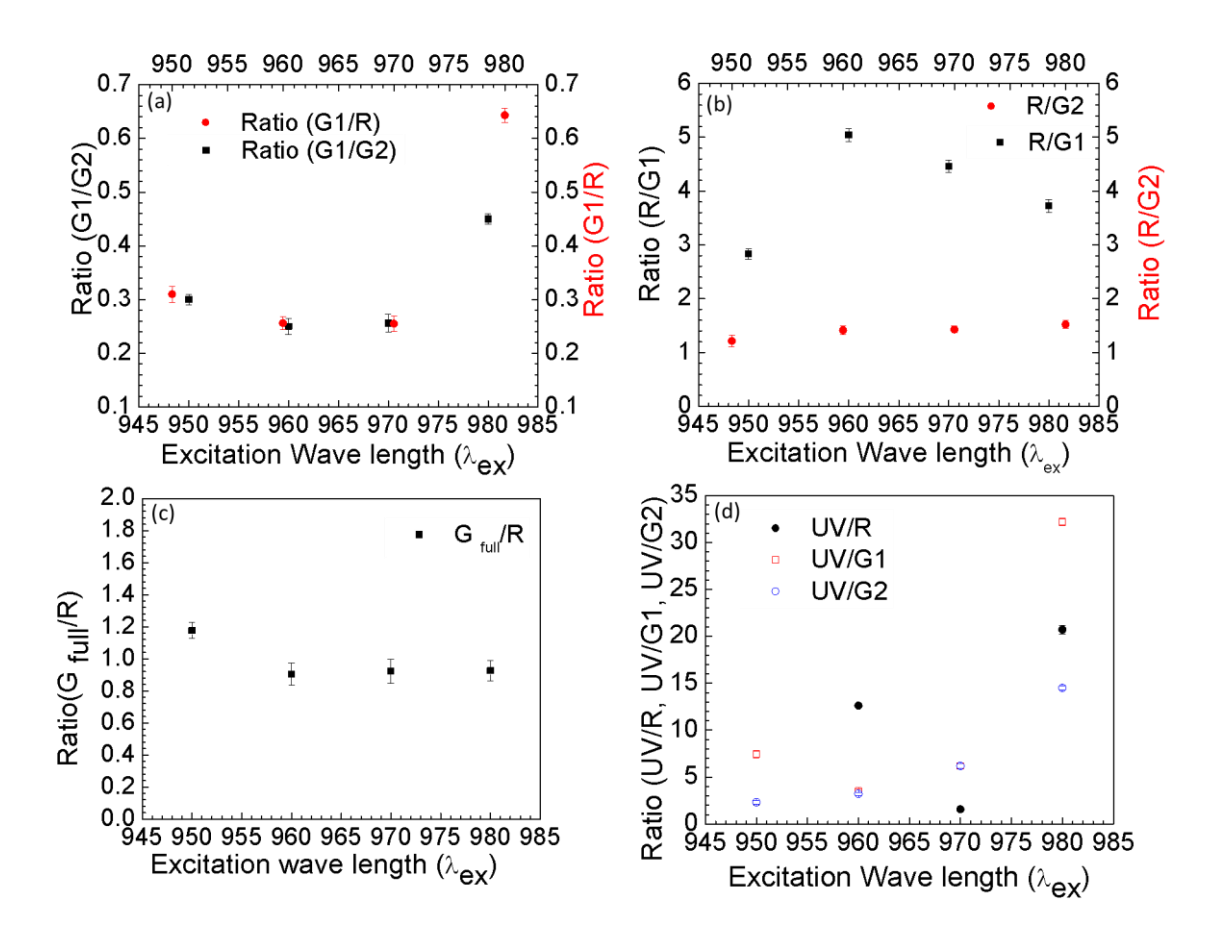


Figure 3.2.14: (a-d) Plots for peak ratios vs excitation wavelengths (nm) (a) G1/R, G1/G2 vs  $\lambda_{ex}$  (b) R/G1, R/G2 vs  $\lambda_{ex}$  (c) Gfull vs  $\lambda_{ex}$  (d) UV/G1, UV/G2, UV/R vs  $\lambda_{ex}$ 

Table 3.2.2: Band Gap Energy (Eg) of UCN-dots with different excitation photon energies (Fs) and single photon energy (FL, PL)

Types of Spectra	Excitation Wavelength	Excited photon energy (eV)	Band gap values(eV)
	$\lambda_{\rm ex}({\rm nm})$	[1240/Wavelength]	
Femtosecond	950nm	1.31eV	5.37eV
Laser(Fs)-spectra	960nm	1.29eV	5.58eV
	970nm	1.28eV	5.83eV
	980nm	1.27eV	6.02eV
Fluorescence-	980nm	1.27eV	2.5eV, 2.35eV, 2.28eV,
spectra(FL)			1.87eV, 1.48eV
Photoluminescence	450nm	2.76eV	3.26eV, 3.05eV, 2.88eV,
spectra(PL)			2.68eV, 2.38eV, 2.26eV,
			2.18eV, 2.04eV,
			1.94eV

Hence, clear red shiftings have been observed with increasing excitation wave lengths. It can be noted that the fitting procedure has been done with highest band energy values which corresponds to  $E_{\rm g}$ . Therefore, the shifting of bands in UV region with change in fs-laser excitations is obvious. Further, the excited photon energy corresponding to the fs-laser excitations have been calculated and found to be 1.30, 1.29, 1.27 and 1.26 eV (table 3.2.2).

Detailed result of excited photon energy and corresponding  $E_g$  values with respect to excitation wavelengths for 980nm ex.- fluorescence (figure 3.2.7), photoluminescence (figure 3.2.8) and fs-luminescence (figure 3.2.10 and figure 3.2.12) are provided in tabulated form (table 3.2.2).

Further, power dependent luminescence properties have also been investigated from figure 3.2.10 and a sharp red sifting is observed for UV emission bands with

decreasing incident powers of 1.09 W, 1.00W, 0.955W, and 0.900W for 950nm, 960nm, 970nm and 980nm irradiations, respectively. To find out the quality of the synthesized UCN-dots of NaYF<sub>4</sub>:Yb<sup>3+</sup>,Er<sup>3+</sup>, from the excited power densities of 15.428 W/cm<sup>2</sup>, 14.154 W/cm<sup>2</sup>, 13.517 W/cm<sup>2</sup>, and 12.739 W/cm<sup>2</sup> the UCQYs have been calculated according to the method reported elsewhere [284], [285] and the values are shown in figure 3.2.15.

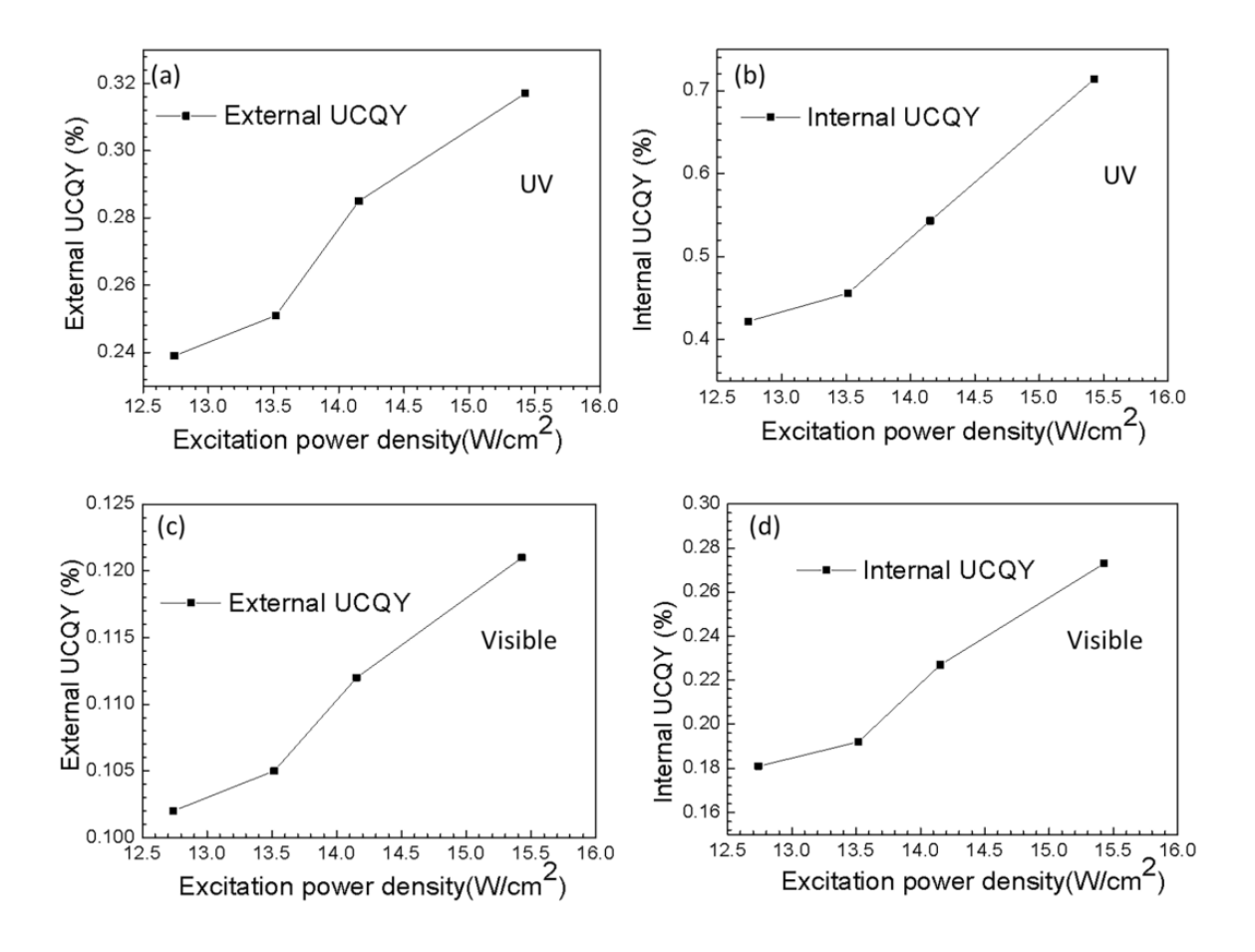


Figure 3.2.15: (a) and (b) Show the External-UCQY (%) and Internal-UCQY (%) with excitation power density for emission in UV regime, respectively; (c) and (d) show External-UCQY (%) and Internal-UCQY (%) with excitation power density for the emission in visible regime, respectively for UCN-dots of NaYF4:Yb<sup>3+</sup>:Er<sup>3+</sup>

However, in the present study for UCN-dot, for visible emissions under fs-laser system both external and internal UCQY. have been calculated according to the method reported elsewhere [284], [285] and found to be (External-UCQY): 0.121 ± 0.003 %, 0.112±0.002%, 0.105±0.001%, 0.102±0.002%; and (Internal-UCQY): 0.273±0.004%, 0.227±0.002%, 0.192±0.002%, 0.181±0.005%; whereas in UV-region they are calculated to be (External-UCQY): 0.317± 0.003%, 0.285 ±0.004%, 0.251±0.002%, 0.239±0.002%; and (Internal-UCQY): 0.714±0.007%, 0.543±0.002%, 0.456±0.001%, 0.422±0.001% under excitation pump powers 1.09 W, 1.00W, 0.955W, and 0.900W, respectively and appear to be efficient for "d" < 4nm UCN-dots while compared with as-said previous observations [284]–[287]. We have observed that UCQY increases with increase in the irradiance. The corresponding UCQY vs. excitation power density results are represented in figure 3.2.15 and brightness vs. excitation power density results for UV emission is shown in figure 3.2.16. Thus with increasing power density both the internal and external UCQY values have increased.

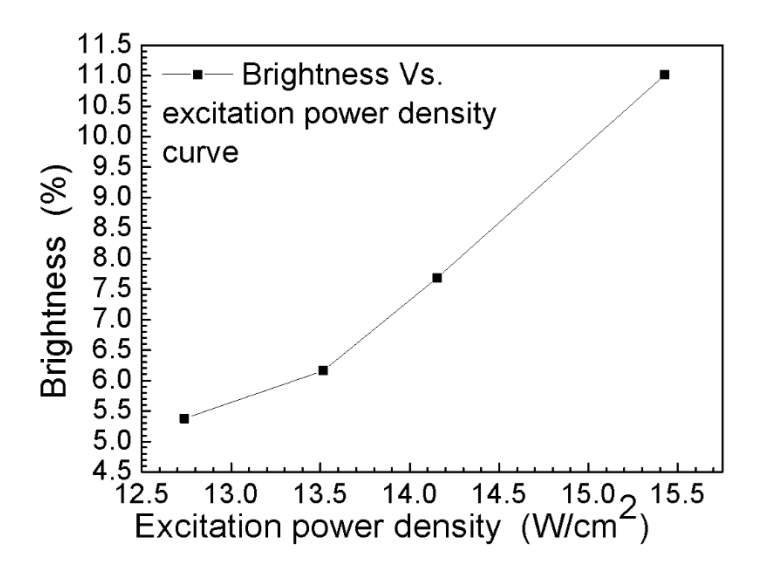


Figure 3.2.16: Brightness (w.r.t internal Q.Y. in UV emission) vs excitation power density curve

It can be noted in this line that Boyer et al. reported the UCQY for different sizes of UCNPs (NaYF<sub>4</sub>:Er<sup>3+</sup>,Yb<sup>3+</sup>) and their values were 0.005%, 0.10%, 0.30% and 3% for 8-10nm, 30nm,100nm and above 100nm sized UCNPs, respectively, once they were excited with 980 nm NIR laser [286]. Chen et al. reported the UCQY values of 0.13%, 0.07%, 0.05% and 0.95% under 540, 660, 800, and 970 nm NIR excitations, respectively for the UCNPs of size 100 nm (NaYF<sub>4</sub>:Er<sup>3+</sup>,Yb<sup>3+</sup>) [284]. In an another study the internal UCQY for core shell UCNPs of size  $\sim$  40 nm ( $\beta$ -NaYF<sub>4</sub>:Er<sup>3+</sup> core, dia. 19.2 nm and  $\beta$ -NaLuF<sub>4</sub> shell with thickness 18.8 nm) was reported as 3% with 1523 nm NIR laser irradiance [285]. Therefore, it can be concluded that the UCN-dots reported in present work exhibited higher UCQY in fs-laser radiation with respect to the UCNPs (NaYF<sub>4</sub>:Er<sup>3+</sup>,Yb<sup>3+</sup>) reported in the earlier works.

However, advent of ultrafast (UF) lasers has revolutionized the field nonlinear optical incentro-symmetry and non-centro-symmetry materials. Electro-optic (E-O) and nonlinear phenomena are realized in materials under the influence of strong electric field and popularly known as Pockels and Kerr effects[288]. Nonlinear phenomena are observed due to the introduction of birefringence by external E-M field and attributed to change in refractive index. The generation of high-power energy upconversion from UCN-dots can be occurred either from the surface or interfaces of the particles. The generation of high-power upconversion emission completes in three steps, namely, first, (i) incident beam of intense UF radiation induced change in birefringence or refractive index in the materials, then (ii)the UCN-dots behave like a nonlinear hertzian oscillator and generates polarized waves from the surface or interfaces and finally (iii) the generated polarized waves interact with each other. The interference of polarized waves generates the high energy upconversion from UCN-dots.

# 3.2.6 Summary and Conclusions of PART II:

NIR to visible upconversion luminescent UCN-dots with cubic phases (NaYF<sub>4</sub>: Yb<sup>+3</sup>; Er<sup>+3</sup>) were synthesized by solvo- thermal decomposition of lanthanide hexahydrate precursors with organic solvents following a novel and straight forward synthesis approach. The average particle size obtained to be 3.4 nm in dia. which are smallest in size reported ever and stable for a minimum of one year with upconversion luminescence. This work further revealed the emission of UV luminescence under interaction with femtosecond laser. Though, owing to their very small sizes, the gross amount of fluorescence intensity was reduced as a large number of cross relaxations were induced during energy-transfer mechanism but still they showed very special property while interacting with femtosecond laser. Importantly, this work revealed that the UCN-dots could be a great potential candidate for emitting highly efficient ultraviolet radiation and useful as UV-emitting nanophosphors which can be used in several bio-applications [289]. Since various bio-applications of UCNPs have already been reported, therefore this work directs us that the unique sizes (3.4 nm) of the UCN-dots could further open a domain of new possibilities in biomedical engineering and medical-fields for improving the treatments of infected cancer cell and tumour cells along with improving the efficiency of several devices where the non-linear optical activities play an important role.

## 3.2.7 Calculation part of number of unit cells present in single UCN-dot:

The number of unit cells in UCN-dot:

The average lattice constant has been found to be = 5.39 ÅAssuming,

UCN-dots to be almost spherical, the volume of one particle has been calculated as  $= V_{UCN\text{-dots}} = 4/3 \times 3.14 \times (1.75)^3 = 22.4379 \text{ nm}^3$ 

[Considering average particle diameter as 3.5nm, radius= 3.5/2= 1.75nm]

Now,

As the crystal structure is cubic-FCC, UCN-dots consist of cubic unit cells, so the volume of the cubic unit cell =  $V_{unit cell} = (a_c)^3 = (5.39 \text{Å})^3 = 156.590 \times 10^{-3} \text{ nm}^3$ .

# Therefore,

The number of unit cells in one UCN-dot particle =  $V_{UCN-dots}/V_{unit\ cell} = 0.143 \times 10^3 \sim$  almost 143 no. of unit cells.

#### Note:

In cubic cell, Number of  $F^-$  ions = 8, so in one particle 1144 no. of  $F^-$ ions are present. Number of  $Na^+/RE^{3+}$  ions = randomly occupy the positions According to previous study, please follow the link <a href="http://dx.doi.org/10.1101/114744">http://dx.doi.org/10.1101/114744</a> As standardized calculation, with rare earth dopants ( $Yb^{3+}$ ,  $Er^{3+}$ ), number of effective Na, F, Yb, Er atoms present are= 2, 8, 1, 1 as fraction of  $Y^{3+}$  ions are substituted by rare earth ions( $Yb^{3+}$  and  $Er^{3+}$ ) [ref-as mentioned above]

# **Chapter 3 RESULT AND DISCUSSION**

# PART-III

3.3 (Part-III): Self-assembled pearl necklace patterned-upconverting nanocrystals with highly efficient blue and ultraviolet emission: femtosecond laser based upconversition properties

**Outcome**: Monami Das Modak, Ganesh Damarla, Somedutta Maity, Anil K. Chaudhary and Pradip Paik; Self-organized dendritic-upconverting nanocrystals with highly efficient blue and ultraviolet emission: femtosecond laser based upconversition roperties; Published in RSC Advances Journal.

# 3.3.1 Introduction:

Dendrimers are attractive due to several unique properties and for their applications in materials, materials science, industrial applications for designing solar cells, sensors and for biomedical medical applications.[290] [291] Rare-earth upconverting materials have been demanded as they are the best energy upconverting (NIR-tovisible) materials ever known, therefore recently researchers are focusing on their design, synthesis and spectroscopic properties. Further, upconverting materials possess potential uses in biological labelling and bio-assays and their extent of uses are increasing remarkably with time [34], [95], [292]–[294]. All these unique features drive us to synthesize dendritic UCNPs having strong upconversion emission. To the best of our knowledge, dendritic UCNPs are never known. A report was found where UCNPs were impregnated in porphyrin dendrimers [295]. In this work we are enabled to prepare dendritic UCNPs in in-situ condition without incorporating any external polymeric dendrimers. The as-prepared UCN-Ds have been formed by consuming all precursors into solid crystal nuclei as white precipitates at lower reaction temperature and then with increasing the reaction temperature crystal growth occurred followed by the formation of dendrimers. The as-prepared dendritic-UCNPs have excellent dispersibility in non-polar solvent (e.g., cyclohexane) and are stable for more than a year. As UCN-Ds exhibit excellent upconversion emission under 980 nm NIR excitation source and 140 femtosecond pulse duration at 80 MHz repetition rate, there is a vast ambit for using them in complex bio-labelling by tuning their spectral properties. Further, for present available systems there are several draw backs in achieving good efficiency for the DNA detection, [296] bio-imaging, [297] sensors and fluorophores,[11], [298], [299] analytes and several other important biomedical applications such as for the treatment of cancers[112], [300]–[302] which can be improved by using UCN-Ds.

Self-assembled materials can be obtained from nature to the laboratory. Self-assembly in living system is biologically controlled whereas; self-assembly formation in laboratory is controlled artificially. The assembly of nanomaterials is purely represented by non-covalent bonding and controlled both by kinetic and thermodynamically. Inside laboratory self-assembly processes are used for designing the artificial nanostructures, such as for assembling proteins, peptides, neucleotides, supramolecular biopolymers etc. and they have myriad applications in biomedicals for developing artificial membranes and for various biofunctions [303]-[305]. Selfassembly of various inorganic (metals/hybrids) nanopartiles is well known [306]— [308]. The formation of self-assembled dendritic nanostructures is very much interesting in the area of modern nanotechnology. Dendritic nanostructure of UCNPs can exhibit unique properties with their associated building blocks (nanoparticles below 10 nm). The self-assembled architectures of nano sized UCNPs can offer a potential platform for future applications, especially in nonlinear optical property based nanotechnology. Dendrimers have become the most exciting nanometre-sized branched architectures, which are formed by repeating nanoscopic building blocks. Hence, the effort of forming such self-assembled dendritic UCNPs can be considered as spontaneous assembly of branched building blocks of nanoparticles. Usually, the interactions between the molecules associated with dendritic net-work structures can be referred to the supramolecular chemistry [309], where non-covalent interactions play major roles between molecules.

In the above line, present work is focused on the synthesis of self-assembled UCN-Ds and their upconversion behavior. The upconversion luminescence of self-assembled dendritic UCNPs are interesting which have been studied here. In a set of experiments, the upconversion behaviors of UCN-Ds have been studied with Femtosecond (Fs) Laser (140-femtosecond pulse duration at 80 MHz repetition rate) along with CW-980nm NIR. Further, visible-to visible upconversion has also been studied. The NIR to UV/vis upconversion properties also is observed for UCN-Ds which is represented

here in detail. At the end, probable mechanisms for the visible-visible/CW-980 NIR/Fs-laser based upconversions with energy band diagrams for different emissions have been elucidated.

## 3.3.2 Experimental observations:

The self-assembly of dendritic network formations and sizes of the as-prepared UCNPs have been shown in figures 3.3.1a - 3.3.1d with different magnification TEM images. TEM was performed using the colloidal solution of UCN-Ds on copper grid (200 mesh, carbon coated). Figures 3.3.1a - 3.3.1c confirm the self-assembled dendritic network formations of synthesized UCN particles. TEM images (figures 3.3.1a, 3.3.1b, 3.3.1c) show the caterpillar-like/pearl chain type necklace formations at different magnification. In-set of figure 3.3.1b clearly shows the density of the particles for different chains. In figure 3.3.1c, lengths of the chains have been shown clearly, where the dotted lines with different colour have been drawn for different chain lengths. Further, it can be noted that the chains are formed with a single row of nanoparticles without overlapping and the distance between two adjacent particles are nearly constant. Most of the regions throughout the sample are able to contain a uniform size of the particles. Overlapping between the particles is almost negligible due to the possible electrostatic interactions.

The high crystallinity is confirmed by high resolution TEM images. Figures 3.3.1d and 3.3.1e show a clear lattice fringes with inter- fringes d of 0.31nm. The crystalline nature of the UCN-Ds further has been confirmed through the XRD analysis (shown in subsequent section). Figure 3.3.1f shows the SAED pattern with clearly visible ring type diffraction pattern.

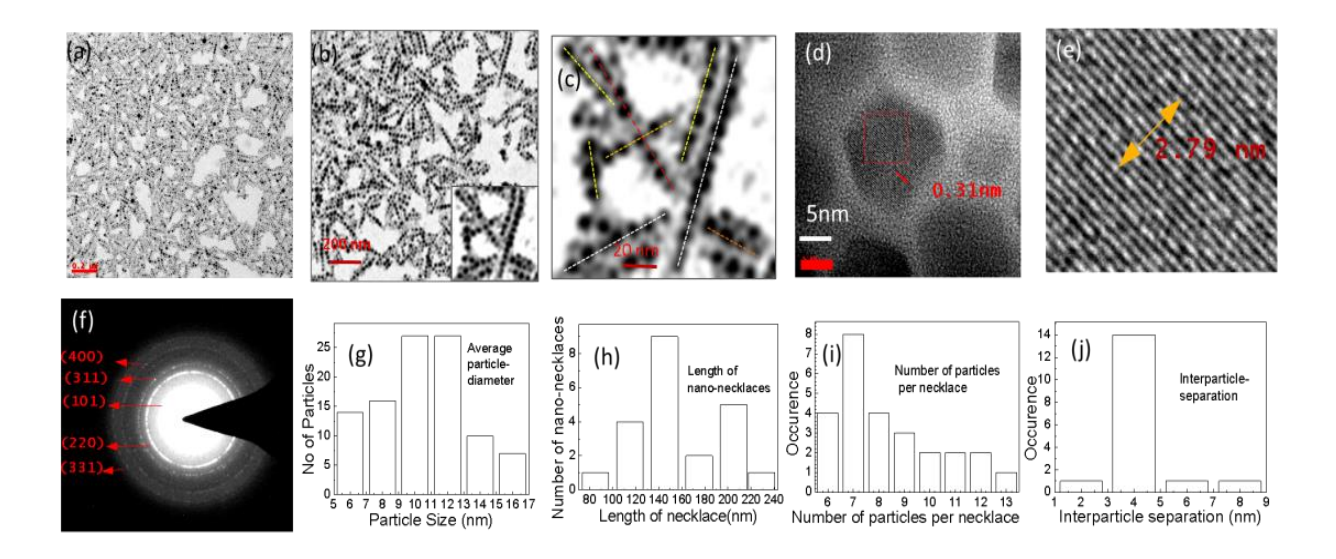


Figure 3.3.1: TEM images of the synthesized colloidal-dendritic UCNPs (UCN-Ds at different magnifications. Panels: (a,b)= 200nm,inset in panel (b) shows the clear formation of dendrimers (c) = 20nm, (d),(e) = High resolution micrograph showing lattice fringes, (f)=SAED ring pattern, Histogram of (g)= particle diameter, (h) nanonecklace length, (i)total number of particles per necklace, (j) interparticle-separation

Figure 3.3.1f has further confirmed five diffraction planes such as (101), (220), (311), (400) and (331) which correspond to the formations of α- and major β-NaYF<sub>4</sub> UCNPs. Figure 3.3.1g represents the average particle diameter and its distribution is found to be average c.a., 10nm±1 nm. Further, the length of nanonecklaces, number of particles per necklace and interparticle separation has also been calculated from TEM results. From figure 3.3.1h, figure 3.3.1i, and figure 3.3.1j, it can be confirmed that the average nanonecklace length of 140nm which consists of 7-13 numbers of particles per necklace and interparticle distance observed to be c.a. 4nm. X-ray diffraction study was performed to confirm the solid state crystalline structure and is shown in figure 3.3.2. The peak positions that appeared are corresponding to the diffraction planes (101), (220), (311), (400) and (331) respectively. The d-spacing values have also been calculated and found to be 2.9Å, 2.0Å, 1.63Å, 1.43Å and 1.26Å, respectively, which are matching for the α-/β-NaYF<sub>4</sub> crystalline phases for UCNPs [8], [254], [310]. The

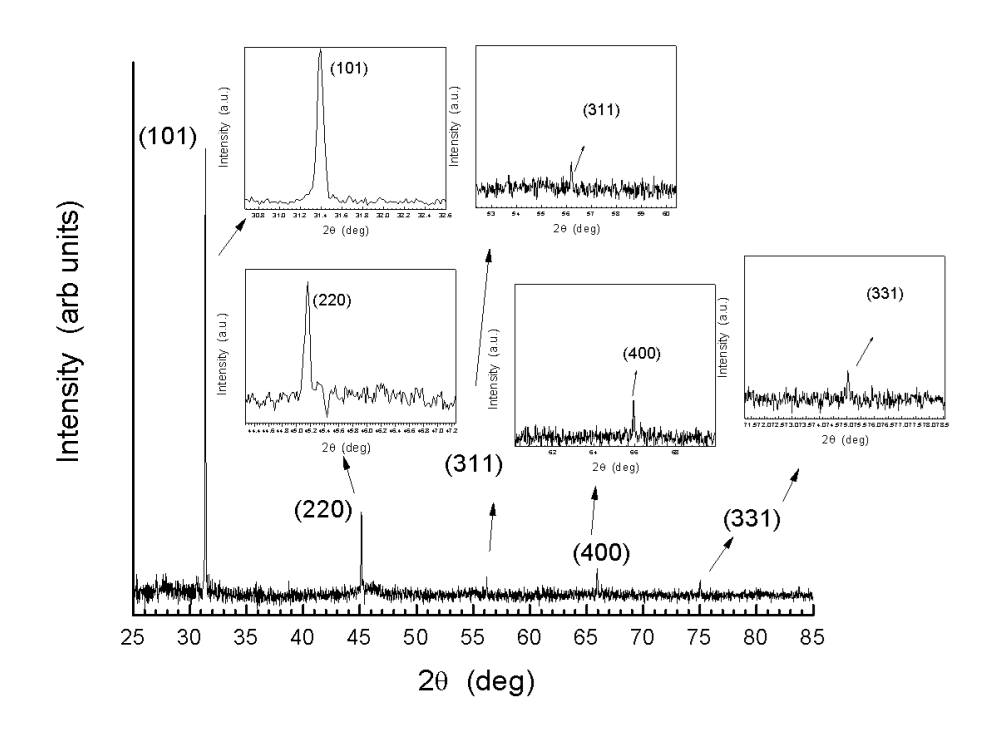


Figure 3.3.2: XRD study of synthesized UCN-Ds confirms the crystalline structure. Insets show the observed peaks with their corresponding crystalline planes according to JCPDS-028-1192

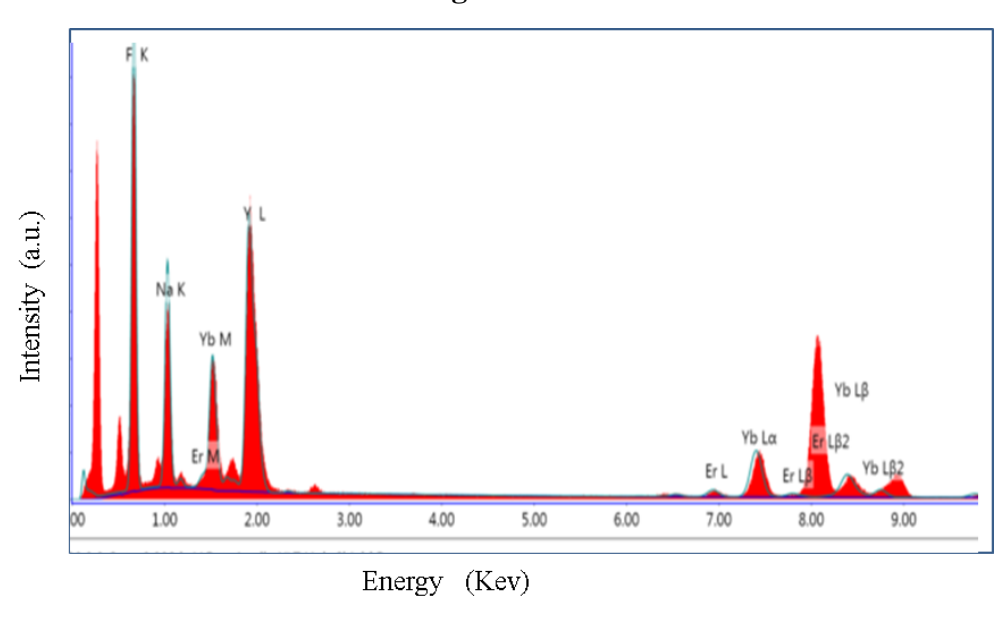


Figure 3.3.3: EDXA spectrum of UCN-Ds confirming the presence of elements

elemental analysis was performed through the Energy Dispersive X-ray Analysis (EDXA) (figure 3.3.3) and confirms for the presence of the elemental Na, Y, F, Er and Yb (table 3.3.1.).

Table 3.3.1: Elemental compositions observed in EDAX spectrum

Element	Weight (%)	Atomic (%)
F	44.79	49.97
Na	54.05	49.83
Er	0.11	0.01
Yb	0.62	0.08
Y	0.42	0.1

The upconversion fluorescence spectrum for UCN-Ds under 980nm NIR CW laser-excitation source is shown in figure 3.3.4. During experiment the power density was maintained to  $1000 \text{ mW/cm}^2$ . From figure 3.3.4, it can be observed that UCN-Ds exhibited a very strong upconversion emission. Intense Emission bands with their maximum positions are appeared at  $\lambda = 526 \text{nm}$ , 545nm and 659nm for the green emission (G), which are much higher in intensity (4.3 times) than that of the red emission band (R). Green emissions band appeared at 526 nm between 509nm and 531nm and at 545nm between 532nm and 570nm are attributed to the transitions in the energy levels-  $2H_{11/2}$ ,  $4S_{3/2}$  (excited energy levels) and  $-4I_{15/2}$  (ground state energy level of  $Er^{3+}$  ion), respectively, through a direct energy transfer mode from sensitizer ion (Yb<sup>3+</sup>) to activator ion ( $Er^{+3}$ ). A less intense (compared to the green emission) red emission bands at 659nm (between 632nm-691nm) has appeared with  $4F_{9/2}$  to  $4I_{15/2}$  energy transfer which follows a less population in  $4F_{9/2}$  energy level through the energy transfer path  $4I_{13/2} \rightarrow 4F_{9/2}$ . Herein,  $4I_{13/2}$  level is populated with non-radiative

relaxations between  $4I_{11/2}$  and  $4I_{13/2}$  energy levels. Further, very weak emission bands are observed at  $\lambda=382$ nm, 411nm and 497nm corresponding to the energy transition modes,  $4G_{11/2}/2H_{9/2} \rightarrow 4I_{15/2}$  and  $4F_{5/2} \rightarrow 4I_{15/2}$ , respectively. These weak emission bands are observed owing to the continuous of input source which excites the  $Er^{3+}$  ions sequentially to the next higher energy levels following the path  $4I_{15/2} \rightarrow 4I_{11/2} \rightarrow 4F_{7/2} \rightarrow 4G_{11/2}$ . It can be noted that, indirect energy transfers and cross relaxations resulted in very weak emission bands [254], [281]. It also can be noted that, for UCN particles (NaYF<sub>4</sub>,Yb<sup>3+</sup>;Tm<sup>3+</sup>), Tm<sup>3</sup> ion is responsible for blue emission (440nm-500nm,)[254] following the energy transition paths,  $1D_2 \rightarrow 3F_4$  and  $1G_4 \rightarrow 3H_6$ . However, for our UCN-Ds, without introducing Tm<sup>3+</sup> precursors we are able to achieve high intense blue emission which could be helpful as blue emitting nanphosphors and can be effective for designing biomedical devices and applications [311].

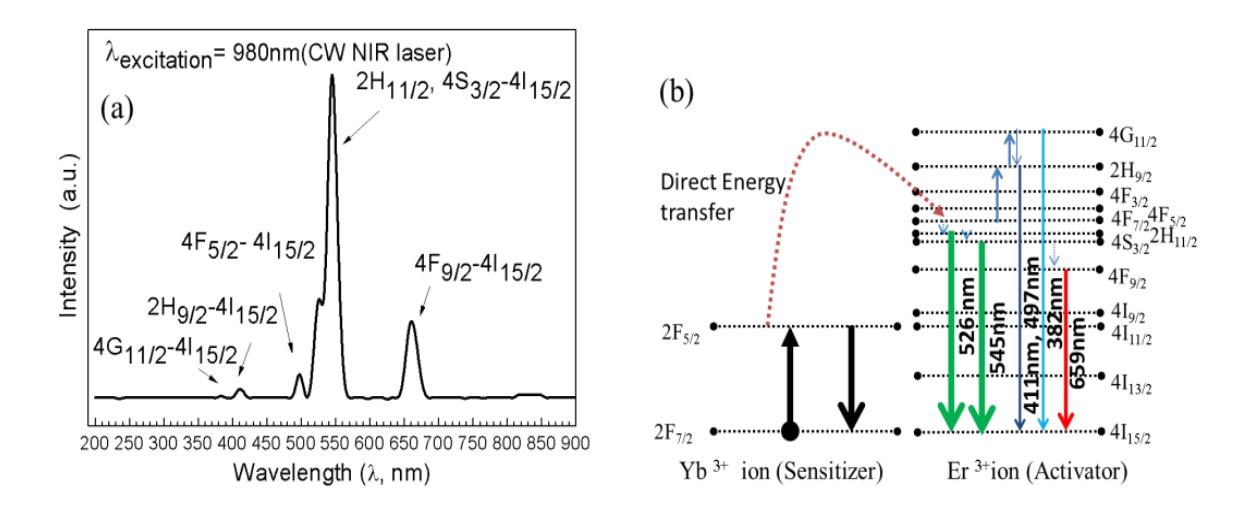


Figure 3.3.4: (a) Upconversion emission spectrum examined with UCN-Ds colloidal solution (b) corresponding energy diagram, under 980nm NIR-laser excitation source

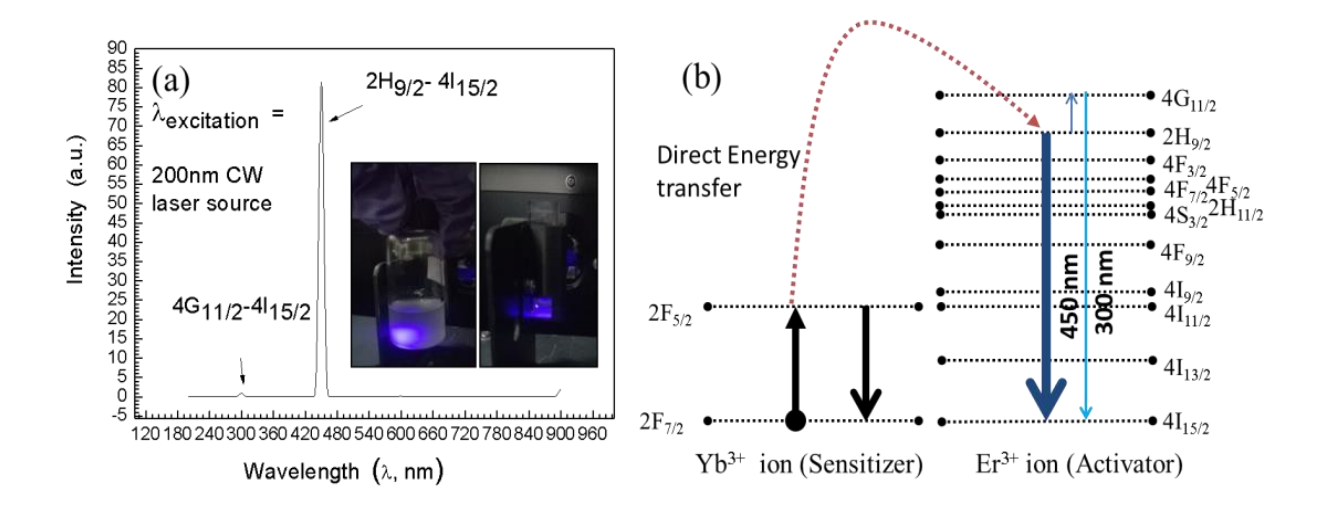


Figure 3.3.5: (a) Upconversion emission spectrum obtained with λexcitation of 200 nm CW laser source. In-set of (a) is showing the blue emission from UCN-ds and (b) is the corresponding energy band diagram

It is very interesting to mention that 980nm NIR excitation resulted weak blue emissive band (figure 3.3.4) but when we examined the sample with lower excitation wavelength source as example,  $\lambda = 200$ nm, then a high intense blue emissions occurred at 450 nm corresponds to the energy transition path,  $2H_{9/2}\rightarrow 4I_{15/2}$ . Figure 3.3.5a represents the emission spectra with their corresponding energy transitions under 200 nm excitation sources and Figure 3.3.5b represents the respective energy level diagram supported by a direct energy transfer from Yb<sup>3+</sup> to Er<sup>3+</sup> ion.

The insets in figure 3.3.5a shows the visible blue emissions of UCN-Ds from the UCN-Ds sample kept in glass bottle and quartz cuvette, with direct irradiation of 200nm wavelength source. Figures 3.3.6a, 3.3.6b show the UCN-Ds solution (during synthesis) in stirring condition within reaction chamber and glass bottle and 4c shows blue emissions for the UCN-Ds just after washing, respectively. These UCN-Ds are stable at least for one year owing to their high surface zeta potential value ( $\xi$ ) of about -55.49mV (figure 3.3.7).

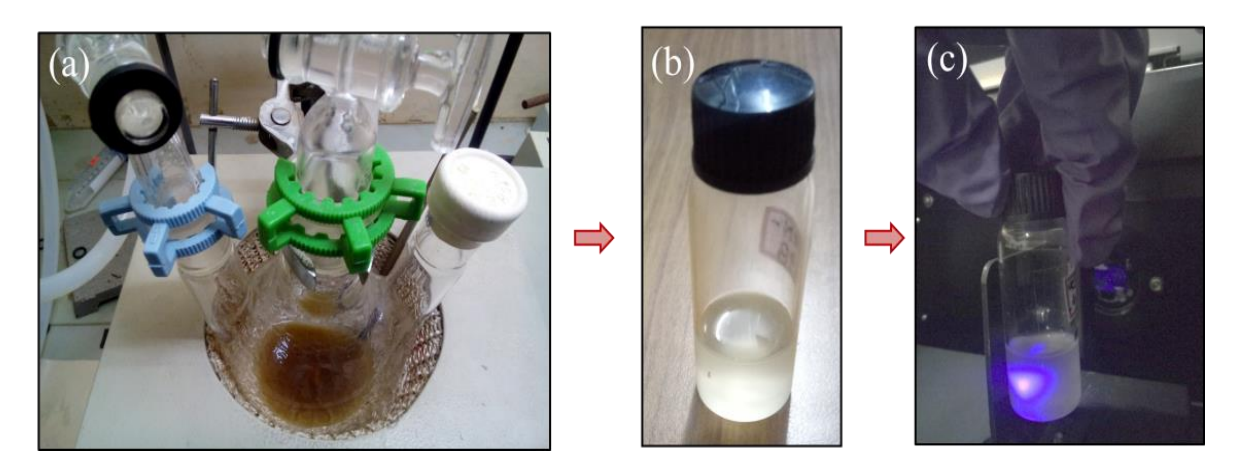


Figure 3.3.6: (a) Image is captured during synthesis (stirring condition) of UCN-Ds at high reaction temperature ( $\sim 330^{\circ}\text{C} - 340^{\circ}\text{C}$ ) with 1 hr 53 mins reaction time (b) UCN-Ds colloidal sample and (c) Intense blue emission in sample glass bottle, after washing done completely

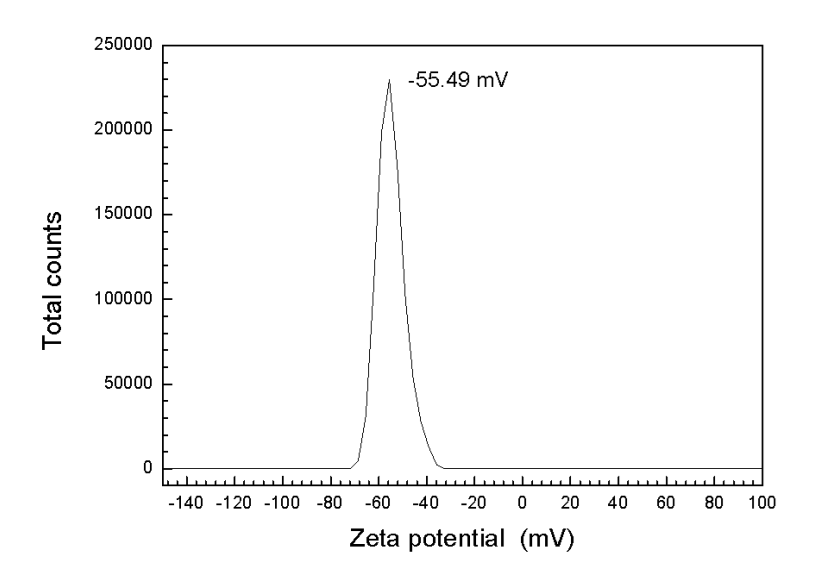


Figure 3.3.7: Zeta potential value found to be -55.49 mV for colloidal aqua solution of UCN-Ds

Figure 3.3.8 shows the Raman spectrum for UCN-Ds, where the bands appeared at 260cm<sup>-1</sup>, 303cm<sup>-1</sup>, 364cm<sup>-1</sup> and 395cm<sup>-1</sup> (below 700cm<sup>-1</sup>) confirm the formation of

hexagonal-phases [271], [312] Beyond  $700\text{cm}^{-1}$ , the appearance of strong bands at  $725\text{cm}^{-1}$ ,  $2887\text{cm}^{-1}$  and  $3512\text{cm}^{-1}$  are evidences for the presence of cubic-phases conjugated with oleic acid (capping agent). Thus, both the results obtained from XRD and Raman confirmed the formation of UCN-Ds with major  $\beta$ -phase along with a less extent of  $\alpha$ -phase.

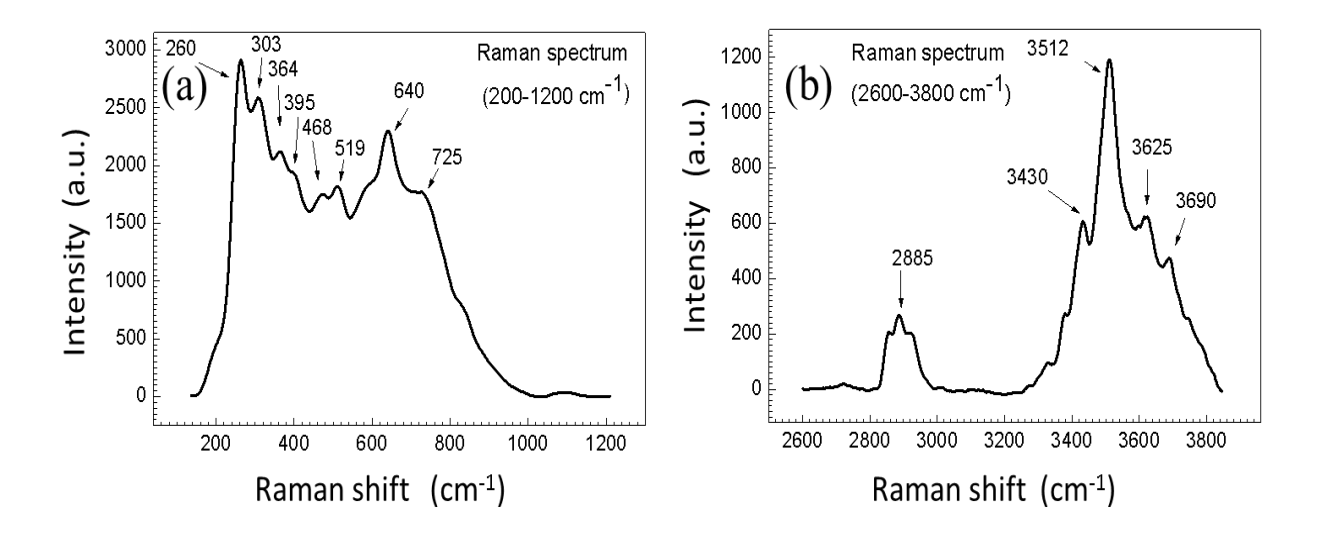


Figure 3.3.8: (a) Raman spectrum between 200-1200nm, (b) Raman spectrum between 2600-3800nm, confirm the presence of both cubic (α) and beta (β) phases in sample. The measurement was recorded at room temperature (figure 3.3.9)

As reported earlier, the appearance of bands due to the presence of vibrational modes above 700cm<sup>-1</sup> are found very weak for the minute quantity of hexagonal crystalline phase in UCNPs. With the formation of α-NaYF<sub>4</sub> phase, the Raman-spectra broadened within 1384cm<sup>-1</sup>-1416cm<sup>-1</sup> and 1041cm<sup>-1</sup>-932cm<sup>-1</sup> along with two additional bands appeared in between 703cm<sup>1</sup>-687cm<sup>-1</sup> and 279cm<sup>-1</sup>-260cm<sup>-1</sup> [313], [273]. Relatively, weaker bands appeared between 700cm<sup>1</sup>-1700cm<sup>-1</sup> and between 2820cm<sup>-1</sup>-2980cm<sup>-1</sup> due to the presence of capping agent (Oleic Acid) [272]. Weakly intense Raman bands appeared between 1073cm<sup>-1</sup> and 1445cm<sup>-1</sup> confirm the presence of asymmetry C-O-C

and CH<sub>3</sub> stretching, respectively, whereas presence of C-CH<sub>3</sub>/C-H/O-H bonds are confirmed by the medium intense bands appeared near 2885 cm<sup>-1</sup> and 3620 cm<sup>-1</sup>.

It is also noticed that the, bands appeared between 3300cm<sup>-1</sup>-3500 cm<sup>-1</sup> are ascribed to the (-N-H) vibration band which contributes for the formations of self-assembled dendritic net- work structures between UCNPs(full range Raman spectrum has provided in figure 3.3.9.

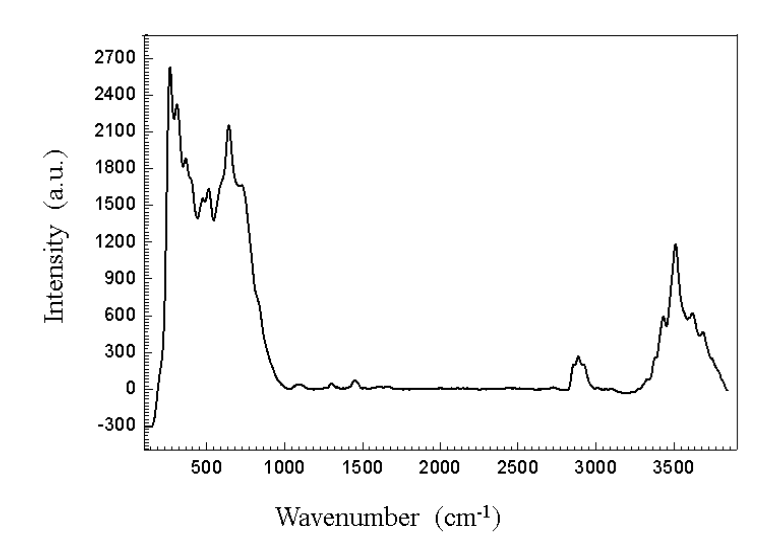


Figure 3.3.9: Raman spectrum of UCN-Ds with entire region

Further, the FTIR spectrum of UCN-Ds is shown in figure 3.3.10 which confirms the presence of various functional groups including N-H bending vibration at 1558cm<sup>-1</sup> and other oleic acid-capped groups at 2921cm<sup>-1</sup>, 2850cm<sup>-1</sup> appearing with highest intensity attached with the UCN-Ds.[314], [315].

However, the present analysis gives us a clear indication of  $\alpha$ - and  $\beta$ -phase formation within UCN-Ds crystals and is further supported by the TEM and XRD results (figure 3.3.1f and figure 3.3.2). The presence of two phases effectively influences for the

enhancement of upconversion efficiency which has been discussed in the subsequent sections.

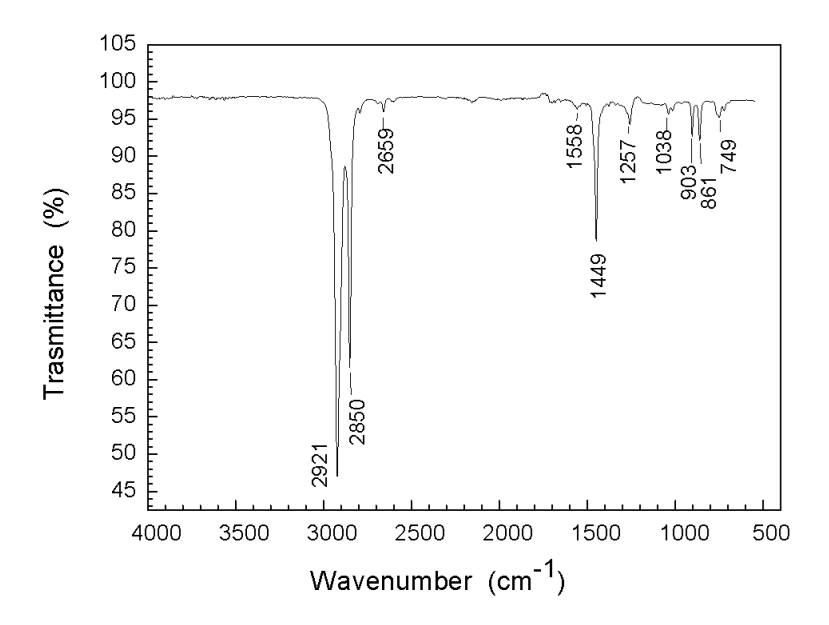


Figure 3.3.10: FTIR spectrum of UCN-Ds confirming the presence of different groups in oleic acid and formation of UCNPs

PL of the UCN-Ds has also been studied. From PL study (figure 3.3.11), a visible-visible upconversion emission band is observed. The excitation wavelength source was used with  $\lambda$ = 450nm and the observed emissions obtained here are in between 400nm-650nm. This is an interesting observation for UCN Ds, which has never been reported even for any type of UCNPs. It can be noted that for all rare earth materials and for UCNPs only NIR to visible upconversion was reported [316],[317].

In another study, NIR-NIR upconversion was also reported previously in literature [150], [274], [311], [318], [319]. However, visible to visible upconversion is a unique phenomenon observed for UCN-Ds, and to the best of our knowledge it has never been reported.

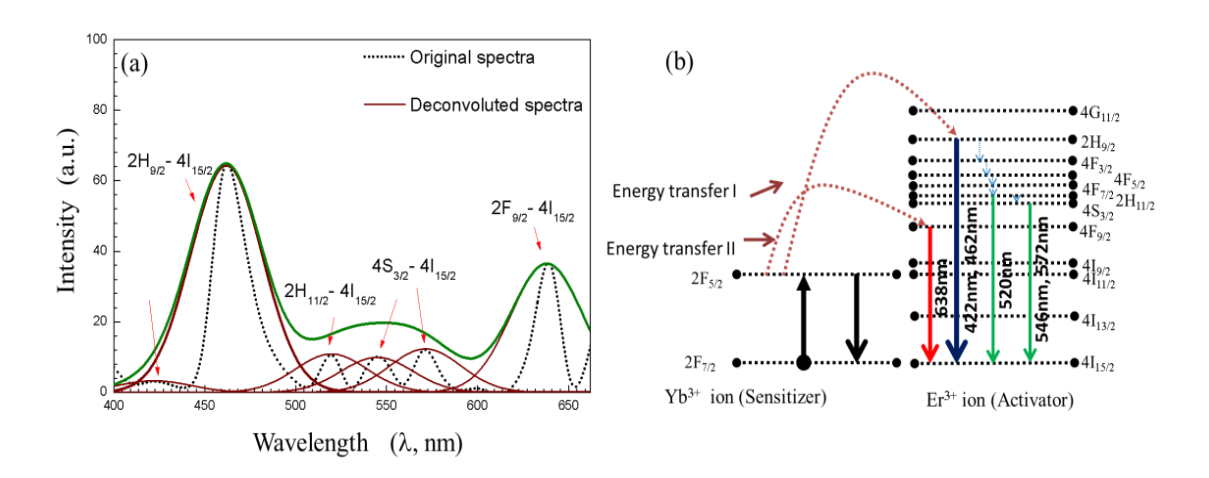


Figure 3.3.11: (a) Photoluminescence (PL) spectra of colloidal UCN-Ds sample obtained with 450 nm excitation wavelength (b) Energy diagram drawn from PL emission spectra in (a)

For UCN-Ds, the observed emission bands with their highest band positions appeared at 422nm, 462nm, 520nm/546nm, 572nm and 638nm correspond to the energy transfers as,  $2H_{9/2}\rightarrow 4I_{15/2}$  and  $2H_{11/2}/4S_{3/2}\rightarrow 4I_{15/2}$  and  $4F_{9/2}\rightarrow 4I_{15/2}$ , respectively. The energy level diagram corresponds to the PL spectra (figure 3.3.11a) is shown in figure 3.3.11b. The band energy diagram includes two incidences of direct energy transfers between two rare earth ions (Yb<sup>3+</sup> and Er<sup>3+</sup>) and passes through several cross relaxations and radiative and non-radiative decays that resulted in a number of emission bands. They are as follows:

Energy transfer-I occurred for  $2F_{5/2} \rightarrow 2H_{9/2}$  transition, energy transfer-II occurs from  $2F_{5/2} \rightarrow 4F_{9/2}$  resulting efficient blue and red emissions with  $2H_{9/2} \rightarrow 4I_{15/2}$  and  $4F_{9/2} \rightarrow 4I_{15/2}$  transitions, respectively. Whereas, the green emissions occurred with four non-radiative relaxations such as,  $2H_{9/2} \rightarrow 4F_{3/2}$ ,  $4F_{3/2} \rightarrow 4F_{5/2}$ ,  $4F_{5/2} \rightarrow 4F_{7/2}$ ,  $4F_{7/2} \rightarrow 2H_{11/2}$  or  $4S_{3/2}$  from  $2H_{9/2}$  level with  $2H_{11/2}/4S_{3/2} \rightarrow 4I_{15/2}$  transitions (figure 3.3.11b)

## 3.3.3 Study of Upconversion luminescence with Femtosecond (Fs)- laser source with different excitation wavelengths.

Interaction of UCN-Ds with Femtosecond-laser (Fs) results in high energy upconversion emissions under five different excitation wavelengths, such as  $\lambda$ = 940nm, 950nm, 960nm, 970nm and 980nm. Each of the incident pump wavelength has yielded distinct emissions in both UV and visible regions. The emission spectra along with their corresponding energy level diagrams are shown in figure 3.3.12 and figure 3.3.13. In energy diagrams, width of each emission band is adjusted according to the intensity of the band received from the emission spectra.

#### 3.3.3.1 Fs-laser 940 nm incident pump wavelength:

Emissive bands are observed between 239nm-397nm in UV/violet region; 474nm (blue emission); 544nm (green emission); 604nm, 670nm and 718nm (red emission bands) in visible region (figure 3.3.12a-i). The energy level diagram with respect to the observed emission wavelengths has been drawn and shown in figure 3.3.12a-ii which states three direct energy transfers from sensitizer (2F<sub>5/2</sub>) to activator ion (4F<sub>7/2</sub> and 4F<sub>9/2</sub>) and thereafter it passes through the different transitions within electronic states of Er<sup>3+</sup> ion. Three major energy transfer occurred and can be represented as, i)  $2F_{5/2}(Yb^{3+}) \rightarrow 4F_{7/2}(Er^{3+})$ ; ii)  $2F_{5/2}(Yb^{3+}) \rightarrow 4F_{9/2}(Er^{3+})$  and iii)  $2F_{5/2}(Yb^{3+}) \rightarrow 4G_{11/2}(Er^{3+})$ , with a total of three non-radiative relaxations such as,  $4G_{11/2}(Er^{3+}) \rightarrow 2H_{9/2}(Er^{3+})$ ,  $4F_{7/2}(Er^{3+}) \rightarrow 2H_{11/2}(Er^{3+})$ ,  $2H_{11/2}(Er^{3+}) \rightarrow 4S_{3/2}(Er^{3+})$ , respectively.

#### 3.3.3.2 Fs-laser 950 nm incident pump wavelength:

During the interaction of UCN-Ds and Fs-laser 950 nm excitation source, emissive bands are obtained in between 265nm- 432nm of UV/violet regions; 455nm (blue

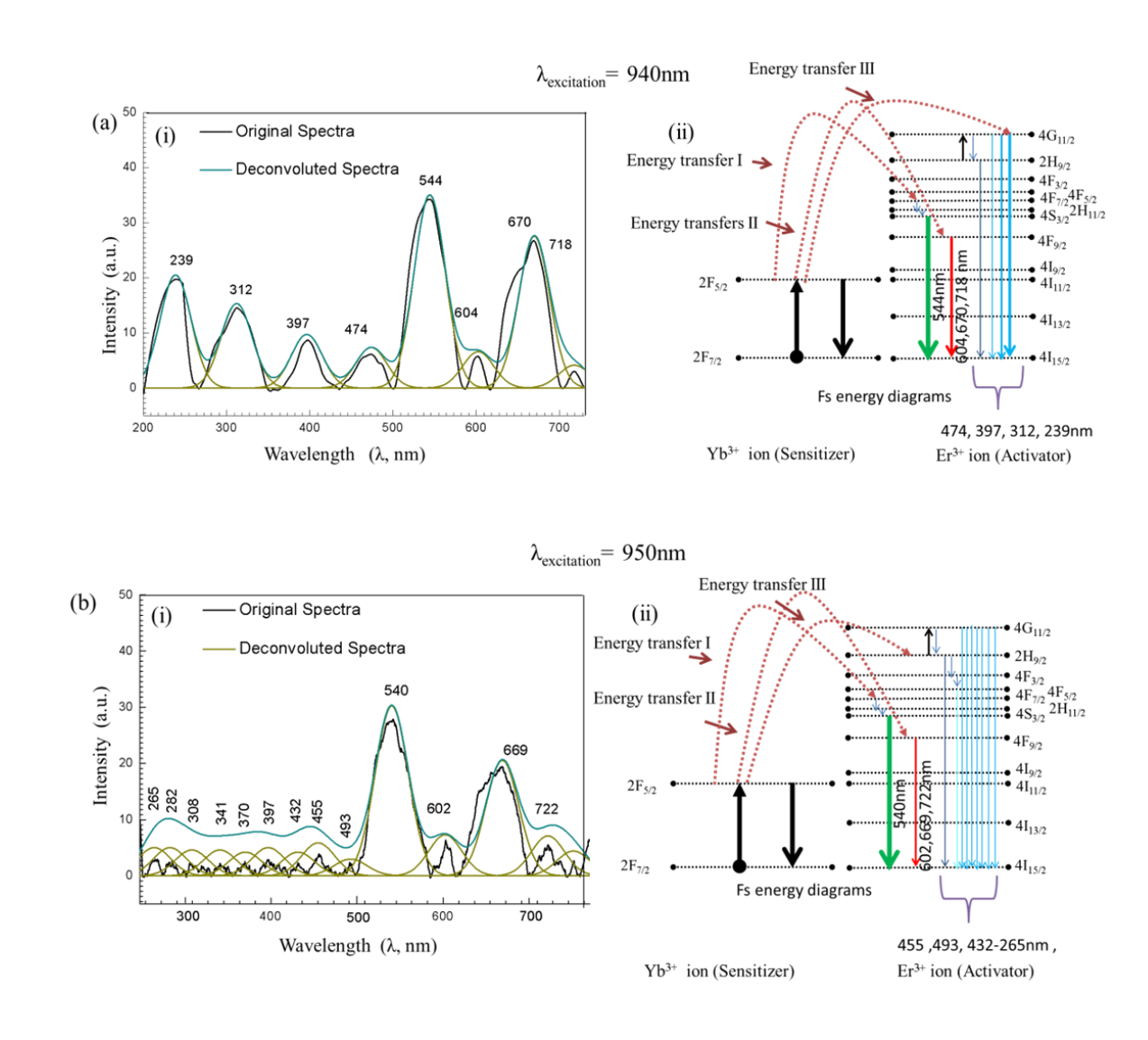


Figure 3.3.12: Upconversion luminescence spectra and their corresponding energy diagram with femtosecond (Fs) arrangement. (a) Spectra(i) and energy level diagram(ii) under 940nm; (b) spectra (i) and energy level diagram(ii) under 950nm; excitation wavelengths

emission); 493nm (intermediate region); 540nm (green emission); 602nm, 669nm and 722nm (red emissions) in visible regions (figure 3.3.12b-i). Intensities of bands in lower wavelengths (265nm-493nm) appeared to be weak compared to the green and red emissions but definitely with few numbers. The energy level diagram is shown in

figure 3.3.12b-ii three direct energy transfers and following energy transitions, i)  $2F_{5/2}(Yb^{3+}) \rightarrow 4F_{7/2}(Er^{3+})$ ; ii)  $2F_{5/2}(Yb^{3+}) \rightarrow 4F_{9/2}(Er^{3+})$  and iii)  $2F_{5/2}(Yb^{3+}) \rightarrow 2H_{9/2}(Er^{3+})$ , with a total of five non-radiative relaxations,  $4G_{11/2}(Er^{3+}) \rightarrow 2H_{9/2}(Er^{3+})$ ,  $2H_{9/2}(Er^{3+}) \rightarrow 4F_{3/2}(Er^{3+})$ ,  $4F_{3/2}(Er^{3+}) \rightarrow 4F_{5/2}(Er^{3+})$ ,  $4F_{7/2}(Er^{3+}) \rightarrow 2H_{11/2}(Er^{3+})$ ,  $2H_{11/2}(Er^{3+}) \rightarrow 4S_{3/2}(Er^{3+})$ .

#### 3.3.3.3 Fs-laser 960 nm incident pump wavelength:

Once UCN-Ds was interacted with Fs-laser (960 nm), emissive bands obtained between 282nm-400nm in UV/violet region; 465nm (blue emission); 545nm (green emission); 604nm, 669nmand 721nm (red emissions) in visible regions (figure 3.3.13a-i). Intensities of bands in lower wavelengths (282nm-465nm) are appeared to be weak compared to the green and red emissions. Green and red emissions obtained in the same intensity.

The corresponding energy level diagram is shown in figure 3.3.13a-ii with three direct energy transfers, such as i)  $2F_{5/2}(Yb^{3+}) \rightarrow 4F_{7/2}(Er^{3+})$ ; ii)  $2F_{5/2}(Yb^{3+}) \rightarrow 4F_{9/2}(Er^{3+})$  and iii)  $2F_{5/2}(Yb^{3+}) \rightarrow 2H_{9/2}(Er^{3+})$ , similar to 950nm, differing only with number of non-radiative relaxations following the energy transfer path,  $4G_{11/2}(Er^{3+}) \rightarrow 2H_{9/2}(Er^{3+})$ ,  $4F_{7/2}(Er^{3+}) \rightarrow 2H_{11/2}(Er^{3+})$ , and  $2H_{11/2}(Er^{3+}) \rightarrow 4S_{3/2}(Er^{3+})$ .

#### 3.3.3.4 Fs-laser 970 nm incident pump wavelength:

UCN-Ds were also interacted with Fs-laser with 970 nm irradiation and emissive bands obtained in between 241nm-447nm in UV/violet regions; 463nm (blue emission); 490nm (intermediate region); 540nm (green emission); 602nm, 655nm and 721nm (red emissions) in visible regions (figure 3.3.13b-i). Emission bands appeared in lower wavelengths (241nm-490nm) are quite strong in intensity; even one high intensity band is appeared with 241nm peak position in UV region. These emission bands can be explained with separate energy band diagram in figure 3.3.13b-ii. Emission occurred due to three direct energy transfers

between the different energy levels, such as i)  $2F_{5/2}(Yb^{3+}) \rightarrow 4F_{7/2}(Er^{3+})$ ; ii)  $2F_{5/2}(Yb^{3+}) \rightarrow 4F_{9/2}(Er^{3+})$  and iii)  $2F_{5/2}(Yb^{3+}) \rightarrow 4G_{11/2}(Er^{3+})$ , including five non-radiative relaxations,  $4G_{11/2}(Er^{3+}) \rightarrow 2H_{9/2}(Er^{3+})$ ,  $2H_{9/2}(Er^{3+}) \rightarrow 4F_{3/2}(Er^{3+})$ ,  $4F_{3/2}(Er^{3+}) \rightarrow 4F_{5/2}(Er^{3+})$ ,  $4F_{7/2}(Er^{3+}) \rightarrow 2H_{11/2}(Er^{3+})$  and  $2H_{11/2}(Er^{3+}) \rightarrow 4S_{3/2}(Er^{3+})$ .

#### 3.3.3.5 Fs-laser 980 nm incident pump wavelength:

Finally, to compare the upconversion of UCN-Ds obtained after interaction with CW-980 nm NIR, the same sample interacted with the Fs-laser with  $\lambda = 980$  nm. Once interacted with Fs-laser the upconversion emissive bands are observed between 243nm-402nm (in UV/violet regions); 473nm (blue emission); 541nm (green emission); 603nm, 660nm and 719nm (red emissions) in visible regions (figure 3.3.13c-i). A very high intensity band is observed in UV region compared to others. The energy level diagram is shown in figure 3.3.13c-ii with three direct energy transfers such as, i)  $2F_{5/2}(Yb^{3+}) \rightarrow 4F_{7/2}(Er^{3+})$ ; ii)  $2F_{5/2}(Yb^{3+}) \rightarrow 4F_{9/2}(Er^{3+})$  and iii)  $2F_{5/2}(Yb^{3+}) \rightarrow 4G_{11/2}(Er^{3+}),$ with three non-radiative relaxations, (i)  $4G_{11/2}(Er^{3+}) \rightarrow 2H_{9/2}(Er^{3+}),$  (ii)  $4F_{7/2}(Er^{3+}) \rightarrow 2H_{11/2}(Er^{3+})$ and (iii)  $2H_{11/2}(Er^{3+}) \rightarrow 4S_{3/2}(Er^{3+})$ . Thus, five emission spectra in figures 3.3.12 and 3.3.13 revealed the high-energy emissions under different excitation wavelengths, which never been observed for CW-NIR laser (980 nm). Among five of them, the highest UV emission (UV<sub>full</sub>) was found under 980nm excitation wavelength. Apart from that, the other emissions green (G)/red(R) are also significant and appear with highest intensity in case of 980nm excitation wavelength. Blue emissions are also observed in each of the cases.

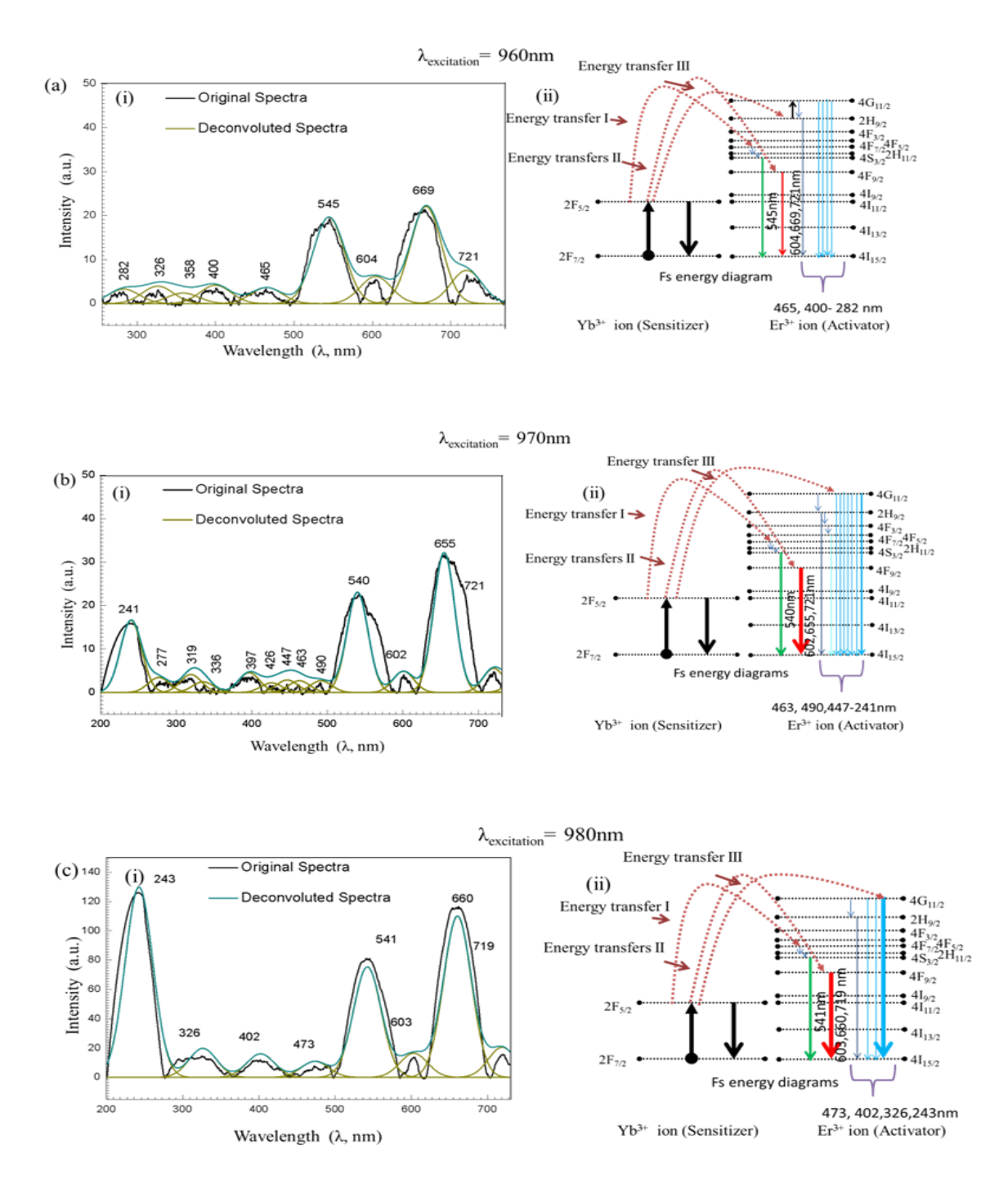


Figure 3.3.13: Upconversion luminescence spectra and their corresponding energy diagram with femtosecond (Fs) arrangement. (a) spectra(i) and energy band diagram(ii) under 960nm; (b) spectra(i) and energy level diagram(ii) under 970nm; (c) spectra(i) and diagram(ii) under 980nm excitation wavelengths

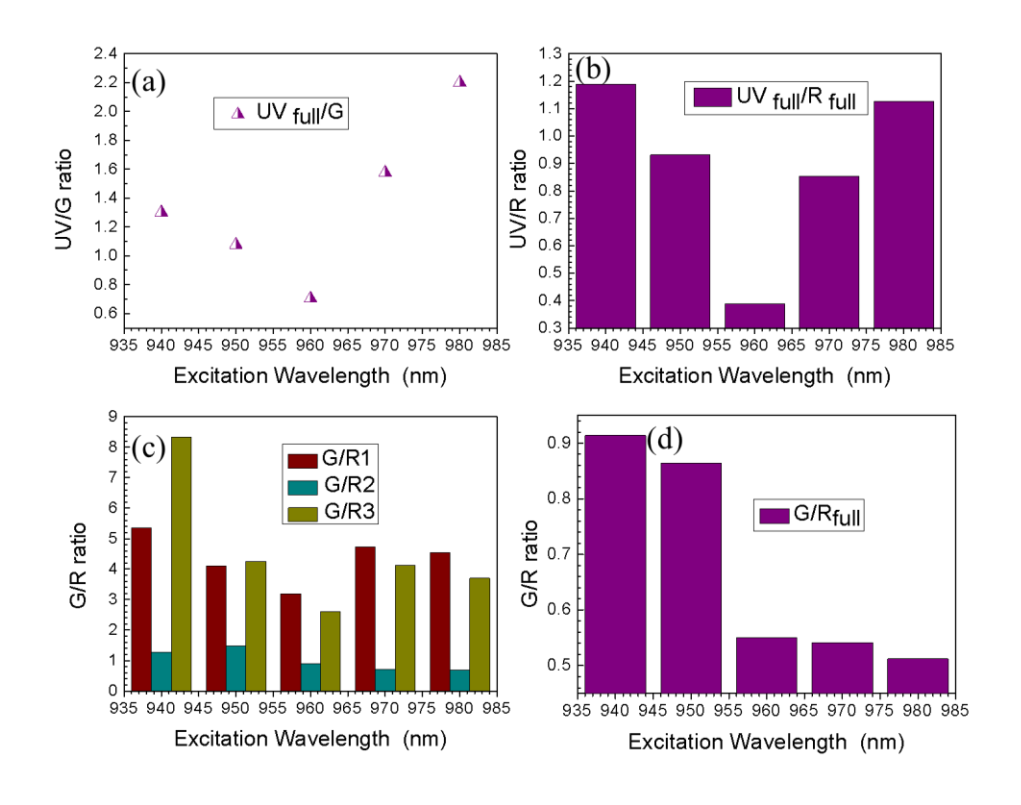


Figure 3.3.14: Shows the ratio plots for the intensity of different emission: (a)  $UV_{full}/G$ , (b)  $UV_{full}/R$  full; (c) G/R1, G/R2, G/R3; (d)  $G/R_{full}$  vs excitation wavelengths

Furthermore, intensity ratios between UV, R and G under Fs-laser treatment were calculated for five different excitation wavelengths and are shown in figure 3.3.14. Intensity changes for different emissions (UV, G and R) under different excitation wavelengths (940nm, 950nm, 960nm, 970nm and 980nm) resulted in different relative ratio plots UV<sub>full</sub>/G; UV<sub>full</sub>/R<sub>full</sub>; G/R1, G/R2, G/R3; and G/R<sub>full</sub> shown in figure 3.3.14a, figure 3.3.14b, figure 3.3.14c, and figure 3.3.14d, respectively. Different in efficient population of photons in different energy levels under 940nm-980nm excitation sources could be the possible reasons for the occurrence of different intensity.

The experimental set-up of Fs-laser has provided in figure 3.3.15.

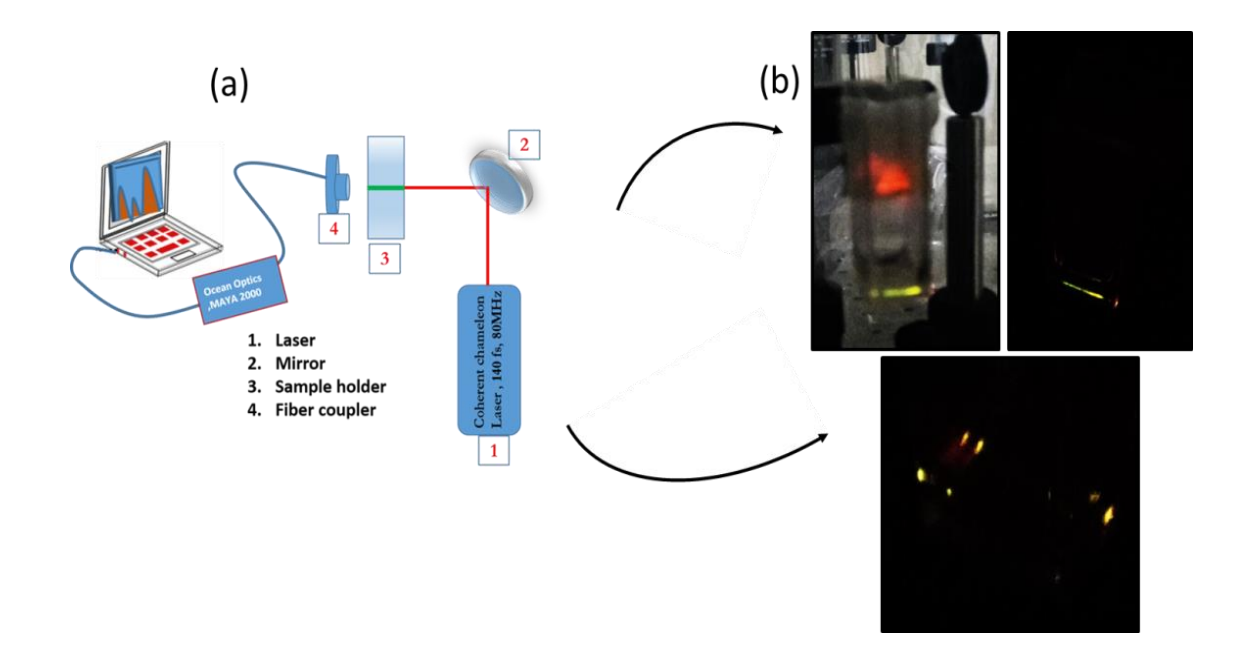


Figure 3.3.15: (a) Schematic of Femtosecond laser (Fs)set-up arrangement (b) Images are captured while visible emissions are observed in cuvette-sample once it is excited with Fs-laser sources

#### 3.3.4 Discussion:

It can be noted that upconversion luminescence properties with Fs-laser irradiation for different rare earth elements along with their applications were reported elsewhere [90], [320]–[327]. Such as YVO4 single crystal upconversion luminescence was observed under infrared (IR) Fs-irradiation which resulted in broad characteristic emission in visible region (350nm-600nm) [320]. For, Ce<sup>+3</sup> doped YAP crystal, upconversion luminescence appeared in both ultraviolet and visible region under a focused 800nm Fs-laser irradiation [321]. Visible emission bands were also found with NaYF<sub>4</sub>–glass ceramic doped with Er<sup>3+</sup> ions under 800nm CW laser treatment [322].

Intracellular imaging of cancer cells (such as HeLa cells, cervical cancer cells, collected on 8 Feb, 1951 from Henrietta Lacks), by using the Fs-pulse laser (100Fs, 920nm) was performed with very high resolution using non-functionalized NaYF<sub>4</sub>:Er<sup>3+</sup>,Yb<sup>3+</sup>.[323] Further, red and green upconversion luminescence was reported with 5% Er<sup>3+</sup> doped NaYF<sub>4</sub> nanocrystals with using two Fs-laser (excitation wavelengths 800nm, 1490nm) simultaneously.[325] Tunable enhanced ultraviolet luminescence can be developed by using UCNPs for recording highly effective and rapid in situ-real time biocompatible photoactivation [324]. Optogenetic proteins have huge applications in neurology and brain science along with cell biology. However, it was found that the narrow excitation wavelength limits the applications of optogenetics which has recently manipulated and improved using tunable Fs-laser system [328]. Moreover, for ultra-deep in-vivo bio-imaging non-linear optical effects using Fs-laser excitation in AIEgen nanocrystals was found effective [329]. By a group of researchers, it is reported that Ti:Sapphire Fs-laser, with pulse duration of about 160 Fs, is very useful for generation of high harmonic as example fifth harmonic generation from photonic crystal and is useful in designing opto-electronic devices with effectively high efficiency [327]. Further, it can be noted that for the rare-earth doped luminescent nanomaterials, colour tuning is having important significance for several applications such as designing of display device, bio-labelling, optoelectronic device etc. The tuned luminescence properties can be developed from Er<sup>3+</sup> doped glass ceramic using 800 nm Fs-laser excitation sources [330]. Thus, the present findings i.e., the development of UCN-Ds and their improved luminescence properties in UV and visible ranges are very interesting and can be used in device making for industrial (optoelectronics) to biomedical such as for disease diagnosis and therapeutic applications by targeting the infected cells with enhanced efficiency.

#### 3.3.5 Summary and Conclusions of PART III:

Dendritic polymers are known for decades, however, dendritic upconveting nanoparticles are never been reported. In this work, dendritic NaYF4 nanoparticles (UCN-Ds) with lanthanides (Yb<sup>+3</sup>, Er<sup>+3</sup>) have been synthesized for the first time with one pot chemical synthesis approach, by controlling the reaction temperature in in-situ condition, without adding any external dendritic polymers during synthesis process. UCN-Ds contain both of the  $\alpha$ - and  $\beta$ -phase within its solid structure and are very stable. Presence of these two phases in dendritic UCNPs could be the cause of high energy upconversion and make them very seminal and are with caterpillar/necklace type of structure.

This self-assembled structural dendritic-network may be allowed for designing 2D nanostructures with defining clear geometry.

Apart from that, the bright blue emission make them very attractive with lower excitation wavelength source with visible to visible upconversion [297], [331]. With higher wavelength source with Fs-laser, UV emission becomes prominent making them a suitable candidate for industrial and biomedical applications [332], [333], [334]. The different emissions (green/red /blue/cyan/UV) could be useful in colour tuning and magnetic sorting [335], [336] by changing their excitation wavelengths.

### **Chapter 3 RESULT AND DISCUSSION**

## **PART-IV**

3.4 (Part-IV): Morphologically controlled upconverting self-assembled superlattices (SAM-SL UCNPs) prepared by one-pot chemical approach: Efficient luminescence observed under different pump powers

Outcome: Manuscript is under preparation

#### 3.4.1 Introduction:

Since the very early age, the design of aligned, self-assembled nanoparticles is having great importance for its uses in various fields including electronic device fabrication to the biomedical applications [1]. Self-assembled materials are available in nature. However, it can also be designed artificially by changing the different interactions between the nanoparticles and through varying the kinetic or the thermodynamic parameters in-situ. Biomaterials possess intrinsic behaviour and comprise selfassembled structures similar to the naturally occurring ones [2]. However, selfassembled structure formation induced by several factors and the mechanism of the formation fundamentally needs to be understood essentially to fine tune its properties [3]–[5]. Nanoparticle superlattice is one of the well-defined self-assembly of highly ordered nanoparticles and is different from material of its bulk phase crystal, isolated nanocrystal and even disordered nanocrystal assemblies, which exhibits different enhanced properties e.g., conductivity, mechanical properties, optical properties, plasmonic properties, etc. depending on its order of packing/arrangement compared to its bulk[6]-[10]. Nanoparticle superlattice can be constituted through the bottom-up self-assembly approach where the process either can be in equilibrium or in a nonequilibrium state. Usually, to achieve the high-quality order of nanoparticles in superlattices, the process involves soft ligands or capping agents which further help to tune/programme the artificial structure and its properties through functionalizing the nanoparticles and by changing the particle-particles binding interactions. These soft ligands further specially control the nearest-neighbour spacing, lattice structure and superlattice properties [6]. Thus, the collective interactions between organized superlattice nanoparticles in both of two dimension (2D) as well as three-dimension (3D) make them effective for usage in electronic and optical devices[11]–[20]. It can be noted that the formation of superlattices in large nanoscale area with synthesizing vastly the monodisperse nanoparticles is critical.

In 1994, Janos Fendler was first introduced the concept of superlatice of nanoparticles [21], [22] and constitute CdS nanoparticle (dia~ 26.5 Å to 34.0 Å) superlattice [21] which was prepared at the air-water interface in a Langmuir film balance and observed the change in fluorescent properties. In the same year using the similar method, at air-water interface in a Langmuir film balance they constitute superlattice of Ag nanoparticle (dia.~100 Å) (multilayer) and observed the change in the optical and eletrooptical properties [22]. In subsequent year 3D quantum dots (QDs) (CdSe, 20Å) superlattice structure (5µm to 50 µm) was made by Murray et al. where the spacing between the dots were controlled within near atomic scale precision [23]. They observed the discreet and size dependent optical absorption and band edge emission due to the quantized electronic transition of the individual QDs. Comparison to the optical properties between colloidal QDs and closed packed superlattice structure, the band spectra were identical, however, the shape of the emission spectra of the QDs in the superlattice was reformed and red-shifting due to the inter-dots coupling was observed [23]. Superlattices of cobalt nanocrystal prepared from solution phase dispersion of Co nanoparticle in octane with oleic acid capping agent with nanocrystal spacing of ~ 4 nm were prepared which exhibited spin-dependent electron tunnelling [24]. In the similar line, nanoparticle superlattice alter the materials properties from its bulk, such as insulator-to-metal transition[25], leads to the enhancement of p-type conductivity (e.g., PbTe/Ag2Te) [8], high order vibrational coherency (e.g, FCC Ag NPs, plasmonic properties [7] etc. with retaining their basic crystal structure [6].

In this chapter, the synthesis of upconversion nanoparticles-superlattices (UCN-SL) in many defined and order structures are reported. Self-assembled UCN-SL are prepared herein by one pot chemical synthesis approach and their upconversion and fluorescent properties have been studied through continuous wave laser (CW-Laser) as well as with femtosecond laser (fs) irradiation.

It can be noted that, a huge number of potential applications of UCNPs make them significant in research due to their unique fluorescence and luminescence properties[26]–[30]. For the first time this work reports on the controlled synthesis for achieving shape and size directed UCN-SL having efficient fluorescence and luminescence properties under continuous wavelength (CW)source as well as femtosecond-laser (fs) source.

Further upconversion emissions at ultraviolet and visible emissions have been investigated. The synthesis procedure applied here to form UCN-SL is a modified approach of the synthesis method developed by our group previously. The entire reaction process was carried out in an inert gas (Argon) atmosphere. The different selfassembly superlattice structure have been formed in in-situ with varying the condition. Usually researchers design this type of assembled structure in at-least 2<sup>nd</sup> stage of the whole synthesis procedure [1], [3]–[5]. However, we are able to prepare such assembled structure in one-pot chemical synthesis approach. The beauty of the process is that the entire synthesis process consumes less time to obtain the self-assembled UCN-SL structures. Further, how the UCN-SL with different architecture exhibited different upconversion luminescence properties also have been elucidated. synthesized UCN-SL structures represented here not only generate new physical properties from bulk materials but also new phenomenon for interactions between particles at nanoscale have been found out. In order to produce the particular selfassembled UCN-SL pattern in synthesized nano- material we followed few controlled reaction parameters. By applying those key factors, the correlative arrangements of nanocrystal building blocks with their sizes and the spacing between those crystals are maintained in a self-assembled long-range order. The precisely engineered nanocrystal sizes and systematic shaped assembly are treated as building blocks to generate improved ones. Additionally, for the different UCN-SLs the different in intensity of emission and their position and shifting, internal upconversion quantum yield (Internal UCQY) and external upconversion quantum yield (External UCQY), photoluminescence behaviour, fs-laser power dependent luminescence and the number of absorbed photons taken part in the process (n, where 'n' is the number of absorbed NIR photons per emission under fs-laser excitation power) has been calculated. The controlled morphology with efficient upconversion fluorescence and luminescence of these UCN-SL structures may discover considerable applications in different fields such as lasers[31], [32], diodes[33], [34], display-techniques and energy -related applications[30], [35]–[42].

#### 3.4.2 Results and Discussion:

As-synthesized ordered self-assembled UCN-SL those nanocrystal-building blocks are obtained according to the method as discussed in the experimental section. The colloidal chemistry plays an important role to self-organize the UCNPs in super lattice array within its colloidal solution. Formations of nanoclusters also occurred in some places on the sample-grid on which the clusters are made-of few individual particles which are isolated from each other in a specific way so as to develop the periodic and parallel array. The stability of the synthesized super lattice colloidal solution proves the presence of some interaction between the particles themselves. As the nanoparticles are covered with ligands-Oleic acid, they are dispersed transparently in solvent (cyclohexane). For superlattice of nanomaterial, it is the structure of surface and crystal on which their chemical and physical properties depend.

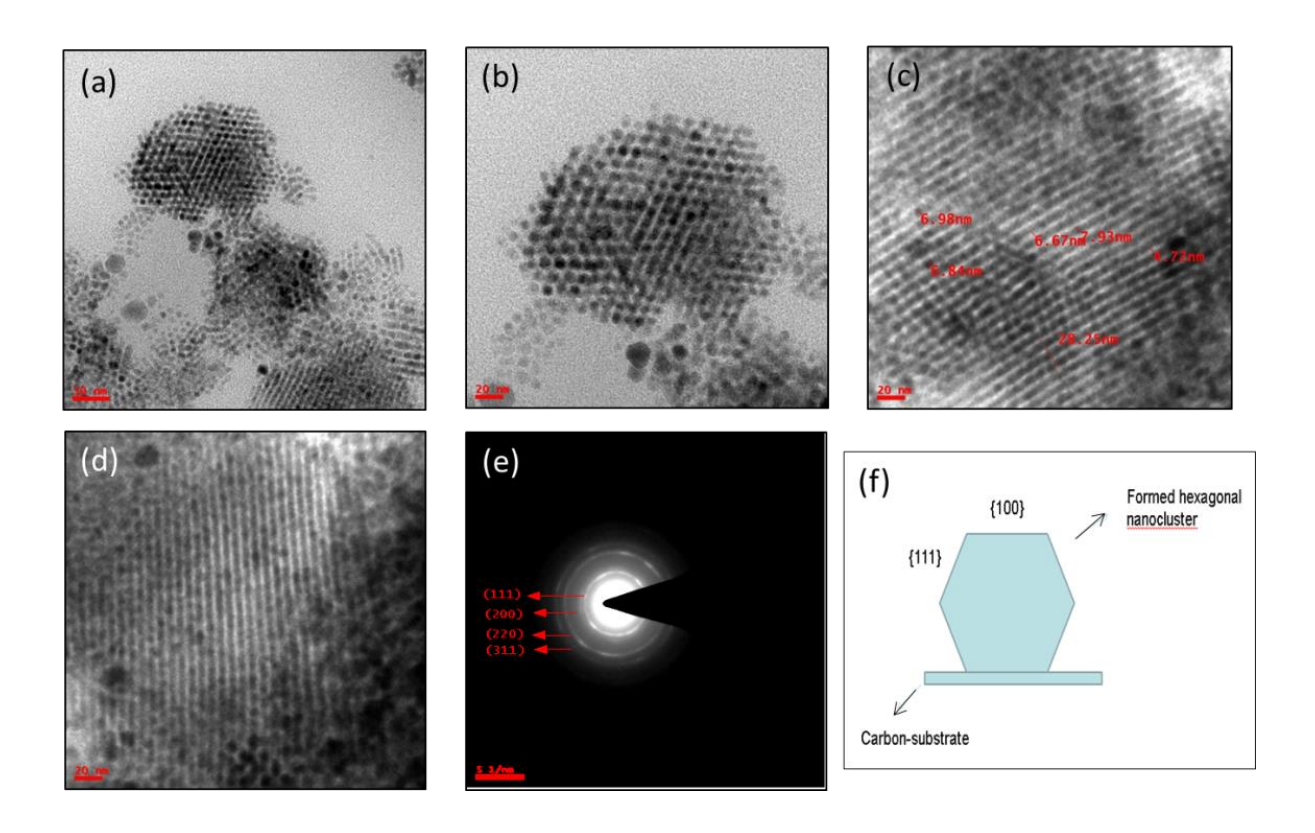


Figure 3.4.1: TEM images of self-assembled formations of UCNPs with 15-20 mins high reaction temperature, panel (a) - 50nm scale bar, panel (b-d) - 20nm scale bar, panel (e)-SAED pattern. (b) - formation of {100} and {111} facets on substrate, (c,d) - formations of UCN-nanochips, (a) show planar defect-twinning effect, panel (f) The cross section of a formed nanocluster on substrate

TEM micrographs (figures 3.4.1-3.4.3) revealed the structures of those size and shape controlled self-assembled nanocrystals. TEM images for different UCN-SL colloidal samples are exhibiting the morphology of self-organized and periodic nature of synthesised materials.

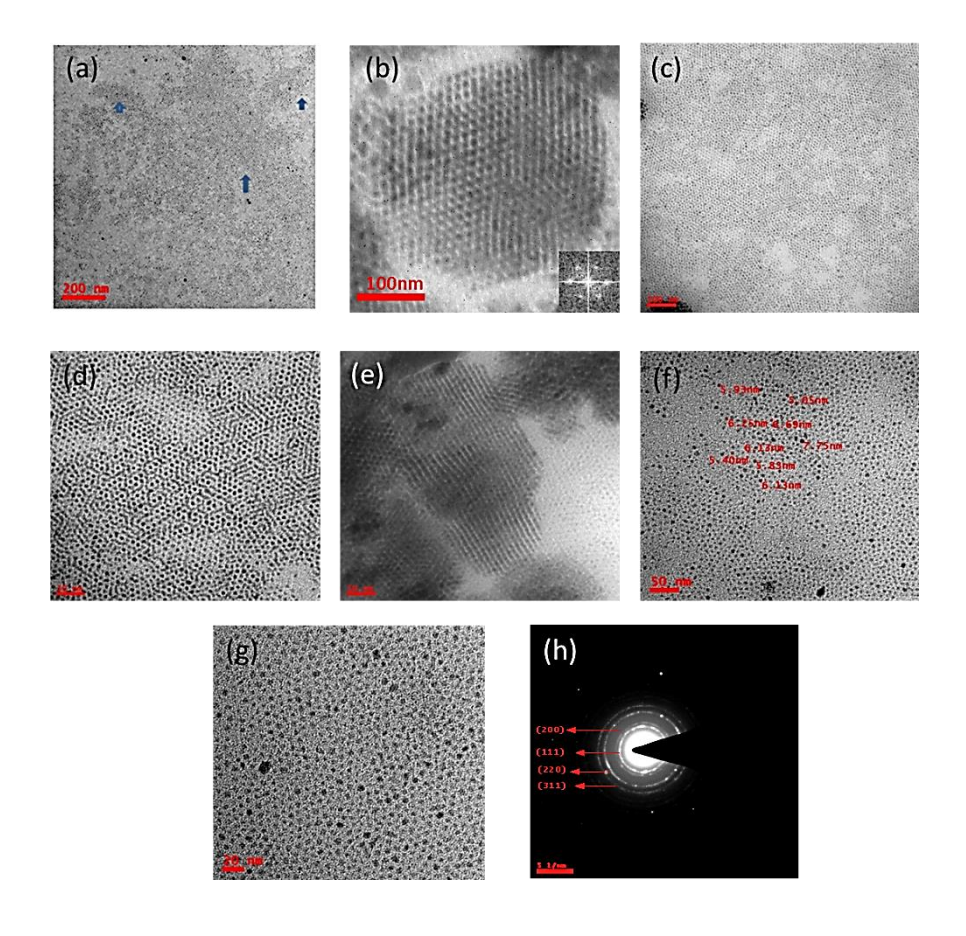


Figure 3.4.2: TEM images of self-assembled formations of UCNPs with 51 mins of high reaction temperature, panel a- 200nm, panel b, c - 100nm, panel d-f- 50nm panel g-20nm, panel h- SAED pattern. (a), (c), (f), (g)- Formation of monodisperse nanoparticles, (a)- Short range particle-packing order, (b) - conversion of an FFT image derived from a hexagonal cluster orientation where the synthesized nanocrystals are oriented along [100], [111] (c)-planar defect with twinning effect, (d)Hexagon arrangement and (e)rod-like parallel assembly of synthesized UCNPs.

In self-assembled superlattices, the shape and size-controlled nanoparticles act like molecules which can be considered as building blocks to construct 2D and 3D self-assembled superlattice-clusters.

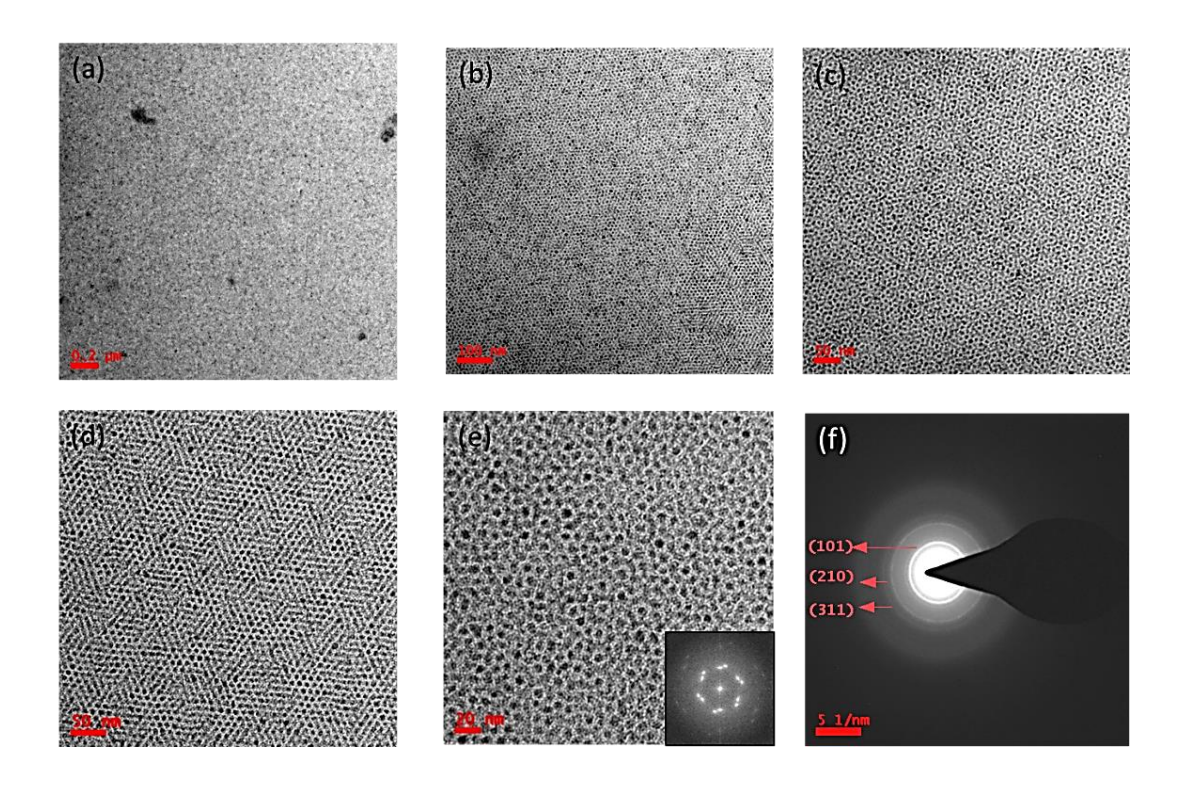


Figure 3.4.3: panel (a) -200nm, panel (b)- 100nm, panel (c,d) – 50nm, panel(e)- 20nm, panel (f)- SAED pattern, (c,d,e) - clear 3D assembly with a complete hexagon-type formations

With the size uniformity and orientational order of particles in SL-structures the crystallography arrays have also been clearly identified. The long chains of organic capping agent (oleic acid) contributed as both as protectors as well as interparticle—bonding between two particles. The TEM studies reveal the formations of three different type of SL-structures obtained from differently prepared samples. Hence, the evaporation-rate of carrier solvent was also responsible to organize different-kinds of self-assembled superlattice structures.

The self-assembled superlattice formations (SAM-SL) of synthesized UCNPs prepared with different reaction conditions have been shown in figures 3.4.1, 3.4.2 and 3.4.3.

In figure 3.4.1, formations of SAM-SL UCNPs is shown with lowest reaction time (15-20 mins). For figure 3.4.2, high reaction temperature (300°C) was maintained for almost 51 mins. In figure 3.4.3, SAM-SL UCNPs were formed after 1 hr, 50 mins of high reaction temperature.

For the first experimental set-up (exset-1; maintained 15-20 mins of high reaction temperature (300°C)), TEM images (figure 3.4.1) revealed the formation of self-assembled structures having [100] and [111] orientation of the organized superlattices. Throughout the sample a number of discrete nanoclusters have been formed. The shape of each cluster is almost hexagonal which are made-up with particles arranged in regular arrays parallel with each other. On nanocluster-surface the distance between two parallel particle-lines is measured to be 5 nm which is uniform throughout the cluster. Throughout one nano-cluster the particles are monodispersely distributed with uniform sizes. This uniform size of the particles is maintained throughout the sample. In each nanocluster, the average diameter of UCNPs is between 7-8 nm. The orientation of the particles along the surfaces of the hexagonal shaped nano-cluster was confirmed by figure 3.4.1b which suggests the formation of {100} and {111} facets on substrate with having thermodynamically unstable crystal growth. The cross section of such a nanocluster-formation is given in figure 3.4.1f. Figures 3.4.1c and 3.4.1d reveal the formations of UCN-nanochips (as looks like a particular disk shape) where the UCN-particles are situated at lower levels of a disk-layer constructing mostly (111) planes along the surface of a cluster though (100) planes have also been appeared through some regions forming 3D-self-assembly.

For second set of experiment (exset-2; reaction performed for 51 mins at reaction temperature of 300°C), TEM images (figure 3.4.2) revealed very interesting results, as shown at different magnification. During experimental procedure, for a longer time materials were heated compared to the previously formed 3D- assembled nanodisk shaped (check 3D/2D-self-assembled superlattices) and unstable superlattice-arrangements are formed throughout having a different kinds of arrangement such as a monodisperse arrangement occurred (as shown in figures 3.4.2f and 3.4.2g), hexagon arrangement with situating one particle inside (figure 3.4.2d), rod-like cluster arrangement with parallel assembly (figure 3.4.2e). Monodisperse particles occupy most of the places in sample as it seems an extra heat was employed into the clusters and self-assembled structure broken into separate monodisperse particles. Hence some places throughout the sample where their arrangement is a perfect hexagon with uniform particle-sizes viewed with 50 nm magnification (see panel 2d) is traced. This phenomenon is very interesting.

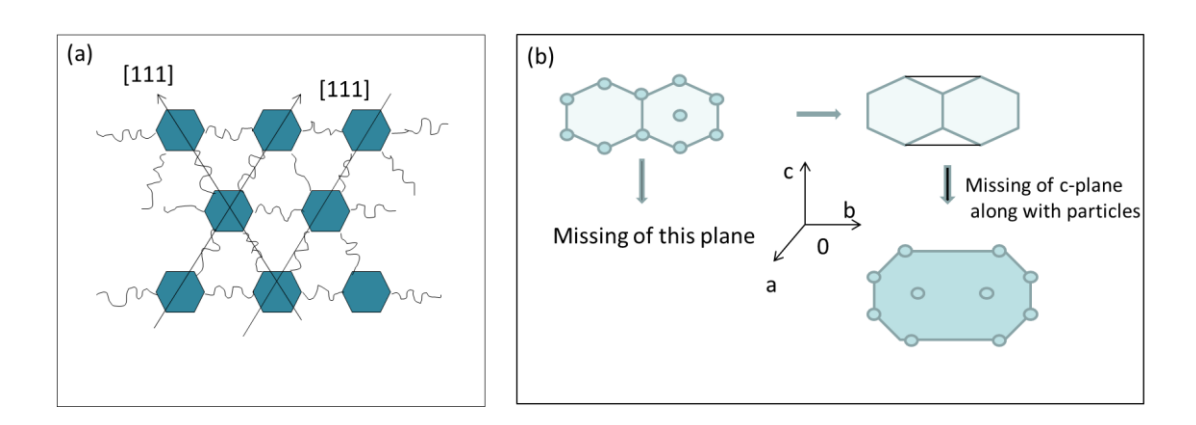


Figure 3.4.4: (a) A bundle of surfactants act as channels between the assembled nanoparticles containing different stretches and vibrations; O-H, C-O, C-C, C-H, CH3; (b) A schematic diagram of planar defects appeared in SAM-SL UCNPs

Thus materials were heated for further longer period of time amount of reaction temperature with corresponding reaction time was not enough to break all such nanoclusters completely into single monodisperse particles but many parts of them were able to overcome the energy barrier and formed discrete single particles. As a result, some portions of the sample are still having cluster-formations, and some are having discrete monodisperse particles.

To analyse and review this interesting part again we increase the reaction time to almost 1hr 50 mins (third experimental set up; exset-3) at 300°C. TEM images for the sample of exset-3 are shown in figure 3.4.3 which a hexagon-shaped arrangement consisting of total of 7 particles, one particle is in middle and surrounded with six similar-sized particles. This type of arrangement was observed throughout the whole substrate are they are in a long-range-order. Further, the TEM images shown in figure 3.4.3 depicts clearly that most of the 2D-superlattices (as shown in figure 3.4.2) have been converted into a 3D-superlattice arrangement (figure 3.4.3). This beautiful 3D arrangement occurred with a number of monodisperse particles. In this arrangement, the average particle sizes varied from 5nm-9nm Thus, from TEM images it is clear that there types of arrangements could be more useful to consider the shape-symmetry of as-synthesized nanocrystals and especially 3D objects with 2D projected image. There is one key parameter for TEM to analyse the packing between the particles; adjustable ratio between particle-size and interparticle distance in the presence of passivated surfactant (here Oleic acid acts as surfactant), whose chain length can be controlled. This key parameter is well controlled in our synthesized material (figure 3.4.4). TEM samples were prepared by placing the droplets of NaYF4:Yb3+; Er3+ superlattice colloidal solution on the grids and then drying properly under ambient temperature (25°C). Though the drying time was different for different sets of three samples, but drying temperature was 25°C. An amount of 8-10 µL of concentrated colloidal solution was taken on TEM grid. Then allowed drying for 20-25 mins. Figure 3.4.2 shows 2D (2-dimensional) monolayer self-assembled superlattice-UCNPs. Particle-packing order is observed in short-range orders as indicated by arrowheads region as it is shown in figure 3.4.2a.

From different views of samples in the prepared grids, the TEM images have been captured for confirming the construction of 3D-SAM-SL-UCNPs models. Figures 3.4.3c and 3.4.3e show the perfect hexagon shaped arrangement with one particle at centre surrounded by six particles and exhibited six-fold symmetry.

From TEM images, for both in 1<sup>st</sup> set (figure 3.4.1) and 2<sup>nd</sup> set (figure 3.4.2), we have traced locations in short-range order arrangements, where planar defects-Twinning effect along with stacking faults have taken place between UCN-particles. In twinning defect, a plane is shared by two subgrains in such a way that one grain can be considered the mirror image of other. Though in our synthesized material this twinning effect is not that strongly observed but still their presence owes to less volume and surface energies of smaller particles introduce such planar defects in the self-assembled UCN-particles.

The other planar defect- Stacking fault has also been observed clearly in figure 3.4.2c by missing the vertical plane (say-plane-c) between two hexagon-shaped nanoparticles. The missing of two or four particles from its regularity is shown in figure 3.4.4b.

In figure 3.4.3, different magnified TEM images have been shown with the formation of completely a new kind of 3D-self-assembly in UCNPs. Figure 3.4.3 confirms the formation of close-packed manolayer having particle-sizes of diameter 6-7nm at different magnifications (scale bar 200nm, 100nm, 50nm, 20nm). Hexagonal-type arrangement has been observed in figures 3.4.3c, 3.4.3d and 3.4.3e, which provide a three-layer assembly. A 3D-assembled SL structure with multilayers is observed in

TEM image (figure 3.4.3d). Following slow evaporation of carrier solvent a 3D-SL (figure 3.4.3d) was obtained with hexagon-type arrangements sharing 12 particles with each other. Thus, figure 3.4.3 indicates that the synthesized nanocrystals are closely packed into superlattice arranged in an almost defect-free 3-D structure. In conclusion, the as-synthesized SAM-SL- UCN nano crystals had tendency to self-assemble into both 2D and 3D owing to their narrow particle-size distribution and uniform particle-sizes.

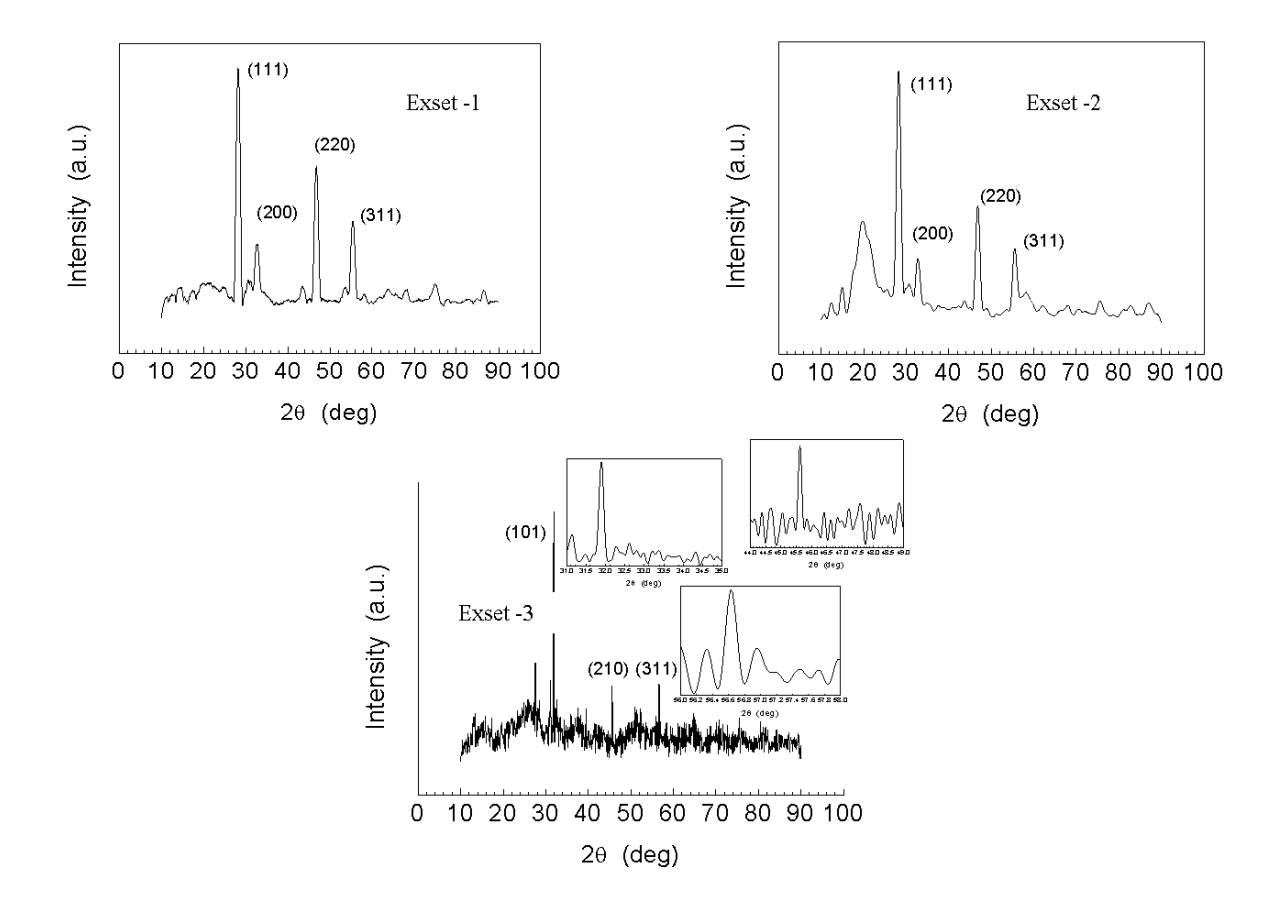


Figure 3.4.5: The XRD pattern for three different Exsets (1,2,3) confirming the appearances of major cubic, mixed crystalline and major hexagonal phases, respectively.

However, TEM analysis for exset-1, exset-2, exset-3 in figure 3.4.1, figure 3.4.2 and figure 3.4.3, respectively, further confirms the formations of complete cubic [(111), (200), (220), (311)] cubic [(111), (200), (220), (311)] and mostly hexagonal phases [(101),(210), (311)],[43]–[47] respectively. The appearances of planes from TEM-SAED pattern for each of the sets are well matched with their resulted diffraction planes received from their corresponding XRD pattern shown in figure 3.4.5. The appearances of those phases have also been confirmed with Raman analysis as discussed in subsequent sections.

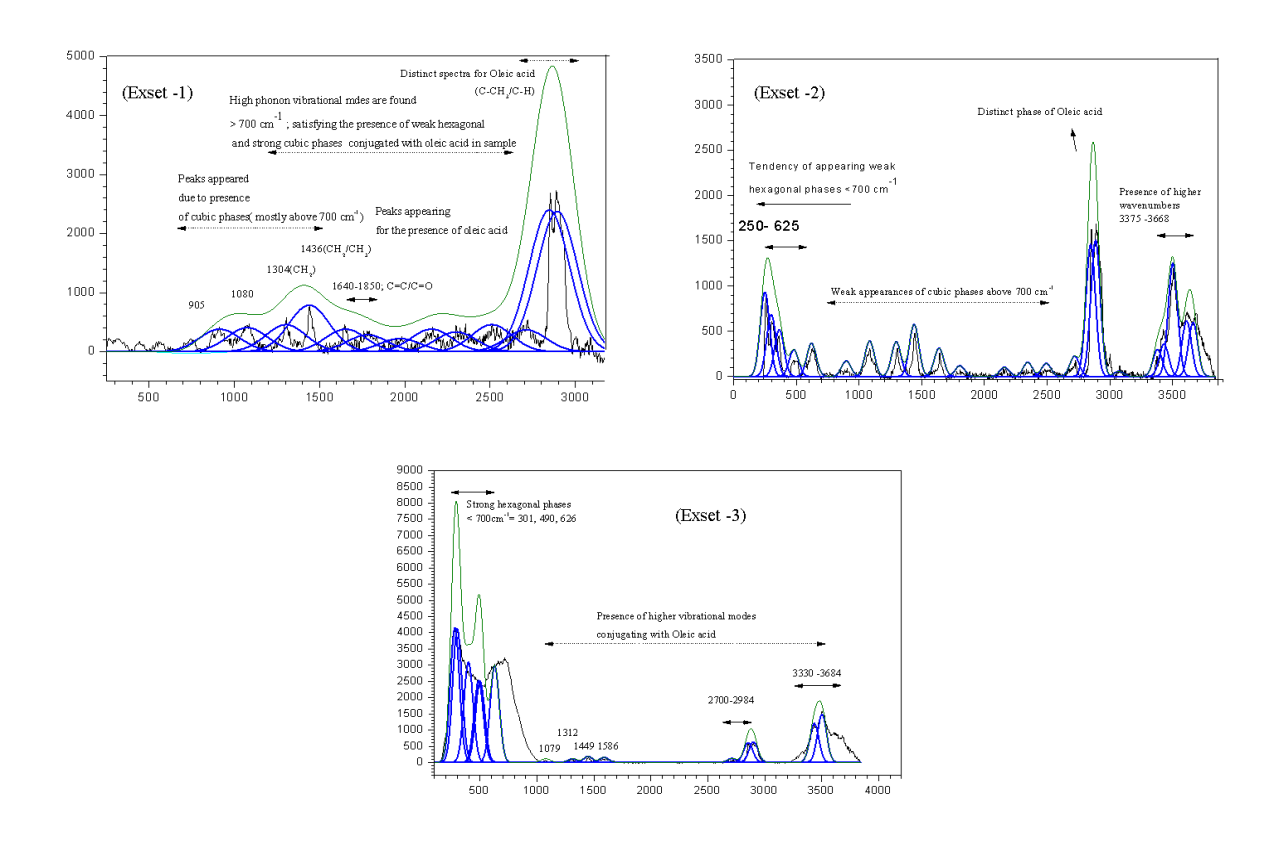


Figure 3.4.6: The Raman analysis strongly indicate the appearances of (a) major cubic (b) cubic and hexagonal (c) major hexagonal phases in exset- 1, 2 and 3 respectively

The Raman spectra of three different synthesized samples are shown in figure 3.4.6 confirming the presence of phases in synthesized samples. For exset-1 sample (figure 3.4.6a), most of the vibrational modes appear beyond 700cm<sup>-1</sup> and confirm the appearance of cubic phases (FCC) conjugated strongly with oleic acid. In sample 2 (figure 3.4.6b), the dominant mode has been appeared near 275 cm<sup>-1</sup> confirming the presence of dominant cubic phases. In exset-3 sample, the presence of hexagonal phases have been confirmed with the appearances of vibrational modes with their maximum positions at 301cm<sup>-1</sup>, 399cm<sup>-1</sup>, 628cm<sup>-1</sup>, 492cm<sup>-1</sup>, 501cm<sup>-1</sup>; though presence of cubic phases with Raman spectrum (figure 3.4.6c) has also been traced with 277cm<sup>-1</sup> and still we can confirm that most of the cubic phases haven transformed into hexagonal phases in this sample 3. The resulted vibrational modes are closely matched with the previous reported results.[48]–[52] Presence of asymmetry CH<sub>3</sub>, C-CH<sub>3</sub>/CH<sub>2</sub> and O-H stretching modes are assigned by 1439 cm<sup>-1</sup>, 2854/2896 cm<sup>-1</sup>, 3333cm<sup>-1</sup> conjugating with oleic acids. Presence of different stretches along with oleic acid has been reported elsewhere [53].

The upconversion fluorescence spectra of three differently synthesized SAM-SL UCNPs are shown in figure 3.4.7a, 3.4.7b and 3.4.7c for exset-1, exset-2, and exset-3, respectively. For exset-1 and exset-3, fluorescence spectra is observed in both of UV and visible wavelength region though intensity of emissions in visible region is much higher than those in UV region. The full range of emission bands are shown in figure 3.4.7a-i and 3.4.7c-ii for exset-1 and exset-3 samples, respectively. The maximum emission band positions are appeared at 267nm, 274nm, 280nm, 287nm, 294nm, 300nm in UV region and at 400nm, 410nm, 420nm 430nm, 439nm, 449nm in visible region under 800nm, 820nm, 840nm, 860nm, 880nm, 900nm of excitation wavelength in NIR range, respectively, for both synthesized samples (exset-1 and exset-3). And interestingly, clear red shifting has been observed in both of the cases with increasing excitation wavelengths.

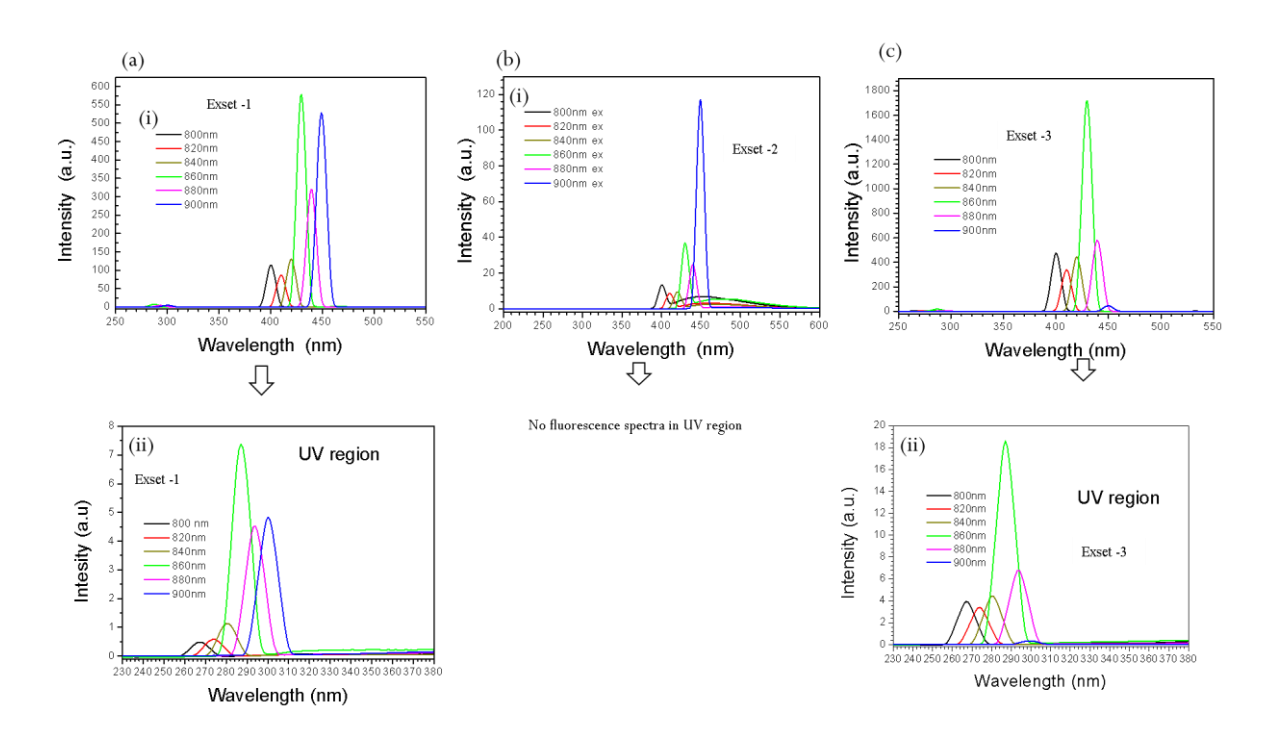


Figure 3.4.7: Fluorescence spectra recorded at room temperature with changing excitation wavelengths from 800nm to 900nm; Fluorescence with (a) exp. Set up 1 (i) Full region (ii) UV region;(b) exp. Set up 2(only full region is shown, no fluorescence occurred in UV region;(c)exp. Set up 3 (i) Full region (ii) UV region

Highest intense emissions band are observed under 860nm (for both in UV and visible) NIR excitation wavelength source. However, for the other synthesized sample (with exset-2) emissions are observed only in visible region with appearing highest intense emissions under 900nm NIR excitation wavelength source and hence the maximum emission band positions are appeared at 401nm, 410nm, 421nm, 430nm, 440nm, 449nm with similar trend of shifting with increasing excitation wavelengths. However the fluorescence intensities of the exset-3 sample is much higher and about 2.9 times for UV region and 2.5 times in visible region compared to the exset-1 sample and about 14.7 times in visible region compared to the exset-2 sample with considering the highest intense band positions in each case. In visible region all of the emission spectra lie in between 400nm -450nm satisfying blue emissions and the other emission bands

lay in the UV region. The corresponding energy band diagram is shown in figure 3.4.8d and follows continuous direct energy transfers from  $Yb^{3+}$  and  $Er^{3+}$  ions. Due to energy transitions  $2F_{7/2}(Yb^{3+})$  -  $2F_{5/2}(Yb^{3+})$  -  $2H_{9/2}$  ( $Er^{3+}$ ) -  $4I_{15/2}(Er^{3+})$  blue emissions occurred and due to the energy transitions  $2F_{7/2}(Yb^{3+})$  -  $2F_{5/2}(Yb^{3+})$  -  $2H_{9/2}$  ( $Er^{3+}$ ) -  $4I_{15/2}(Er^{3+})$ , the less intense UV emissions occurred. The intense visible blue emission from the as-prepared colloidal SAM-SL-UCNPs solutions in quartz - cuvette is shown in figure 3.4.8e.

# Upconversion luminescence with 140-femtosecond laser pulses (80 MHz repetition rate) under 950-990nm NIR excitation sources:

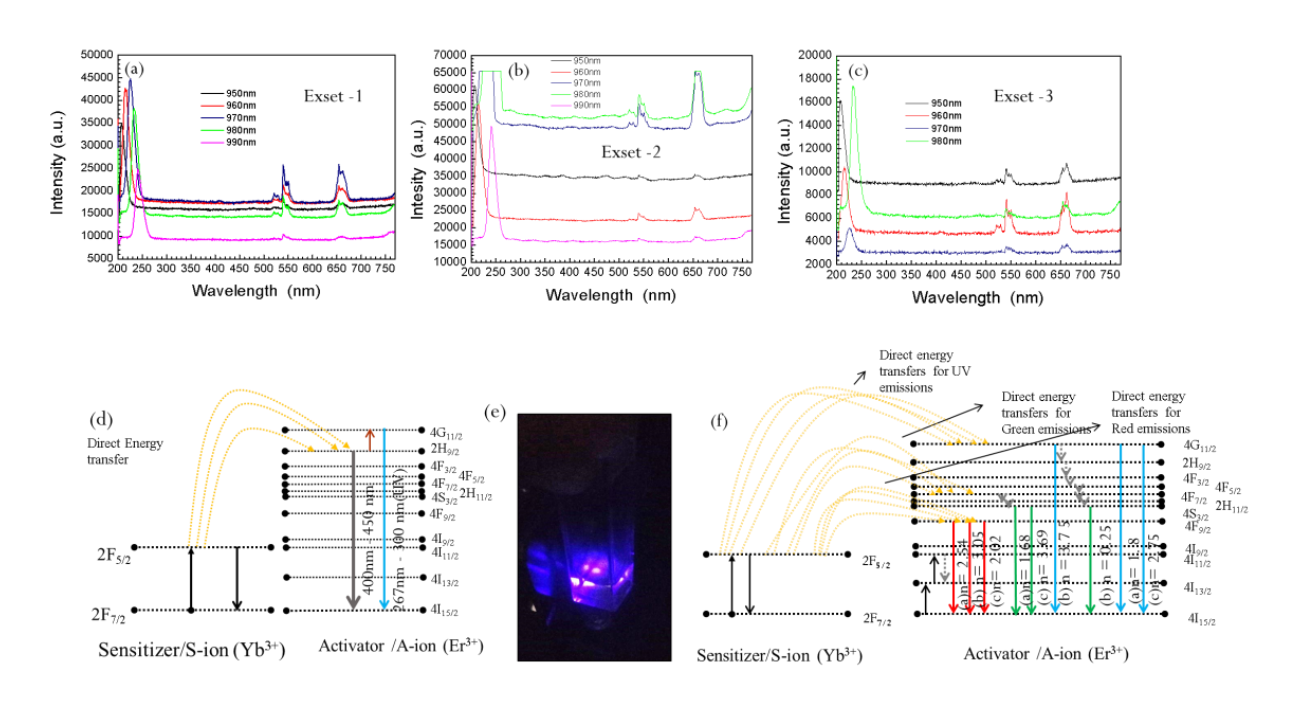


Figure 3.4.8: Fs-laser based upconversion spectra for (a)Exset-1 (b) Exset-2 (c) Exset 3)(d)Energy level diagram of synthesized SAM-SL –UCNPs (e) Intense visible blue emissions under NIR excitation sources (800-900nm). : (f) associated energy level diagram of different SAM-SL-UCNPs under femtosecond laser source

High energy upconversion luminescence was observed due to the interactions of three SAM-SL-UCNPs colloidal sample-solution with 140-femtosecond laser pulses under different NIR excitation sources. Hence, upconversion emissions in both of the UV and visible region are observed. Emission bands are observed in between 200nm-270nm for UV region and in between 500nm-680nm for visible region in each of three cases.

Remarkable shifting has been occurred in UV region, however in visible region no such shifting have been occurred under different NIR excitation sources. Intense band positions are appeared at 207nm, 215nm, 225nm, 233nm, 241nm for 950nm, 960nm, 970nm, 980nm, 990nm of NIR excitation wavelengths for 2<sup>nd</sup> sample (exset-2). Whether, any distinct bands have not appeared under 970nm and 980nm sources, although for 950nm 960nm, 990nm excitations the distinct bands are appeared. It is further notice that, the corresponding red shifting are occurred by 8nm, 10nm, 8nm and 8nm with increasing excitation wavelengths from 950nm towards 990nm, respectively. The corresponding spectra received under Fs laser treatment is shown in figures 3.4.8 (a-c) for Exsets (1-3), respectively and the schematic of their corresponding energy level diagram is shown in figure 3.4.8f.

However, no observable band-shifting has been occurred in three different samples rather than emission intensities. Based on the baseline corrections of intensities under different pump wavelengths, the "n" value has been calculated using power law equation (1) [54]–[58],

$$I_{IIC} \sim I_{FS}^n \tag{1}$$

Where, I<sub>UC</sub> = luminescence intensity

and,  $I_{Fs}$  = laser excitation power

'n' represents the number of absorbed photons per photon emitted under the Fs-laser excitation power ( $I_{Fs}$ ) and this has been calculated from the slopes of  $log(I_{UC})$  versus  $log(I_{Fs})$ (figure 3.4.9) and their values are mentioned in figures 3.4.9a, 3.4.9b, 3.4.9c i.e. for UV, green and red emissions for three different cases. In UV regions, the 'n' values have been evaluated to be 1.8, 3.75 and 2.75; in green visible regions, the values are 1.68, 0.25, 3.69; and for red emissions, values are found to be 2.54, 3.05,2.02 satisfying direct energy transfers from Yb<sup>3+</sup> (S-ion) to Er<sup>3+</sup> (A-ion) [Yb<sup>3+</sup> (2F<sub>5/2</sub>) - Er<sup>3+</sup> (4G<sub>11/2</sub>,4F<sub>7/2</sub>, 4F<sub>9/2</sub>)].

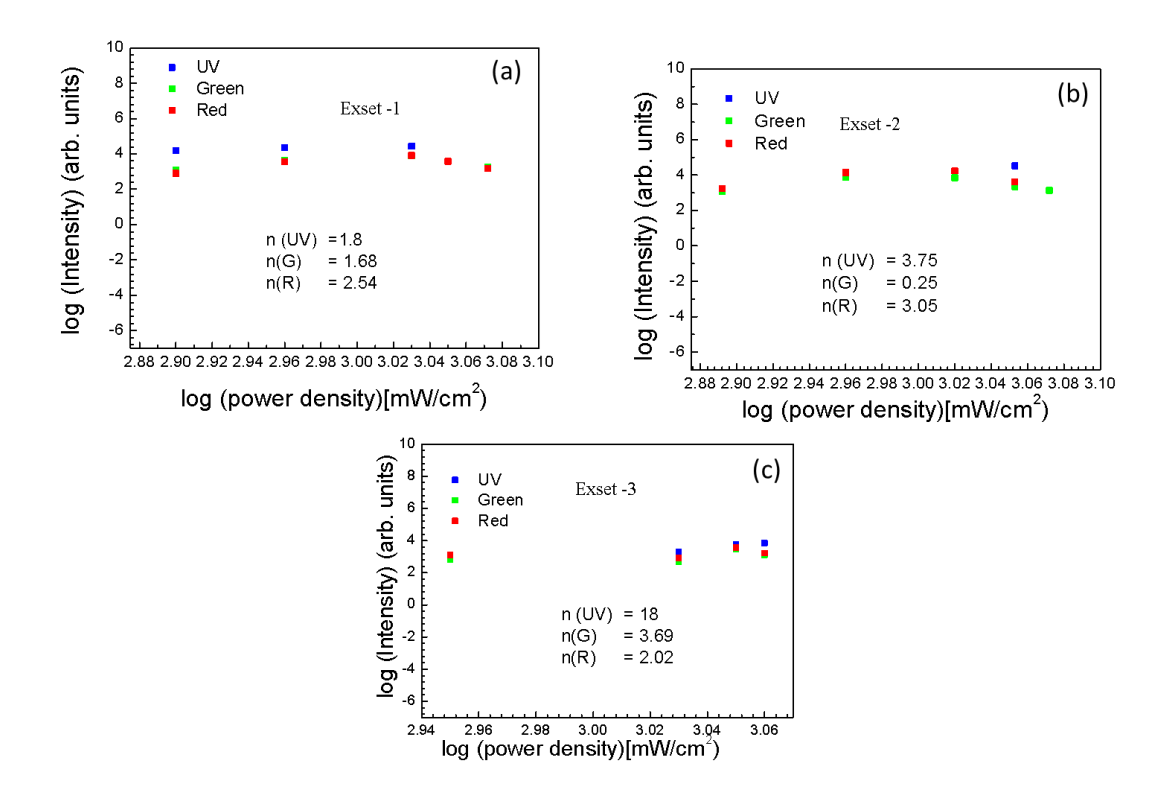


Figure 3.4.9: "n" –values received from fs-laser power dependent formula and have been derived in deep UV, green and red visible regions for three Exp. Sets -1, 2 and 3 in (a)(b)(c), respectively. The highest values occurred for Exset – 3

It is further found out that most of the "n" values are appeared to be almost = 2 or >2 which further confirmed us that minimum a pair of photons can be transferred from Sion (sensitizer) to A-ion (activator) for UV, green and red emissions. From figure 3.4.9b, it is confirmed that the 'n' value of 0.25 indicates that green emission, for sample 2 (exset-2), does not result for any direct energy transfer, however, it comes due to cross relaxations between energy levels. Based on these results, an energy level

Table 3.4.1: Tabulated form of "n" values in three different Experimental sets (Exsets) along with their corresponding energy level diagram

Parameters	Exset-1 (Designated as "a" in figure 3.4.9a)	Exset-2 (Designated as "b" in figure 3.4.9b)	Exset-3 (Designated as "c" in figure 3.4.9c)
"n"- values with their corresponding emissions	1.8(UV emission), 1.68(G emission), 2.54(R emission),	3.75(UV emission), 0.25(G emission), 3.05(R emission),	18(UV emission), 3.69(G emission), 2.02(R emission),
Corresponding energy transfers (UV, Green, Red)			
	$\begin{array}{ll} G & emission = 2F_{7/2} - \\ 2F_{5/2} - 4F_{7/2} - 2H_{11/2} - \\ 4S_{3/2} - 4I_{15/2} \end{array}$	G emission(much quenched value) = $2F_{7/2}-2F_{5/2} - 4G_{11/2}$ - $2H_{9/2}$ - $4F_{3/2}$ - $4F_{5/2}$ - $4F_{7/2}$ - $2H_{11/2}$ - $4S_{3/2}$ - $4I_{15/2}$ (More no. of non-radiative relaxations present)	
	$\begin{array}{ll} R & emission = & 2F_{7/2} \text{-} \\ 2F_{5/2} - 4F_{9/2} - 4I_{15/2} \end{array}$	$\begin{array}{c} R \ emission = \ 2F_{7/2} - \\ 2F_{5/2} - 4F_{9/2} - 4I_{15/2} \end{array}$	$\begin{array}{ll} R \ emission = \ 2F_{7/2} - \\ 2F_{5/2} - 4F_{9/2} - 4I_{15/2} \end{array}$

diagram has been drawn to represent the energy transfer and mechanisms which are responsible for the different emissions as it is shown in figure 3.4.8f (The corresponding "n"- values are also associated with the different emissions under three different sets of experiment). Further the energy transition bands, 'n' and emission colours have been shown in a tabulated form (table 3.4.1).

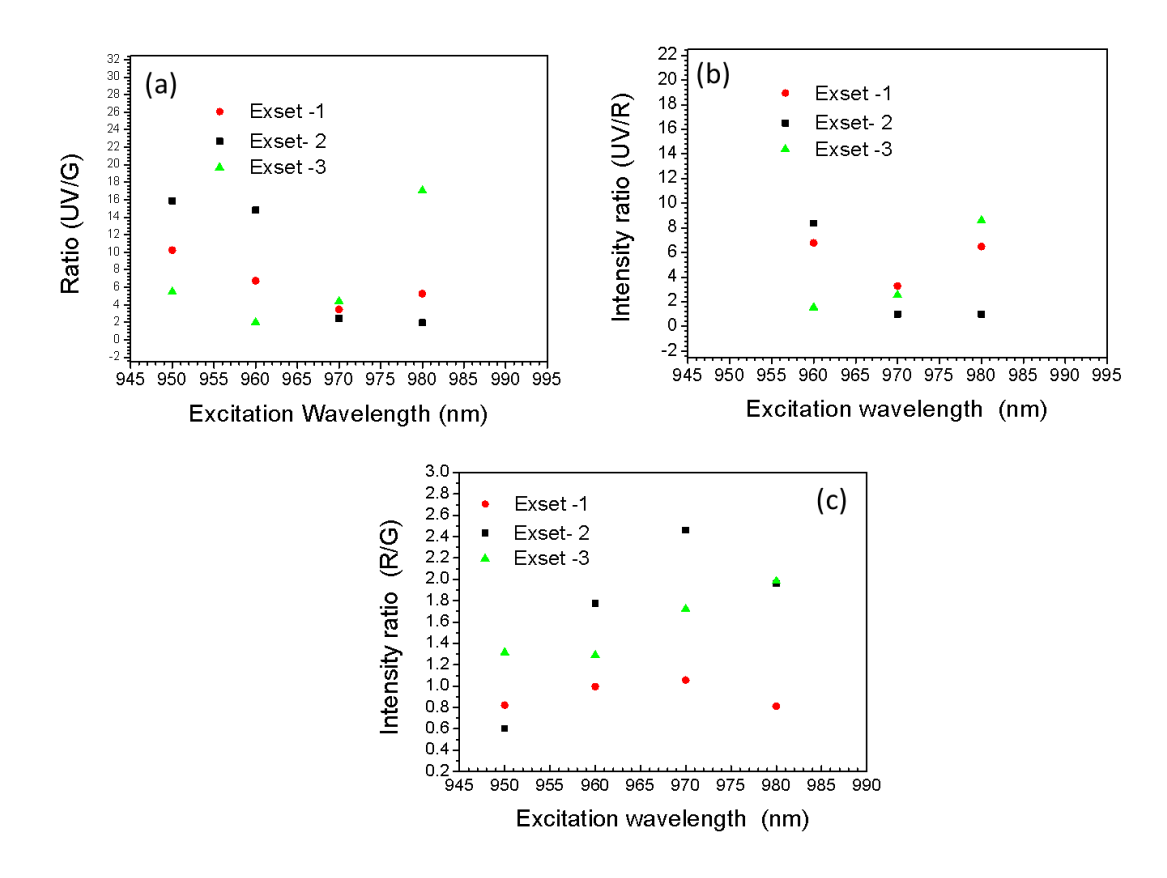


Figure 3.4.10: Ratio plots for the intensities of different emissions of three SAM-SL-UCNPs colloidal solutions with different excitation radiations (a) ratio of UV/Green emission intensity, (b) ratio of UV/Red emission intensity (c) ratio of red/green emission intensity

Table 3.4.2: Tabulated form of intensity ratio values in UV and visible region under different excitation wavelengths:

UV reg	ion			Visible regi	on	
Ex.		UC	Ratio	Ex. W.L.	Highest	Ratio
W.L.		intensity	values	(λ)	intensity	values
(λ)		(λ)	(λ)		(λ)	
960		25278	2.27	970(G)	7722	2.79
970	(exset-1)	26734	2.40	970(R)	8154	2.28
960		33235	2.99	980(G)	7112	2.56
990	(exset-2)	33422	3.01	970(R)	16923	4.74
980		11098		960(G)	2772	
	(exset-3)			960(R)	3573	-

The efficient populations of photons in different energy levels could be the possible reason of occurring different intense emission bands under NIR sources (950nm-990nm excitation wavelengths). One tabulated form of the intensity ratio values in UV and visible region is shown in table 3.4.2 (with corresponding to figure 3.4.10).

The Quantum yield values (figure 3.4.11) have been determined for different superlattice UCNPs and they are found to be as follows (table 3.4.3, tables 3.4.4, 3.4.5):

Table 3.4.3: Shows the Quantum Yield (QY) for the different samples

Samples	Quantum Yield (QY)		
	UV region	Vis- region	
Exset-1	0.032 %-0.22%	0.076%-0.22%	
Exset-2	0.054% - 1.44%	0.124% - 1.44%	
Exset-3	0.08% - 1.17%	0.19% - 1.17%	

## Tabulated forms of different Quantum yield (Q.Y.) values in three different Experimental sets: (Exsets)

Table 3.4.4: Shows the External Quantum yield

Q.Y. values	Exset-1	Exset-2	Exset-3
External Q.Y. values	UV emission= $0.039\%(\lambda_{ex}=960\text{nm})$ $0.032\%(\lambda_{ex}=970\text{nm})$ $0.039\%(\lambda_{ex}=980\text{nm})$ $0.044\%(\lambda_{ex}=990\text{nm})$	UV emission= $0.129\%(\lambda_{ex}=950\text{nm})$ $0.088\%(\lambda_{ex}=960\text{nm})$ $0.085\%(\lambda_{ex}=970\text{nm})$ $0.054\%(\lambda_{ex}=980\text{nm})$	$\begin{array}{l} \text{UV emission=} \\ 0.12\% (\ \lambda_{ex} = 950 \text{nm}) \\ 0.099\% (\ \lambda_{ex} = 960 \text{nm}) \\ 0.08\% (\ \lambda_{ex} = 970 \text{nm}) \\ 0.103\% (\ \lambda_{ex} = 980 \text{nm}) \end{array}$
	G emission= $0.097\%$ ( $\lambda_{ex}$ =960nm) $0.076\%$ ( $\lambda_{ex}$ =970nm) $0.092\%$ ( $\lambda_{ex}$ =980nm) $0.097\%$ ( $\lambda_{ex}$ =990nm)	G emission= $0.336\%$ ( $\lambda_{ex}$ =950nm) $0.222\%$ ( $\lambda_{ex}$ =960nm) $0.204\%$ ( $\lambda_{ex}$ =970nm) $0.124\%$ ( $\lambda_{ex}$ =980nm)	G emission= $0.31\%$ ( $\lambda_{ex}$ =950nm) $0.25\%$ ( $\lambda_{ex}$ =960nm) $0.19\%$ ( $\lambda_{ex}$ =970nm) $0.24\%$ ( $\lambda_{ex}$ =980nm)
	$\begin{array}{l} \text{R emission=} \\ 0.119\% (\ \lambda_{ex} \! = \! 960\text{nm}) \\ 0.093\% (\ \lambda_{ex} \! = \! 970\text{nm}) \\ 0.111\% (\ \lambda_{ex} \! = \! 980\text{nm}) \\ 0.118\% (\ \lambda_{ex} \! = \! 990\text{nm}) \end{array}$	R emission= $0.406\%(\lambda_{ex}=950\text{nm})$ $0.268\%(\lambda_{ex}=960\text{nm})$ $0.247\%(\lambda_{ex}=970\text{nm})$ $0.151\%(\lambda_{ex}=980\text{nm})$	$\begin{array}{l} \text{R emission=} \\ 0.38\% (\ \lambda_{ex} \! = \! 950 \text{nm}) \\ 0.31\% (\ \lambda_{ex} \! = \! 960 \text{nm}) \\ 0.23\% (\ \lambda_{ex} \! = \! 970 \text{nm}) \\ 0.29\% (\ \lambda_{ex} \! = \! 980 \text{nm}) \end{array}$

Table 3.4.5: Shows the Internal Quantum yield

Q.Y. values	Exset-1	Exset-2	Exset-3
Internal Q.Y. values	UV emission= 0.21%( λ <sub>ex</sub> =960nm) 0.16%( λ <sub>ex</sub> =970nm) 0.17%( λ <sub>ex</sub> =980nm) 0.22%( λ <sub>ex</sub> =990nm)	UV emission= $1.44\%$ ( $\lambda_{ex}$ =950nm) $0.65\%$ ( $\lambda_{ex}$ =960nm) $0.58\%$ ( $\lambda_{ex}$ =970nm) $0.29\%$ ( $\lambda_{ex}$ =980nm)	UV emission= $1.17\%(\lambda_{ex}=950\text{nm})$ $0.798\%(\lambda_{ex}=960\text{nm})$ $0.52\%(\lambda_{ex}=970\text{nm})$ $0.77\%(\lambda_{ex}=980\text{nm})$
	G emission= 0.21%( λ <sub>ex</sub> =960nm) 0.16%( λ <sub>ex</sub> =970nm) 0.19%( λ <sub>ex</sub> =980nm) 0.22%( λ <sub>ex</sub> =990nm)	G emission= $1.44\%(950\text{nm})$ $0.65\%(\lambda_{ex}=960\text{nm})$ $0.58\%(\lambda_{ex}=970\text{nm})$ $0.29\%(\lambda_{ex}=980\text{nm})$	G emission= $1.17\%(\lambda_{ex}=950\text{nm})$ $0.799\%(\lambda_{ex}=960\text{nm})$ $0.52\%(\lambda_{ex}=970\text{nm})$ $0.77\%(\lambda_{ex}=980\text{nm})$
	R emission= 0.21%( λ <sub>ex</sub> =960nm) 0.16%( λ <sub>ex</sub> =970nm) 0.20%( λ <sub>ex</sub> =980nm) 0.22%( λ <sub>ex</sub> =990nm)	R emission= $1.44\%$ ( $\lambda_{ex}$ =950nm) $0.65\%$ ( $\lambda_{ex}$ =960nm) $0.58\%$ ( $\lambda_{ex}$ =970nm) $0.29\%$ ( $\lambda_{ex}$ =980nm)	R emission= $1.17\%(\lambda_{ex}=950\text{nm})$ $0.799\%(\lambda_{ex}=960\text{nm})$ $0.52\%(\lambda_{ex}=970\text{nm})$ $0.766\%(\lambda_{ex}=980\text{nm})$

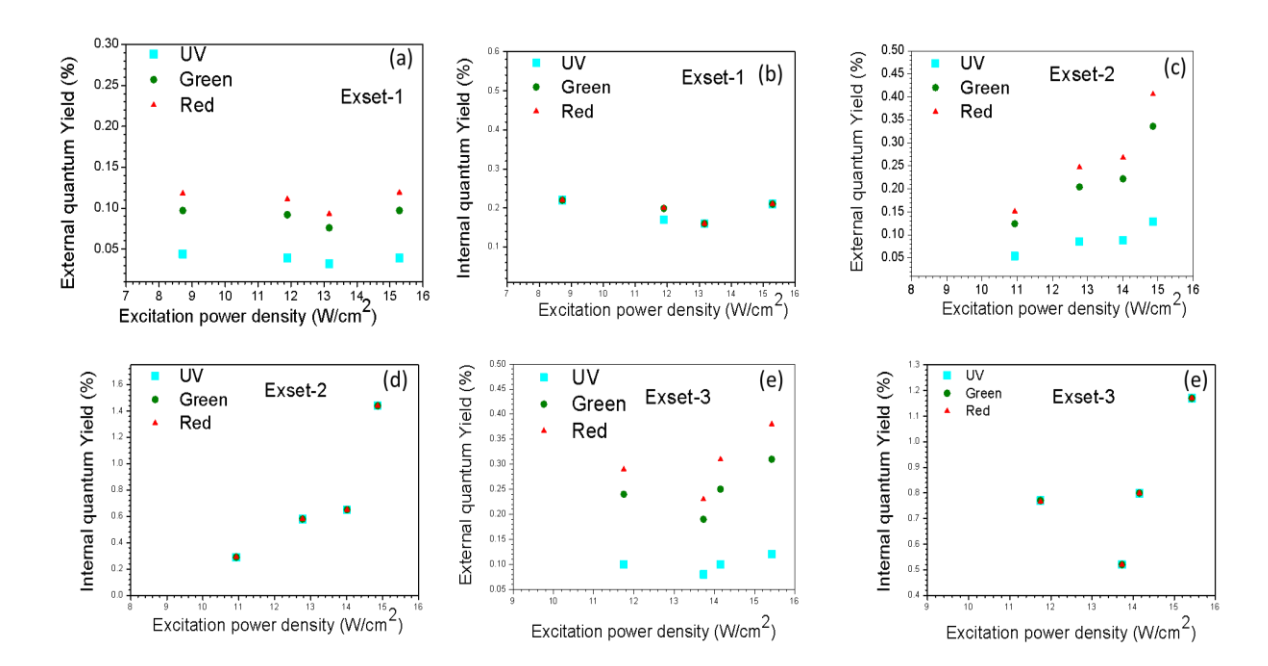


Figure 3.4.11: Plots for External and internal Quantum yields of Exset-1(a&b), Exset-2(c&d), and Exset-3(e&f), respectively

#### 3.4.3 Discussion:

The synthesized SAM-SL-UCNPs are appeared as an autonomous organization of upconverting nanoparticles without any kind of intervention or using any interfacial assembly method separately as reported earlier.[59] The self-assembled superlattice formations can be considered as static-self-assembly (which are stable after formations). A one-pot chemical synthesis approach was applied for preparation of these UCNPs with narrow particle size distribution (particle size 5-9nm). TEM images have provided direct proof of such formations. The synthesized SAM-SL-UCNPs are stable and did not proclaim any oxidation. The nearly spherical UCNPs had a great tendency to form 2D and 3D superlattice structures. The formations of such 2D and 3D superlattice structure patterns controlling ambient reaction parameters must be having strong importance in several practical applications such as plasmonic metamaterials[60]–[64], solar cells[65], [66], due to their nanoscale-architectures and can also open new windows in bioimaging [67], [68] and photodynamic therapy [69], [70] and so on. The morphologically controlled SAM-SL-UCNPs with bright fluorescence introducing high intense blue emissions and generation of high energy upconversion under femtosecond laser treatment make them unique. The applications of upconversion emissions under different femtosecond irradiations are well known to us[71]-[75]. Now, the combination of self-assembled morphology along with strong upconversion emissions (strong fluorescence under 800nm-900nm NIR irradiations and strong luminescence mainly in UV region under 950nm-990nm NIR irradiations) could open strong applications in bio-fields which is under investigations.

Significant up-conversion properties have been observed in three different structural configurations, exset- 1, exset- 2, exset - 3. In three of the cases, in UV region, emission bands in between 204-265nm have been found with their maximum values appeared at 207nm, 215nm, 225nm, 233nm and 241nm. In visible-region, the emission bands are located  $\sim$  536-560nm (Green emissions) with maximum value at 539nm and

~644-675nm (Red emission) with maximum values at 654nm and 662nm. However, no observable shiftings have been traced with different configurations but obviously these up-conversion properties appeared with different intensity values (calculated with baseline corrections).

In UV region, for exset -1, highest intense upconversion band is observed under 960nm and 970nm excitation wavelength (ex. w.l.). For exset -2, the maximum intensity observed under 960nm and 990nm ex. w.l. For exset -3, it was observed under 980 nm excitation.

Considering visible-region, highest upconversion intensities appeared under 970nm, 980nm 960nm ex. w.l. for green emissions in exset -1, exset-2 and exset-3, respectively. Whereas, for red emissions, the maximum intensity values arisen under 970nm, 970nm, 960nm excitation wavelength in exset -1, exset-2 and exset-3, respectively.

However, for UV section, in exset-1, the highest upconversion intensity has been appeared to be 2.27 (960nm excitation), 2.4(970nm excitation) times higher compared to that in exset-3(980nm excitation); while in exset-2, the highest upconversion intensity appeared to be 2.99 (960nm excitation), 3.01(990nm excitation) times higher compared to that in exset-3(980nm excitation).

In visible-emission wavelength section, for exset-1 and exset-2, highest up-conversion intensity has been emerged to be 2.79 (970nm excitation), 2.56 (980nm excitation) times higher, respectively, for green emissions and 2.28(970nm excitation), 4.74(970nm excitation) times higher, respectively, for red emission compared to those in exset-3(960nm excitation)

Delayed nucleation path has been maintained for synthesising cubic ( $\alpha$ ) and hexagonal ( $\beta$ ) phase UCNPs from their corresponding rare-earth precursors. Hence, growth process of both phases ( $\alpha$  and  $\beta$ ) and transition operation ( $\alpha$ - $\beta$ ) have been disclosed with XRD, TEM, Fluorescence/Luminescence techniques. Several analyses direct us, UC emission was influenced by the growth of superlattice nanocrystals, and more specifically, emission intensity was affected owing to nucleation and phase-transition operations. Moreover, different emissive intensity ratios found to be sensitive with different phases-appearances in three formations of exset-1,2,3.

However, a prolonged heat treatment method could be the reason of appearing different uniform, monodisperse SAMUCNPs which followed four steps(figure 3.4.12) during synthesis, they are (i) A delayed - nucleation (ii) Growth with imparting monomers (iii) size-depletion and, (iv) Accumulation. Hence, as the heat treatment was continued to 20 mins, cubic (a) UCN-phases started to arise in solution and further with a prolonged time a turbid solution was formed confining a modest increment of nanocrystal-sizes. The co-precipitation between rare-earth precursors and NaF developed α-phased nanocrystals. A sufficient amount of decomposed NaF could fast the growth rate of monomers ( $\alpha$ -NaYF<sub>4</sub>: Yb, Er) whose concentration became high after a certain time-interval. During this period, the monomers maintained their uniformity in solution (say, in exset-1) by manifesting (111), (100) planes as admitted with HRTEM images. These facets were sustained by strong binding of major capping agents on crystal-surface (RE<sup>3+</sup> and COO<sup>-</sup>). Afterwards, the exhausting and stabilizing nature of monomers was revealed while the monomer-size remained invariant. This condition, could occur while they consumed entirely in solution with restricting Ostwald's-ripening process[76]–[78]. This situation could be happened due to appearance of weak van der Waal's forces of interactions between capping agent (oleic acid) molecules and RE<sup>3+</sup> ions on nanocrystal-surfaces.

Further,  $\alpha$ – $\beta$  phase transition started to arrive in solution (say, in exset-2) with a further prolonged heat treatment by allowing dissolution and recrystallization followed by Ostwald-ripening process. Hence, a complete  $\alpha$  –  $\beta$  phase transition took place (say, in exset -3).

Additionally, in present investigation, it can be seen that the highest upconversion intensity ( $I_{HUC}$ ) has been affected by the appearances of  $\alpha/\beta/\text{mixed}$  crystalline phases and appeared to be maximum in both UV and visible region while accumulated mixed phases ( $\alpha$  and  $\beta$ ) in solution. The red to green emission ratios ( $f_{r/g}$ ) has been found to be 1.06, 2.38, 1.28 for cubic, mixed and hexagonal phases, respectively i.e. highest in mixed occurrence (say, exset-2). Moreover, the,  $\alpha-\beta$  phase transition operation can be considered to be a delayed nucleation growth process with accumulating sufficient amount of  $\alpha$ -UCN monomers.

The two factors- surface - reaction and diffusion of monomers, which has influenced the growth of nanocrystals. Hence, the growth of nanocrystals could be expressed as [79], [80];

$$J = 4\pi b^2 \gamma \ dC/db \tag{2}$$

Where, b= radius of plane through which the flux (J) can pass

 $\gamma$  = Diffusional co eff.

C= Monomers concentration at a length b'

Concerning several literature on nucleation and growth of nanocrystals, it can be concluded that it could be possible to occur nucleation and growth of nanocrystals simultaneously as described by Finke-Watzky mechanism [81–84]where a nucleation (P - Q) would happen leisurely and an autocatalytic crystal-growth (P+Q= 2Q) would

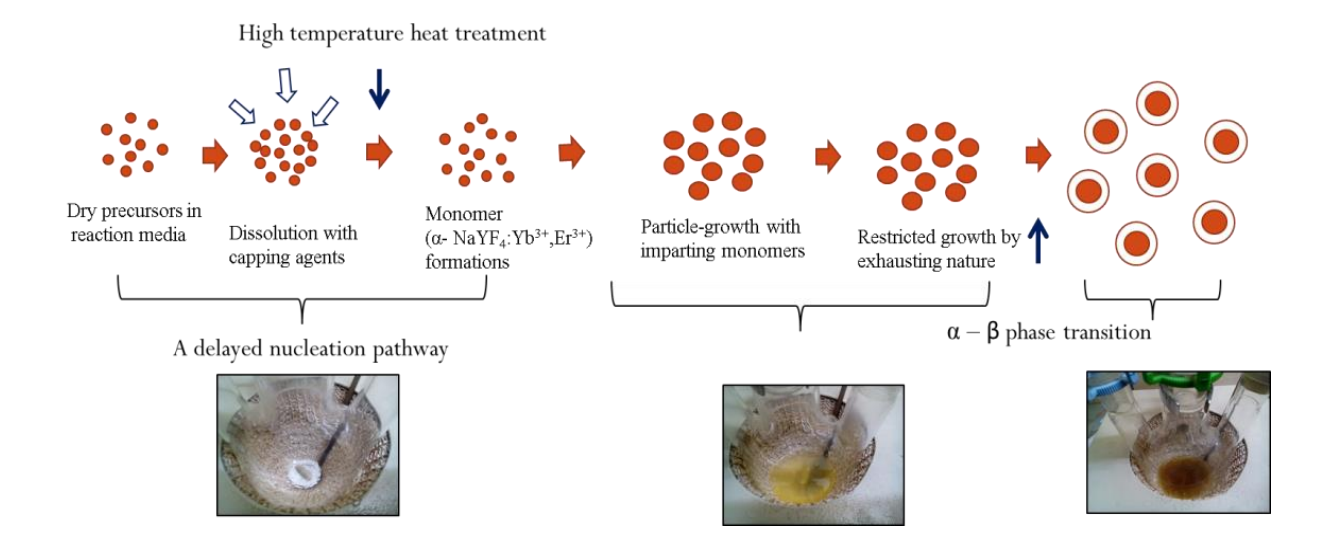


Figure 3.4.12: A schematic of the whole process succeeding the nucleation and growth mechanism along with  $\alpha-\beta$  phase transition. The corresponding exp. investigations are also placed.

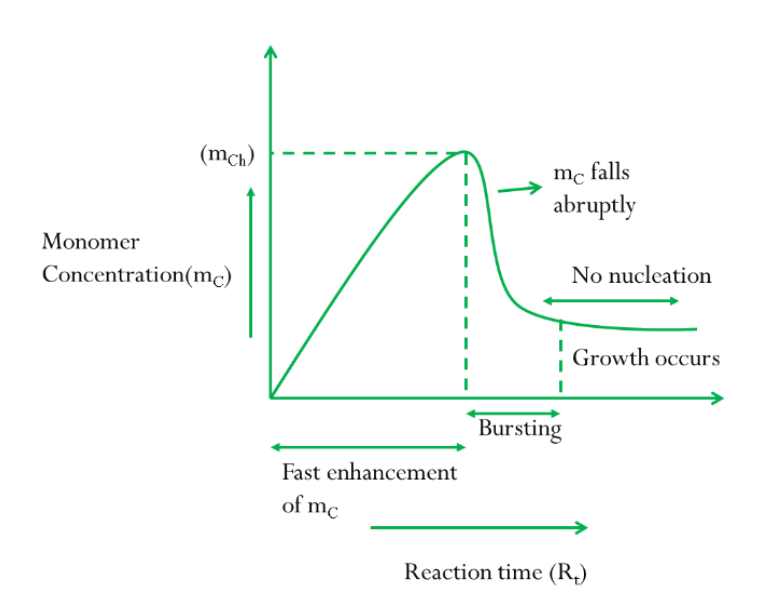


Figure 3.4.13: The mechanism associated with the formation of monomers and particle-growth

take place. The principal theory of leisure nucleation and autocatalytic growth process would follow Lamer Mechanism [85], [86] (figure 3.4.13) which completes in three steps to separate nucleation and growth into distinct stages. The following stages are:

(1) A fast enhancement of monomer – concentration, (2) Burst in nucleation after a certain period of reaction-minimizing monomer-concentration abruptly and (3) afterwards, growth arises by diffusing nucleates in solution.

Furthermore, UCN superlattices with different architecture and periodicity are the high ordered UCN superlattice exhibited leads to the variation of quantum yields. However,  $I_{UC}$  and  $f_{r/g}$  is influenced by the amount  $\alpha$  and  $\beta$  contents in synthesized nanocrystals. It can also be believed that the phase-controlled SAMUCNPs bearing high quality crystal which could be potential candidates for making sensors, emitters and display techniques along with several bio imaging and bio-medicines.

## 3.4.4 Summary and Conclusions of PART IV:

In this work, we report that under different reaction conditions, NaYF<sub>4</sub> based UCNPs were able to develop several self-assembled super lattice structures (as confirmed by different TEM images) with exhibiting bright fluorescence under CW 980 nm NIR and luminescence under 140 femtosecond laser treatment. By applying different synthetic conditions, the fluorescence and luminescence properties are well tuned with differently synthesized self-assembled structures. The SAMSLs are confined with a few soft ligands or capping agents and it is believed that presence or alignment of them along with the bulk material play an important role in tuning their optical properties. In summary, we have synthesized three different UCN-SL structures and examined all properties on their colloidal solutions. The increment of high reaction temperature induced more amount of hexagonal phases compared to its cubic. Hence, the number of absorbed photon per emission has been calculated for each of the emission [e.g. UV, Visible (Green, Red)] individually and has been found to be 1.5 - 5.

The intensity ratios have been plotted as UV/Green, UV/Red, Red /Green for three sets of experimental samples. Further, the quantum yield values (for both internal and external Q.Y. values) have also been enumerated along with several excitation power densities vs Q.Y. plots for each of the emissions received under Fs –laser facility and these values lie in the range between 0.032 %(Min) - 1.44 % (Max). The growth mechanism of the UCN-SLs structures (from Exset-1 - Exset-3) has also been scrutinized along with phase-transition (monomers - monodispersed NPs) (The schematic in figure 3.4.12 shows the entire growth) process. So, moreover, by observing optical properties and Q.Y. values we can assure that the shape directed assembling strategy of the synthesized nanocrystals can promote the bio and energy related nanophosphor applications.

# 4 SUMMARY, CONCLUSIONS AND SCOPE of this WORK

In this chapter, the **summary and conclusions** of the present dissertation have been elucidated. The whole dissertation consists of four chapters-Introduction, Experimental section, Results and Discussion, and summary and conclusions section. The third chapter (results and discussion part) is sub-divided into five parts. A short summary is given on those four chapters:

**Chapter 1**: This chapter presents the background of UCNPs (synthesis, characterizations and their applications) with introducing literature reviews. At the end of this chapter the motivation and objectives of the present dissertation have been explained.

**Chapter 2:** This chapter deals with the experimental part, which includes basis principles of different characterization techniques, synthesis methods, and materials used to complete the present dissertation work. The synthesis methods to prepare different morphological UCNPs have been described in detail. To synthesize  $\alpha$  and  $\beta$  –NaYF<sub>4</sub> upconverting nanocrystals three different hexahydrate precursors have been used in hot-surfactant solutions and details of those precursors have also been mentioned in this section. UCN-hexagonal, UCN-dots, UCN-Ds, SAM-SL-UCNPs have been synthesized in unique pathways following thermal decompositions solvothermal treatments. In each of the cases, the reaction parameters were varied in a precisely controlled way to form monodisperse and self-assembled nanocrystals which were identified and confirmed with different characterization techniques. During synthesis, the successive growth stages of nanocrystals are- Nucleation, Particle growth, Dissolution resulting contracting particle sizes, and Aggregation. The  $\alpha$  to  $\beta$ -phase transition i.e. transition from α-UCNPs (NaYF4: Yb, Er - monomers) to β-UCNPs (NaYF4: Yb, Er monodisperse nanoparticles occurs by amplifying or limiting Ostwald-ripening process. Precursor-decomposition took place around 100°C of mantle- reaction temperature and under this condition, the carbon species (fluorinated / oxyfluorinated) started to release from solution. Beyond 20 mins of reaction time, the  $\alpha$ -phases started to appear in solution.

However, a delayed nucleation pathway is required to synthesize moodisperse UCNPs rather than a rapid nucleation pathway. For nucleation, the reaction temperature controls the crystallite size. The co-precipitation between decomposed NaF and rare earth precursors results in formations of  $\alpha$ -NaYF<sub>4</sub> as accumulation of NaF in solution can burst nucleation and can fast the growth rate of  $\alpha$ -NaYF<sub>4</sub> nanocrystals, immediately nanocrystal-sizes enhance. However, decomposition rate of NaF in solution increases with increasing temperature but is

independent of precursor's concentration. During this period, the monomer concentration ( $\alpha$ -NaYF<sub>4</sub>- concentration) becomes high by obstructing Ostwald ripening process and exposing (111) and (100) facets in nanocrystals and afterwards, nanocrystal-size remains invariant which further reveals the unstable and exhausting behavior of monomers owing to reduced bonding-integration (probably dominant van der Waal's interactions between oleic acid and nanocrystal surface). While all the monomers consume entirely (nanoparticle size distribution becomes broadened during this period), with time being, dissolution and recrystallization start to occur in solution with stimulating Ostwald ripening process owing to broadened size distribution. In this dissolution and recrystallization process, the  $\alpha$  to  $\beta$  phase transition starts to appear.

More importantly, the presence of  $\alpha$  and  $\beta$ -phases in differently synthesized UCNPs affected different upconversion emission spectra (fluorescence, luminescence, photoluminescence) resulting in different intensity-ratio values.

In  $3^{rd}$  chapter, part I, high quality hexagonal UCNPs have been synthesized with uniform size distribution. Emission properties were tuned controlling reaction parameters and have been found to be highly efficient. The synthesized NaYF<sub>4</sub> nanocrystals with Yb<sup>3+</sup> and Er<sup>3+</sup> have been proven to be the best UCNPs reported ever in literature because they are able to show emission even after decreasing the laser power density below 50 mW/cm<sup>2</sup>.

In 3<sup>rd</sup> chapter, part II, UCN-dots have been synthesized with thermal decomposition of lanthanide precursors. The average particle size has been found to be to be 3.4 nm in diameter which are smallest in size reported ever and are stable for a minimum of one year exhibiting upconversion emissions. This work further revealed the emission of UV luminescence from synthesized UCN-dots under interaction with femtosecond laser of 140 femtosecond pulsed at 80 MHz repetition rate.

In  $3^{rd}$  chapter, part III, controlling reaction parameters in in-situ condition and without incorporating any external dendritic polymers during synthesis, Upconverting nanodendrites (UCN-Ds) have been developed for the first time. UCN-Ds contain both of the  $\alpha$ - and  $\beta$ -phase within its solid structure and are very stable (up to a minimum of 2 years). Presence of these two phases in dendritic UCNPs could be the cause of high energy upconversion and make them very seminal and are with caterpillar/necklace type of structure.

In 3<sup>rd</sup> chapter, part IV, the formations of self-assembled-superlattices of upconverting nanophosphors over multiple-magnified scales prepared by one-pot chemical approach is reported. The different types nanoparticle superlattice have been constituted through the bottom-up self-assembly approach where the process is either in an equilibrium or in a non-equilibrium state. The synthesis method is optimized with a minimum amount of heating rate.

The upconversion emissions at ultraviolet and visible emissions have been investigated. The synthesis procedure applied here to form UCN-SL is a modified approach of the synthesis method developed by our group previously. The entire reaction process was carried out in an inert gas (Argon) atmosphere. The different self-assembly superlattice structures have been formed in-situ with varying the conditions. The as-synthesized nanophosphors can display sharp and bright luminescence (both in ultraviolet and visible region) and fluorescence (mostly in visible region) under Ti-Sapphire 140-femtosecond laser pulses at 80 MHz repetition rate with 950nm-990nm excitation wavelengths and under 980nm continuous wave laser sources, respectively.

The beauty of our process is that the entire synthesis process consumes less time to obtain the self-assembled UCN-SL structures. Further, how the UCN-SL with different architecture exhibited different upconversion luminescence properties also have been

elucidated. As-synthesized UCN-SL structures represented here are not only to generate new physical properties from bulk materials but also new phenomenon for interactions between particles at nanoscale have also been found out. In order to produce the particular self-assembled UCN-SL pattern in synthesized nano- material we followed few controlled reaction parameters. By applying those key factors, the correlative arrangements of nanocrystal building blocks with their sizes and the spacing between those crystals are maintained in a self-assembled long-range order. The precisely engineered nanocrystal sizes and systematic shaped-assembly treat as building blocks to generate improved entities. Additionally, for the different UCN-SLs the different in intensity of emission and their position and shifting, internal upconversion quantum yield (Internal UCQY) and external upconversion quantum yield (External UCQY), photoluminescence behaviour, fs-laser power dependent luminescence and the number of absorbed photons taking part in the process (n, where 'n' is the number of absorbed NIR photons per emission under fs-laser excitation power) have been calculated. The controlled morphology with efficient upconversion fluorescence and luminescence of these UCN-SL structures may discover considerable applications in different fields such as lasers, diodes, display-techniques and energy – related applications. The mean particle-sizes are varied from 5nm-8nm. The substantially improved design of nanphosphors will boost biological and energy related nanophosphor applications.

In differently synthesized UCNPs, size and phases have been controlled to achieve multicolor tuned emissions. In previous study on UCNPs and their applications, different methods have been applied to enhance upconversion efficiency by optimizing precursors concentrations and local chemical environment and modifying morphologies. It has always been spellbinding to improve anti-Stokes luminescence in rare-earth dopes nanoparticles owing to their several applications in display devices, lasers, bio-imaging, labeling and sensing and sustaining with eminent photo stability, NIR-to-visible upconversion and long luminescence-lifetime which can make them potential candidates for competitive bio-labels even in commercial purposes.

The energy transferred from sensitizer  $(Yb^{3+} \text{ for NaYF}_4: Yb^{3+}, Er^{3+} \text{ nanocrystals})$  to activator ion  $(Er^{3+} \text{ for NaYF}_4: Yb^{3+}, Er^{3+} \text{ nanocrystals})$  can also be tuned with respect to upconversion enhancement (in each of the synthesized UCNPs different energy level diagrams to represent the transferred energy from sensitizer to activator ions are introduced).

### Scope for future work on synthesized materials:

In part I, the synthesized UCNPs have huge responses for applications in display technologies and lasers. In part V, the formations of thin-films could be useful further for making laser devices and smart cards for detection purposes.

In part II, III, and IV the synthesized UCN-nano-dots below 5 nm, self-assembled dendritic (chain/necklace types) and UCN-SL have never been reported respectively. Up-conversion at UV region has never been reported. These combinations in material make them unique under different circumstances and none of the work reported on the femtosecond laser study and properties. Thus these works carry a huge novelty. Previously, our research group reported a couple of works on upconverting materials including UCN-core shell materials with therapeutic applications. Therefore, we strongly believe that UCN-dots and UCN-Ds and SAM-UCN-SL materials reported here with unique sizes and morphologies could be potential candidate for optoelectronic devices and for therapeutic applications. It can be further noted that smaller sizes of nano particles are acceptable much more by the living cells and if size is below 8 nm, then they can be easily excreted through kidney which actually much more important for the use of nanomaterials/this type of materials for therapeutic applications. So, in such case synthesized UCN-dots could be a perfect candidate.

# **References:**

- [1] J.-C. Boyer, L. A. Cuccia, and J. A. Capobianco, "Synthesis of colloidal upconverting NaYF4: Er3+/Yb3+ and Tm3+/Yb3+ monodisperse nanocrystals.," *Nano Lett.*, vol. 7, no. 3, pp. 847–52, 2007.
- [2] K. W. Krämer, D. Biner, G. Frei, H. U. Güdel, M. P. Hehlen, and S. R. Lüthi, "Hexagonal Sodium Yttrium Fluoride Based Green and Blue Emitting Upconversion Phosphors," *Chem. Mater.*, vol. 16, no. 7, pp. 1244–1251, Apr. 2004.
- [3] J. F. Suyver, J. Grimm, K. W. Krämer, and H. U. Güdel, "Highly efficient near-infrared to visible up-conversion process in NaYF4:Er3+,Yb3+," *J. Lumin.*, vol. 114, no. 1, pp. 53–59, 2005.
- [4] J. Zhao *et al.*, "Controlled Synthesis, Formation Mechanism, and Great Enhancement of Red Upconversion Luminescence of NaYF4:Yb3+, Er3+

  Nanocrystals/Submicroplates at Low Doping Level," *J. Phys. Chem. B*, vol. 112, no. 49, pp. 15666–15672, Dec. 2008.
- [5] J. F. Suyver, J. Grimm, M. K. van Veen, D. Biner, K. W. Krämer, and H. U. Güdel, "Upconversion spectroscopy and properties of NaYF4 doped with Er3+, Tm3+ and/or Yb3+," *J. Lumin.*, vol. 117, no. 1, pp. 1–12, 2006.
- [6] S. Schietinger, T. Aichele, H.-Q. Wang, T. Nann, and O. Benson, "Plasmon-Enhanced Upconversion in Single NaYF4:Yb3+/Er3+ Codoped Nanocrystals," *Nano Lett.*, vol. 10, no. 1, pp. 134–138, 2010.
- [7] X. Feng *et al.*, "Converting Ceria Polyhedral Nanoparticles into Single-Crystal Nanospheres," *Science* (80-. )., vol. 312, no. 5779, pp. 1504 LP 1508, Jun. 2006.
- [8] S. Heer, K. Kömpe, H. U. Güdel, and M. Haase, "Highly efficient multicolour upconversion emission in transparent colloids of lanthanide-doped NaYF4 nanocrystals," *Adv. Mater.*, vol. 16, no. 23–24, pp. 2102–2105, 2004.
- [9] S. Sivakumar, F. C. J. M. van Veggel, and M. Raudsepp, "Bright White Light through Up-Conversion of a Single NIR Source from Sol–Gel-Derived Thin Film Made with Ln3+-Doped LaF3 Nanoparticles," *J. Am. Chem. Soc.*, vol. 127, no. 36, pp. 12464–

- 12465, Sep. 2005.
- [10] O. Ehlert, R. Thomann, M. Darbandi, and T. Nann, "A Four-Color Colloidal Multiplexing Nanoparticle System," *ACS Nano*, vol. 2, no. 1, pp. 120–124, Jan. 2008.
- [11] F. Wang and X. Liu, "Upconversion Multicolor Fine-Tuning: Visible to Near-Infrared Emission from Lanthanide-Doped NaYF4 Nanoparticles," *J. Am. Chem. Soc.*, vol. 130, no. 17, pp. 5642–5643, Apr. 2008.
- [12] F. Auzel, "Upconversion and Anti-Stokes Processes with f and d Ions in Solids," *Chem. Rev.*, vol. 104, no. 1, pp. 139–174, Jan. 2004.
- [13] J. F. Suyver *et al.*, "Novel materials doped with trivalent lanthanides and transition metal ions showing near-infrared to visible photon upconversion," *Opt. Mater. (Amst).*, vol. 27, no. 6, pp. 1111–1130, 2005.
- [14] F. Wang and X. Liu, "Recent advances in the chemistry of lanthanide-doped upconversion nanocrystals," *Chem. Soc. Rev.*, vol. 38, no. 4, pp. 976–989, 2009.
- [15] F. Wang *et al.*, "Simultaneous phase and size control of upconversion nanocrystals through lanthanide doping," *Nature*, vol. 463, pp. 1061–1065, Feb. 2010.
- [16] G. S. and C. Yi and G. M., "Synthesis of Hexagonal-Phase NaYF4: Yb,Er and NaYF4:Yb,Tm Nanocrystals with Efficient Up-Conversion Fluorescence," *Adv. Funct. Mater.*, vol. 16, pp. 2324–2329, 2006.
- [17] W. G. van Sark, J. de Wild, J. K. Rath, A. Meijerink, and R. E. I. Schropp, "Upconversion in solar cells," *Nanoscale Res. Lett.*, vol. 8, no. 1, p. 81, 2013.
- [18] Z. Q. Li *et al.*, "Core/shell structured NaYF4:Yb3+/Er3+/Gd+3nanorods with Au nanoparticles or shells for flexible amorphous silicon solar cells," *Nanotechnology*, vol. 23, no. 2, p. 25402, 2011.
- [19] D. Li and G. Chen, "Chapter 9 Upconversion-Enhanced Dye-Sensitized Solar Cells,"
   M. Soroush and K. K. S. B. T.-D.-S. S. C. Lau, Eds. Academic Press, 2019, pp. 325–340.
- [20] W.-J. Ho, C.-Y. Wei, J.-J. Liu, W.-C. Lin, and C.-H. Ho, "Performance characterization of planar silicon solar cells using NIR up-conversion layer comprising

- YF3:Yb3+/Er3+ phosphors," *Vacuum*, vol. 166, pp. 1–5, 2019.
- [21] H. C. Swart, "Lanthanide activated phosphors for solar cell applications," in *Proc.SPIE*, 2019, vol. 11043.
- [22] J. Dutta, V. K. Rai, M. M. Durai, and R. Thangavel, "Development of Y2O3: Ho3+/Yb3+ Upconverting Nanophosphors for Enhancing Solar Cell Efficiency of Dye-Sensitized Solar Cells," *IEEE J. Photovoltaics*, vol. 9, no. 4, pp. 1040–1045, 2019.
- [23] X. Xie and X. Liu, "Upconversion goes broadband," *Nat. Mater.*, vol. 11, pp. 842–843, Sep. 2012.
- [24] G.-B. Shan and G. P. Demopoulos, "Near-Infrared Sunlight Harvesting in Dye-Sensitized Solar Cells Via the Insertion of an Upconverter-TiO2 Nanocomposite Layer," *Adv. Mater.*, vol. 22, no. 39, pp. 4373–4377, Oct. 2010.
- [25] W. Zou, C. Visser, J. A. Maduro, M. S. Pshenichnikov, and J. C. Hummelen, "Broadband dye-sensitized upconversion of near-infrared light," *Nat. Photonics*, vol. 6, pp. 560–564, Jul. 2012.
- [26] Y. Shang, S. Hao, C. Yang, and G. Chen, "Enhancing Solar Cell Efficiency Using Photon Upconversion Materials," *Nanomaterials*, vol. 5, no. 4, 2015.
- [27] J. Yu *et al.*, "Enhanced Near-Infrared to Visible Upconversion Nanoparticles of Ho3+-Yb3+-F- Tri-Doped TiO2 and Its Application in Dye-Sensitized Solar Cells with 37% Improvement in Power Conversion Efficiency," *Inorg. Chem.*, vol. 53, no. 15, pp. 8045–8053, Aug. 2014.
- [28] R. Naccache, F. Vetrone, and J. A. Capobianco, "Lanthanide-Doped Upconverting Nanoparticles: Harvesting Light for Solar Cells," *ChemSusChem*, vol. 6, no. 8, pp. 1308–1311, Aug. 2013.
- [29] S. Pillai and M. A. Green, "Plasmonics for photovoltaic applications," *Sol. Energy Mater. Sol. Cells*, vol. 94, no. 9, pp. 1481–1486, 2010.
- [30] G. Kakavelakis, K. Petridis, and E. Kymakis, "Recent advances in plasmonic metal and rare-earth-element upconversion nanoparticle doped perovskite solar cells," *J. Mater. Chem. A*, vol. 5, no. 41, pp. 21604–21624, 2017.

- [31] Z. Zhou *et al.*, "Upconversion induced enhancement of dye sensitized solar cells based on core–shell structured β-NaYF4:Er3+, Yb3+@SiO2 nanoparticles," *Nanoscale*, vol. 6, no. 4, pp. 2052–2055, 2014.
- [32] S. J. Park, H. W. Jang, J. Y. Park, J. W. Chung, H. K. Yang, and B. K. Moon, "Gd2O3:Pr3+ nanospheres as bi-functional contrast agents for optical and magnetic resonance imaging properties," *Ceram. Int.*, vol. 45, no. 5, pp. 5958–5964, 2019.
- [33] Y. Il Park *et al.*, "Nonblinking and Nonbleaching Upconverting Nanoparticles as an Optical Imaging Nanoprobe and T1 Magnetic Resonance Imaging Contrast Agent," *Adv. Mater.*, vol. 21, no. 44, pp. 4467–4471, 2009.
- [34] L. Wang *et al.*, "Fluorescence Resonant Energy Transfer Biosensor Based on Upconversion-Luminescent Nanoparticles," *Angew. Chemie Int. Ed.*, vol. 44, no. 37, pp. 6054–6057, Sep. 2005.
- [35] D. Tu *et al.*, "Time-Resolved FRET Biosensor Based on Amine-Functionalized Lanthanide-Doped NaYF4 Nanocrystals," *Angew. Chemie Int. Ed.*, vol. 50, no. 28, pp. 6306–6310, Jul. 2011.
- [36] L. Mattsson, K. D. Wegner, N. Hildebrandt, and T. Soukka, "Upconverting nanoparticle to quantum dot FRET for homogeneous double-nano biosensors," *RSC Adv.*, vol. 5, no. 18, pp. 13270–13277, 2015.
- [37] S. Jiang and Y. Zhang, "Upconversion Nanoparticle-Based FRET System for Study of siRNA in Live Cells," *Langmuir*, vol. 26, no. 9, pp. 6689–6694, May 2010.
- [38] B. Jin *et al.*, "Upconversion nanoparticles based FRET aptasensor for rapid and ultrasenstive bacteria detection," *Biosens. Bioelectron.*, vol. 90, pp. 525–533, 2017.
- [39] J. Wu, H. Wang, H. Yang, J. Chen, and H. Yang, "A novel arginine bioprobe based on up-conversion fluorescence resonance energy transfer," *Anal. Chim. Acta*, 2019.
- [40] W. J. Kim, M. Nyk, and P. N. Prasad, "Color-coded multilayer photopatterned microstructures using lanthanide (III) ion co-doped NaYF4nanoparticles with upconversion luminescence for possible applications in security," *Nanotechnology*, vol. 20, no. 18, p. 185301, 2009.

- [41] C. Zhang, L. Yang, J. Zhao, B. Liu, M.-Y. Han, and Z. Zhang, "White-Light Emission from an Integrated Upconversion Nanostructure: Toward Multicolor Displays Modulated by Laser Power," *Angew. Chemie Int. Ed.*, vol. 54, no. 39, pp. 11531–11535, Sep. 2015.
- [42] Q. Dou, N. M. Idris, and Y. Zhang, "Sandwich-structured upconversion nanoparticles with tunable color for multiplexed cell labeling," *Biomaterials*, vol. 34, no. 6, pp. 1722–1731, 2013.
- [43] M. You *et al.*, "Household Fluorescent Lateral Flow Strip Platform for Sensitive and Quantitative Prognosis of Heart Failure Using Dual-Color Upconversion Nanoparticles," *ACS Nano*, vol. 11, no. 6, pp. 6261–6270, Jun. 2017.
- [44] H. Liu *et al.*, "Tunable Resonator-Upconverted Emission (TRUE) Color Printing and Applications in Optical Security," *Adv. Mater.*, vol. 31, no. 15, p. 1807900, Apr. 2019.
- [45] B. Xue *et al.*, "Regulating the color output and simultaneously enhancing the intensity of upconversion nanoparticles via a dye sensitization strategy," *J. Mater. Chem. C*, 2019.
- [46] L.-L. Li *et al.*, "Biomimetic Surface Engineering of Lanthanide-Doped Upconversion Nanoparticles as Versatile Bioprobes," *Angew. Chemie Int. Ed.*, vol. 51, no. 25, pp. 6121–6125, Jun. 2012.
- [47] S. Radunz, E. Andresen, C. Würth, A. Koerdt, H. R. Tschiche, and U. Resch-Genger, "Simple Self-Referenced Luminescent pH Sensors Based on Upconversion Nanocrystals and pH-Sensitive Fluorescent BODIPY Dyes," *Anal. Chem.*, vol. 91, no. 12, pp. 7756–7764, Jun. 2019.
- [48] M. K. Mahata and K. T. Lee, "Development of near-infrared sensitized core—shell—shell upconverting nanoparticles as pH-responsive probes," *Nanoscale Adv.*, vol. 1, no. 6, pp. 2372–2381, 2019.
- [49] J. Dutta and V. K. Rai, "APTES Modified GO-PEI-Er3+/Yb3+: NaYF4 Upconverting Nanoparticles Hybrid Film-Based Optical pH Sensor and NIR Photoelectric Response," *IEEE Sens. J.*, vol. 19, no. 10, pp. 3609–3615, 2019.

- [50] B. Kumar, A. Murali, and S. Giri, "Upconversion Nanoplatform for FRET-Based Sensing of Dopamine and pH," *ChemistrySelect*, vol. 4, no. 19, pp. 5407–5414, May 2019.
- [51] M. Schäferling, "Nanoparticle-based luminescent probes for intracellular sensing and imaging of pH," Wiley Interdiscip. Rev. Nanomedicine Nanobiotechnology, vol. 8, no. 3, pp. 378–413, May 2016.
- [52] D. Chen et al., "Multimodal Nanoprobe Based on Upconversion Nanoparticles for Monitoring Implanted Stem Cells in Bone Defect of Big Animal," ACS Biomater. Sci. Eng., vol. 4, no. 2, pp. 626–634, Feb. 2018.
- [53] Y. Pu, J. Leng, D. Wang, J. Wang, N. R. Foster, and J. Chen, "Recent progress in the green synthesis of rare-earth doped upconversion nanophosphors for optical bioimaging from cells to animals," *Chinese J. Chem. Eng.*, vol. 26, no. 10, pp. 2206–2218, 2018.
- [54] D. K. Chatterjee, A. J. Rufaihah, and Y. Zhang, "Upconversion fluorescence imaging of cells and small animals using lanthanide doped nanocrystals," *Biomaterials*, vol. 29, no. 7, pp. 937–943, 2008.
- [55] D. K. Chatterjee and Z. Yong, "Upconverting nanoparticles as nanotransducers for photodynamic therapy in cancer cells," *Nanomedicine*, vol. 3, no. 1, pp. 73–82, Jan. 2008.
- [56] H. S. Mader, P. Kele, S. M. Saleh, and O. S. Wolfbeis, "Upconverting luminescent nanoparticles for use in bioconjugation and bioimaging," *Curr. Opin. Chem. Biol.*, vol. 14, no. 5, pp. 582–596, 2010.
- [57] R. Tian *et al.*, "Construction of lanthanide-doped upconversion nanoparticle-Uelx Europaeus Agglutinin-I bioconjugates with brightness red emission for ultrasensitive in vivo imaging of colorectal tumor," *Biomaterials*, vol. 212, pp. 64–72, 2019.
- [58] X. J. Li, K. J. Wu, W. Q. Zhang, and Z. G. Qi, "Ln 3 + DOPED UPCONVERSION NANOPARTICLES FOR POTENTIAL DUAL MODAL BIO-IMAGING APPLICATION," vol. 13, no. 3, pp. 595–601, 2018.

- [59] F. W. Pratiwi, C. W. Kuo, B.-C. Chen, and P. Chen, "Recent advances in the use of fluorescent nanoparticles for bioimaging," *Nanomedicine*, Jul. 2019.
- [60] M.-K. Tsang, Y.-T. Wong, and J. Hao, "Upconversion Nanomaterials for Biodetection and Multimodal Bioimaging Using Photoluminescence BT - Nanotechnology Characterization Tools for Biosensing and Medical Diagnosis," C. S. S. R. Kumar, Ed. Berlin, Heidelberg: Springer Berlin Heidelberg, 2018, pp. 249–275.
- [61] Q. Liu, M. Xu, T. Yang, B. Tian, X. Zhang, and F. Li, "Highly Photostable Near-IR-Excitation Upconversion Nanocapsules Based on Triplet–Triplet Annihilation for in Vivo Bioimaging Application," *ACS Appl. Mater. Interfaces*, vol. 10, no. 12, pp. 9883–9888, Mar. 2018.
- [62] T. Vaneckova *et al.*, "Upconversion nanoparticle bioconjugates characterized by capillary electrophoresis," *Electrophoresis*, vol. 39, no. 17, pp. 2246–2252, Sep. 2018.
- [63] Y. Sun *et al.*, "A supramolecular self-assembly strategy for upconversion nanoparticle bioconjugation," *Chem. Commun.*, vol. 54, no. 31, pp. 3851–3854, 2018.
- [64] N. M. Idris, M. K. Gnanasammandhan, J. Zhang, P. C. Ho, R. Mahendran, and Y. Zhang, "In vivo photodynamic therapy using upconversion nanoparticles as remote-controlled nanotransducers," *Nat. Med.*, vol. 18, pp. 1580–1585, Sep. 2012.
- [65] X. Ran, F. Pu, J. Ren, and X. Qu, "DNA-Regulated Upconverting Nanoparticle Signal Transducers for Multivalued Logic Operation," *Small*, vol. 10, no. 8, pp. 1500–1503, Apr. 2014.
- [66] H. Wang, C. Dong, P. Zhao, S. Wang, Z. Liu, and J. Chang, "Lipid coated upconverting nanoparticles as NIR remote controlled transducer for simultaneous photodynamic therapy and cell imaging," *Int. J. Pharm.*, vol. 466, no. 1, pp. 307–313, 2014.
- [67] M. K. G. Jayakumar, N. M. Idris, and Y. Zhang, "Remote activation of biomolecules in deep tissues using near-infrared-to-UV upconversion nanotransducers," *Proc. Natl. Acad. Sci.*, vol. 109, no. 22, pp. 8483 LP – 8488, May 2012.
- [68] M. K. Thakur et al., "Optically coupled engineered upconversion nanoparticles and

- graphene for a high responsivity broadband photodetector," *Nanoscale*, vol. 11, no. 19, pp. 9716–9725, 2019.
- [69] Y. Zhang *et al.*, "KMnF3:Yb3+,Er3+ Core-Active-Shell Nanoparticles with Broadband Down-Shifting Luminescence at 1.5 μm for Polymer-Based Waveguide Amplifiers," *Nanomaterials*, vol. 9, no. 3, 2019.
- [70] L. Cheng et al., "Facile Preparation of Multifunctional Upconversion Nanoprobes for Multimodal Imaging and Dual-Targeted Photothermal Therapy," Angew. Chemie Int. Ed., vol. 50, no. 32, pp. 7385–7390, Aug. 2011.
- [71] H. Xu, L. Cheng, C. Wang, X. Ma, Y. Li, and Z. Liu, "Polymer encapsulated upconversion nanoparticle/iron oxide nanocomposites for multimodal imaging and magnetic targeted drug delivery," *Biomaterials*, vol. 32, no. 35, pp. 9364–9373, 2011.
- [72] Y. Liu *et al.*, "Amplified stimulated emission in upconversion nanoparticles for superresolution nanoscopy," *Nature*, vol. 543, pp. 229–233, Feb. 2017.
- [73] Q. Zhan *et al.*, "Achieving high-efficiency emission depletion nanoscopy by employing cross relaxation in upconversion nanoparticles," *Nat. Commun.*, vol. 8, no. 1, p. 1058, 2017.
- [74] D. Yang *et al.*, "Ultra-small BaGdF5-based upconversion nanoparticles as drug carriers and multimodal imaging probes," *Biomaterials*, vol. 35, no. 6, pp. 2011–2023, 2014.
- [75] R. Scheps, "Upconversion laser processes," *Prog. Quantum Electron.*, vol. 20, no. 4, pp. 271–358, 1996.
- [76] E. Downing, L. Hesselink, J. Ralston, and R. Macfarlane, "A Three-Color, Solid-State, Three-Dimensional Display," *Science* (80-.)., vol. 273, no. 5279, pp. 1185–1189, 2006.
- [77] C.R. Ronda, "Physics and chemistry of luminescent materials," in *Physics and chemistry of luminescent materials*, 2000, pp. 123–128.
- [78] M. Haase and H. Schäfer, "Upconverting Nanoparticles," *Angew. Chemie Int. Ed.*, vol. 50, no. 26, pp. 5808–5829, Jun. 2011.
- [79] M.-F. Joubert, "Photon avalanche upconversion in rare earth laser materials," Opt.

- Mater. (Amst)., vol. 11, no. 2, pp. 181–203, 1999.
- [80] S. D. Jackson, "Cross relaxation and energy transfer upconversion processes relevant to the functioning of 2 μm Tm3+-doped silica fibre lasers," *Opt. Commun.*, vol. 230, no. 1, pp. 197–203, 2004.
- [81] F. van de Rijke *et al.*, "Up-converting phosphor reporters for nucleic acid microarrays," *Nat. Biotechnol.*, vol. 19, no. 3, pp. 273–276, 2001.
- [82] J. Hampl *et al.*, "Upconverting Phosphor Reporters in Immunochromatographic Assays," *Anal. Biochem.*, vol. 288, no. 2, pp. 176–187, 2001.
- [83] S. F. Lim *et al.*, "In Vivo and Scanning Electron Microscopy Imaging of Upconverting Nanophosphors in Caenorhabditis elegans," *Nano Lett.*, vol. 6, no. 2, pp. 169–174, Feb. 2006.
- [84] H. Zhang, Y. Li, I. A. Ivanov, Y. Qu, Y. Huang, and X. Duan, "Plasmonic Modulation of the Upconversion Fluorescence in NaYF4:Yb/Tm Hexaplate Nanocrystals Using Gold Nanoparticles or Nanoshells," *Angew. Chemie Int. Ed.*, vol. 49, no. 16, pp. 2865–2868, Apr. 2010.
- [85] S. Eustis and M. A. El-Sayed, "Why gold nanoparticles are more precious than pretty gold: Noble metal surface plasmon resonance and its enhancement of the radiative and nonradiative properties of nanocrystals of different shapes," *Chem. Soc. Rev.*, vol. 35, no. 3, pp. 209–217, 2006.
- [86] W. L. Barnes, A. Dereux, and T. W. Ebbesen, "Surface plasmon subwavelength optics," *Nature*, vol. 424, no. 6950, pp. 824–830, 2003.
- [87] J.-C. Boyer, F. Vetrone, L. A. Cuccia, and J. A. Capobianco, "Synthesis of Colloidal Upconverting NaYF<sub>4</sub> Nanocrystals Doped with Er<sup>3+</sup>,Yb<sup>3+</sup> and Tm<sup>3+</sup>,Yb<sup>3+</sup> via Thermal Decomposition of Lanthanide Trifluoroacetate Precursors," *J. Am. Chem. Soc*, vol. 128, no. 23, pp. 7444–7445, 2006.
- [88] J.-C. Boyer, F. Vetrone, L. A. Cuccia, and J. A. Capobianco, "Synthesis of Colloidal Upconverting NaYF4 Nanocrystals Doped with Er3+, Yb3+ and Tm3+, Yb3+ via Thermal Decomposition of Lanthanide Trifluoroacetate Precursors," *J. Am. Chem.*

- Soc., vol. 128, no. 23, pp. 7444-7445, 2006.
- [89] Z. Li and Y. Zhang, "An efficient and user-friendly method for the synthesis of hexagonal-phase {NaYF}4:Yb, Er/Tm nanocrystals with controllable shape and upconversion fluorescence," *Nanotechnology*, vol. 19, no. 34, p. 345606, Jul. 2008.
- [90] Y. Dong *et al.*, "Blue upconversion luminescence generation in Ce3\$+\$:Gd2SiO5 crystals by infrared femtosecond laser irradiation," *Opt. Express*, vol. 14, no. 5, pp. 1899–1904, Mar. 2006.
- [91] L. Wang and Y. Li, "Controlled Synthesis and Luminescence of Lanthanide Doped NaYF4 Nanocrystals," *Chem. Mater.*, vol. 19, no. 4, pp. 727–734, Feb. 2007.
- [92] Y. Sun, H. Liu, X. Wang, X. Kong, and H. Zhang, "Optical Spectroscopy and Visible Upconversion Studies of YVO4:Er3+ Nanocrystals Synthesized by a Hydrothermal Process," *Chem. Mater.*, vol. 18, no. 11, pp. 2726–2732, May 2006.
- [93] C. Li, Z. Quan, J. Yang, P. Yang, and J. Lin, "Highly Uniform and Monodisperse β-NaYF4:Ln3+ (Ln = Eu, Tb, Yb/Er, and Yb/Tm) Hexagonal Microprism Crystals: Hydrothermal Synthesis and Luminescent Properties," *Inorg. Chem.*, vol. 46, no. 16, pp. 6329–6337, Aug. 2007.
- [94] C. Mi, Z. Tian, C. Cao, Z. Wang, C. Mao, and S. Xu, "Novel Microwave-Assisted Solvothermal Synthesis of NaYF4:Yb,Er Upconversion Nanoparticles and Their Application in Cancer Cell Imaging," *Langmuir*, vol. 27, no. 23, pp. 14632–14637, Dec. 2011.
- [95] G. Yi *et al.*, "Synthesis, Characterization, and Biological Application of Size-Controlled Nanocrystalline NaYF4:Yb,Er Infrared-to-Visible Up-Conversion Phosphors," *Nano Lett.*, vol. 4, no. 11, pp. 2191–2196, Nov. 2004.
- [96] Y. Wei, F. Lu, X. Zhang, and D. Chen, "Synthesis of Oil-Dispersible Hexagonal-Phase and Hexagonal-Shaped NaYF4:Yb,Er Nanoplates," *Chem. Mater.*, vol. 18, no. 24, pp. 5733–5737, Nov. 2006.
- [97] Y. Sun *et al.*, "Controlled synthesis and morphology dependent upconversion luminescence of NaYF4:Yb, Er nanocrystals," *Nanotechnology*, vol. 18, no. 27, p.

- 275609, 2007.
- [98] G.-S. Yi and G.-M. Chow, "Water-Soluble NaYF4:Yb,Er(Tm)/NaYF4/Polymer Core/Shell/Shell Nanoparticles with Significant Enhancement of Upconversion Fluorescence," *Chem. Mater.*, vol. 19, no. 3, pp. 341–343, Feb. 2007.
- [99] J.-H. Zeng, J. Su, Z.-H. Li, R.-X. Yan, and Y.-D. Li, "Synthesis and Upconversion Luminescence of Hexagonal-Phase NaYF4:Yb, Er3+ Phosphors of Controlled Size and Morphology," *Adv. Mater.*, vol. 17, no. 17, pp. 2119–2123, Sep. 2005.
- [100] H.-X. Mai *et al.*, "High-Quality Sodium Rare-Earth Fluoride Nanocrystals: Controlled Synthesis and Optical Properties," *J. Am. Chem. Soc.*, vol. 128, no. 19, pp. 6426–6436, May 2006.
- [101] F. Wang *et al.*, "Tuning upconversion through energy migration in core–shell nanoparticles," *Nat. Mater.*, vol. 10, pp. 968–973, Oct. 2011.
- [102] H. Schäfer, P. Ptacek, H. Eickmeier, and M. Haase, "Synthesis of Hexagonal Yb3+,Er3+-Doped NaYF4 Nanocrystals at Low Temperature," *Adv. Funct. Mater.*, vol. 19, no. 19, pp. 3091–3097, 2009.
- [103] C. Zhang and J. Chen, "Facile EG/ionic liquid interfacial synthesis of uniform RE3+ doped NaYF4 nanocubes," *Chem. Commun.*, vol. 46, no. 4, pp. 592–594, 2010.
- [104] E. R. Cooper, C. D. Andrews, P. S. Wheatley, P. B. Webb, P. Wormald, and R. E. Morris, "Ionic liquids and eutectic mixtures as solvent and template in synthesis of zeolite analogues," *Nature*, vol. 430, no. 7003, pp. 1012–1016, 2004.
- [105] X. Wang, J. Zhuang, Q. Peng, and Y. Li, "A general strategy for nanocrystal synthesis," *Nature*, vol. 437, no. 7055, pp. 121–124, 2005.
- [106] I. V Kubrakova and E. S. Toropchenova, "Microwave heating for enhancing efficiency of analytical operations (Review)," *Inorg. Mater.*, vol. 44, no. 14, pp. 1509–1519, 2008.
- [107] Y.-J. Zhu, W.-W. Wang, R.-J. Qi, and X.-L. Hu, "Microwave-Assisted Synthesis of Single-Crystalline Tellurium Nanorods and Nanowires in Ionic Liquids," *Angew. Chemie Int. Ed.*, vol. 43, no. 11, pp. 1410–1414, Mar. 2004.

- [108] H.-Q. Wang and T. Nann, "Monodisperse Upconverting Nanocrystals by Microwave-Assisted Synthesis," *ACS Nano*, vol. 3, no. 11, pp. 3804–3808, Nov. 2009.
- [109] A. B. Panda, G. Glaspell, and M. S. El-Shall, "Microwave Synthesis and Optical Properties of Uniform Nanorods and Nanoplates of Rare Earth Oxides," *J. Phys. Chem. C*, vol. 111, no. 5, pp. 1861–1864, Feb. 2007.
- [110] S. Beyazit et al., "Versatile Synthetic Strategy for Coating Upconverting Nanoparticles with Polymer Shells through Localized Photopolymerization by Using the Particles as Internal Light Sources," Angew. Chemie Int. Ed., vol. 53, no. 34, pp. 8919–8923, Aug. 2014.
- [111] F. Wang, D. Banerjee, Y. Liu, X. Chen, and X. Liu, "Upconversion nanoparticles in biological labeling {,} imaging {,} and therapy," *Analyst*, vol. 135, no. 8, pp. 1839–1854, 2010.
- [112] D. K. Chatterjee, M. K. Gnanasammandhan, and Y. Zhang, "Small Upconverting Fluorescent Nanoparticles for Biomedical Applications," *Small*, vol. 6, no. 24, pp. 2781–2795, Dec. 2010.
- [113] G. Jiang, J. Pichaandi, N. J. J. Johnson, R. D. Burke, and F. C. J. M. van Veggel, "An Effective Polymer Cross-Linking Strategy To Obtain Stable Dispersions of Upconverting NaYF4 Nanoparticles in Buffers and Biological Growth Media for Biolabeling Applications," *Langmuir*, vol. 28, no. 6, pp. 3239–3247, Feb. 2012.
- [114] S. Dühnen and M. Haase, "Study on the Intermixing of Core and Shell in NaEuF4/NaGdF4 Core/Shell Nanocrystals," *Chem. Mater.*, vol. 27, no. 24, pp. 8375–8386, Dec. 2015.
- [115] M. D. Wisser *et al.*, "Strain-Induced Modification of Optical Selection Rules in Lanthanide-Based Upconverting Nanoparticles," *Nano Lett.*, vol. 15, no. 3, pp. 1891–1897, Mar. 2015.
- [116] O. S. N. Ghosh, "Chitosan conjugation: A facile approach to enhance the cell viability of LaF3: Yb, Er upconverting nanotransducers in human breast cancer cells," *Carbohydr. Polym.*, Dec. 2014.

- [117] X. Xu *et al.*, "α-NaYb(Mn)F4:Er3+/Tm3+@NaYF4 UCNPs as 'Band-Shape' Luminescent Nanothermometers over a Wide Temperature Range," *ACS Appl. Mater. Interfaces*, vol. 7, no. 37, pp. 20813–20819, Sep. 2015.
- [118] S. Chen *et al.*, "Near-infrared deep brain stimulation via upconversion nanoparticle—mediated optogenetics," *Science* (80-. )., vol. 359, no. 6376, pp. 679 LP 684, Feb. 2018.
- [119] X. Chen *et al.*, "Theranostic system based on NaY(Mn)F4:Yb/Er upconversion nanoparticles with multi-drug resistance reversing ability," *J. Mater. Chem. B*, vol. 6, no. 21, pp. 3586–3599, 2018.
- [120] G. Jalani, R. Naccache, D. H. Rosenzweig, L. Haglund, F. Vetrone, and M. Cerruti, "Photocleavable Hydrogel-Coated Upconverting Nanoparticles: A Multifunctional Theranostic Platform for NIR Imaging and On-Demand Macromolecular Delivery," *J. Am. Chem. Soc.*, vol. 138, no. 3, pp. 1078–1083, Jan. 2016.
- [121] L. Rao *et al.*, "Cancer Cell Membrane-Coated Upconversion Nanoprobes for Highly Specific Tumor Imaging," *Adv. Mater.*, vol. 28, no. 18, pp. 3460–3466, May 2016.
- [122] Z.-Q. Liang, S.-L. Zhao, Y. Cui, L.-J. Tian, J.-J. Zhang, and Z. Xu, "Phase transformation and morphology tuning ofβ-NaYF4:Yb3+,Er3+nanocrystals through K+ions codoping," *Chinese Phys. B*, vol. 24, no. 3, p. 37801, 2015.
- [123] J. Yang *et al.*, "Size-Tailored Synthesis and Luminescent Properties of One-Dimensional Gd2O3:Eu3+ Nanorods and Microrods," *J. Phys. Chem. C*, vol. 111, no. 49, pp. 18148–18154, Dec. 2007.
- [124] X. Ye *et al.*, "Morphologically controlled synthesis of colloidal upconversion nanophosphors and their shape-directed self-assembly," *Proc. Natl. Acad. Sci.*, vol. 107, no. 52, pp. 22430 LP 22435, Dec. 2010.
- [125] Q. Dou and Y. Zhang, "Tuning of the Structure and Emission Spectra of Upconversion Nanocrystals by Alkali Ion Doping," *Langmuir*, vol. 27, no. 21, pp. 13236–13241, Nov. 2011.
- [126] X. Xie, N. Gao, R. Deng, Q. Sun, Q.-H. Xu, and X. Liu, "Mechanistic Investigation of

- Photon Upconversion in Nd3+-Sensitized Core-Shell Nanoparticles," *J. Am. Chem. Soc.*, vol. 135, no. 34, pp. 12608–12611, Aug. 2013.
- [127] H.-X. Mai, Y.-W. Zhang, L.-D. Sun, and C.-H. Yan, "Highly Efficient Multicolor Up-Conversion Emissions and Their Mechanisms of Monodisperse NaYF4:Yb,Er Core and Core/Shell-Structured Nanocrystals," *J. Phys. Chem. C*, vol. 111, no. 37, pp. 13721–13729, 2007.
- [128] Q. Lü, F. Guo, L. Sun, A. Li, and L. Zhao, "Silica-/titania-coated Y2O3:Tm3+, Yb3+ nanoparticles with improvement in upconversion luminescence induced by different thickness shells," *J. Appl. Phys.*, vol. 103, no. 12, p. 123533, Jun. 2008.
- [129] Z. Chen *et al.*, "Versatile Synthesis Strategy for Carboxylic Acid–functionalized Upconverting Nanophosphors as Biological Labels," *J. Am. Chem. Soc.*, vol. 130, no. 10, pp. 3023–3029, Mar. 2008.
- [130] E. A. Grebenik *et al.*, "Feasibility study of the optical imaging of a breast cancer lesion labeled with upconversion nanoparticle biocomplexes," *J. Biomed. Opt.*, vol. 18, no. 7, pp. 1–11, Jul. 2013.
- [131] S. Shikha, X. Zheng, and Y. Zhang, "Upconversion Nanoparticles-Encoded Hydrogel Microbeads-Based Multiplexed Protein Detection," *Nano-Micro Lett.*, vol. 10, no. 2, p. 31, 2017.
- [132] U. Kostiv *et al.*, "RGDS- and TAT-Conjugated Upconversion of NaYF4:Yb3+/Er3+&SiO2 Nanoparticles: In Vitro Human Epithelioid Cervix Carcinoma Cellular Uptake, Imaging, and Targeting," *ACS Appl. Mater. Interfaces*, vol. 8, no. 31, pp. 20422–20431, Aug. 2016.
- [133] M.-K. Tsang, W. Ye, G. Wang, J. Li, M. Yang, and J. Hao, "Ultrasensitive Detection of Ebola Virus Oligonucleotide Based on Upconversion Nanoprobe/Nanoporous Membrane System," ACS Nano, vol. 10, no. 1, pp. 598–605, Jan. 2016.
- [134] S. Doughan, Y. Han, U. Uddayasankar, and U. J. Krull, "Solid-Phase Covalent Immobilization of Upconverting Nanoparticles for Biosensing by Luminescence Resonance Energy Transfer," ACS Appl. Mater. Interfaces, vol. 6, no. 16, pp. 14061–

- 14068, Aug. 2014.
- [135] M. Kamimura, D. Miyamoto, Y. Saito, K. Soga, and Y. Nagasaki, "Preparation of PEG and Protein Co-immobilized Upconversion Nanophosphors as Near-infrared Biolabeling Materials," *J. Photopolym. Sci. Technol.*, vol. 21, no. 2, pp. 183–187, 2008.
- [136] M. Freitag, N. Möller, A. Rühling, C. A. Strassert, B. J. Ravoo, and F. Glorius, "Photocatalysis in the Dark: Near-Infrared Light Driven Photoredox Catalysis by an Upconversion Nanoparticle/Photocatalyst System," *ChemPhotoChem*, vol. 3, no. 1, pp. 24–27, Jan. 2019.
- [137] O. Faklaris *et al.*, "Detection of Single Photoluminescent Diamond Nanoparticles in Cells and Study of the Internalization Pathway," *Small*, vol. 4, no. 12, pp. 2236–2239, Dec. 2008.
- [138] I. P. Chang, K. C. Hwang, and C.-S. Chiang, "Preparation of Fluorescent Magnetic Nanodiamonds and Cellular Imaging," *J. Am. Chem. Soc.*, vol. 130, no. 46, pp. 15476– 15481, Nov. 2008.
- [139] F. Vetrone and J. A. Capobianco, "Lanthanide-doped fluoride nanoparticles: luminescence, upconversion, and biological applications," *Int. J. Nanotechnol.*, vol. 5, no. 9–12, pp. 1306–1339, Jan. 2008.
- [140] Y.-Z. Shao *et al.*, "A novel one-step synthesis of Gd3+-incorporated mesoporous SiO2 nanoparticles for use as an efficient MRI contrast agent," *Contrast Media Mol. Imaging*, vol. 6, no. 2, pp. 110–118, Mar. 2011.
- [141] J.-C. Boyer, M.-P. Manseau, J. I. Murray, and F. C. J. M. van Veggel, "Surface Modification of Upconverting NaYF4 Nanoparticles with PEG-Phosphate Ligands for NIR (800 nm) Biolabeling within the Biological Window," *Langmuir*, vol. 26, no. 2, pp. 1157–1164, Jan. 2010.
- [142] A. Dong *et al.*, "A Generalized Ligand-Exchange Strategy Enabling Sequential Surface Functionalization of Colloidal Nanocrystals," *J. Am. Chem. Soc.*, vol. 133, no. 4, pp. 998–1006, Feb. 2011.

- [143] M. Nichkova, D. Dosev, S. J. Gee, B. D. Hammock, and I. M. Kennedy, "Microarray Immunoassay for Phenoxybenzoic Acid Using Polymer Encapsulated Eu:Gd2O3 Nanoparticles as Fluorescent Labels," *Anal. Chem.*, vol. 77, no. 21, pp. 6864–6873, Nov. 2005.
- [144] Q. Liu, C. Li, T. Yang, T. Yi, and F. Li, "'Drawing' upconversion nanophosphors into water through host–guest interaction," *Chem. Commun.*, vol. 46, no. 30, pp. 5551–5553, 2010.
- [145] L. Wang, P. Li, and L. Wang, "Luminescent and hydrophilic LaF3-polymer nanocomposite for DNA detection," *Luminescence*, vol. 24, no. 1, pp. 39–44, Jan. 2009.
- [146] A. Son, A. Dhirapong, D. K. Dosev, I. M. Kennedy, R. H. Weiss, and K. R. Hristova, "Rapid and quantitative DNA analysis of genetic mutations for polycystic kidney disease (PKD) using magnetic/luminescent nanoparticles," *Anal. Bioanal. Chem.*, vol. 390, no. 7, pp. 1829–1835, 2008.
- [147] L. Cheng, K. Yang, S. Zhang, M. Shao, S. Lee, and Z. Liu, "Highly-sensitive multiplexed in vivo imaging using pegylated upconversion nanoparticles," *Nano Res.*, vol. 3, no. 10, pp. 722–732, 2010.
- [148] L. Cheng, K. Yang, M. Shao, S.-T. Lee, and Z. Liu, "Multicolor In Vivo Imaging of Upconversion Nanoparticles with Emissions Tuned by Luminescence Resonance Energy Transfer," *J. Phys. Chem. C*, vol. 115, no. 6, pp. 2686–2692, Feb. 2011.
- [149] Y. Ma *et al.*, "Labeling and long-term tracking of bone marrow mesenchymal stem cells in vitro using NaYF4:Yb3+,Er3+ upconversion nanoparticles," *Acta Biomater.*, vol. 42, pp. 199–208, 2016.
- [150] M. Nyk, R. Kumar, T. Y. Ohulchanskyy, E. J. Bergey, and P. N. Prasad, "High Contrast in Vitro and in Vivo Photoluminescence Bioimaging Using Near Infrared to Near Infrared Up-Conversion in Tm3+ and Yb3+ Doped Fluoride Nanophosphors," *Nano Lett.*, vol. 8, no. 11, pp. 3834–3838, Nov. 2008.
- [151] Q. Zhan et al., "Using 915 nm Laser Excited Tm3+/Er3+/Ho3+-Doped NaYbF4

- Upconversion Nanoparticles for in Vitro and Deeper in Vivo Bioimaging without Overheating Irradiation," *ACS Nano*, vol. 5, no. 5, pp. 3744–3757, May 2011.
- [152] Y.-H. Chien *et al.*, "Near-Infrared Light Photocontrolled Targeting, Bioimaging, and Chemotherapy with Caged Upconversion Nanoparticles in Vitro and in Vivo," *ACS Nano*, vol. 7, no. 10, pp. 8516–8528, Oct. 2013.
- [153] X. Zhu, J. Zhou, M. Chen, M. Shi, W. Feng, and F. Li, "Core–shell Fe3O4@NaLuF4:Yb,Er/Tm nanostructure for MRI, CT and upconversion luminescence tri-modality imaging," *Biomaterials*, vol. 33, no. 18, pp. 4618–4627, 2012.
- [154] M. He et al., "Dual Phase-Controlled Synthesis of Uniform Lanthanide-Doped NaGdF4 Upconversion Nanocrystals Via an OA/Ionic Liquid Two-Phase System for In Vivo Dual-Modality Imaging," Adv. Funct. Mater., vol. 21, no. 23, pp. 4470–4477, 2011.
- [155] H. Xing *et al.*, "Multifunctional nanoprobes for upconversion fluorescence, MR and CT trimodal imaging," *Biomaterials*, vol. 33, no. 4, pp. 1079–1089, 2012.
- [156] Y. Il Park *et al.*, "Theranostic Probe Based on Lanthanide-Doped Nanoparticles for Simultaneous In Vivo Dual-Modal Imaging and Photodynamic Therapy," *Adv. Mater.*, vol. 24, no. 42, pp. 5755–5761, Nov. 2012.
- [157] K. Liu *et al.*, "Covalently Assembled NIR Nanoplatform for Simultaneous Fluorescence Imaging and Photodynamic Therapy of Cancer Cells," *ACS Nano*, vol. 6, no. 5, pp. 4054–4062, May 2012.
- [158] H. Guo, H. Qian, N. M. Idris, and Y. Zhang, "Singlet oxygen-induced apoptosis of cancer cells using upconversion fluorescent nanoparticles as a carrier of photosensitizer," *Nanomedicine Nanotechnology, Biol. Med.*, vol. 6, no. 3, pp. 486– 495, 2010.
- [159] S. Cui *et al.*, "Amphiphilic chitosan modified upconversion nanoparticles for in vivo photodynamic therapy induced by near-infrared light," *J. Mater. Chem.*, vol. 22, no. 11, pp. 4861–4873, 2012.

- [160] C. Wang, L. Cheng, H. Xu, and Z. Liu, "Towards whole-body imaging at the single cell level using ultra-sensitive stem cell labeling with oligo-arginine modified upconversion nanoparticles," *Biomaterials*, vol. 33, no. 19, pp. 4872–4881, 2012.
- [161] K. J. Si, Y. Chen, Q. Shi, and W. Cheng, "Nanoparticle Superlattices: The Roles of Soft Ligands," *Adv. Sci.*, vol. 5, no. 1, p. 1700179, Jan. 2018.
- [162] A. Courty, A. Mermet, P. A. Albouy, E. Duval, and M. P. Pileni, "Vibrational coherence of self-organized silver nanocrystals in f.c.c. supra-crystals," *Nat. Mater.*, vol. 4, no. 5, pp. 395–398, 2005.
- [163] J. J. Urban, D. V Talapin, E. V Shevchenko, C. R. Kagan, and C. B. Murray, "Synergism in binary nanocrystal superlattices leads to enhanced p-type conductivity in self-assembled PbTe/Ag2Te thin films," *Nat. Mater.*, vol. 6, no. 2, pp. 115–121, 2007.
- [164] K. C. Ng *et al.*, "Free-Standing Plasmonic-Nanorod Superlattice Sheets," *ACS Nano*, vol. 6, no. 1, pp. 925–934, Jan. 2012.
- [165] K. J. Si *et al.*, "Giant Plasmene Nanosheets, Nanoribbons, and Origami," *ACS Nano*, vol. 8, no. 11, pp. 11086–11093, Nov. 2014.
- [166] E. P. Holowka, D. J. Pochan, and T. J. Deming, "Charged Polypeptide Vesicles with Controllable Diameter," *J. Am. Chem. Soc.*, vol. 127, no. 35, pp. 12423–12428, Sep. 2005.
- [167] T. Fukui *et al.*, "Control over differentiation of a metastable supramolecular assembly in one and two dimensions," *Nat. Chem.*, vol. 9, no. 5, pp. 493–499, 2017.
- [168] J. Kang, D. Miyajima, T. Mori, Y. Inoue, Y. Itoh, and T. Aida, "A rational strategy for the realization of chain-growth supramolecular polymerization," *Science* (80-.)., vol. 347, no. 6222, pp. 646–651, Feb. 2015.
- [169] E. V Shevchenko, D. V Talapin, A. L. Rogach, A. Kornowski, M. Haase, and H. Weller, "Colloidal Synthesis and Self-Assembly of CoPt3 Nanocrystals [J. Am. Chem. Soc. 2002, 124, 11480–11485].," J. Am. Chem. Soc., vol. 124, no. 46, p. 11480–11485, Nov. 2002.
- [170] E. V Shevchenko et al., "Self-Assembled Binary Superlattices of CdSe and Au

- Nanocrystals and Their Fluorescence Properties," *J. Am. Chem. Soc.*, vol. 130, no. 11, pp. 3274–3275, Mar. 2008.
- [171] H. Ma and J. Hao, "Ordered patterns and structures via interfacial self-assembly: superlattices, honeycomb structures and coffee rings," *Chem. Soc. Rev.*, vol. 40, no. 11, pp. 5457–5471, 2011.
- [172] Z. Sumer and A. Striolo, "Nanoparticles shape-specific emergent behaviour on liquid crystal droplets," *Mol. Syst. Des. Eng.*, 2020.
- [173] A. C. Santos *et al.*, "Sonication-assisted Layer-by-Layer self-assembly nanoparticles for resveratrol delivery," *Mater. Sci. Eng. C*, vol. 105, p. 110022, 2019.
- [174] "Peptide Self-Assembly Nanoparticles Loaded with Panobinostat to Activate Latent Human Immunodeficiency Virus," *J. Biomed. Nanotechnol.*, vol. 15, no. 5, pp. 979–992, 2019.
- [175] C. Huang, C. Chang, K. Lee, J. Wang, and C. Liu, "Excitation-Wavelength-Dependent and Substrate-Dependent Photoluminescence From the Nonconjugated Polymeric Thin Film With Self-Assembly Nanoparticles," *IEEE Photonics J.*, vol. 10, no. 6, pp. 1–8, 2018.
- [176] M. Hamer, R. M. Caraballo, P. J. Eaton, and C. Medforth, "Nanoparticles as template for porphyrin nanostructure growth," *J. Porphyr. Phthalocyanines*, vol. 23, no. 04n05, pp. 526–533, Apr. 2019.
- [177] J. Liang, W. Guo, J. Liu, H. Qin, P. Gao, and H. Xiao, "Synthesis of in-situ SiC nanowires by self-assembly nanoparticles on carbon fibers and their photoluminescence properties," *J. Alloys Compd.*, vol. 797, pp. 101–109, 2019.
- [178] Y. Wang *et al.*, "Redox-responsive self-assembly PEG nanoparticle enhanced triptolide for efficient antitumor treatment," *Sci. Rep.*, vol. 8, no. 1, p. 12968, 2018.
- [179] S. Long, Q. Qiao, L. Miao, and Z. Xu, "A self-assembly/disassembly two-photo ratiometric fluorogenic probe for bacteria imaging," *Chinese Chem. Lett.*, vol. 30, no. 3, pp. 573–576, 2019.
- [180] "Virus Envelope-Like Self-Assembled Nanoparticles Based on -CD/PEG for Antigens

- Targeting to Dendritic Cells," *J. Biomed. Nanotechnol.*, vol. 13, no. 11, pp. 1490-1499(10), 2017.
- [181] S. R. Jamnani, H. M. Moghaddam, S. G. Leonardi, and G. Neri, "A novel conductometric sensor based on hierarchical self-assembly nanoparticles Sm2O3 for VOCs monitoring," *Ceram. Int.*, vol. 44, no. 14, pp. 16953–16959, 2018.
- [182] J. Qiu *et al.*, "Preparation and characterization of casein-carrageenan conjugates and self-assembled microcapsules for encapsulation of red pigment from paprika," *Carbohydr. Polym.*, vol. 196, pp. 322–331, 2018.
- [183] Y. Kobayashi and N. Arai, "Janus or homogeneous nanoparticle mediated self-assembly of polymer electrolyte fuel cell membranes," *RSC Adv.*, vol. 8, no. 33, pp. 18568–18575, 2018.
- [184] T. Palacios-Hernandez, H. Luo, E. A. Garcia, L. A. Pacheco, and M. Herrera-Alonso, "Nanoparticles from Amphiphilic Heterografted Macromolecular Brushes with Short Backbones," *Macromolecules*, vol. 51, no. 8, pp. 2831–2837, Apr. 2018.
- [185] A. Popielec, M. Agnes, K. Yannakopoulou, É. Fenyvesi, and T. Loftsson, "Self-assembled cyclodextrin-based nanoparticles for meropenem stabilization," *J. Drug Deliv. Sci. Technol.*, vol. 45, pp. 20–27, 2018.
- [186] V. J. Drew, H.-Y. Huang, Z.-H. Tsai, H.-H. Tsai, and C.-L. Tseng, "Preparation of gelatin/epigallocatechin gallate self-assembly nanoparticles for transdermal drug delivery," *J. Polym. Res.*, vol. 24, no. 11, p. 188, 2017.
- [187] Z. Hou *et al.*, "Nanoparticles of Short Cationic Peptidopolysaccharide Self-Assembled by Hydrogen Bonding with Antibacterial Effect against Multidrug-Resistant Bacteria," *ACS Appl. Mater. Interfaces*, vol. 9, no. 44, pp. 38288–38303, Nov. 2017.
- [188] Y. Fan, J. Yi, Y. Zhang, and W. Yokoyama, "Fabrication of curcumin-loaded bovine serum albumin (BSA)-dextran nanoparticles and the cellular antioxidant activity," *Food Chem.*, vol. 239, pp. 1210–1218, 2018.
- [189] Wang, P. M. Rørvik, A. T. J. van Helvoort, R. Holmestad, T. Grande, and M.-A. Einarsrud, "Self-Assembled Growth of PbTiO3 Nanoparticles into Microspheres and

- Bur-like Structures," Chem. Mater., vol. 19, no. 9, pp. 2213–2221, May 2007.
- [190] S. Kundu, A. Das, A. Basu, M. F. Abdullah, and A. Mukherjee, "Guar gum benzoate nanoparticle reinforced gelatin films for enhanced thermal insulation, mechanical and antimicrobial properties," *Carbohydr. Polym.*, vol. 170, pp. 89–98, 2017.
- [191] Y. Hao *et al.*, "Covalent self-assembled nanoparticles with pH-dependent enhanced tumor retention and drug release for improving tumor therapeutic efficiency," *J. Mater. Chem. B*, vol. 5, no. 11, pp. 2133–2144, 2017.
- [192] M. Gujrati, A. M. Vaidya, M. Mack, D. Snyder, A. Malamas, and Z.-R. Lu, "Cancer Therapy: Targeted Dual pH-Sensitive Lipid ECO/siRNA Self-Assembly Nanoparticles Facilitate In Vivo Cytosolic sieIF4E Delivery and Overcome Paclitaxel Resistance in Breast Cancer Therapy (Adv. Healthcare Mater. 22/2016)," *Adv. Healthc. Mater.*, vol. 5, no. 22, p. 2836, Nov. 2016.
- [193] S. Kundu *et al.*, "Antifungal ouzo nanoparticles from guar gum propionate," *RSC Adv.*, vol. 6, no. 108, pp. 106563–106571, 2016.
- [194] S. Guo, K. Pham, D. Li, S. R. Penzak, and X. Dong, "Novel in situ self-assembly nanoparticles for formulating a poorly water-soluble drug in oral solid granules, improving stability, palatability, and bioavailability," *Int. J. Nanomedicine*, vol. 11, pp. 1451–1460, Apr. 2016.
- [195] K. Pham, D. Li, S. Guo, S. Penzak, and X. Dong, "Development and in vivo evaluation of child-friendly lopinavir/ritonavir pediatric granules utilizing novel in situ self-assembly nanoparticles," *J. Control. Release*, vol. 226, pp. 88–97, 2016.
- [196] B. Shi, K. Jie, Y. Zhou, J. Zhou, D. Xia, and F. Huang, "Nanoparticles with Near-Infrared Emission Enhanced by Pillararene-Based Molecular Recognition in Water," *J. Am. Chem. Soc.*, vol. 138, no. 1, pp. 80–83, Jan. 2016.
- [197] X. Fan, Q. He, S. Sun, H. Li, Y. Pei, and Y. Xu, "Nanoparticles self-assembled from multiple interactions: a novel near-infrared fluorescent sensor for the detection of serum albumin in human sera and turn-on live-cell imaging," *Chem. Commun.*, vol. 52, no. 6, pp. 1178–1181, 2016.

- [198] Y. Liu, J. Liang, S. Wei, L. Liu, and M. Liao, "Nanoparticles based on β-conglycinin and chitosan: Self-assembly, characterization, and drug delivery," *J. Appl. Polym. Sci.*, vol. 132, no. 22, Jun. 2015.
- [199] C. Schiraldi *et al.*, "Nanoparticles for the delivery of zoledronic acid to prostate cancer cells: A comparative analysis through time lapse video-microscopy technique," *Cancer Biol. Ther.*, vol. 15, no. 11, pp. 1524–1532, Nov. 2014.
- [200] X.-Q. Zhang *et al.*, "Nanoparticles Containing a Liver X Receptor Agonist Inhibit Inflammation and Atherosclerosis," *Adv. Healthc. Mater.*, vol. 4, no. 2, pp. 228–236, Jan. 2015.
- [201] Y. Wang *et al.*, "Self-assembled nanoparticles of cholesterol-modifiedO-carboxymethyl chitosan as a novel carrier for paclitaxel," *Nanotechnology*, vol. 19, no. 14, p. 145101, 2008.
- [202] L.-Y. Chen, J.-Q. Xu, H. Choi, H. Konishi, S. Jin, and X.-C. Li, "Rapid control of phase growth by nanoparticles," *Nat. Commun.*, vol. 5, no. 1, p. 3879, 2014.
- [203] S. Mukherjee, A. Datta, N. Biswas, A. Giglia, and S. Nannarone, "How Langmuir—Blodgett trilayers act as templates for directed self-assembly of nanoparticles," *Mater. Res. Express*, vol. 1, no. 2, p. 25006, 2014.
- [204] A. de la Escosura-Muñiz, M. Espinoza-Castañeda, M. Hasegawa, L. Philippe, and A. Merkoçi, "Nanoparticles-based nanochannels assembled on a plastic flexible substrate for label-free immunosensing," *Nano Res.*, vol. 8, no. 4, pp. 1180–1188, 2015.
- [205] C. Yan *et al.*, "Synthesis of Tat tagged and folate modified N-succinyl-chitosan self-assembly nanoparticles as a novel gene vector," *Int. J. Biol. Macromol.*, vol. 72, pp. 751–756, 2015.
- [206] S. ICHIKAWA, S. IWAMOTO, and J. WATANABE, "Formation of Biocompatible Nanoparticles by Self-Assembly of Enzymatic Hydrolysates of Chitosan and Carboxymethyl Cellulose," *Biosci. Biotechnol. Biochem.*, vol. 69, no. 9, pp. 1637– 1642, Jan. 2005.
- [207] Y. Li, J. Zhang, Z. Liu, M. Liu, H. Lin, and R. Che, "Morphology-dominant

- microwave absorption enhancement and electron tomography characterization of CoO self-assembly 3D nano-flowers," *J. Mater. Chem. C*, vol. 2, no. 26, pp. 5216–5222, 2014.
- [208] J. P. Salvage *et al.*, "Novel biocompatible phosphorylcholine-based self-assembled nanoparticles for drug delivery," *J. Control. Release*, vol. 104, no. 2, pp. 259–270, 2005.
- [209] C.-L. Zhang and S.-H. Yu, "Nanoparticles meet electrospinning: recent advances and future prospects," *Chem. Soc. Rev.*, vol. 43, no. 13, pp. 4423–4448, 2014.
- [210] M. Chen *et al.*, "Preparation and characterization of self-assembled nanoparticles of 6-O-cholesterol-modified chitosan for drug delivery," *Carbohydr. Polym.*, vol. 84, no. 4, pp. 1244–1251, 2011.
- [211] C. X. Chen Kuan-ting, Yao Jun, Ruan Wen-hui, Wei Qin-jun, Lu Ya-jie, "Preparation of a Novel Self-assembly Nanoparticle Based on Amphiphilic γ-Polyglutamic Acid Derivatives as a Protein Carrier," *China Biotechnol.*, vol. 33, no. 4, pp. 101–105, 2013.
- [212] J.-L. Feng *et al.*, "Fabrication and Characterization of Stable Soy β-Conglycinin—Dextran Core—Shell Nanogels Prepared via a Self-Assembly Approach at the Isoelectric Point," *J. Agric. Food Chem.*, vol. 63, no. 26, pp. 6075–6083, Jul. 2015.
- [213] H. Hong, Cheol Am; Jeong, Eun Hye; Lee, "Self-assembled 3-D nucleic acid nanoparticles for the efficient delivery of therapeutic RNAs," *Polym. Sci. Technol.*, vol. 24, no. 3, pp. 250–253, 2013.
- [214] "Novel Nanoparticles Generated by Polymeric Amphiphiles with Conjugated Small Molecules for Anti-Tumor Drug Delivery," *J. Biomed. Nanotechnol.*, vol. 9, no. 8, 2013.
- [215] Z. Khatun, M. Nurunnabi, G. R. Reeck, K. J. Cho, and Y. Lee, "Oral delivery of taurocholic acid linked heparin–docetaxel conjugates for cancer therapy," *J. Control. Release*, vol. 170, no. 1, pp. 74–82, 2013.
- [216] M. Fan, "Fabrication, modification and self-assembly of metallic nano-particles for localized surface plasmon resonance and surface enhanced vibrational spectroscopy

- applications," *Available from Univ. Vitoria Libr.*, p. http://dspace.library.uvic.ca/handle/1828/4269, 2012.
- [217] Z. Hussain, H. Katas, M. C. I. Mohd Amin, E. Kumolosasi, F. Buang, and S. Sahudin, "Self-assembled polymeric nanoparticles for percutaneous co-delivery of hydrocortisone/hydroxytyrosol: An ex vivo and in vivo study using an NC/Nga mouse model," *Int. J. Pharm.*, vol. 444, no. 1, pp. 109–119, 2013.
- [218] "Monodisperse Nanoparticles from Self-Assembling Amphiphilic Cyclodextrins: Modulable Tools for the Encapsulation and Controlled Release of Pharmaceuticals," *Med. Chem. (Los. Angeles).*, vol. 8, no. 4, 2012.
- [219] M. Marra *et al.*, "New self-assembly nanoparticles and stealth liposomes for the delivery of zoledronic acid: a comparative study," *Biotechnol. Adv.*, vol. 30, no. 1, pp. 302–309, 2012.
- [220] C. Hanske *et al.*, "Solvent-Assisted Self-Assembly of Gold Nanorods into Hierarchically Organized Plasmonic Mesostructures," *ACS Appl. Mater. Interfaces*, vol. 11, no. 12, pp. 11763–11771, Mar. 2019.
- [221] R. J. Castellano, C. Akin, G. Giraldo, S. Kim, F. Fornasiero, and J. W. Shan, "Electrokinetics of scalable, electric-field-assisted fabrication of vertically aligned carbon-nanotube/polymer composites," *J. Appl. Phys.*, vol. 117, no. 21, p. 214306, Jun. 2015.
- [222] G. Salzano *et al.*, "Self-assembly nanoparticles for the delivery of bisphosphonates into tumors," *Int. J. Pharm.*, vol. 403, no. 1, pp. 292–297, 2011.
- [223] S. Guo *et al.*, "Amphiphilic and biodegradable methoxy polyethylene glycol-block-(polycaprolactone-graft-poly(2-(dimethylamino)ethyl methacrylate)) as an effective gene carrier," *Biomaterials*, vol. 32, no. 3, pp. 879–889, 2011.
- [224] J. Cao, Y. Chen, N. Chen, and X. Luo, "The preparation of phosphorylcholine-containing poly(Llactide) nanoparticles with solvent evaporation method," *e-Polymers*, vol. 10, no. 1, p. 74, 2010.
- [225] Z. Cao, Q. Yu, H. Xue, G. Cheng, and S. Jiang, "Nanoparticles for Drug Delivery

- Prepared from Amphiphilic PLGA Zwitterionic Block Copolymers with Sharp Contrast in Polarity between Two Blocks," *Angew. Chemie Int. Ed.*, vol. 49, no. 22, pp. 3771–3776, May 2010.
- [226] Y. Gao, Z. Zhang, L. Chen, W. Gu, and Y. Li, "Chitosan N-betainates/DNA self-assembly nanoparticles for gene delivery: In vitro uptake and transfection efficiency," *Int. J. Pharm.*, vol. 371, no. 1, pp. 156–162, 2009.
- [227] I. Hajdu *et al.*, "Nanoparticles prepared by self-assembly of Chitosan and poly-γ-glutamic acid," *Colloid Polym. Sci.*, vol. 286, no. 3, pp. 343–350, 2008.
- [228] R. Nishiyabu *et al.*, "Nanoparticles of Adaptive Supramolecular Networks Self-Assembled from Nucleotides and Lanthanide Ions," *J. Am. Chem. Soc.*, vol. 131, no. 6, pp. 2151–2158, Feb. 2009.
- [229] S. Qu *et al.*, "Nanoparticles, Helical Fibers, and Nanoribbons of an Achiral Twin-Tapered Bi-1,3,4-oxadiazole Derivative with Strong Fluorescence," *Langmuir*, vol. 25, no. 3, pp. 1713–1717, Feb. 2009.
- [230] M. Wang, D. W. P. M. Löwik, A. D. Miller, and M. Thanou, "Targeting the Urokinase Plasminogen Activator Receptor with Synthetic Self-Assembly Nanoparticles," *Bioconjug. Chem.*, vol. 20, no. 1, pp. 32–40, Jan. 2009.
- [231] R. Wang, I. U. Arachchige, S. L. Brock, and G. Mao, "Nanoparticles as Seeds for Organic Crystallization," in *Nanoparticles: Synthesis, Stabilization, Passivation, and Functionalization*, vol. 996, American Chemical Society, 2008, pp. 25–358.
- [232] S. Barik and S. Valiyaveettil, *PMSE 83-Oligo* (p-phenylene) containing Y-shaped chromophore as chemosensor material: Synthesis, characterization and self-assembly study. 2008.
- [233] Y.-H. Lee, C.-S. Tseng, and Y.-L. Wei, "Fabrication and characterization of CdSe/ZnS quantum dots-doped polystyrene microspheres prepared by self-assembly," *J. Mater. Res.*, vol. 27, no. 22, pp. 2829–2836, 2012.
- [234] M. Teshima, "Delivery of liposomal anti-inflammatory agents using chemical modification: development of self-assembly nanoparticles," *Yakuzaigaku*, vol. 67, no.

- 4, pp. 242–245, 2007.
- [235] D. Maysinger, "Nanoparticles and cells: good companions and doomed partnerships," *Org. Biomol. Chem.*, vol. 5, no. 15, pp. 2335–2342, 2007.
- [236] "Nanoparticles from Polylactide and Polyether Block Copolymers: Formation, Properties, Encapsulation, and Release of PyreneFluorescent Model of Hydrophobic Drug," *J. Nanosci. Nanotechnol.*, vol. 6, no. 9–10, pp. 3242–3251, 2006.
- [237] M. Lu and O. Gursky, "Aggregation and fusion of low-density lipoproteins in vivo and in vitro," *Biomol. Concepts*, vol. 4, no. 5, pp. 501–518, 2013.
- [238] J. H. He *et al.*, "Micro-Cantilever Resonance Sensor for Biomolecular Detection by Using Self-Assembly Nano-Particles," in *Proc.SPIE*, 2006, vol. 6112.
- [239] Y. Gohon *et al.*, "Well-Defined Nanoparticles Formed by Hydrophobic Assembly of a Short and Polydisperse Random Terpolymer, Amphipol A8-35," *Langmuir*, vol. 22, no. 3, pp. 1281–1290, Jan. 2006.
- [240] K. Kostarelos and A. D. Miller, "Synthetic, self-assembly ABCD nanoparticles; a structural paradigm for viable synthetic non-viral vectors," *Chem. Soc. Rev.*, vol. 34, no. 11, pp. 970–994, 2005.
- [241] C. Wu, J. Fu, and Y. Zhao, "Novel Nanoparticles Formed via Self-Assembly of Poly(ethylene glycol-b-sebacic anhydride) and Their Degradation in Water," *Macromolecules*, vol. 33, no. 24, pp. 9040–9043, Nov. 2000.
- [242] A. Baranowska-Korczyc, E. Stelmach, B. Paterczyk, K. Maksymiuk, and A. Michalska, "Ultrasmall self-assembly poly(N-isopropylacrylamide-butyl acrylate) (polyNIPAM-BA) thermoresponsive nanoparticles," *J. Colloid Interface Sci.*, vol. 542, pp. 317–324, 2019.
- [243] K. Kumar, V. Penugurti, G. Levi, Y. Mastai, B. Manavathi, and P. Paik, "Bio-inspired synthesis of a hierarchical self-assembled zinc phosphate nanostructure in the presence of cowpea mosaic virus: in vitro cell cycle, proliferation and prospects for tissue regeneration," *Biomed. Mater.*, vol. 13, no. 1, p. 15013, 2017.
- [244] C. Yan, J. Gu, H. Jing, J. Taishi, and R. J. Lee, "Tat-Tagged and Folate-Modified N-

- Succinyl-chitosan (Tat-Suc-FA) Self-assembly Nanoparticle for Therapeutic Delivery OGX-011 to A549 Cells," *Mol. Pharm.*, vol. 14, no. 6, pp. 1898–1905, Jun. 2017.
- [245] L. Liu *et al.*, "Self-assembled nanoparticles based on the c(RGDfk) peptide for the delivery of siRNA targeting the VEGFR2 gene for tumor therapy," *Int. J. Nanomedicine*, vol. 9, pp. 3509–3526, Jul. 2014.
- [246] J. Shi, Z. Xiao, N. Kamaly, and O. C. Farokhzad, "Self-Assembled Targeted Nanoparticles: Evolution of Technologies and Bench to Bedside Translation," Acc. Chem. Res., vol. 44, no. 10, pp. 1123–1134, Oct. 2011.
- [247] K. Y. Choi *et al.*, "Self-assembled hyaluronic acid nanoparticles for active tumor targeting," *Biomaterials*, vol. 31, no. 1, pp. 106–114, 2010.
- [248] H. Tan, R. Santbergen, A. H. M. Smets, and M. Zeman, "Plasmonic Light Trapping in Thin-film Silicon Solar Cells with Improved Self-Assembled Silver Nanoparticles," *Nano Lett.*, vol. 12, no. 8, pp. 4070–4076, Aug. 2012.
- [249] Sampaio, K. C. Beverly, and J. R. Heath, "DC Transport in Self-Assembled 2D Layers of Ag Nanoparticles," *J. Phys. Chem. B*, vol. 105, no. 37, pp. 8797–8800, Sep. 2001.
- [250] M. Gao, B. Richter, S. Kirstein, and H. Möhwald, "Electroluminescence Studies on Self-Assembled Films of PPV and CdSe Nanoparticles," *J. Phys. Chem. B*, vol. 102, no. 21, pp. 4096–4103, May 1998.
- [251] M. Yang, Y. Yang, H. Yang, G. Shen, and R. Yu, "Layer-by-layer self-assembled multilayer films of carbon nanotubes and platinum nanoparticles with polyelectrolyte for the fabrication of biosensors," *Biomaterials*, vol. 27, no. 2, pp. 246–255, 2006.
- [252] H. Radecka, J. Radecki, I. Grabowska, and K. Kurzątkowska, "Electrochemical Sensors and Biosensors Based on Self-Assembled Monolayers: Application of Nanoparticles for Analytical Signals Amplification," in *Functional Nanoparticles for Bioanalysis, Nanomedicine, and Bioelectronic Devices Volume 1*, vol. 1112, American Chemical Society, 2012, pp. 11–293.
- [253] S. Imar, C. Maccato, C. Dickinson, F. Laffir, M. Vagin, and T. McCormac, "Enhancement of Nitrite and Nitrate Electrocatalytic Reduction through the

- Employment of Self-Assembled Layers of Nickel- and Copper-Substituted Crown-Type Heteropolyanions," *Langmuir*, vol. 31, no. 8, pp. 2584–2592, Mar. 2015.
- [254] J.-C. Boyer, L. A Cuccia, and J. Capobianco, "Synthesis of Colloidal Upconverting NaYF 4: Er 3+/Yb 3+ and Tm 3+/Yb 3+ Monodisperse Nanocrystals," *Nano Lett.*, vol. 7, pp. 847–852, 2007.
- [255] O. V Salata, "Applications of nanoparticles in biology and medicine," *J. Nanobiotechnology*, vol. 2, no. 1, p. 3, Apr. 2004.
- [256] J. S. Patton and P. R. Byron, "Inhaling medicines: delivering drugs to the body through the lungs," *Nat. Rev. Drug Discov.*, vol. 6, pp. 67–74, Jan. 2007.
- [257] W. B. Tan, N. Huang, and Y. Zhang, "Ultrafine biocompatible chitosan nanoparticles encapsulating multi-coloured quantum dots for bioapplications," *J. Colloid Interface Sci.*, vol. 310, no. 2, pp. 464–470, 2007.
- [258] S.-T. Yang *et al.*, "Carbon Dots for Optical Imaging in Vivo," *J. Am. Chem. Soc.*, vol. 131, no. 32, pp. 11308–11309, 2009.
- [259] D. K. Yi, S. T. Selvan, S. S. Lee, G. C. Papaefthymiou, D. Kundaliya, and J. Y. Ying, "Silica-Coated Nanocomposites of Magnetic Nanoparticles and Quantum Dots Scheme 1. Synthesis of SiO2/MP-QD Nanocomposites," *J. Am. Chem. Soc*, vol. 127, p. 22, 2005.
- [260] K. Li *et al.*, "Photostable fluorescent organic dots with aggregation-induced emission (AIE dots) for noninvasive long-term cell tracing," *Sci. Rep.*, vol. 3, p. 1150, Jan. 2013.
- [261] B. Zhang, J. Cheng, D. Li, X. Liu, G. Ma, and J. Chang, "A novel method to make hydrophilic quantum dots and its application on biodetection," *Mater. Sci. Eng. B*, vol. 149, no. 1, pp. 87–92, 2008.
- [262] Y. Yang *et al.*, "In Vitro and In Vivo Uncaging and Bioluminescence Imaging by Using Photocaged Upconversion Nanoparticles," *Angew. Chemie Int. Ed.*, vol. 51, no. 13, pp. 3125–3129, 2012.
- [263] L. Cheng, C. Wang, and Z. Liu, "Upconversion nanoparticles and their composite nanostructures for biomedical imaging and cancer therapy," *Nanoscale*, vol. 5, no. 1,

- pp. 23–37, 2013.
- [264] H.-Q. Wang, M. Batentschuk, A. Osvet, L. Pinna, and C. J. Brabec, "Rare-Earth Ion Doped Up-Conversion Materials for Photovoltaic Applications," *Adv. Mater.*, vol. 23, no. 22-23, pp. 2675–2680, 2011.
- [265] H. A. Atwater and A. Polman, "Plasmonics for improved photovoltaic devices," *Nat. Mater.*, vol. 9, pp. 205–213, Feb. 2010.
- [266] A. C. Atre, A. Garc\'\ia-Etxarri, H. Alaeian, and J. A. Dionne, "Toward high-efficiency solar upconversion with plasmonic nanostructures," *J. Opt.*, vol. 14, no. 2, p. 24008, Jan. 2012.
- [267] M. Eichelbaum and K. Rademann, "Plasmonic Enhancement or Energy Transfer? On the Luminescence of Gold-, Silver-, and Lanthanide-Doped Silicate Glasses and Its Potential for Light-Emitting Devices," Adv. Funct. Mater., vol. 19, no. 13, pp. 2045– 2052, 2009.
- [268] X. Huang, "Broadband dye-sensitized upconversion: A promising new platform for future solar upconverter design," *J. Alloys Compd.*, vol. 690, pp. 356–359, 2017.
- [269] B. D. Hall, D. Zanchet, and D. Ugarte, "Estimating nanoparticle size from diffraction measurements," *J. Appl. Crystallogr.*, vol. 33, no. 6, pp. 1335–1341, Dec. 2000.
- [270] L. E. MacKenzie *et al.*, "The theoretical molecular weight of NaYF<sub&gt;4&lt;/sub&gt;:RE upconversion nanoparticles," *bioRxiv*, p. 114744, Jan. 2017.
- [271] D. T. Klier and M. U. Kumke, "Analysing the effect of the crystal structure on upconversion luminescence in Yb3+{,}Er3+-co-doped NaYF4 nanomaterials," *J. Mater. Chem. C*, vol. 3, no. 42, pp. 11228–11238, 2015.
- [272] S. Wilhelm, T. Hirsch, W. M. Patterson, E. Scheucher, T. Mayr, and O. S. Wolfbeis, "Multicolor upconversion nanoparticles for protein conjugation.," *Theranostics*, vol. 3, no. 4, pp. 239–248, 2013.
- [273] H. Assaaoudi, G.-B. Shan, N. Dyck, and G. P. Demopoulos, "Annealing-induced ultra-efficient NIR-to-VIS upconversion of nano-/micro-scale α and β NaYF4:Er3+{,}Yb3+

- crystals," CrystEngComm, vol. 15, no. 23, pp. 4739–4746, 2013.
- [274] G. Chen, T. Y. Ohulchanskyy, R. Kumar, H. Ågren, and P. N. Prasad, "Ultrasmall Monodisperse NaYF4:Yb3+/Tm3+ Nanocrystals with Enhanced Near-Infrared to Near-Infrared Upconversion Photoluminescence," *ACS Nano*, vol. 4, no. 6, pp. 3163–3168, Jun. 2010.
- [275] O. A. Aktsipetrov *et al.*, "Magnetization-induced second- and third-harmonic generation in magnetophotonic crystals," *J. Opt. Soc. Am. B*, vol. 22, no. 1, pp. 176–186, Jan. 2005.
- [276] W. Yu, W. Xu, H. Song, and S. Zhang, "Temperature-dependent upconversion luminescence and dynamics of NaYF4:Yb3+/Er3+ nanocrystals: influence of particle size and crystalline phase," *Dalt. Trans.*, vol. 43, no. 16, pp. 6139–6147, 2014.
- [277] J. Shan, M. Uddi, R. Wei, N. Yao, and Y. Ju, "The Hidden Effects of Particle Shape and Criteria for Evaluating the Upconversion Luminescence of the Lanthanide Doped Nanophosphors," *J. Phys. Chem. C*, vol. 114, no. 6, pp. 2452–2461, Feb. 2010.
- [278] D. Lu, S. K. Cho, S. Ahn, L. Brun, C. J. Summers, and W. Park, "Plasmon Enhancement Mechanism for the Upconversion Processes in NaYF4:Yb3+,Er3+ Nanoparticles: Maxwell versus Förster," ACS Nano, vol. 8, no. 8, pp. 7780–7792, Aug. 2014.
- [279] P. G. and H. U. G. J.F.Suyver, A. Aebischer, S. Garcia-Revilla, "2005, 71," *Phy. Rev. B. Condens. Matter Phys.*, vol. 71, pp. 1–9, 2005.
- [280] J. D. Kingsley, G. E. Fenner, and S. V Galginaitis, "KINETICS AND EFFICIENCY OF INFRARED-TO-VISIBLE CONVERSION IN LaF3:Yb,Er," *Appl. Phys. Lett.*, vol. 15, no. 4, pp. 115–117, 1969.
- [281] H. Song *et al.*, "Three-photon upconversion luminescence phenomenon for the green levels in Er3+/Yb3+ codoped cubic nanocrystalline yttria," *Solid State Commun.*, vol. 132, no. 6, pp. 409–413, 2004.
- [282] L. Li, J. Hu, W. Yang, and A. P. Alivisatos, "Band Gap Variation of Size- and Shape-Controlled Colloidal CdSe Quantum Rods," *Nano Lett.*, vol. 1, no. 7, pp. 349–351, Jul.

- 2001.
- [283] G. Dukovic, F. Wang, D. Song, M. Y. Sfeir, T. F. Heinz, and L. E. Brus, "Structural Dependence of Excitonic Optical Transitions and Band-Gap Energies in Carbon Nanotubes," *Nano Lett.*, vol. 5, no. 11, pp. 2314–2318, Nov. 2005.
- [284] G. Chen, T. Y. Ohulchanskyy, A. Kachynski, H. Ågren, and P. N. Prasad, "Intense Visible and Near-Infrared Upconversion Photoluminescence in Colloidal LiYF4:Er3+ Nanocrystals under Excitation at 1490 nm," ACS Nano, vol. 5, no. 6, pp. 4981–4986, Jun. 2011.
- [285] S. Fischer, N. J. J. Johnson, J. Pichaandi, J. C. Goldschmidt, and F. C. J. M. van Veggel, "Upconverting core-shell nanocrystals with high quantum yield under low irradiance: On the role of isotropic and thick shells," *J. Appl. Phys.*, vol. 118, no. 19, p. 193105, Nov. 2015.
- [286] J.-C. Boyer and F. Veggel, "Absolute Quantum Yield Measurements of Colloidal NaYF4: Er3+, Yb3+ Upconverting Nanoparticles," *Nanoscale*, vol. 2, pp. 1417–1419, Aug. 2010.
- [287] S. Hatami *et al.*, "Absolute photoluminescence quantum yields of IR26 and IR-emissive Cd1–xHgxTe and PbS quantum dots method- and material-inherent challenges," *Nanoscale*, vol. 7, no. 1, pp. 133–143, 2015.
- [288] M. Melnichuk and L. T. Wood, "Direct Kerr electro-optic effect in noncentrosymmetric materials," *Phys. Rev. A*, vol. 82, no. 1, p. 13821, Jul. 2010.
- [289] Y.-H. Chien, K. K. Chan, S. H. K. Yap, and K.-T. Yong, "NIR-responsive nanomaterials and their applications; upconversion nanoparticles and carbon dots: a perspective," *J. Chem. Technol. Biotechnol.*, vol. 93, no. 6, pp. 1519–1528, Jun. 2018.
- [290] D. Astruc, E. Boisselier, and C. Ornelas, "Dendrimers Designed for Functions: From Physical, Photophysical, and Supramolecular Properties to Applications in Sensing, Catalysis, Molecular Electronics, Photonics, and Nanomedicine," *Chem. Rev.*, vol. 110, no. 4, pp. 1857–1959, Apr. 2010.
- [291] C. C. Lee, J. A. MacKay, J. M. J. Fréchet, and F. C. Szoka, "Designing dendrimers for

- biological applications," Nat. Biotechnol., vol. 23, no. 12, pp. 1517–1526, 2005.
- [292] C. ZHANG, L. SUN, Y. ZHANG, and C. YAN, "Rare earth upconversion nanophosphors: synthesis, functionalization and application as biolabels and energy transfer donors," *J. Rare Earths*, vol. 28, no. 6, pp. 807–819, 2010.
- [293] M. Wang, G. Abbineni, A. Clevenger, C. Mao, and S. Xu, "Upconversion nanoparticles: synthesis, surface modification and biological applications," *Nanomedicine Nanotechnology, Biol. Med.*, vol. 7, no. 6, pp. 710–729, 2011.
- [294] G. Chen, H. Qiu, P. N. Prasad, and X. Chen, "Upconversion Nanoparticles: Design, Nanochemistry, and Applications in Theranostics," *Chem. Rev.*, vol. 114, no. 10, pp. 5161–5214, May 2014.
- [295] T. V Esipova *et al.*, "Dendritic upconverting nanoparticles enable in vivo multiphoton microscopy with low-power continuous wave sources," *Proc. Natl. Acad. Sci.*, vol. 109, no. 51, pp. 20826 LP 20831, Dec. 2012.
- [296] L. Wang and Y. Li, "Green upconversion nanocrystals for DNA detection," *Chem. Commun.*, no. 24, pp. 2557–2559, 2006.
- [297] Q. Liu, T. Yang, W. Feng, and F. Li, "Blue-Emissive Upconversion Nanoparticles for Low-Power-Excited Bioimaging in Vivo," *J. Am. Chem. Soc.*, vol. 134, no. 11, pp. 5390–5397, Mar. 2012.
- [298] Z. Li, Y. Zhang, and S. Jiang, "Multicolor Core/Shell-Structured Upconversion Fluorescent Nanoparticles," *Adv. Mater.*, vol. 20, no. 24, pp. 4765–4769, Dec. 2008.
- [299] V. Muhr *et al.*, "Particle-Size-Dependent Förster Resonance Energy Transfer from Upconversion Nanoparticles to Organic Dyes," *Anal. Chem.*, vol. 89, no. 9, pp. 4868–4874, May 2017.
- [300] C. Hazra, V. N. K. B. Adusumalli, and V. Mahalingam, "3,5-Dinitrobenzoic Acid-Capped Upconverting Nanocrystals for the Selective Detection of Melamine," *ACS Appl. Mater. Interfaces*, vol. 6, no. 10, pp. 7833–7839, May 2014.
- [301] Y. Ma, S. Huang, M. Deng, and L. Wang, "White Upconversion Luminescence Nanocrystals for the Simultaneous and Selective Detection of 2,4,6-Trinitrotoluene and

- 2,4,6-Trinitrophenol," ACS Appl. Mater. Interfaces, vol. 6, no. 10, pp. 7790–7796, May 2014.
- [302] L. Y. Ang, M. E. Lim, L. C. Ong, and Y. Zhang, "Applications of upconversion nanoparticles in imaging, detection and therapy," *Nanomedicine*, vol. 6, no. 7, pp. 1273–1288, Sep. 2011.
- [303] L.-L. Li, H.-W. An, B. Peng, R. Zheng, and H. Wang, "Self-assembled nanomaterials: design principles, the nanostructural effect, and their functional mechanisms as antimicrobial or detection agents," *Mater. Horizons*, vol. 6, pp. 1794–1811, 2019.
- [304] G. Pandit, K. Roy, U. Agarwal, and S. Chatterjee, "Self-Assembly Mechanism of a Peptide-Based Drug Delivery Vehicle," *ACS Omega*, vol. 3, no. 3, pp. 3143–3155, Mar. 2018.
- [305] S. Whitelam and R. L. Jack, "The statistical mechanics of dynamic pathways to self-assembly," *Annu. Rev. Phys. Chem.*, vol. 66, pp. 143–163, 2015.
- [306] A. Saini, R. Kaur, N. Singh, A. Kuwar, and N. Kaur, "High Performance Fluorescent Turn-On Probe for Amitriptyline Based on Hybrid Nanoassembly of Organic—Inorganic Nanoparticles," *ACS Appl. Bio Mater.*, vol. 2, no. 1, pp. 135–143, Jan. 2019.
- [307] M. Dolci *et al.*, "Nanoparticle Assembling through Click Chemistry Directed by Mixed SAMs for Magnetic Applications," *ACS Appl. Nano Mater.*, vol. 2, no. 1, pp. 554–565, Jan. 2019.
- [308] D. Perahia, R. Traiphol, and U. H. F. Bunz, "From Molecules to Supramolecular Structure: Self Assembling of Wirelike Poly(p-phenyleneethynylene)s," *Macromolecules*, vol. 34, no. 2, pp. 151–155, Jan. 2001.
- [309] M.-C. Daniel and D. Astruc, "Gold Nanoparticles: Assembly, Supramolecular Chemistry, Quantum-Size-Related Properties, and Applications toward Biology, Catalysis, and Nanotechnology," *Chem. Rev.*, vol. 104, no. 1, pp. 293–346, 2004.
- [310] K. N. Reddy, M. A. H. Shareef, and N. Pandaraiah, "Growth and X-ray study of NaYF4 crystals," *J. Mater. Sci. Lett.*, vol. 2, no. 2, pp. 83–84, 1983.
- [311] M. Lee et al., "Highly Efficient Visible Blue-Emitting Black Phosphorus Quantum

- Dot: Mussel-Inspired Surface Functionalization for Bioapplications," *ACS Omega*, vol. 2, no. 10, pp. 7096–7105, Oct. 2017.
- [312] X. Luo and K. Akimoto, "Upconversion properties in hexagonal-phase NaYF4:Er3+/NaYF4 nanocrystals by off-resonant excitation," *Appl. Surf. Sci.*, vol. 273, pp. 257–260, 2013.
- [313] C. Renero-Lecuna *et al.*, "Origin of the High Upconversion Green Luminescence Efficiency in β-NaYF4:2%Er3+,20%Yb3+," *Chem. Mater.*, vol. 23, no. 15, pp. 3442–3448, Aug. 2011.
- [314] Z. Li, H. Miao, Y. Fu, Y. Liu, R. Zhang, and B. Tang, "Fabrication of NaYF4:Yb,Er Nanoprobes for Cell Imaging Directly by Using the Method of Hydrion Rivalry Aided by Ultrasonic," *Nanoscale Res. Lett.*, vol. 11, no. 1, p. 441, 2016.
- [315] M. He *et al.*, "A general strategy for the synthesis of upconversion rare earth fluoride nanocrystalsvia a novel OA/ionic liquid two-phase system," *Chem. Commun.*, vol. 47, no. 33, pp. 9510–9512, 2011.
- [316] J. A. Capobianco, F. Vetrone, J. C. Boyer, A. Speghini, and M. Bettinelli, "Visible upconversion of Er3+ doped nanocrystalline and bulk Lu2O3," *Opt. Mater. (Amst).*, vol. 19, no. 2, pp. 259–268, 2002.
- [317] H. Guo, N. Dong, M. Yin, W. Zhang, L. Lou, and S. Xia, "Visible Upconversion in Rare Earth Ion-Doped Gd2O3 Nanocrystals," *J. Phys. Chem. B*, vol. 108, no. 50, pp. 19205–19209, Dec. 2004.
- [318] T.-Y. Hsieh *et al.*, "Neurotensin-Conjugated Reduced Graphene Oxide with Multi-Stage Near-Infrared-Triggered Synergic Targeted Neuron Gene Transfection In Vitro and In Vivo for Neurodegenerative Disease Therapy," *Adv. Healthc. Mater.*, vol. 5, no. 23, pp. 3016–3026, Dec. 2016.
- [319] A. Xia *et al.*, "Core–shell NaYF4:Yb3+,Tm3+@FexOy nanocrystals for dual-modality T2-enhanced magnetic resonance and NIR-to-NIR upconversion luminescent imaging of small-animal lymphatic node," *Biomaterials*, vol. 32, no. 29, pp. 7200–7208, 2011.
- [320] L. Yang et al., "Three-photon-excited upconversion luminescence of YVO4 single

- crystal by infrared femtosecond laser irradiation," *Opt. Express*, vol. 13, no. 25, pp. 10157–10162, Dec. 2005.
- [321] L. Yang *et al.*, "Three-photon-excited upconversion luminescence of Ce3\$+\$: YAP crystal by femtosecond laser irradiation," *Opt. Express*, vol. 14, no. 1, pp. 243–247, Jan. 2006.
- [322] X. Shang *et al.*, "Upconversion luminescence mechanisms of Er3+ ions under excitation of an 800 nm laser," *Phys. Chem. Chem. Phys.*, vol. 17, no. 17, pp. 11481–11489, 2015.
- [323] F. Vetrone *et al.*, "Intracellular imaging of HeLa cells by non-functionalized NaYF4: Er3+{,} Yb3+ upconverting nanoparticles," *Nanoscale*, vol. 2, no. 4, pp. 495–498, 2010.
- [324] J. Shen *et al.*, "Tunable Near Infrared to Ultraviolet Upconversion Luminescence Enhancement in (α-NaYF4:Yb,Tm)/CaF2 Core/Shell Nanoparticles for In situ Real-time Recorded Biocompatible Photoactivation," *Small*, vol. 9, no. 19, pp. 3213–3217, Oct. 2013.
- [325] X. Shang *et al.*, "Fine tunable red-green upconversion luminescence from glass ceramic containing 5%Er 3+:NaYF 4 nanocrystals under excitation of two near infrared femtosecond lasers," *J. Appl. Phys.*, vol. 116, no. 6, pp. 063101–1, 2014.
- [326] M. H. Yuan, H. H. Fan, Q. F. Dai, S. Lan, X. Wan, and S. L. Tie, "Upconversion luminescence from aluminoborate glasses doped with Tb3\$+\$, Eu3\$+\$ and Dy3\$+\$ under the excitation of 2.6-μm femtosecond laser pulses," *Opt. Express*, vol. 23, no. 17, pp. 21909–21918, Aug. 2015.
- [327] P. Tzankov *et al.*, "High-power fifth-harmonic generation of femtosecond pulses in the vacuum ultraviolet using a Ti:sapphire laser," *Opt. Express*, vol. 15, no. 10, pp. 6389–6395, May 2007.
- [328] W. Ji *et al.*, "Accurate manipulation of optogenetic proteins with wavelength tunable femtosecond laser system," *J. Appl. Phys.*, vol. 125, no. 16, p. 163105, Apr. 2019.
- [329] Z. Zheng et al., "Aggregation-Induced Nonlinear Optical Effects of AIEgen

- Nanocrystals for Ultra-Deep in Vivo Bio-Imaging." 17-Jul-2019.
- [330] L.-Z. Deng *et al.*, "Tuning up-conversion luminescence in Er3+-doped glass ceramic by phase-shaped femtosecond laser field with optimal feedback control," *Front. Phys.*, vol. 14, no. 1, p. 13602, 2018.
- [331] O. S. Kwon, H. S. Song, J. Conde, H. Il Kim, N. Artzi, and J. H. Kim, "Dual-color emissive upconversion nanocapsules for differential cancer bioimaging in vivo," *ACS Nano*, vol. 10, no. 1, pp. 1512–1521, 2016.
- [332] B. Del Rosal and D. Jaque, "Upconversion nanoparticles for in vivo applications: limitations and future perspectives," *Methods Appl. Fluoresc.*, vol. 7, no. 2, p. 022001, 2019.
- [333] Y. Liu, X. Meng, and W. Bu, "Upconversion-based photodynamic cancer therapy," *Coord. Chem. Rev.*, vol. 379, pp. 82–98, 2019.
- [334] G. Yi *et al.*, "Synthesis, characterization, and biological application of size-controlled nanocrystalline NaYF 4:Yb,Er infrared-to-visible up-conversion phosphors," *Nano Lett.*, vol. 4, no. 11, pp. 2191–2196, 2004.
- [335] J. H. Kim, F. Deng, F. N. Castellano, and J. H. Kim, "Red-to-Blue/Cyan/Green Upconverting Microcapsules for Aqueous- and Dry-Phase Color Tuning and Magnetic Sorting," *ACS Photonics*, vol. 1, no. 4, pp. 382–388, 2014.
- [336] X. Zhang *et al.*, "Engineering the color output in a single upconversion microtube via intervention of the electronic population," *J. Lumin.*, vol. 205, no. January 2018, pp. 374–379, 2019.
- [337] A. Taleb, C. Petit, and M. P. Pileni, "Optical Properties of Self-Assembled 2D and 3D Superlattices of Silver Nanoparticles," *J. Phys. Chem. B*, vol. 102, no. 12, pp. 2214–2220, Mar. 1998.
- [338] M. P. Pileni, A. Taleb, and C. Petit, "Silver metal nanosized particles: Control of particle size, self assemblies in 2D and 3D superlattices and optical properties," *J. Dispers. Sci. Technol.*, vol. 19, no. 2–3, pp. 185–206, Jan. 1998.
- [339] T. Teranishi, M. Hosoe, T. Tanaka, and M. Miyake, "Size Control of Monodispersed Pt

- Nanoparticles and Their 2D Organization by Electrophoretic Deposition," *J. Phys. Chem. B*, vol. 103, no. 19, pp. 3818–3827, May 1999.
- [340] D. V Talapin, E. V Shevchenko, C. B. Murray, A. V Titov, and P. Král, "Dipole–Dipole Interactions in Nanoparticle Superlattices," *Nano Lett.*, vol. 7, no. 5, pp. 1213–1219, May 2007.
- [341] F. J. Di Salvo, D. E. Moncton, and J. V Waszczak, "Electronic properties and superlattice formation in the semimetal  ${\text{TiSe}}_{2}$ ," *Phys. Rev. B*, vol. 14, no. 10, pp. 4321–4328, Nov. 1976.
- [342] M. S. Gudiksen, L. J. Lauhon, J. Wang, D. C. Smith, and C. M. Lieber, "Growth of nanowire superlattice structures for nanoscale photonics and electronics," *Nature*, vol. 415, no. 6872, pp. 617–620, 2002.
- [343] W. Feng *et al.*, "Synthesis of Superlattice InSe Nanosheets with Enhanced Electronic and Optoelectronic Performance," *ACS Appl. Mater. Interfaces*, vol. 11, no. 20, pp. 18511–18516, May 2019.
- [344] M. Jiang, W. Mao, X. Zhou, C. Kan, and D. Shi, "Wavelength-Tunable Waveguide Emissions from Electrically Driven Single ZnO/ZnO:Ga Superlattice Microwires," *ACS Appl. Mater. Interfaces*, vol. 11, no. 12, pp. 11800–11811, Mar. 2019.
- [345] A. A. Shokri and R. Jamshidi, "Optical filtering devices in SiO2/AlGaAs superlattice structures," *Superlattices Microstruct.*, vol. 125, pp. 220–232, 2019.
- [346] C. Guo *et al.*, "Sulfide treatment passivation of mid-/long-wave dual-color infrared detectors based on type-II InAs/GaSb superlattices," *Opt. Quantum Electron.*, vol. 51, no. 3, p. 73, 2019.
- [347] N. A. Kotov, F. C. Meldrum, C. Wu, and J. H. Fendler, "Monoparticulate Layer and Langmuir-Blodgett-Type Multiparticulate Layers of Size-Quantized Cadmium Sulfide Clusters: A Colloid-Chemical Approach to Superlattice Construction," *J. Phys. Chem.*, vol. 98, no. 11, pp. 2735–2738, Mar. 1994.
- [348] F. C. Meldrum, N. A. Kotov, and J. H. Fendler, "Utilization of Surfactant-Stabilized Colloidal Silver Nanocrystallites in the Construction of Mono- and Multiparticulate

- Langmuir-Blodgett Films," Langmuir, vol. 10, no. 7, pp. 2035–2040, Jul. 1994.
- [349] C. B. Murray, C. R. Kagan, and M. G. Bawendi, "Self-Organization of CdSe Nanocrystallites into Three-Dimensional Quantum Dot Superlattices," *Science* (80-. )., vol. 270, no. 5240, pp. 1335–1338, Nov. 1995.
- [350] C. T. Black, C. B. Murray, R. L. Sandstrom, and S. Sun, "Spin-Dependent Tunneling in Self-Assembled Cobalt-Nanocrystal Superlattices," *Science* (80-.)., vol. 290, no. 5494, pp. 1131–1134, Nov. 2000.
- [351] C. P. Collier, R. J. Saykally, J. J. Shiang, S. E. Henrichs, and J. R. Heath, "Reversible Tuning of Silver Quantum Dot Monolayers Through the Metal-Insulator Transition," *Science* (80-.)., vol. 277, no. 5334, pp. 1978–1981, Sep. 1997.
- [352] Y. Hu, J. F. Honek, B. C. Wilson, and Q.-B. Lu, "Design, synthesis and photocytotoxicity of upconversion nanoparticles: Potential applications for near-infrared photodynamic and photothermal therapy," *J. Biophotonics*, vol. 0, no. 0, p. e201900129, Jul. 2019.
- [353] N. M. Idris, M. K. G. Jayakumar, A. Bansal, and Y. Zhang, "Upconversion nanoparticles as versatile light nanotransducers for photoactivation applications," *Chem. Soc. Rev.*, vol. 44, no. 6, pp. 1449–1478, 2015.
- [354] X. Li, F. Zhang, and D. Zhao, "Lab on upconversion nanoparticles: optical properties and applications engineering via designed nanostructure," *Chem. Soc. Rev.*, vol. 44, no. 6, pp. 1346–1378, 2015.
- [355] B. Zhou, B. Shi, D. Jin, and X. Liu, "Controlling upconversion nanocrystals for emerging applications," *Nat. Nanotechnol.*, vol. 10, p. 924, Nov. 2015.
- [356] A. Fernandez-Bravo *et al.*, "Continuous-wave upconverting nanoparticle microlasers," *Nat. Nanotechnol.*, vol. 13, no. 7, pp. 572–577, 2018.
- [357] G. Haider *et al.*, "A Highly-Efficient Single Segment White Random Laser," *ACS Nano*, vol. 12, no. 12, pp. 11847–11859, Dec. 2018.
- [358] P. Du, X. Huang, and J. S. Yu, "Facile synthesis of bifunctional Eu3+-activated NaBiF4 red-emitting nanoparticles for simultaneous white light-emitting diodes and

- field emission displays," Chem. Eng. J., vol. 337, pp. 91–100, 2018.
- [359] A. Kumari, M. Mondal, V. K. Rai, and S. N. Singh, "Photoluminescence study in Ho3+/Tm3+/Yb3+/Li+:Gd2(MoO4)3 nanophosphors for near white light emitting diode and security ink applications," *Methods Appl. Fluoresc.*, vol. 6, no. 1, p. 15003, 2017.
- [360] Z. Qiu, J. Shu, J. Liu, and D. Tang, "Dual-Channel Photoelectrochemical Ratiometric Aptasensor with up-Converting Nanocrystals Using Spatial-Resolved Technique on Homemade 3D Printed Device," *Anal. Chem.*, vol. 91, no. 2, pp. 1260–1268, Jan. 2019.
- [361] P. Du, L. Luo, and J. S. Yu, "Upconversion emission and cathodoluminescence of Er3+-doped NaYbF4 nanoparticles for low-temperature thermometry and field emission displays," *Appl. Phys. A*, vol. 123, no. 3, p. 157, 2017.
- [362] F. Wang and X. Liu, "Multicolor Tuning of Lanthanide-Doped Nanoparticles by Single Wavelength Excitation," *Acc. Chem. Res.*, vol. 47, no. 4, pp. 1378–1385, Apr. 2014.
- [363] X. Huang *et al.*, "Realizing highly efficient multicolor tunable emissions from Tb3+ and Eu3+ co-doped CaGd2(WO4)4 phosphors via energy transfer by single ultraviolet excitation for lighting and display applications," *Dye. Pigment.*, vol. 151, pp. 202–210, 2018.
- [364] J. Zhang, C. Mi, H. Wu, H. Huang, C. Mao, and S. Xu, "Synthesis of NaYF4:Yb/Er/Gd up-conversion luminescent nanoparticles and luminescence resonance energy transfer-based protein detection," *Anal. Biochem.*, vol. 421, no. 2, pp. 673–679, 2012.
- [365] Y. Numata, H. Kobayashi, N. Oonami, Y. Kasai, and H. Tanaka, "Simultaneous determination of oleic and elaidic acids in their mixed solution by Raman spectroscopy," *J. Mol. Struct.*, vol. 1185, pp. 200–204, 2019.
- [366] J. F. Suyver, A. Aebischer, S. Garc\'\ia-Revilla, P. Gerner, and H. U. Güdel, "Anomalous power dependence of sensitized upconversion luminescence," *Phys. Rev. B*, vol. 71, no. 12, pp. 125123(1–9), Mar. 2005.
- [367] J. Cheng, E. H. Hill, Y. Zheng, T. He, and Y. Liu, "Optically active plasmonic resonance in self-assembled nanostructures," *Mater. Chem. Front.*, vol. 2, no. 4, pp.

- 662–678, 2018.
- [368] D. Lu, C. Mao, S. K. Cho, S. Ahn, and W. Park, "Experimental demonstration of plasmon enhanced energy transfer rate in NaYF4:Yb3+,Er3+ upconversion nanoparticles," *Sci. Rep.*, vol. 6, p. 18894, Jan. 2016.
- [369] J. Liu *et al.*, "Recent Advances of Plasmonic Nanoparticles and their Applications," *Materials*, vol. 11, no. 10. 2018.
- [370] N. J. Greybush *et al.*, "Plasmon-Enhanced Upconversion Luminescence in Single Nanophosphor–Nanorod Heterodimers Formed through Template-Assisted Self-Assembly," *ACS Nano*, vol. 8, no. 9, pp. 9482–9491, Sep. 2014.
- [371] L. Wang *et al.*, "Reversible Near-Infrared Light Directed Reflection in a Self-Organized Helical Superstructure Loaded with Upconversion Nanoparticles," *J. Am. Chem. Soc.*, vol. 136, no. 12, pp. 4480–4483, Mar. 2014.
- [372] S. P. Hill, T. Dilbeck, E. Baduell, and K. Hanson, "Integrated Photon Upconversion Solar Cell via Molecular Self-Assembled Bilayers," *ACS Energy Lett.*, vol. 1, no. 1, pp. 3–8, Jul. 2016.
- [373] N. Kimizuka, N. Yanai, and M. Morikawa, "Photon Upconversion and Molecular Solar Energy Storage by Maximizing the Potential of Molecular Self-Assembly," *Langmuir*, vol. 32, no. 47, pp. 12304–12322, Nov. 2016.
- [374] Q. Liu *et al.*, "Multifunctional rare-earth self-assembled nanosystem for tri-modal upconversion luminescence /fluorescence /positron emission tomography imaging," *Biomaterials*, vol. 32, no. 32, pp. 8243–8253, 2011.
- [375] Y. Feng *et al.*, "Assembly of upconversion nanophotosensitizer in vivo to achieve scatheless real-time imaging and selective photodynamic therapy," *Biomaterials*, vol. 201, pp. 33–41, 2019.
- [376] D. Pan et al., "Self-Assembled Porphyrin-Based Nanoparticles with Enhanced Near-Infrared Absorbance for Fluorescence Imaging and Cancer Photodynamic Therapy," ACS Appl. Bio Mater., vol. 2, no. 3, pp. 999–1005, Mar. 2019.
- [377] S. K. Mahajan and J. Parashar, "Upconversion emission of Ag nanoparticles with

- Er3+/Yb3+ ions in tellurite glasses under 980nm laser excitation," *AIP Conf. Proc.*, vol. 2142, no. 1, p. 70001, Aug. 2019.
- [378] S. T. Gentry, S. F. Kendra, and M. W. Bezpalko, "Ostwald Ripening in Metallic Nanoparticles: Stochastic Kinetics," *J. Phys. Chem. C*, vol. 115, no. 26, pp. 12736–12741, Jul. 2011.
- [379] W.-S. Wang, L. Zhen, C.-Y. Xu, W.-Z. Shao, and Z.-L. Chen, "Formation of CdMoO4 porous hollow nanospheres via a self-assembly accompanied with Ostwald ripening process and their photocatalytic performance," *CrystEngComm*, vol. 15, no. 39, pp. 8014–8021, 2013.
- [380] P. W. Voorhees, "Ostwald Ripening of Two-Phase Mixtures," *Annu. Rev. Mater. Sci.*, vol. 22, no. 1, pp. 197–215, Aug. 1992.
- [381] H.-X. Mai, Y.-W. Zhang, L.-D. Sun, and C.-H. Yan, "Size- and Phase-Controlled Synthesis of Monodisperse NaYF4:Yb,Er Nanocrystals from a Unique Delayed Nucleation Pathway Monitored with Upconversion Spectroscopy," *J. Phys. Chem. C*, vol. 111, no. 37, pp. 13730–13739, Sep. 2007.
- [382] N. T. K. Thanh, N. Maclean, and S. Mahiddine, "Mechanisms of Nucleation and Growth of Nanoparticles in Solution," *Chem. Rev.*, vol. 114, no. 15, pp. 7610–7630, Aug. 2014.
- [383] M. A. Watzky and R. G. Finke, "Nanocluster Size-Control and 'Magic Number' Investigations. Experimental Tests of the 'Living-Metal Polymer' Concept and of Mechanism-Based Size-Control Predictions Leading to the Syntheses of Iridium(0) Nanoclusters Centering about Four Sequential Magic," *Chem. Mater.*, vol. 9, no. 12, pp. 3083–3095, Dec. 1997.
- [384] M. A. Watzky, E. E. Finney, and R. G. Finke, "Transition-Metal Nanocluster Size vs Formation Time and the Catalytically Effective Nucleus Number: A Mechanism-Based Treatment," *J. Am. Chem. Soc.*, vol. 130, no. 36, pp. 11959–11969, Sep. 2008.
- [385] C. Besson, E. E. Finney, and R. G. Finke, "A Mechanism for Transition-Metal Nanoparticle Self-Assembly," *J. Am. Chem. Soc.*, vol. 127, no. 22, pp. 8179–8184, Jun.

2005.

- [386] S. Yao *et al.*, "Insights into the Formation Mechanism of Rhodium Nanocubes," *J. Phys. Chem. C*, vol. 116, no. 28, pp. 15076–15086, Jul. 2012.
- [387] V. K. LaMer and R. H. Dinegar, "Theory, Production and Mechanism of Formation of Monodispersed Hydrosols," *J. Am. Chem. Soc.*, vol. 72, no. 11, pp. 4847–4854, Nov. 1950.
- [388] V. K. La Mer, "Nucleation in Phase Transitions.," *Ind. Eng. Chem.*, vol. 44, no. 6, pp. 1270–1277, Jun. 1952.

## Synthesis and Design of Upconversion Nanostructures and their Luminescence Properties

by Monami Das Modak

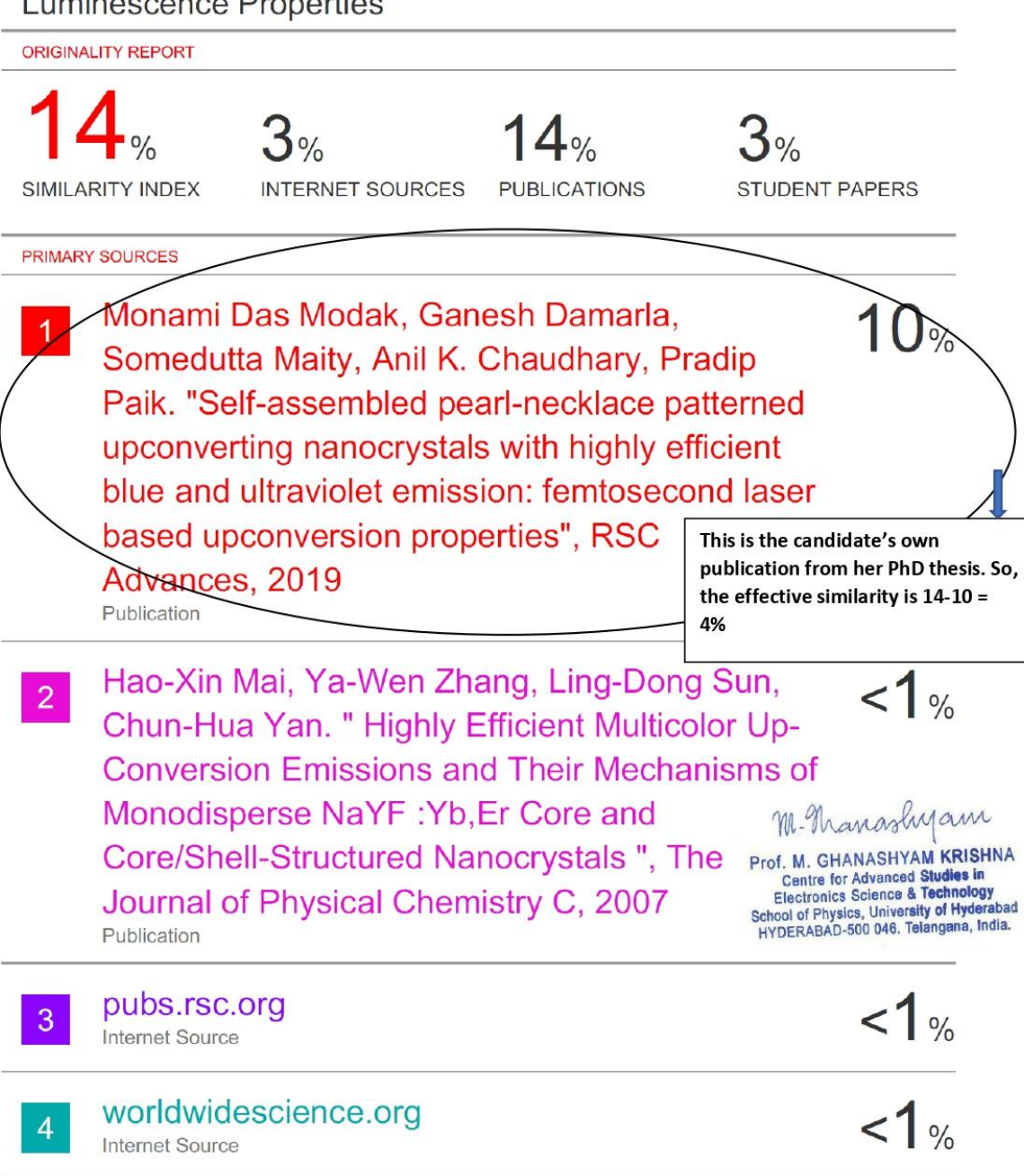
Submission date: 08-Aug-2020 08:00AM (UTC+0530)

**Submission ID: 1367153400** 

File name: Monami\_PhD\_Dissertation.pdf (5.82M)

Word count: 38067 Character count: 216221

## Synthesis and Design of Upconversion Nanostructures and their Luminescence Properties



5	Submitted to University of Leeds Student Paper	<1%
6	Cedric Bouzigues, Thierry Gacoin, Antigoni Alexandrou. "Biological Applications of Rare- Earth Based Nanoparticles", ACS Nano, 2011 Publication	<1%
7	aip.scitation.org Internet Source	<1%
8	pubs.acs.org Internet Source	<1%
9	Submitted to Delhi Technological University Student Paper	<1%
10	Damarla Ganesh, Elaprolu Narsimha Rao, Mottamchetty Venkatesh, Kommu Nagarjuna et al. "Time-Domain Terahertz Spectroscopy and Density Functional Theory Studies of Nitro/Nitrogen-Rich Aryl-Tetrazole Derivatives", ACS Omega, 2020	<1%
11	pure.uva.nl Internet Source	<1%
12	www.freepatentsonline.com Internet Source	<1%
13	Chen, Guanying, Hailong Qiu, Paras N. Prasad, and Xiaoyuan Chen. "Upconversion	<1%

## Nanoparticles: Design, Nanochemistry, and Applications in Theranostics", Chemical Reviews

Publication

Annapoorani, K., N. Suriya Murthy, T.R. Ravindran, and K. Marimuthu. "Influence of Er3+ ion concentration on spectroscopic properties and luminescence behavior in Er3+ doped Strontium telluroborate glasses", Journal of Luminescence, 2016.

<1%

Xiangfu Wang, Jingtang Xu, Jihong Yu, Yanyan Bu, Jose Marques-Hueso, Xiaohong Yan.
"Morphology control, spectrum modification and extended optical applications of rare earth ions doped phosphors", Physical Chemistry Chemical Physics, 2020

<1%

Fiorenzo Vetrone, J. Christopher Boyer, John A. Capobianco, Adolfo Speghini, Marco Bettinelli. "
Effect of Yb Codoping on the Upconversion
Emission in Nanocrystalline Y O :Er ", The
Journal of Physical Chemistry B, 2003
Publication

<1%

link.springer.com

Publication

<1%

John-Christopher Boyer, Louis A. Cuccia, John

A. Capobianco. "Synthesis of Colloidal <1% Upconverting NaYF: Er /Yb and Tm /Yb Monodisperse Nanocrystals ", Nano Letters, 2007 Publication Jintao Kong, Xiaoying Shang, Wei Zheng, <1% 19 Xueyuan Chen, Datao Tu, Meng Wang, Jun Song, Junle Qu. "Revisiting the Luminescence Decay Kinetics of Energy Transfer Upconversion", The Journal of Physical Chemistry Letters, 2020 Publication nanoscalereslett.springeropen.com <1% 20 Internet Source G. Cabello-Guzmán, C. Caro-Díaz, A. 21 Fernandez-Perez, G.E. Buono-Core, B. Chornik. "Study of the influence of Er/Ln co-doping in La2O3 thin films on their up-conversion properties (where Ln = Ho or Nd)", Optical Materials, 2020 Publication Angang Dong, Xingchen Ye, Jun Chen, Yijin <1% 22 Kang, Thomas Gordon, James M. Kikkawa, Christopher B. Murray. "A Generalized Ligand-**Exchange Strategy Enabling Sequential Surface** Functionalization of Colloidal Nanocrystals", Journal of the American Chemical Society, 2011 Publication

<1% Kunmeng Li, Enlv Hong, Bing Wang, Zhiyu 23 Wang, Liwen Zhang, Ruixia Hu, Baiqi Wang. "Advances in the application of upconversion nanoparticles for detecting and treating cancers", Photodiagnosis and Photodynamic Therapy, 2019 Publication Submitted to Birla Institute of Technology and <1% 24 Science Pilani Student Paper Submitted to Savitribai Phule Pune University 25 Student Paper Liang, Zhiqin, Yue Cui, Suling Zhao, Lijiao Tian, 26 Junjie Zhang, and Zheng Xu. "The enhanced upconversion fluorescence and almost unchanged particle size of β-NaYF4:Yb3+, Er3+ nanoparticles by codoping with K+ ions", Journal of Alloys and Compounds, 2014. Publication Hao Dong, Shuo-Ren Du, Xiao-Yu Zheng, <1% Guang-Ming Lyu, Ling-Dong Sun, Lin-Dong Li, Pei-Zhi Zhang, Chao Zhang, Chun-Hua Yan. "Lanthanide Nanoparticles: From Design toward Bioimaging and Therapy", Chemical Reviews, 2015 Publication

28	Ding, Q "Investigation of up-conversion luminescent properties of Er^3^+/Yb^3^+ codoped ZrO"2-Al"2O"3 powders", Optical Materials, 200703 Publication	<1%
29	Submitted to Chungnam National University Student Paper	<1%
30	onlinelibrary.wiley.com Internet Source	<1%
31	Bu, Y "Preparation and upconversion properties of Ba"2ErF"7 and Ba"2ErF"7:Yb^3^+ powders", Journal of Luminescence, 201001	<1%
32	D. T. Klier, M. U. Kumke. "Analysing the effect of the crystal structure on upconversion luminescence in Yb ,Er -co-doped NaYF nanomaterials ", Journal of Materials Chemistry C, 2015	<1%
33	K. Naveen Kumar, L. Vijayalakshmi, Jungwook Choi. "Investigation of Upconversion Photoluminescence of Yb /Er :NaLaMgWO Noncytotoxic Double-Perovskite Nanophosphors ", Inorganic Chemistry, 2019	<1%
34	Submitted to Universiti Teknologi Malaysia	

	Student Paper	<1%
35	Submitted to University of Central Florida Student Paper	<1%
36	etd.lib.metu.edu.tr Internet Source	<1%
37	Aldahiri, Reema Hassan. "Corrosion Inhibition Study of Selected Metals in Acidic Medium by Eco-Friendly Plant Extracts Doped with Metallic Oxide Nanoparticles = در اسة تثبيط التآكل لمعادن مختارة عنادة صديقة للبيئة مطعمة في الوسط الحمضي باستخدام مستخلصات نباتية صديقة للبيئة مطعمة في الوسط الحمضي باستخدام مستخلصات نباتية صديقة للبيئة الصغر في المناهية الصغر (King Abdulaziz University: Scientific Publishing Centre, 2020 Publication	<1%
38	Ye Chang-Hui. "Optical Properties of Self- Organized PbS Quantum Dot Superlattices", Chinese Physics Letters, 10/01/2000	<1%
39	Xiaofei Shi, Maxim S. Molokeev, Xuejiao Wang, Zhihao Wang, Qi Zhu, Ji-Guang Li. " Crystal Structure of NaLuW O ·2H O and Down/Upconversion Luminescence of the Derived NaLu(WO): Yb/Ln Phosphors (Ln = Ho, Er, Tm) ", Inorganic Chemistry, 2018	<1%
40	Submitted to University of Strathclyde	

	Student Paper	<1%
41	Submitted to Universiti Sains Malaysia Student Paper	<1%
42	Submitted to Tampereen teknillinen yliopisto Student Paper	<1%
43	Helmut Schäfer. "Synthesis of Hexagonal Yb <sup>3+</sup> ,Er <sup>3+</sup> -Doped NaYF <sub>4</sub> Nanocrystals at Low Temperature", Advanced Functional Materials, 08/31/2009 Publication	<1%
44	vtechworks.lib.vt.edu Internet Source	<1%
45	www.everbeenmagnet.com Internet Source	<1%
46	Submitted to Mapua Institute of Technology Student Paper	<1%
47	Qin, G "Infrared-to-visible upconversion luminescence of Er^3^+ and Yb^3^+ co-doped germanate glass", Journal of Non-Crystalline Solids, 20041101	<1%
48	"X-Ray Spectrometry: Recent Technological Advances", Wiley, 2004 Publication	<1%

49	Tian, Y "Morphology and phase evolvement of Yb^3^+/Er^3^+ co-doped NaYF"4 microtubes prepared with YF"3 submicrospindles as precursor", Journal of Alloys and Compounds, 20111013 Publication	<1%
50	pesona.mmu.edu.my Internet Source	<1%
51	Submitted to Kingston University Student Paper	<1%
52	Magda A. Antoniak, Szymon J. Zelewski, Robert Oliva, Andrzej Żak, Robert Kudrawiec, Marcin Nyk. "Combined Temperature and Pressure Sensing Using Luminescent NaBiF: Yb,Er Nanoparticles ", ACS Applied Nano Materials, 2020 Publication	<1%
53	Yadong Li. "A general strategy for nanocrystal synthesis", Nature, 09/01/2005	<1%
54	Submitted to Institute of Graduate Studies, UiTM Student Paper	<1%
55	inldigitallibrary.inl.gov Internet Source	<1%
56	Submitted to Middle East Technical University Student Paper	<1%

57	Hussain , Mohammad Musarraf. "Development of New Sensors for the Detection of Bio-Molecules and Heavy Metal Ions = تطوير حساسات المعادن الثقيلة المعادن الثقيلة ", King المعادن الثقيلة كالمعادن الثقيلة (Centre Publication	<1%
58	Submitted to Macquarie University Student Paper	<1%
59	Gnach, Anna, and Artur Bednarkiewicz.  "Lanthanide-doped up-converting nanoparticles: Merits and challenges", Nano Today, 2012.  Publication	<1%
60	Submitted to University of Durham Student Paper	<1%
61	Submitted to Manipal University Student Paper	<1%
62		<1 <sub>%</sub>

Mohd Azam, Vineet Kumar Rai. " Effect of the

64	Addition of Pb O and TiO on the Optical Properties of Er /Yb :TeO –WO Glasses ", ACS Omega, 2019 Publication	<1%
65	Huang, Jing, Yantang Huang, Tianjiao Wu, Yu Huang, and Peijin Zhang. "High efficiency white luminescence in Tm3+/Er3+/Yb3+ tri-doped oxyfluoride glass ceramic microsphere pumped by 976nm laser", Journal of Luminescence, 2015.  Publication	<1%
66	Lu, Dawei, Suehyun K. Cho, Sungmo Ahn, Loic Brun, Christopher J. Summers, and Wounjhang Park. "Plasmon Enhancement Mechanism for the Upconversion Processes in NaYF4:Yb3+,Er3+ Nanoparticles: Maxwell versus Förster", ACS Nano Publication	<1%
67	Submitted to Imperial College of Science, Technology and Medicine Student Paper	<1%
Exclud	e quotes On Exclude matches < 14 words	

Exclude bibliography